Shocks, Superbubbles, and Filaments: Investigations into Large Scale Gas Motions in Giant Molecular Clouds

by

Andrew Richard Pon
BSc, University of Calgary, 2008

A Dissertation Submitted in Partial Fulfillment of the
Requirements for the Degree of

DOCTOR OF PHILOSOPHY

in the Department of Physics and Astronomy

Shocks, Superbubbles, and Filaments: Investigations into Large Scale Gas Motions in Giant Molecular Clouds

by

Andrew Richard Pon
BSc, University of Calgary, 2008

Supervisory Committee

Dr. Doug Johnstone, Co-Supervisor
(Department of Physics and Astronomy)

Dr. Jon Willis, Co-Supervisor
(Department of Physics and Astronomy)

Dr. Charles Curry, Outside Member
(School of Earth and Ocean Sciences)

Supervisory Committee

Dr. Doug Johnstone, Co-Supervisor
(Department of Physics and Astronomy)

Dr. Jon Willis, Co-Supervisor
(Department of Physics and Astronomy)

Dr. Charles Curry, Outside Member
(School of Earth and Ocean Sciences)

ABSTRACT

Giant molecular clouds (GMCs), out of which stars form, are complex, dynamic systems, which both influence and are shaped by the process of star formation. In this dissertation, I examine three different facets of the dynamical motions within GMCs.

Collapse modes in different dimensional objects. Molecular clouds contain lower dimensional substructures, such as filaments and sheets. The collapse properties of finite filaments and sheets differ from those of spherical objects as well as infinite sheets and filaments. I examine the importance of local collapse modes of small central perturbations, relative to global collapse modes, in different dimensional objects to elucidate whether strong perturbations are required for molecular clouds to fragment to form stars. I also calculate the dependence of the global collapse timescale upon the aspect ratio of sheets and filaments. I find that lower dimensional objects are more readily fragmented, and that for a constant density, lower dimensional objects and clouds with larger aspect ratios collapse more slowly. An edge-driven collapse mode also exists in sheets and filaments and is most important in elongated filaments. The failure to consider the geometry of a gas cloud is shown to lead to an overestimation of the star formation rate by up to an order of magnitude.

Molecular tracers of turbulent energy dissipation. Molecular clouds contain supersonic turbulence that simulations predict will decay rapidly via shocks. I use shock models to predict which species emit the majority of the turbulent energy dissipated in shocks and find that carbon monoxide, CO, is primarily responsible for radiating away this energy. By combining these shock models with estimates for the turbulent energy dissipation rate of molecular clouds, I predict the expected shock spectra of CO from molecular clouds. I compare the results of these shock models to predictions for the emission from the unshocked gas in GMCs and show that mid-to-high rotational transitions of CO (e.g., J= 8 $\rightarrow$ 7), should be dominated by shocked gas emission and should trace the turbulent energy being dissipated in molecular clouds.

Orion-Eridanus superbubble. The nearby Orion star forming region has created a large bubble of hot plasma in the local interstellar medium referred to as the Orion-Eridanus superbubble. This bubble is unusual in that it is highly elongated, is believed to be oriented roughly parallel to the galactic plane, and contains bright filamentary features on the Eridanus side. I fit models for a wind driven bubble in an exponential atmosphere to the Orion-Eridanus superbubble and show that the elongation of the bubble cannot be explained by such a model in which the scale height of the galactic disk is the typical value of 150 pc. Either a much smaller scale height must be adopted or some additional physics must be added to the model. I also show that the Eridanus filaments cannot be equilibrium objects ionized by the Orion star forming region.

Contents

List of Tables

List of Figures

ACKNOWLEDGEMENTS

I would first like to thank my family for all of their support, love, and encouragement in getting to this point in my education. I would also like to thank my supervisor, Doug Johnstone, for continuing to push me to look at new aspects of my projects and for providing a seemingly unending stream of interesting scientific ideas to examine. Also, my thanks to my committee for their continuing efforts in keeping me on track to graduate. The rest of the graduate students, and post-docs, that have been at UVic or HIA during my graduate career have also provided much needed levity and breaks from research and writing, as well as invaluable support and guidance in all things astronomical. It has been an absolute pleasure to become friends with all of the astronomy group out in Victoria. In particular, the star formation group has been a wonderful resource to bounce ideas off of, solve coding issues, or just vent about current events to. I also want to thank AJ Maxwell in particular for just plain being awesome and to thank Sara Cox for letting me share this journey with her.

And would it have been worth it, after all,
After the cups, the marmalade, the tea,
Among the porcelain, among some talk of you and me,
Would it have been worth while,
To have bitten off the matter with a smile,
To have squeezed the universe into a ball
To roll it toward some overwhelming question,
To say: "I am Lazarus, come from the dead,
Come back to tell you all, I shall tell you all"
T.S. Eliot

DEDICATION

To all of those no longer with us.

Chapter 1

Introduction

Do I dare
Disturb the universe?
In a minute there is time
For decisions and revisions which a minute will reverse.
T.S. Eliot

By energy, the Universe is 69% dark energy, 26% dark matter and only 4.8% baryonic matter (Planck Collaboration et al., 2013). Stars make up 10% of the baryonic matter and thus, only represent 0.5% of the Universe's energy density (Ryden, 2003). The cosmic microwave background composes 95% of the total energy density of photons in the Universe (Dole et al., 2006). Optical photons, primarily from stars, and infrared photons, primarily due to the reprocessing of optical starlight by dust grains, have roughly equivalent energy densities and account for almost all of the remaining photon energy density of the Universe (Dole et al., 2006).

While only a small component of the Universe, stars are critically important to the evolution and observation of many astrophysical systems. Stars serve as one of the most important tracers of baryonic matter in the Universe. The motions of stars also provide valuable information about the dark matter content of the universe (e.g., Oort 1932; Zwicky 1933), and the light emitted during the explosions of white dwarves, in type Ia supernovae, has been used to identify and study dark energy (e.g., Riess et al. 1998). Life, as we know it, develops on planetary systems orbiting stars, such that the primary source of energy for life is stars. Stars, through their lives and deaths, are also primarily responsible for the creation of most elements heavier than helium in the Universe.

Stars are not static, ever lasting objects, but rather, are continually being formed and dying throughout the Universe. All stages of stellar lifecycles are active areas of research, including the processes through which stars are formed. While a general picture of star formation has emerged, there are still numerous details that are still very uncertain in the current model of star formation.

1.1 STAR FORMATION

Stars are often divided by mass into high-mass stars and low-mass stars, with the division based roughly on the notion that high-mass stars are stars massive enough to produce a core collapse supernova. The dividing point between low-mass stars and high-mass stars is typically chosen to be around eight solar masses (McKee & Ostriker, 2007), where one solar mass is 1.9891×10^{33} g (Wilkins, 1989). The initial mass function of stars (IMF), denoting the relative number of stars of each mass formed, shows that low-mass stars are much more abundant than high-mass stars by number and total mass (e.g., Salpeter 1955; Kroupa 2001; Chabrier 2005). High-mass stars, however, dominate the stellar energy budget of the Galaxy, because of the large mass dependence of stellar luminosity (e.g., Zinnecker & Yorke 2007). The strong winds, ionizing radiation fluxes and supernova explosions from high-mass stars also have significant impacts on the dynamics of the interstellar medium (ISM) around sites of high-mass star forming regions (e.g., Zinnecker & Yorke 2007). Due to the different physical processes that become important with higher mass stars, star formation is often broken down into low-mass and high-mass star formation.

Most stars form within giant molecular clouds (GMCs) (Lada & Lada, 2003). In particular, low-mass stars form from gas overdensities, which have densities on the order of 10^6 particles per cubic centimeter and sizes of 0.1 parsecs, that are referred to as prestellar cores (Stahler & Palla, 2005; Di Francesco et al., 2007). One parsec is 3.0857×10^{18} cm, or approximately 3 light years (Wilkins, 1989). Figure 1.1 shows Barnard 68 (B68), which has the properties of a typical prestellar core, although B68 is more isolated than most cores. Prestellar cores have lower velocity dispersions than their surrounding molecular clouds (Pineda et al., 2010) and, as star formation proceeds, these cores gravitationally collapse to form hydrostatically supported, gravitationally bound central objects composed primarily of molecular hydrogen, which are labeled first hydrostatic cores. The first hydrostatic core stage is a very short lived stage, lasting only a few thousand years (e.g., Omukai 2007), and

thus, while this stage was first predicted by Larson (1969), no confirmed detection of a first hydrostatic core has yet to have been made. There are, however, numerous first hydrostatic core candidates in the literature (e.g., Enoch et al. 2010; Chen et al. 2010; Dunham et al. 2011; Pineda et al. 2011; Schnee et al. 2012). As a first hydrostatic core accretes additional mass from its surrounding envelope, the temperature at the center of the core must increase in order for the thermal pressure of the core to remain balanced against the additional weight of the outer layers of the core. Once the temperature in a first hydrostatic core increases to approximately 2000 K, the molecular hydrogen dissociates and the core collapses once again (e.g., Omukai 2007). A second, smaller hydrostatic core eventually forms and this object is referred to as a protostar.

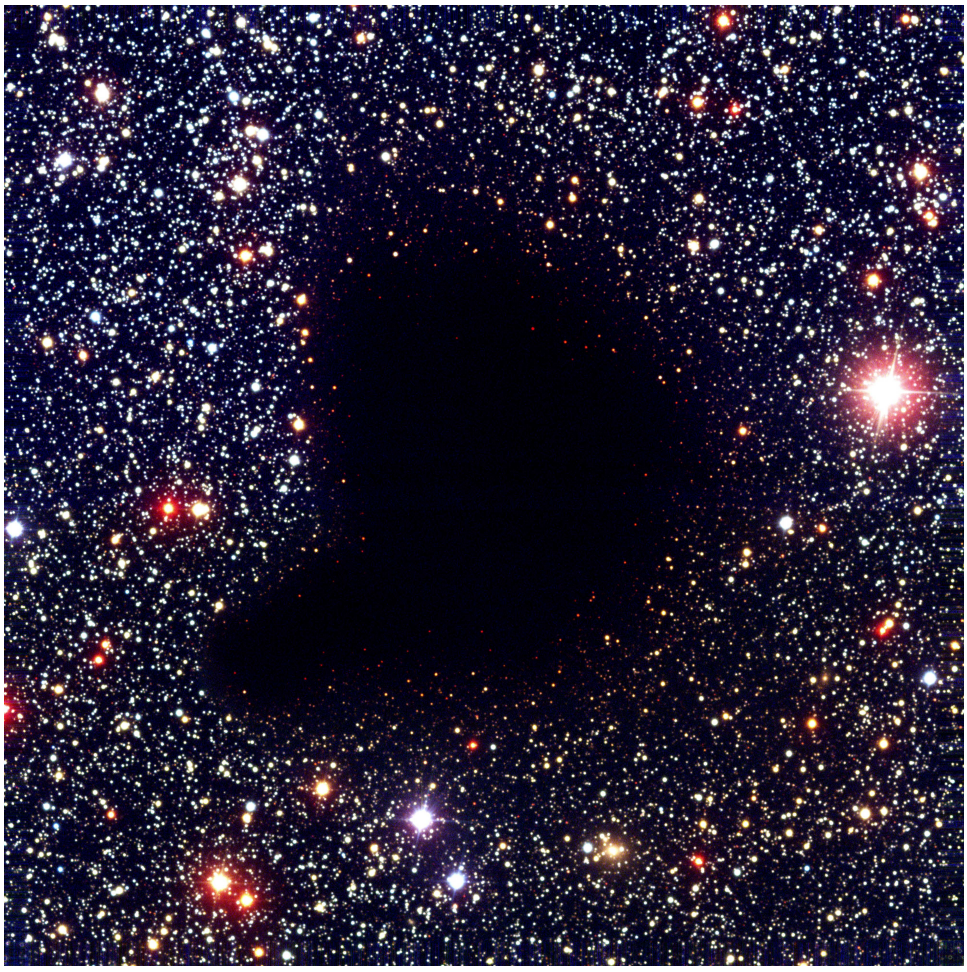

Figure 1.1: Barnard 68 (B68), which has the properties of a typical prestellar core, other than being more isolated than is typical. Image credit: ESO.

There are four general phases of low-mass protostellar evolution. Depending on whether protostars are classified based upon their intrinsic physical state or their observable emitted light, they are split into four "stages" or "classes", respectively. These parallel systems have been set up such that each stage roughly reflects what is occurring within protostellar systems of the same class, although this one to one relationship of class and stage does not hold for all objects (Evans et al., 2009). Stage 0 protostars are the youngest protostars and are protostars with masses less than the mass in their envelopes and disks (Andre et al., 1993). At this stage, a protostar will accrete gas from its surrounding envelope and a significant molecular outflow and accretion disk will develop. A class 0 protostar is defined as being an object where either the bolometric temperature is less than 70 K (Chen et al., 1995) or the total submillimeter luminosity is less than 0.5% of the total bolometric luminosity of the system (Andre et al., 1993), indicating that there is little flux coming directly from the central object. Once the mass of a protostar becomes greater than the surrounding envelope and disk, the protostar is considered to be a stage I protostar (Crapsi et al., 2008). The observational characteristics of a class I protostar is that it has a near infrared (2 μm) to mid-infrared (20 μm) slope greater than 0.3, such that there is still significant flux coming from the envelope but some flux coming from the central object. Upon the complete dissipation of the envelope, the object becomes a stage II protostar (Evans et al., 2009) and the corresponding class II protostar is one where the two to 20 micron slope is between -2 and zero (Lada, 1987). For a class II protostar, the central object provides most of the flux, but there is still considerable infrared excess emission coming from the disk around the protostar. The final stage of protostellar evolution, stage III, occurs when the disk dissipates (Evans et al., 2009). The corresponding class III object has a two to 20 micron slope less than -2, as the far infrared disk emission becomes negligible (Lada, 1987). The initiation of nuclear burning in the core of an object denotes the transition from the object being a protostar to being a main sequence star. Figure 1.2 shows the spectral energy distributions (SEDs) for these protostellar classes. For reviews of these classes, see Andre et al. (2000) and McKee & Ostriker (2007).

High-mass star formation differs from low-mass star formation in that a high-mass central protostar must accrete greater amounts of gas, even though the high-mass protostar is more luminous and produces a higher radiation pressure (e.g, Zinnecker & Yorke 2007). High-mass star formation typically occurs in the largest and densest giant molecular clouds (Zinnecker & Yorke, 2007). For instance, some infrared dark

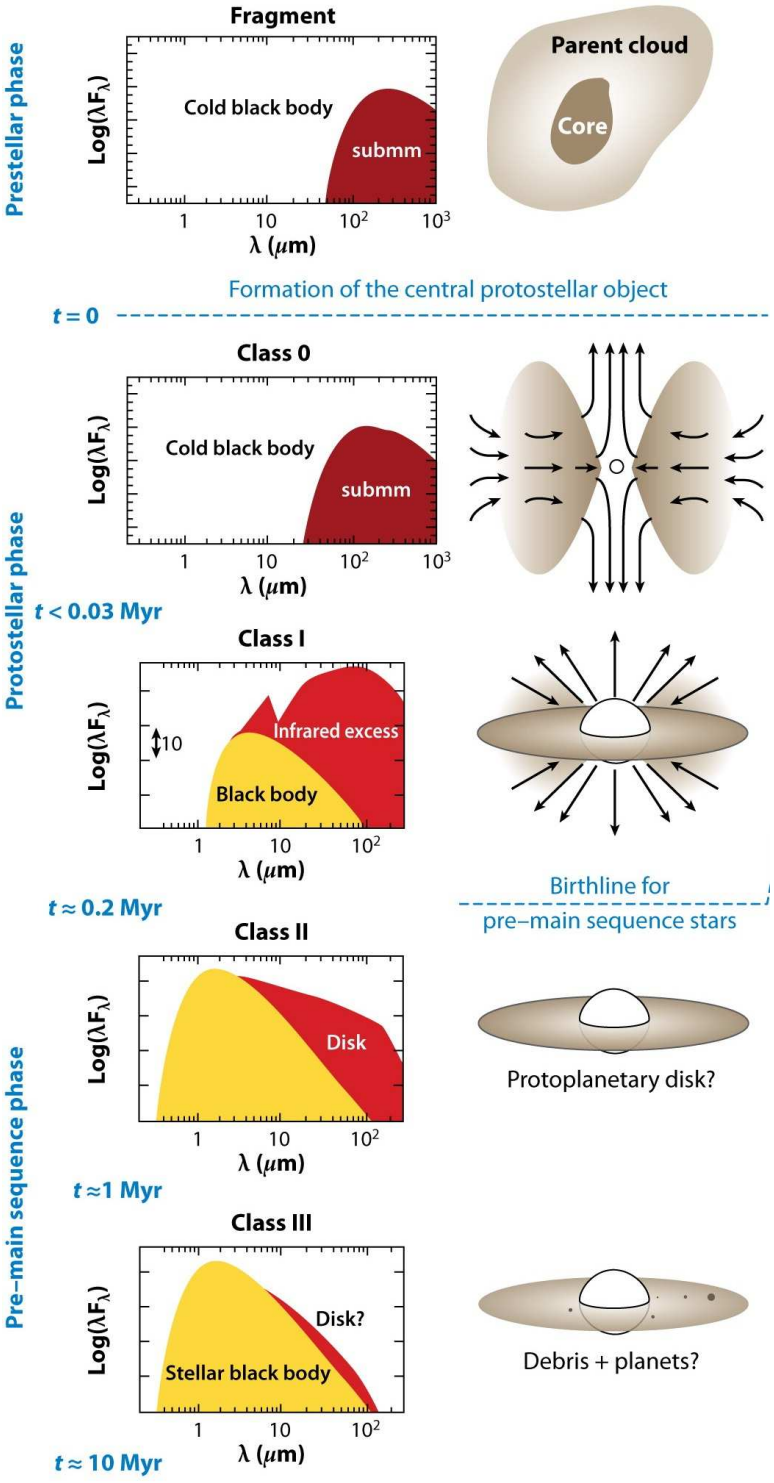

Figure 1.2: Spectral energy distributions of the different protostellar classes are shown in the left hand column. The right hand column shows a rough sketch of what is occurring in the protostellar system during each class. This figure is taken from Dauphas & Chaussidon (2011).

clouds (IRDCs), which are filamentary cloud structures with large enough column densities to appear dark against the eight micron Galactic background, are known to be the sites of high-mass star formation (Rathborne et al., 2006). These IRDCs have velocity dispersions between two and ten km s^{-1}, similar to but slightly higher than low-mass star forming regions, and have typical densities closer to 10^5 cm^{-3}, rather than 10^3 cm^{-3} as in low-mass star forming regions (Rathborne et al., 2006).

The monolithic collapse model for high-mass star formation has high-mass star formation occurring as a scaled up version of low-mass star formation (McKee & Tan, 2003; Krumholz & McKee, 2008). In this model, high-mass stars form in relatively isolated, high-mass starless cores and the final mass of a star is dependent only upon the initial mass of its starless core. The competitive accretion model for high-mass star formation, on the other hand, suggests that in high-mass star forming regions, stars accrete from both their gravitationally bound, surrounding cores and from the ambient gas in their surroundings (Bonnell et al., 1998, 2004). In this competitive accretion model, the final mass of a star is independent of the mass of its prestellar core and stars at the center of a cluster grow to be more massive because more material is funneled to the center of the cluster by the global potential of the cluster. It should be noted that both of these processes, monolithic collapse and competitive accretion, also take place in low-mass star formation, although competitive accretion is typically considered more in the context of high-mass star formation. It has also been proposed that the most massive stars may also form from the mergers of multiple protostars and prestellar cores (Bonnell & Bate, 2002).

While understanding the physics of collapsing prestellar cores and the subsequent evolution of protostars is clearly important for deciphering the process of star formation, such knowledge alone is not sufficient to fully characterize star formation. Prestellar cores must first be assembled within large complexes of molecular gas, referred to as giant molecular clouds (Stahler & Palla, 2005). The properties of the ambient gas in GMCs and the nature of the interplay between this gas and star forming cores have significant impacts on the process of star formation and must be understood to obtain a complete picture of star formation.

1.2 GIANT MOLECULAR CLOUDS

GMCs typically have masses between ten thousand and ten million solar masses (McKee & Ostriker, 2007), are between one and 100 parsecs in size (Solomon et al.,

1987) and have mean densities on the order of 100 to 1000 particles cm^{-3} (McKee & Ostriker, 2007). The gas in GMCs is extremely dilute compared to terrestrial gases, as the Earth's atmosphere has a density approximately 16 magnitudes larger than GMCs. While the mean free path length of a gas particle in a GMC is on the order of a hundred million kilometers and the time between collisions of gas particles is on the order of years, the gas in a GMC can still be treated as a fluid since the relevant length scales and timescales for processes in GMCs are much larger.

1.2.1 Composition

Giant molecular clouds are composed primarily of molecular gas, as opposed to the rest of the interstellar medium, which is primarily composed of atomic or ionized gas. The interiors of GMCs are also not in pressure equilibrium with the interstellar medium, as the self-gravity of a GMC allows for the interior of the GMC to reach higher pressures than the ISM (Stahler & Palla, 2005).

The interiors of molecular clouds have a rich molecular chemistry, with well over 200 molecules discovered to date (Tielens, 2005). Molecules that have been detected in the interstellar medium include water, N_2H^+, CS, HCO^+, NH_3, SiO, CH^+, methanol, ethanol, HC_9N and even Buckminsterfullerene (e.g., Arce et al. 2007; Pon et al. 2009; Godard et al. 2009; Bergin et al. 2010; Sakai et al. 2010; Cami et al. 2010; Sellgren et al. 2010). The wide range of detectable molecular species allows for observations of numerous environments, as various species and transitions probe different physical conditions. For instance, molecular species freeze out of the gas phase at differing extinctions, by accreting onto dust grains, and some transitions, such as low J transitions of ^{12}CO, tend to be optically thick, such that they preferentially trace the exteriors of molecular clouds (e.g., Di Francesco et al. 2007). A molecular transition will also generally be most sensitive to gas with a density near the critical density of the transition, which is the density at which the populations of the two relevant states for the transition become primarily populated by collisions (Tielens, 2005). The critical density for a transition, n_{crit}, is given by

$$n_{crit} = \frac{A}{\gamma}, \tag{1.1}$$

where A is the Einstein A coefficient of the transition, denoting the spontaneous emission rate of the transition, and γ is the collisional de-excitation coefficient of the

transition.

At the very edge of a GMC, the ultraviolet photons of the interstellar radiation field (ISRF) control the chemistry of the gas and, as such, this region is referred to as a photodissociated or photon dominated region (PDR). In a PDR, the ultraviolet (UV) flux is high enough that most species are either in an atomic or ionic phase (Wolfire et al., 2010). Once the ultraviolet photons of the ISRF are attenuated to the point where molecular hydrogen is not readily dissociated, most of the atomic hydrogen in the GMC is converted into molecular hydrogen (Stahler & Palla, 2005). At slightly higher extinctions, the second most abundant molecule in GMCs, CO, begins to form, but the dominant component by mass in GMCs is by far H_2, as the mass fraction of CO is only approximately 10^{-4} (Glover & Mac Low, 2011).

The exterior layer of a GMC, in which H_2 exists but CO does not, has been given the name of dark molecular gas (Wolfire et al., 2010). This name comes from the fact that CO is often used to trace the structure of GMCs, as H_2 emits very weakly (Solomon et al., 1987). H_2 emission is weak because H_2 does not have a permanent electric dipole and because the lowest energy rotational transition of H_2 corresponds to a temperature on the order of thousands of Kelvin (Stahler & Palla, 2005), whereas the mean gas temperature of a GMC is on the order of 20 K (Glover & Mac Low, 2011).

The 21 cm line of atomic hydrogen provides an excellent tracer of the neutral atomic hydrogen in the cool, neutral portion of the ISM (e.g., Kalberla et al. 2005). This 21 cm line arises from a transition between hyperfine energy levels that are differentiated by the alignment or anti-alignment of the spins of the proton and electron in a hydrogen atom. The hydrogen Balmer alpha line at 656 nm, also known as Hα, provides an effective tracer of ionized hydrogen in the cool, ionized portion of the ISM (e.g., Haffner et al. 2003).

Dust grains, with sizes on the order of 0.1 microns, are also present in molecular clouds (Stahler & Palla, 2005). A typical gas to dust mass ratio is approximately 100 (Stahler & Palla, 2005) and the continuum emission from this dust can be used to trace the structure of molecular clouds (e.g., Di Francesco et al. 2008).

1.2.2 Thermal Characteristics

The mean gas temperature of a molecular cloud is between 10 and 20 Kelvin and this temperature is primarily set by cosmic ray heating (Goldsmith, 2001). Typical

estimates for the cosmic ray ionization rate in molecular clouds are between 1×10^{-17} s^{-1} and 5×10^{-17} s^{-1} (Williams et al., 1998; van der Tak & van Dishoeck, 2000; Doty et al., 2002; Wakelam et al., 2005; Bergin et al., 2006; Maret & Bergin, 2007; Goicoechea et al., 2009), but there is a two order of magnitude spread in values, with results as low as 10^{-16} s^{-1} (Caselli et al., 1998; Liszt, 2003; Doty et al., 2004) and as high as 10^{-18} s^{-1} (Caselli et al., 1998, 2002; Flower et al., 2007; Hezareh et al., 2008).

The dominant heating mechanisms for the exterior and interior of molecular clouds are the ISRF and cosmic rays, respectively (e.g., Kaufman et al. 1999; Goldsmith 2001). Magnetic processes, such as magnetic reconnection, as well as feedback from young stars, in the form of molecular outflows, winds and radiation, can also heat the gas within molecular clouds (e.g., Lazarian 2005; McKee & Ostriker 2007). The most important cooling mechanisms for molecular clouds are dust continuum radiation and molecular line emission (Kaufman et al., 1999). CO rotational transitions are important coolants for the interiors of molecular clouds while lines from ionized carbon atoms, such as the [C II] 158 μm line, play an important cooling role in the outskirts of clouds (Kaufman et al., 1999; Goldsmith, 2001). The CO $J = 1 \rightarrow 0$ transition occurs at a frequency of 115.2712 GHz and most CO transitions up to the $J = 8 \rightarrow 7$ transition at 921.7997 GHz are readily observable from the ground (Remijan et al., 2007).

1.2.3 Magnetic Fields

Magnetic fields might play an important role in regulating the speed of star formation, because strong magnetic fields prevent ionized molecules from crossing field lines (e.g., Shu 1977; Mouschovias & Spitzer 1976). While neutral particles do not interact directly with magnetic fields, collisions between neutrals and ions slow the diffusion of neutral molecules across field lines. This slow diffusion occurs on the ambipolar diffusion timescale, which is on the order of 25 Myr (Mac Low & Klessen, 2004). It is, however, currently unclear whether magnetic fields have the necessary strength to limit gravitational collapse (Crutcher et al., 2009; Mouschovias & Tassis, 2009). Magnetic fields are capable of supporting clouds with masses less than the magnetic critical mass, M_Φ, which is given by Crutcher et al. (2009) as

$$M_\Phi = \frac{\Phi}{2\pi\sqrt{G}}, \tag{1.2}$$

where Φ is the magnetic flux and G is the gravitational constant of the Universe, 6.67384×10^{-8} cm^{-3} g s^{-2} (Mohr et al., 2012). This criterion for magnetic support is often described in terms of subcritical or supercritical mass to flux ratios, where a cloud with a supercritical mass to flux ratio cannot be supported by magnetic fields alone. Observations of magnetic fields via Zeeman splitting seem to indicate that most molecular clouds are slightly magnetically supercritical (Crutcher et al., 2010).

The relationship between magnetic field strength, B, and number density, n, can be parameterized as

$$B = b\, n^k\, \mu\mathrm{G}, \tag{1.3}$$

where b and k are fitting parameters. Crutcher (1999) compile Zeeman splitting observations and find that the best fit comes from b = 1 and k = 0.5, although Crutcher et al. (2010) find that b = 1 and k = $\frac{2}{3}$ provides the best fit, based upon a more recent compilation of Zeeman splitting observations. This scaling relation between magnetic field strength and density is not very tight, as the Crutcher et al. (2010) data have a two order of magnitude range in magnetic field strengths for most densities.

1.2.4 Velocity Structure

The presence of supersonic turbulence in GMCs, which should also help support a GMC from collapsing, has been inferred from molecular line observations of GMCs, in which the observed line widths are significantly larger than what would be expected from thermal motions alone (e.g., Zuckerman & Evans 1974; Larson 1981; Solomon et al. 1987; McKee & Ostriker 2007). Thermal motions are expected to create line widths of

$$\Delta V_{thermal} = \sqrt{8\ln(2) \times \frac{kT}{m}}, \tag{1.4}$$

where $V_{thermal}$ is the expected full width at half maximum (FWHM) due to thermal motions thermal, k is the Boltzmann constant of $1.3806488 \times 10^{-16}$ erg K^{-1} (Mohr et al., 2012), T is the temperature of the gas and m is the molecular mass of the species emitting the line (Myers et al., 1991). For typical molecular cloud temperatures and molecular weights, thermal motions should create line widths on the order of 0.1 km s^{-1}, whereas observed molecular line widths are typically of the order of a few kilometers per second (Larson, 1981; Solomon et al., 1987).

Turbulence in GMCs is most likely in the form of magnetohydrodynamic (MHD)

waves, since the typically observed turbulent velocities are on the order of the Alfvén speed (Crutcher, 1999). The Alfvén speed, v_A is given by

$$v_A = \frac{B}{\sqrt{4\pi\,\rho}}, \tag{1.5}$$

where B is the magnetic field strength in gauss and ρ is the gas density. Typical values for the magnetic field strength, gas density and Alfvén speed in a molecular cloud are 10 μG, 1000 cm^{-3}, and 0.5 km s^{-1}, respectively, although the magnetic field strength and density can vary significantly, especially between low-mass and high-mass star forming regions.

Correlations have been found between the sizes, densities and velocity dispersions of GMCs and these correlations are collectively referred to as being part of Larson's laws (Larson, 1981; Solomon et al., 1987). Solomon et al. (1987) find that the best fit relations are

$$\sigma = 0.72\,(R/\mathrm{pc})^{0.5}\ \mathrm{km\ s^{-1}}, \tag{1.6}$$

$$\rho = 134\,(R/\mathrm{pc})^{-1}\,\mathrm{M_\odot\ pc^{-3}}, \tag{1.7}$$

where R is an effective radius and σ is the velocity width of the ^{12}CO J = 1 $\rightarrow$ 0 line. The other two parts of Larson's laws state that most GMCs are in Virial equilibrium and have approximately the same column density (Larson, 1981; Lombardi et al., 2010).

For a Kolmogorov energy cascade, in which incompressible turbulence is driven on large scales and the turbulent energy cascades to smaller scales at a rate independent of scale, until being dissipated at some very small viscous length scale, the expected relationship between the size and velocity dispersion of a cloud is, (Elmegreen & Scalo, 2004),

$$\sigma \propto r^{\frac{1}{3}}. \tag{1.8}$$

This is close to the observed Larson's laws relationship and the small discrepancy may be due to the fact that the turbulence in GMCs is compressible (Elmegreen & Scalo, 2004).

Since supersonic hydrodynamic turbulence decays on the order of a free fall time (e.g., Goldreich & Kwan 1974; Field 1978; Elmegreen 1985), maintaining turbulent motions inside of GMCs for their entire lifetimes is a significant problem, especially for the models of long lived GMCs. It was believed that MHD turbulence would decay an

order of magnitude more slowly than hydrodynamic turbulence (Arons & Max, 1975), but simulations of MHD turbulence have shown that MHD turbulence also decays on the order of a free fall time at the driving scale of the turbulence (Gammie & Ostriker, 1996; Mac Low et al., 1998; Stone et al., 1998; Mac Low, 1999; Padoan & Nordlund, 1999; Ostriker et al., 2001). In most MHD turbulence simulations, turbulent energy is dissipated via numerical and artificial viscosity and is assumed to be dissipated as heat. Furthermore, since most of these simulations use isothermal equations of state, this dissipated turbulent energy is not followed further. While Basu & Murali (2001) compare the CO J = 1 $\rightarrow$ 0 luminosities of molecular clouds to what they predict should be seen from molecular clouds, based on estimated turbulent dissipation rates, little progress has been made in determining where this turbulent energy goes and whether there are any observational signatures of this dissipated energy. I will return to this problem of finding observational signatures of dissipated turbulent energy in Chapter 4.

There is no clear consensus on whether turbulence is driven on size scales comparable to the size of a cloud, on scales on the order of the size of protostellar outflows or on scales larger than the size of a cloud. Support for small-scale driving comes from studies of protostellar outflows, which have found that outflows contain as much energy as the turbulence does in star forming regions with sizes similar to the 1 pc wide NGC 1333 star forming region (e.g., Quillen et al. 2005; Curtis et al. 2010). Arce et al. (2010) also estimate outflow timescales and find that outflow luminosities are larger than the turbulent dissipation rate in five of the six star forming regions in Perseus that they examine, thereby showing that outflows easily have enough energy to drive the turbulence. Matzner (2007) find that the velocity dispersion in NGC 1333 is consistent with turbulence being driven by protostellar outflows and Swift & Welch (2008) determine that the dominant energy injection scale in L1551 is 0.05 pc, or about one thirtieth of the total size of L1551. Various models of star forming regions also suggest that outflows may sustain turbulent motions in GMCs (e.g., Carroll et al. 2009).

On the other hand, many studies of density and velocity structure in molecular clouds find that the observed structures are only consistent with driving at size scales at, or above, the size of the clouds (e.g., Ossenkopf & Mac Low 2002; Brunt 2003; Heyer & Brunt 2004; Brunt et al. 2009; Padoan et al. 2009). It is also unclear whether protostellar outflows can drive turbulence on cloud scales, as Arce et al. (2010) note that the outflows in the Perseus complex do not have enough energy to sustain all

of the turbulence in the complex and Banerjee et al. (2007) present simulations in which protostellar jets do not drive turbulence far from the jets. Falgarone et al. (2009) find significant velocity shears, along with relatively large line widths in the Polaris Flare molecular cloud, which harbours no protostars (André et al., 2010), indicating that turbulence is present within molecular clouds before any protostellar feedback occurs. Models of H II regions and simulations of gravitationally contracting clouds also produce scenarios in which turbulence is driven at scales on the order of the size of the cloud (e.g., Matzner 2002; Vázquez-Semadeni et al. 2006).

1.2.5 Substructure and Star Formation

High resolution observations show that GMCs have significant substructure, with dense filaments being fairly ubiquitous (Schneider & Elmegreen, 1979; Bally et al., 1987; Johnstone et al., 2003; Myers, 2009; Molinari et al., 2010; André et al., 2010; Men'shchikov et al., 2010). Early Herschel Space Observatory observations appear to suggest that these filaments have a characteristic width of 0.1 pc (Arzoumanian et al., 2011). Isothermal filaments have a critical line density above which they cannot be supported by thermal pressure (Ostriker, 1964) and prestellar cores are preferentially found within filaments with line densities above this critical value (André et al., 2010). The critical line density is

$$\lambda_{crit} = \frac{2\,c_s^2}{G}, \tag{1.9}$$

where c_s is the sound speed of the gas. The sound speed is given by the equation

$$c_s^2 = \frac{k\,T}{\mu\,m_p}, \tag{1.10}$$

where k is Boltzmann's constant and $\mu\,m_p$ is the mean mass per particle. For typical sound speeds of a few tenths of a kilometer per second, the critical line density is around 15 solar masses per parsec (André et al., 2010). Prestellar cores also tend to be located only in regions with column densities roughly above 10^{22} cm^{-2} (Kirk et al., 2006).

The core mass functions (CMFs) of various clouds, which describe the distributions of core masses in the clouds, have roughly the same shape as the initial mass function, which describes the mass distribution of stars when they begin core hydrogen fusion, although the core masses are generally larger than the stellar masses by a factor of about three (Motte et al., 1998; Johnstone et al., 2000; Nutter & Ward-Thompson,

2007; Ward-Thompson et al., 2007; Enoch et al., 2008; Sadavoy et al., 2010; André et al., 2010). Figure 1.3 shows a comparison of the CMF of Aquila and the standard IMFs of Kroupa (2001) and Chabrier (2005). This similarity between CMFs and the IMF seems to indicate that the distribution of stellar masses is determined before the class 0 protostellar stage, although further fragmentation of the observed prestellar cores is possible (André et al., 2009). Models of cloud fragmentation due to turbulence have had some success in producing CMFs that have the same shape as the IMF and thus, the properties of turbulence in a GMC may control the form of the IMF (e.g., Padoan & Nordlund 2002).

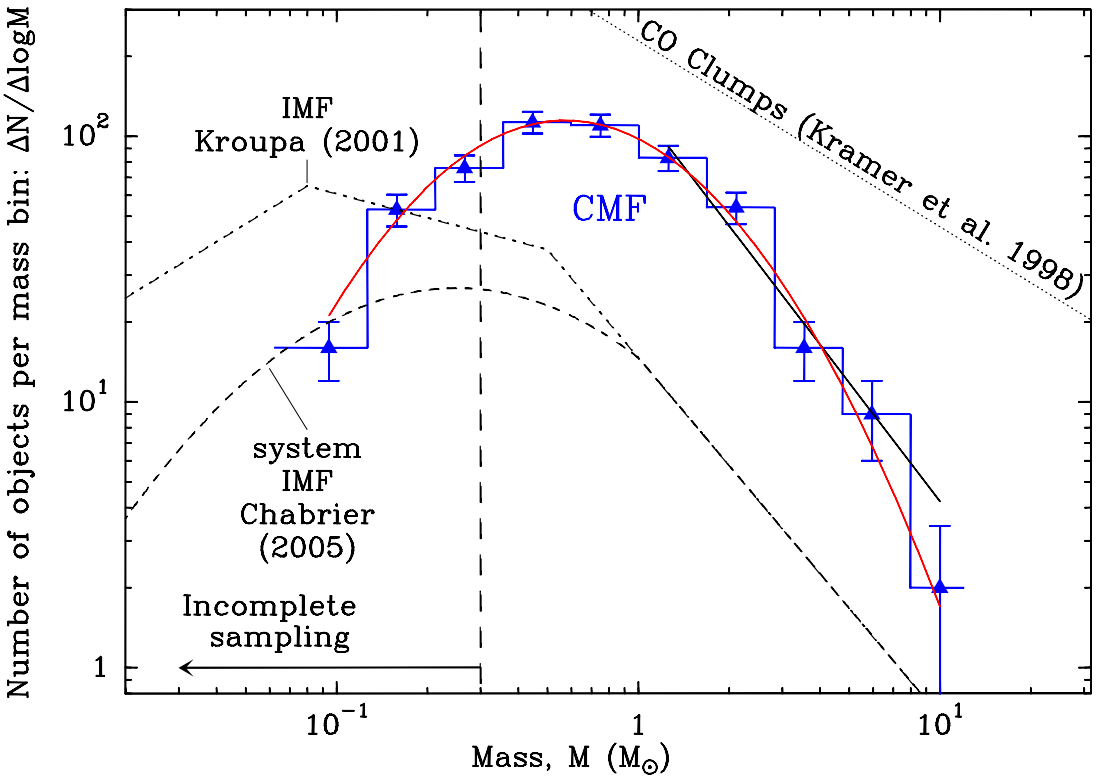

Figure 1.3: Core mass function for the Aquila star forming region as derived from Herschel observations. The black line shows a power-law fit to the high-mass end of the CMF and the red line shows a lognormal fit. The IMF for single stars (Kroupa, 2001), the IMF for multiple systems (Chabrier, 2005) and the mass distribution of diffuse CO clumps (Kramer et al., 1998) are also shown. This figure is from André et al. (2010).

An alternative suggestion to this turbulent fragmentation picture is that core formation may be governed by gravitational fragmentation processes (e.g., Larson 1985; Hartmann 2002). Because star forming regions are observed to have significant fila-

mentary substructure, the formation of gravitationally bound cores may be controlled by the gravitational collapse of filaments when their linear densities exceed the critical line density for radial stability (André et al., 2010). The characteristic length scale for this gravitational fragmentation should be the Jean's length (e.g., Motte et al. 1998; Hartmann 2002). The Jean's length is the length scale at which thermal pressure can no longer support a gas cloud against its own gravity and is roughly the scale at which gravitational collapse proceeds faster than a sound wave can cross the region (Stahler & Palla, 2005). The Jean's length, R_J, is approximately

$$R_J = \frac{c_s}{\sqrt{\rho\, G}}. \tag{1.11}$$

A summary of different core formation scenarios, as summarized by André et al. (2009), is given in Figure 1.4.

Core Formation Scenarios		
Models	Gravitational Fragmentation (linear perturbations)	Turbulent Fragmentation (non-linear perturbations)
Weak B	Short (few Myr) timescale infall mildly supersonic ordered curved field lines initial CMF very narrow	Very short (< Myr) timescale infall highly supersonic field lines distorted initial CMF is broad, IMF-like
Strong B	Long ($\sim$ 10 Myr) timescale subsonic infall small field line curvature initial CMF very narrow	Short (few Myr) timescale subsonic relative infall and supersonic systematic speeds ordered field lines initial CMF is broad, IMF-like

Figure 1.4: Summary of different core formation scenarios by André et al. (2009).

Prestellar cores do not dominate the mass of a GMC. While virtually all dense clumps are found at visual extinctions greater than five, the majority of the mass in GMCs exists at lower visual extinctions (Kirk et al., 2006; Goldsmith et al., 2008). The mass in stars in a GMC at a particular time is typically on the order of 2% of the total mass of the GMC (Myers et al., 1986) and this fraction is referred to as the instantaneous star formation efficiency (SFE_i). This instantaneous star formation efficiency is given by

$$SFE_i = \frac{M_*(t)}{M_{gas}(t) + M_*(t)}, \tag{1.12}$$

where $M_*(t)$ is the mass of stars in the cloud and $M_{gas}(t)$ is the mass of gas in the cloud at a time t (Vázquez-Semadeni et al., 2010). Over the entire lifetime of a GMC,

approximately 5% of the mass of the GMC will be converted into stars (Williams & McKee, 1997). The fractional mass of a GMC that is turned into stars over the entire lifetime of the GMC is referred to as the star formation efficiency, SFE, and can be estimated via the equation

$$\mathrm{SFE} = \frac{\tau \dot{M}}{M}, \tag{1.13}$$

where τ is the lifetime of the GMC, $\dot{M}$ is the average star formation rate and M is the total mass of the GMC (Mac Low & Klessen, 2004). The observed rate of star formation in the Galaxy is a few solar masses per year (e.g., Smith et al. 1978; Diehl et al. 2006; Misiriotis et al. 2006; Murray & Rahman 2010; Robitaille & Whitney 2010).

What sets the global rate of star formation in a galaxy is not yet fully understood, but it may be partially controlled by the stability of a galactic disk. The gas within a galactic disk can be supported against gravitational collapse by both thermal and rotational support, and the balance of gravity against these support mechanisms can be expressed by the Toomre Q parameter:

$$Q = \frac{\kappa \, c_s}{\pi G \, \Sigma}, \tag{1.14}$$

where κ is the epicyclic frequency of the disk and Σ is the surface density of the disk. Disks with $Q > 1$ are rotationally supported while disks with $Q < 1$ are unstable to fragmentation (e.g., Shu 1992). Note that larger rotational speeds, indicated by larger values of κ, and larger thermal pressures, indicated by larger values of c_s, lead to greater stability for a disk while larger disk masses, indicated by larger values of Σ, tend to produce gravitationally unstable disks.

Since gravity is a global force, giant molecular clouds are prone to global gravitational collapse modes as well as local collapse modes, which lead to the fragmentation of the clouds. For the observed IMF to be produced, local collapse modes must operate on timescales less than the global collapse modes. This could occur if there are large, localized density enhancements within a cloud, since the free-fall collapse timescale of a uniform density sphere, τ_{3D}, is

$$\tau_{3D} = \sqrt{\frac{3\pi}{32 G \, \rho}}, \tag{1.15}$$

(e.g., Binney & Tremaine 1987). Such density enhancements could be created by

turbulent compressions. Alternatively, support mechanisms, such as turbulence or magnetic fields, may be responsible for slowing the global collapse of molecular clouds while allowing local collapse modes to proceed (e.g., Shu 1977; Krumholz et al. 2006; Li & Nakamura 2006). For typical GMC densities, the free fall timescale is approximately two to five Myr. The sound crossing time of a GMC, which is the time it takes for a sound wave to traverse the diameter of a molecular cloud, is also on the order of a few megayears. The relative importance of global and local collapse modes will be investigated in more detail in Chapters 2 and 3.

1.2.6 Lifetime of GMCs

The life cycle of a GMC is not well constrained, as there is no consensus on either the formation or destruction mechanisms of GMCs. For instance, a GMC may be formed from global gravitational instabilities in a galactic disk, compression of atomic gas by supernovae or the Parker instability (e.g., Hennebelle et al. 2009). The Parker instability is a MHD instability wherein the vertical collapse of a segment of a magnetized disk creates magnetic field lines perpendicular to the disk, which in turn serve to funnel more gas into the collapsing region of the disk (Parker, 1966). Recently, work has been done on examining whether the collision of two atomic gas flows can form a GMC (Ballesteros-Paredes et al., 1999; Hennebelle & Pérault, 1999; Koyama & Inutsuka, 2000; Hartmann et al., 2001; Koyama & Inutsuka, 2002; Audit & Hennebelle, 2005; Gazol et al., 2005; Heitsch et al., 2005; Vázquez-Semadeni et al., 2006, 2007; Hennebelle & Audit, 2007; Hennebelle et al., 2008; Heitsch & Hartmann, 2008; Banerjee et al., 2009). This formation mechanism of colliding flows also suggests a destruction mechanism for a GMC, as a collision between an atomic flow and a GMC might disperse the GMC via ram pressure stripping (Hartmann et al., 2001).

Feedback from stars formed within a GMC may also lead to the destruction of the GMC. While a protostar is accreting, a powerful molecular outflow is launched from the protostar and surveys of nearby star forming regions have revealed that the energy in these outflows can range from 1% of the binding energy of the star forming region to almost twice the binding energy (Matzner, 2007; Curtis et al., 2010). As such, these outflows have the energy needed to disperse their surrounding gas, but it is unclear whether these outflows can efficiently couple to the gas in a GMC on large enough scales to effectively disperse the cloud (Arce et al., 2010). A more effective pathway to the destruction of a GMC might come from the formation of O and B stars. These

stars are very luminous and their high energy fluxes, coupled with their strong winds, can form large, hot, low density bubbles of ionized material, referred to as H II regions, that can grow to become hundreds to thousands of parsecs in size (Basu et al., 1999; Hoare et al., 2007; Bagetakos et al., 2011). These bubbles can also be formed by the supernova explosions of O and B stars (Mac Low & Klessen, 2004; Stahler & Palla, 2005). Bubbles formed from clusters of OB stars are referred to as superbubbles, due to their large sizes. The feedback from stars that have formed in GMCs does not always have to be destructive, as the compressions induced by outflows and H II regions may also trigger new rounds of star formation (e.g., Elmegreen & Lada 1977; Mac Low & Klessen 2004). A nearby superbubble, the Orion-Eridanus superbubble, will be examined in more detail in Chapter 5.

Unsurprisingly, considering that the formation and destruction mechanisms of molecular clouds are not well known, the lifetimes of GMCs are also not agreed upon. One scenario, based upon derived lifetimes of approximately 30 Myr (e.g., Blitz & Shu 1980), proposes that GMCs are relatively long lived compared to their free fall times, which are on the order of 1 Myr. In this scenario turbulent motions and magnetic fields oppose the gravitational collapse of GMCs (e.g., Shu 1977; Krumholz et al. 2006; Li & Nakamura 2006). Another scenario suggests that GMCs are relative short lived, with lifetimes less than 10 Myr, and are rapidly dispersed before most of their mass is converted into stars (see Mac Low & Klessen 2004 for a review).

1.3 DISSERTATION OVERVIEW

The large scale, dynamical state of giant molecular clouds plays a critical role in star formation, as it affects the rate of star formation as well as the IMF. The goal of this dissertation is to further the astronomical community's understanding of the large scale gas dynamics within giant molecular clouds. In the following chapters, I present research that I have conducted on three facets of the dynamical nature of molecular clouds. Chapters 2 and 3 focus on the collapse modes that can be induced in molecular clouds by gravity alone, while Chapter 4 examines the energetic consequences of supersonic turbulence being present within molecular clouds. Finally, Chapter 5 presents an examination of how feedback from the Orion star forming region has affected the surrounding ISM.

Local collapse modes must occur on faster timescales than the global collapse timescales of giant molecular clouds in order for the observed CMF to be produced.

The collapse modes of spheres, infinite sheets and infinite filaments are reasonably well known (e.g., Stodólkiewicz 1963; Ostriker 1964; Larson 1969; Penston 1969; Shu 1977; Larson 1985; Inutsuka & Miyama 1992, 1997; Nakamura et al. 1993; Fiege & Pudritz 2000; Myers 2009), but the collapse modes of finite circular sheets and cylinders are much less well understood. In Chapter 2, I investigate how the collapse timescales of finite molecular clouds and small density perturbations within these molecular clouds vary as a function of the shape of the molecular clouds by analytically calculating collapse timescales for spheres, circular sheets and cylinders with uniform densities except in small central perturbations where the density is slightly enhanced. In this chapter, I probe the conditions necessary for local collapse modes to dominate over global collapse modes, such that molecular clouds will fragment into prestellar cores. This chapter has been published as Pon et al. (2011). I was responsible for conducting all of the analytic calculations presented in this chapter, producing all of the figures and writing all of the text.

In Chapter 3, I continue to use analytically derived collapse timescales of circular sheets and cylinders to investigate how collapse timescales vary as a function of the aspect ratio of a molecular cloud. I also examine where momentum is deposited in these collapsing objects to determine whether filamentary and sheet-like molecular cloud structures will collapse homologously or whether their collapse will be dominated by an infalling edge. In this chapter, I calculate how much the star formation rate of a molecular cloud can be overestimated if the geometry of the cloud is not taken into account. This chapter has been published as Pon et al. (2012b). I was responsible for conducting all of the analytic calculations presented in this chapter, producing all of the figures and writing all of the text.

Simulations of magnetohydrodynamic (MHD) turbulence, similar to that believed to exist in molecular clouds, show that the turbulence decays on the order of a crossing time, which is much less than the expected lifetime of a molecular cloud (Gammie & Ostriker, 1996; Mac Low et al., 1998; Stone et al., 1998; Mac Low, 1999; Padoan & Nordlund, 1999; Ostriker et al., 2001). These simulations, however, often use isothermal equations of state and assume that the turbulent energy is dissipated as heat and rapidly radiated away, since infrared and submillimeter opacities are relatively low. That is, these simulations do not reveal how this energy is radiated from clouds and whether there are any observational signatures of this turbulent energy dissipation. In Chapter 4, I use a modified version of the Kaufman & Neufeld (1996a) code to produce models of C-type, MHD shocks for initial conditions consistent with turbu-

lent motions within giant molecular clouds. These simulations reveal which cooling mechanisms are responsible for dissipating energy within low velocity shocks. I scale these shock models to the total rate of turbulent energy dissipation in MHD simulations of molecular clouds to determine the observable spectrum coming from shocked gas. This spectrum is then compared to the results of the photodissociation region (PDR) models of Kaufman et al. (1999), which estimate the CO spectrum that would be emitted from the unshocked gas within a molecular cloud, in order to determine whether there are any observable signatures of these low velocity shocks. This chapter has been published as Pon et al. (2012a). While Dr. Kaufman was responsible for running the shock code and PDR code used for this work, I was responsible for all of the analysis presented in this chapter, as well as producing the figures and text of this chapter.

The Orion-Eridanus superbubble is a highly elongated superbubble that has been created by the Orion star forming region, which is the nearest high-mass star forming region to the Sun still forming stars. While relatively nearby, the elongation and orientation of the superbubble have never been adequately explained. The Orion-Eridanus superbubble also contains prominent filamentary features on the Eridanus side of the superbubble whose origins are not well known. In Chapter 5, I fit Kompaneets models, models of superbubbles being blown into exponential atmospheres by constant driving sources, to the Orion-Eridanus superbubble. Two models are found that reasonably fit the morphology of the superbubble and I examine whether the parameters of these models are realistic, given the accepted structure of the ISM in the Galactic disk. I also determine where the ionization front within the bubble would be, given the parameters of the two best fitting models. I investigate whether the filaments on the Eridanus side of the superbubble are equilibrium structures ionized by the Orion star forming region or whether an alternative explanation for these filaments is required. This chapter forms the basis of Pon, A., Johnstone, D., Bally, J., & Heiles, C. (2013, in prep.), which will be submitted to the Astrophysical Journal shortly. I have been responsible for all of the modeling presented in this chapter, as well as producing all of the figures and text in this chapter. I have, however, used small pieces of code from Dr. Shantanu Basu to determine how the $\tilde{y}$ parameter of a Kompaneets model scales with time and to determine the column density of a superbubble wall.

In Chapter 6, I summarize the results of this dissertation and discuss future avenues of extending this research.

Chapter 2

Modes of Star Formation in Finite Molecular Clouds

Should I, after tea and cakes and ices,
Have the strength to force the moment to its crisis?
But though I have wept and fasted, wept and prayed,
Though I have seen my head (grown slightly bald) brought in upon a platter,
I am no prophet – and heres no great matter;
I have seen the moment of my greatness flicker,
And I have seen the eternal Footman hold my coat, and snicker,
And in short, I was afraid.
T.S. Eliot

2.1 ABSTRACT

We analytically investigate the modes of gravity-induced star formation possible in idealized finite molecular clouds where global collapse competes against both local Jeans instabilities and discontinuous edge instabilities. We examine these timescales for collapse in spheres, discs, and cylinders, with emphasis on the structure, size, and degree of internal perturbations required in order for local collapse to occur before global collapse. We find that internal, local collapse is more effective for the lower dimensional objects. Spheres and discs, if unsupported against global collapse, must either contain strong perturbations or must be unrealistically large in order for small density perturbations to collapse significantly faster than the entire cloud. We

find, on the other hand, that filamentary geometry is the most favorable situation for the smallest perturbations to grow before global collapse overwhelms them and that filaments containing only a few Jeans masses and weak density perturbations can readily fragment. These idealized solutions are compared with simulations of star-forming regions in an attempt to delineate the role of global, local, and edge instabilities in determining the fragmentation properties of molecular clouds. The combined results are also discussed in the context of recent observations of Galactic molecular clouds.

2.2 INTRODUCTION

Stars primarily form in clustered environments inside of molecular clouds containing tens of thousands of solar masses of material or more (Lada & Lada, 2003). These star-forming molecular clouds must fragment to give rise to the observed initial mass function (IMF) of stars, with a characteristic mass on the order of a solar mass (e.g., Bonnell et al. 2007), and cannot be solely dominated by large scale, global collapse modes. Gravitational collapse within a molecular cloud leads to the formation of individual stars; however, the mechanism driving the formation and shape of the IMF is poorly constrained. While turbulence is believed to play a key role in producing significant inhomogeneity from which fragmentation can occur, gravity must also contribute (e.g., Bonnell et al. 2007). In fact, the idea that gravity is driving supersonic motions (or "turbulence") in molecular clouds has been around for awhile (e.g., Goldreich & Kwan 1974; Ferrini et al. 1983; Falgarone & Puget 1986). Beyond the monolithic collapse envisioned by Zuckerman & Evans (1974) in their critique of Goldreich & Kwan (1974), recent numerical and analytical studies show that global gravity can indeed drive "turbulent" motions without leading directly to "catastrophic" collapse (e.g., Hartmann et al. 2001; Hartmann 2002; Ballesteros-Paredes et al. 2007; Vázquez-Semadeni et al. 2007; Field et al. 2008; Heitsch & Hartmann 2008). Depending on the morphology of the cloud, the fragmentation that occurs during such a large scale collapse might also lead to an IMF distribution of stars. In this scenario, the observed supersonic motions of the gas are determined by the geometry of the cloud, which depends strongly upon the initial conditions of the cloud.

Spatially resolved observations of star-forming molecular clouds usually exhibit rather complex geometries, including substructure often associated with lower dimensionality, such as sheets and filaments (e.g., Schneider & Elmegreen 1979; Bally

et al. 1987; Lada et al. 1999; Hartmann 2002; Johnstone et al. 2003; Lada et al. 2007; Myers 2009; Molinari et al. 2010; André et al. 2010). Filamentary structures have also been noted to form in molecular cloud simulations, although their formation mechanism varies with the type of model used, be it driven or decaying supersonic turbulence (e.g., Padoan et al. 2007; Bate 2009), flow collisions (e.g., Vázquez-Semadeni et al. 2010), or global gravitational accelerations (e.g., Burkert & Hartmann 2004; Hartmann & Burkert 2007).

In the absence of turbulent motions, the collapse properties of isothermal spheres (e.g., Larson 1969; Penston 1969; Shu 1977), infinitely large, isothermal sheets (e.g., Larson 1985; Myers 2009), and infinitely long, isothermal cylinders (e.g., Stodólkiewicz 1963; Ostriker 1964; Inutsuka & Miyama 1992, 1997; Nakamura et al. 1993; Fiege & Pudritz 2000) have been thoroughly studied. Equilibrium configurations of infinite sheets perturbed to form successive, parallel filaments and infinite, isothermal filaments perturbed to form strings of dense cores have also been found (Schmid-Burgk, 1967; Curry, 2000; Myers, 2009). Yet, the collapse of *finitely* long cylinders and discs, and the subsequent interplay between global and local collapse modes, are much less well understood. Previous simulations of finite cylinders show that these cylinders can fragment into multiple condensations (e.g., Bastien 1983; Bastien et al. 1991), while the disc simulations of Burkert & Hartmann (2004) show no sign of local collapse modes. These disc simulations are dominated by the global collapse of the disc and the subsequent build up of mass along the outer ring of the disc (see also Hsu et al. 2010).

In this paper, we compare analytic estimates for the global collapse timescales to the local collapse timescales of small density perturbations embedded in different dimensional objects. We analyze whether small density perturbations are capable of collapsing significantly faster than the entire cloud for spherical, disc shaped, and filamentary clouds to determine whether strong perturbations, possibly induced by turbulent motions, are required to fragment these differently shaped molecular clouds. We present our analytic results in §2.3. In §2.4, we discuss these results in context of recent observations and simulations and we present a summary of our findings in §2.5.

2.3 MODES OF COLLAPSE - ANALYTIC THEORY

To understand the importance of global gravity in molecular clouds, we consider the large scale gravitational forces at play in comparison to the growth of local perturbations within a cloud. For a uniform sphere of arbitrary radius, the collapse is quickest for the largest scale (e.g., Larson 1985), since gravity is a long-range force and global collapse is inevitable provided the region contains more than a Jeans mass of material and support from effects such as magnetic fields and rotation are negligible. In two-dimensions, however, an infinite sheet can be constructed for which there is no global gravitational force in the plane and the collapse is dominated by objects with radii similar to the thickness of the sheet (Larson, 1985). A similar argument can be made for infinite one-dimensional cylinders (Larson, 1985; Inutsuka & Miyama, 1992, 1997). As noted by Burkert & Hartmann (2004) the lack of global gravity in these systems depends entirely on the infinite nature of the sheet or cylinder. In the following we show how the global gravitational collapse depends on both the dimensionality and the finite nature of simple geometries: spheres, discs, and cylinders.

2.3.1 Thermal Support

Thermal support is always present in a molecular cloud and will oppose gravitational collapse. This thermal support is most effective on small scales and can be overcome on larger scales. The Jeans length is the size scale above which, in three dimensions, thermal pressure is no longer capable of supporting an isothermal cloud. The Jeans length, R_J, is given by:

$$R_J = c_s \left(\frac{\pi}{G\,\rho} \right)^{\frac{1}{2}}, \tag{2.1}$$

where c_s is the isothermal sound speed, G is the gravitational constant, and ρ is the mass density of the gas. For isothermal, infinite sheets, a stable equilibrium configuration can be found for all surface densities such that thermal pressure counteracts gravity. In these equilibrium configurations, the scale height of the gas is on the order of the Jeans length of the material in the midplane (Spitzer, 1942, 1978) and small perturbations in the plane of the disc will only collapse if they are larger than the scale height of the gas (Larson, 1985). For infinite, isothermal cylinders, the characteristic radius of an equilibrium configuration and the size scale on which thermal

support is effective are on the order of the Jeans length at the central axis of the cylinder (Stodólkiewicz, 1963; Ostriker, 1964). Unlike infinite isothermal sheets, infinite isothermal cylinders have a critical mass per unit length value above which no equilibrium configuration exists (Ostriker, 1964).

In the following sections, we only consider the effect of gravity and do not explicitly include any thermal effects in calculating collapse timescales, although we do interpret our results in light of the Jeans length being the minimum scale which can collapse. We also do not consider the effects of turbulence, rotation, magnetic fields, or deviations from isothermality.

2.3.2 3D - Sphere

For a sphere of density ρ and radius $R \gg R_J$, the instantaneous global collapse time, t_g, is given by

$$t_g = \left(\frac{3}{2\pi\, G\, \rho}\right)^{1/2}. \tag{2.2}$$

The above instantaneous global collapse time differs by less than a factor of two from the collapse timescale obtained by properly following the changes in the strength of the gravitational acceleration over time (e.g., Carroll & Ostlie 2007). A small region, $R_1 \ll R$, at the centre of the sphere with an enhanced density $(1+\epsilon)\rho$, where $\epsilon \ll 1$, might act as a seed for local collapse. Since the density is only slightly enhanced, the Jeans length for this region is very similar to the unperturbed Jeans length and the region is stable against *local* collapse when $R_1 < R_J$. However, provided $R_1 > R_J$, the local collapse time, t_l, for this inner region approaches

$$t_l = \left(\frac{3}{2\pi\, G\, (1+\epsilon)\rho}\right)^{1/2}, \tag{2.3}$$

where we have ignored the residual support due to thermal pressure. Comparing these two timescales reveals the difficulty in fragmenting an almost uniform spherical molecular cloud:

$$t_l = (1+\epsilon)^{-1/2}\, t_g. \tag{2.4}$$

For small amplitude density perturbations, there is little time for the local collapse to proceed before the global collapse consumes the entire spherical cloud. In three dimensions, local collapse beats global collapse *only* if there are significant inhomogeneities (strong perturbations) in the medium. Tohline (1980) showed that the growth of this perturbation is even slower, relative to the global collapse timescale, if the perturbation is induced after global collapse has begun.

2.3.3 2D - Disc

2.3.3.1 Accelerations

For an infinitely thin disc with constant surface density Σ and radius $R \gg R_J$, the central acceleration at a distance of $r > R$ from the center of this disc is

$$a_{\rm ext} = 4G\,\Sigma \left[K\left(\frac{R}{r}\right) - E\left(\frac{R}{r}\right) \right], \tag{2.5}$$

where K and E are the first and second complete elliptic integrals respectively (Wyse & Mayall, 1942). The central acceleration of a point inside of the disc, i.e., $r < R$, is (Wyse & Mayall, 1942):

$$a_{\rm int} = 4G\,\Sigma \frac{R}{r} \left[K\left(\frac{r}{R}\right) - E\left(\frac{r}{R}\right) \right]. \tag{2.6}$$

For a perturbed disc with surface density $(1+\epsilon)\,\Sigma$ inside of $R_1 \ll R$, the net acceleration is

$$a_{\rm net} = \begin{cases} 4G\,\Sigma\frac{R}{r}\left(\left[K\left(\frac{r}{R}\right) - E\left(\frac{r}{R}\right) \right] + \epsilon\frac{R_1}{R} \left[K\left(\frac{r}{R_1}\right) - E\left(\frac{r}{R_1}\right) \right] \right), & r < R_1 \\ 4G\,\Sigma\frac{R}{r}\left(\left[K\left(\frac{r}{R}\right) - E\left(\frac{r}{R}\right) \right] + \epsilon\frac{r}{R} \left[K\left(\frac{R_1}{r}\right) - E\left(\frac{R_1}{r}\right) \right] \right), & R_1 < r < R. \end{cases} \tag{2.7}$$

For the case of $R_1 < r < R$, Burkert & Hartmann (2004) showed that these elliptic integrals can be expanded to lowest order to give:

$$a_{\rm net} = \frac{\pi G\,\Sigma\, r}{R}\left(1 + \frac{\epsilon R R_1^2}{r^3}\right). \tag{2.8}$$

Figure 2.1 compares the accelerations of a perturbed disc calculated from the

above exact and approximate solutions. For simplicity, G, Σ, and R_1 have all been set to 1, ϵ has been set to 0.1, and R has been set to 100. The approximate solution of Equation 2.8 reproduces the exact accelerations of Equation 2.7 for intermediate radii between R_1 and R, but underestimates the accelerations closer to R_1 and R.

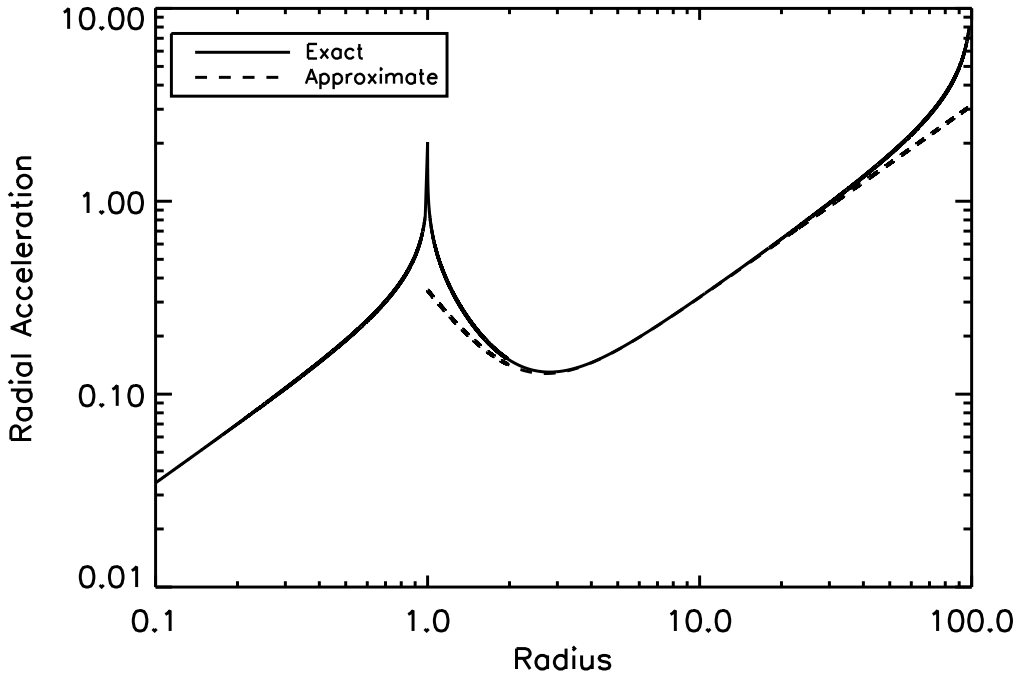

Figure 2.1: Accelerations of a perturbed disc with $R = 100$, $G = 1$, $\Sigma = 1$, $\epsilon = 0.1$, and $R_1 = 1$. The solid line shows the exact solution for the central accelerations while the dashed line shows the lowest order approximation to the exact solution. The exact acceleration becomes infinite at radii of 1 and 100.

2.3.3.2 Timescales

The square of the instantaneous collapse time at r is

$$t^2(r) = \frac{2r}{a_{net}(r)},$$

$$t^2(r) = \frac{2R}{\pi G \Sigma}\left(1 + \frac{\epsilon R R_1^2}{r^3}\right)^{-1}. \quad (2.9)$$

The global collapse timescale, t_g, can be determined by considering the collapse

time when $r = R$. That is

$$t_g^2(R) = \frac{2R}{\pi G\,\Sigma}\left(1+\frac{\epsilon\,R_1^2}{R^2}\right)^{-1}. \tag{2.10}$$

Given that the initial surface density perturbation is small, $\epsilon \ll 1$, and $R_1 \ll R$:

$$\begin{aligned}\frac{\epsilon\,R_1^2}{R^2} &\ll 1,\\ t_g^2 &= \frac{2R}{\pi G\,\Sigma}.\end{aligned} \tag{2.11}$$

Thus, the global timescale is not changed significantly due to the small perturbation.

Equation 2.9 can now be re-written as

$$t^2(r) = t_g^2\left(1+\frac{\epsilon\,R\,R_1^2}{r^3}\right)^{-1}. \tag{2.12}$$

Note that the collapse time $t(r)$ is equal to the global collapse time and independent of r unless $\epsilon > 0$. When there is a density enhancement, however, the local time for collapse is dependent on r and thus, smaller regions can collapse faster than the global collapse.

Assuming that the perturbed region is large enough to be Jeans unstable, $R_1 > R_J$, the timescale for collapse of a local region with radius R_1 is approximately

$$\begin{aligned}t_l^2 &= t^2(R_1),\\ t_l^2 &= t_g^2\left(1+\frac{\epsilon\,R}{R_1}\right)^{-1}.\end{aligned} \tag{2.13}$$

For this to be significantly smaller than the global collapse timescale

$$\begin{aligned}\frac{\epsilon\,R}{R_1} &\gg 1,\\ \epsilon &\gg \frac{R_1}{R}.\end{aligned} \tag{2.14}$$

Thus, it is possible to find a combination of perturbation length and amplitude that results in significantly enhanced local collapse. For a small density perturbation, $\epsilon = 0.1$, the perturbation length must be approximately 100 times smaller than the

disc's total radius in order for the local collapse timescale to be 3 times smaller than the global collapse timescale. Recognizing that thermal support in the disc requires $R_1 > R_J$ for local collapse to occur, such a disc would need to have assembled more than 10^4 Jeans masses of material! Even for a large perturbation, $\epsilon = 1$, the disc would still need more than 100 Jeans masses for the local collapse mode to be 3 times faster than the global collapse mode.

Figure 2.2 shows the collapse timescales for a disc with $R_1 = G = \Sigma = 1$, $\epsilon = 0.1$, and $R/R_1 = 100$. The solid line shows the timescales calculated from the exact accelerations while the dashed line shows the timescales calculated from the approximate accelerations given by Equation 2.8. The timescales for collapse interior to a radius of R_1 are approximately a factor of three faster than the collapse timescales for the outer parts of the disc and the timescale for collapse at R_1, as calculated from the approximate accelerations, is roughly equal to the collapse timescales for most points inside of R_1 as calculated from the exact accelerations.

The exact accelerations lead to collapse timescales approaching zero at radii of R and R_1, while the approximate accelerations produce timescales that do not show this asymptotic behavior. These extremely small collapse times are artifacts of having an infinitely thin disc with infinitely sharp edges and no thermal support. Real discs have finite heights and smoother edges, which should suppress this asymptotic behavior. We will come back to the issue of these infinitely small collapse timescales at the edges in Section 2.3.5.

Thermal pressure provides for support against collapse on scales smaller than the Jeans length, R_J, and thus, the above analysis suggests that the preferred size of the perturbed region is $R_1 \sim R_J$, since this provides the greatest leverage on the local to global collapse timescale. This length scale is also associated with the scale height of a thermally supported disc and is close to the preferred scale for disc fragmentation in infinite sheets (Larson, 1985).

2.3.4 1D - Cylinder

2.3.4.1 Accelerations

For a one dimensional cylinder of length $2L$ and line density λ, the net acceleration a distance $d < L$ from the center of the cylinder, along the central axis of the cylinder,

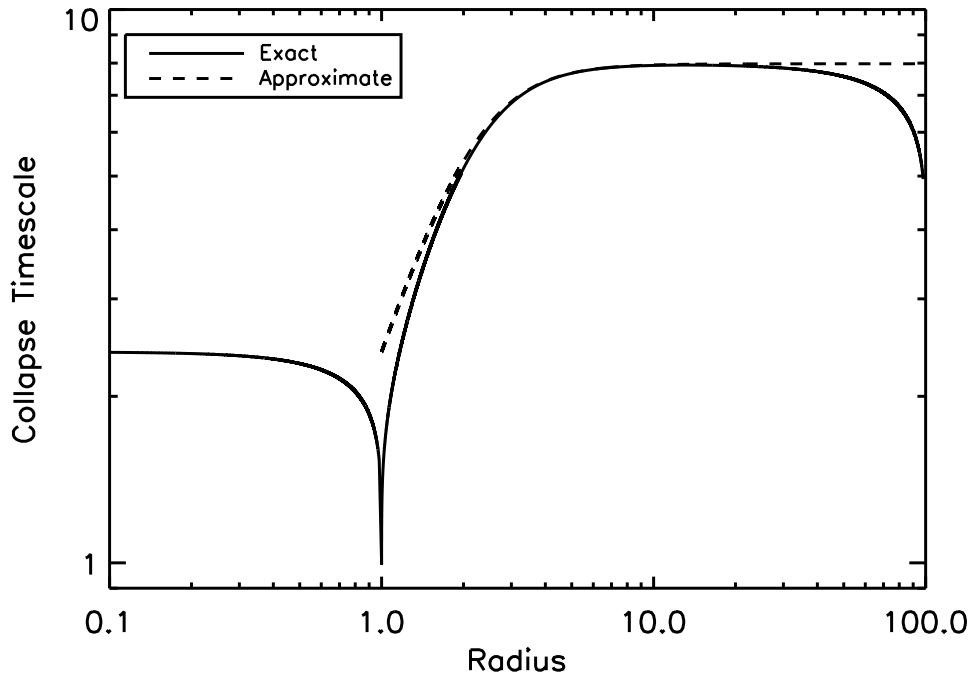

Figure 2.2: Collapse timescales of a perturbed disc with $R = 100$, $G = 1$, $\Sigma = 1$, $\epsilon = 0.1$, and $R_1 = 1$. The solid line shows the timescales calculated from the exact accelerations while the dashed line shows the timescales calculated from the approximate accelerations. The collapse timescale, based upon the exact accelerations, becomes zero at radii of 1 and 100.

is

$$\begin{aligned} a_{int}(d) &= \int_0^{L+d} \frac{G\lambda\, dr}{r^2} - \int_0^{L-d} \frac{G\lambda\, dr}{r^2}, \\ a_{int}(d) &= \int_{L-d}^{L+d} \frac{G\lambda\, dr}{r^2}, \\ a_{int}(d) &= \frac{G\lambda}{L-d} - \frac{G\lambda}{L+d}. \end{aligned} \tag{2.15}$$

The net acceleration a distance $d > L$ from the center of the cylinder, and along the central axis of the cylinder, is

$$\begin{aligned} a_{ext}(d) &= \int_{d-L}^{L+d} \frac{G\lambda\, dr}{r^2}, \\ a_{ext}(d) &= \frac{G\lambda}{d-L} - \frac{G\lambda}{L+d}. \end{aligned} \tag{2.16}$$

If the above described cylinder is perturbed such that its density becomes $(1+\epsilon)\,\lambda$ within a distance of L_1 of the center of the cylinder, then the acceleration a distance d from the center will be

$$a_{\rm net}(d) = \begin{cases} \frac{G\lambda}{L-d} - \frac{G\lambda}{L+d} + \frac{G\lambda\,\epsilon}{L_1-d} - \frac{G\lambda\,\epsilon}{L_1+d}, & d < L_1 \\ \frac{G\lambda}{L-d} - \frac{G\lambda}{L+d} + \frac{G\lambda\,\epsilon}{d-L_1} - \frac{G\lambda\epsilon}{L_1+d}, & L_1 < d < L. \end{cases} \tag{2.17}$$

For the case of $L_1 < d < L$, expanding to lowest order gives

$$\begin{aligned} a_{\rm net}(d) &= G\lambda \left(\frac{1}{L} \left[(1+\frac{d}{L}) - (1-\frac{d}{L}) \right] + \frac{\epsilon}{d} \left[(1+\frac{L_1}{d}) - (1-\frac{L_1}{d}) \right] \right), \\ a_{\rm net}(d) &= \frac{G\lambda\, 2d}{L^2} \left(1 + \frac{\epsilon\, L_1\, L^2}{d^3} \right). \end{aligned} \tag{2.18}$$

Figure 2.3 shows the accelerations of a perturbed cylinder as calculated from the above exact and approximate equations. For simplicity, λ, G, and L_1 are set to 1 while ϵ and L are set to 0.1 and 10 respectively. Just as with the disc, Equation 2.18 accurately reproduces the accelerations at intermediate radii but underestimates the accelerations near L_1 and L.

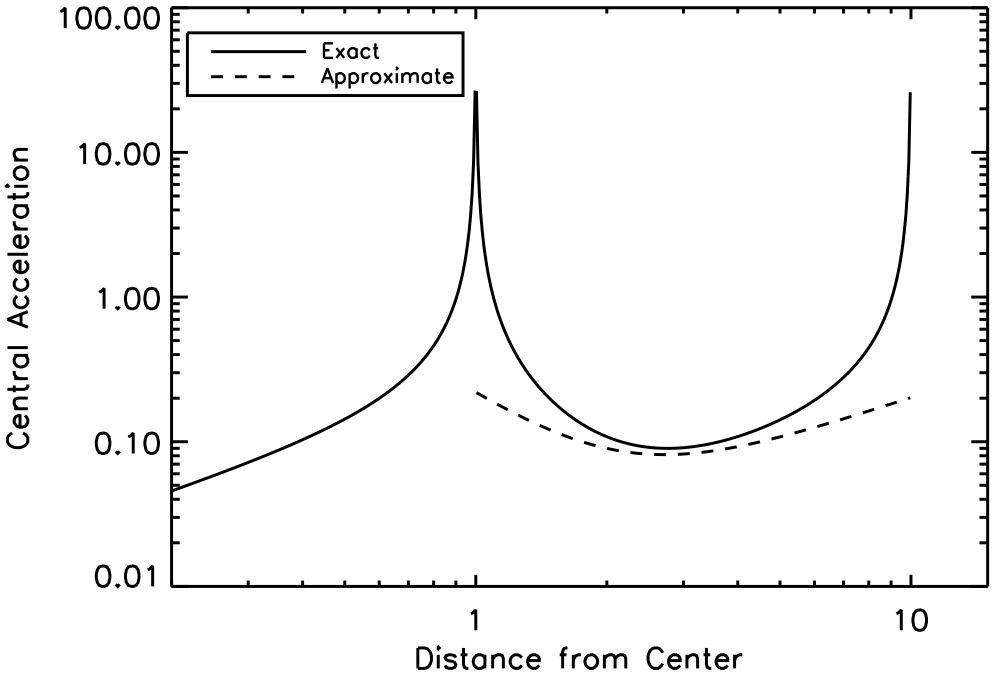

Figure 2.3: Accelerations of a perturbed cylinder with $L_1 = 1$, $G = 1$, $\lambda = 1$, $\epsilon = 0.1$, and $L = 10$. The solid line shows the exact solution for the central accelerations while the dashed line shows the lowest order approximation to the exact solution. The exact acceleration becomes infinite at distances of 1 and 10.

2.3.4.2 Timescales

The square of the instantaneous collapse time is approximately

$$t^2(d) = \frac{L^2}{G\lambda}\left(1+\frac{\epsilon\, L_1\, L^2}{d^3}\right)^{-1}. \tag{2.19}$$

The square of the global collapse time is thus

$$\begin{aligned} t_g^2 &= t^2(L), \\ t_g^2 &= \frac{L^2}{G\lambda}\left(1+\frac{\epsilon\, L_1}{L}\right)^{-1}. \end{aligned} \tag{2.20}$$

For small perturbations

$$\begin{aligned} \frac{\epsilon\, L_1}{L} &\ll 1, \\ t_g^2 &= \frac{L^2}{G\lambda}. \end{aligned} \tag{2.21}$$

Just as with the disc, the global collapse time is essentially the same in a perturbed and unperturbed cylinder and Equation 2.19 can be written as

$$t^2(d) = t_g^2\left(1+\frac{\epsilon\, L_1\, L^2}{d^3}\right)^{-1}. \tag{2.22}$$

When $\epsilon = 0$, the local collapse time is essentially the global collapse time. The presence of a line density perturbation speeds up the local internal collapse.

The square of the collapse timescale for a local region of size L_1 is

$$\begin{aligned} t_l^2 &= t^2(L_1), \\ t_l^2 &= t_g^2\left(1+\frac{\epsilon L^2}{L_1^2}\right)^{-1}. \end{aligned} \tag{2.23}$$

Equation 2.23 indicates that the smaller the perturbed region is in comparison to the total length of the cylinder, the faster the local collapse will be in comparison to global collapse.

For the local collapse timescale to be significantly shorter than the global collapse

timescale

$$\begin{aligned} \frac{\epsilon L^2}{L_1^2} &\gg 1, \\ L_1 &\ll \sqrt{\epsilon} L. \end{aligned} \tag{2.24}$$

More specifically, for the local collapse timescale to be a factor of three smaller than the global collapse timescale,

$$\begin{aligned} \left(\frac{t_g}{t_l}\right)^2 &> 10, \\ L_1 &\lesssim 0.3\sqrt{\epsilon} L. \end{aligned} \tag{2.25}$$

If $\epsilon = 0.1$, then the perturbation length must be approximately 10 times smaller than the cylinder's length in order for the local collapse timescale to be three times smaller than the global collapse timescale. Taking $L_1 = R_J$ as the minimum size for a gravitationally unstable weak perturbation, this implies a minimum finite cylinder mass of a few tens of Jeans masses. A large perturbation, $\epsilon = 1$, would require a cylinder with approximately ten Jeans masses in order for the local collapse timescale to be three times smaller than the global collapse timescale.

Figure 2.4 shows the collapse timescales for a perturbed cylinder with $L_1 = G = \lambda = 1$, $\epsilon = 0.1$, and $L/L_1 = 10$. The solid line shows the timescales calculated from the exact accelerations while the dashed line shows the timescales calculated from the approximate accelerations given by Equation 2.18. The collapse times for points interior to L_1 are approximately a factor of three smaller than the collapse times for most points beyond L_1. Just as for the disc, the collapse timescale abruptly drops to zero at L and L_1 due to the sharp jumps in density at these points. In more realistic filaments, these density changes would be more gradual and the actual collapse timescales would more closely resemble the collapse timescales derived from the approximate accelerations of Equation 2.18. As in the 2D case, the collapse timescale at L_1 calculated from the approximate accelerations is roughly equal to the collapse timescales for most points interior to L_1, as calculated from the exact accelerations.

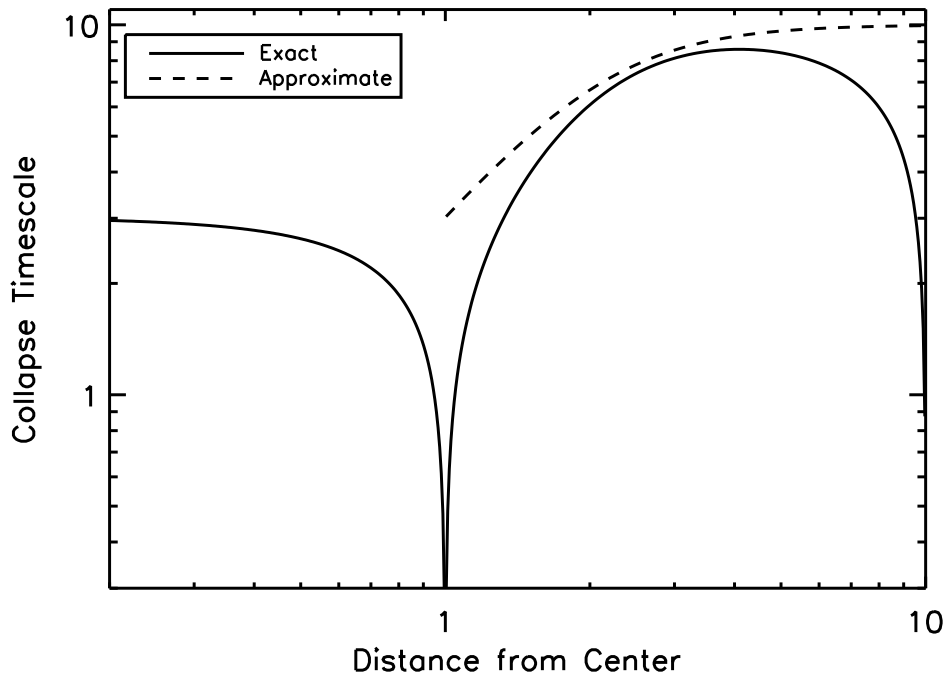

Figure 2.4: Collapse timescales of a perturbed cylinder with $L_1 = 1$, $G = 1$, $\lambda = 1$, $\epsilon = 0.1$, and $L = 10$. The solid line shows the timescales calculated from the exact accelerations while the dashed line shows the timescales calculated from the approximate accelerations. The collapse timescale, based upon the exact accelerations, becomes zero at radii of 1 and 10.

2.3.5 Edge Effects - A Hybrid Collapse Mode

In the above models, the collapse timescales become infinitely small at density boundaries. This behavior is clearly unphysical and originates from our assumption that the disc and filament are infinitely thin. To investigate the significance of this assumption with respect to our results, we have calculated the accelerations along the central axis of a cylinder with uniform density ρ, total height $2L$, and radius R. We find that the acceleration a distance $d < L$ from the center of the cylinder, but still along the central axis, is

$$a(d) = 2\pi\, G\, \rho\, \left(2d + \sqrt{R^2 + (L-d)^2} - \sqrt{R^2 + (L+d)^2}\right). \tag{2.26}$$

Evaluating this at the edge of the cylinder, $d = L$, gives a *finite* acceleration of

$$a(d) = 2\pi\, G\, \rho\, \left(2L + R - \sqrt{R^2 + 4L^2}\right), \tag{2.27}$$

thus proving that it was the infinite thinness of our prior models that led to the infinitely small collapse timescales.

As before, these accelerations can easily be turned into instantaneous collapse timescales. Figure 2.5 shows the collapse timescales for two cylinders, both with $G = 1$ and $L = 10$, where one cylinder has a radius $R = 1$ and uniform volume density $\rho = 1$ and the other cylinder is infinitely thin and has a line density equivalent to that of the other cylinder, namely $\lambda = \pi$. The collapse timescales of the two cylinders are essentially identical except for points very close to the end of the cylinders. The collapse timescales of the finite cylinder only exceed those of the infinitely thin cylinder by a factor of two or more for points within 0.02 L of the end. Since there is such a good agreement between the collapse timescales and since our global collapse timescales were calculated from our approximate accelerations, which did not trace the sharp increases in acceleration at the edges, our above analysis of the ratio of local to global collapse timescales should be valid for both infinitely thin and finite sized objects.

Figure 2.5 also shows that while a finite radius cylinder does not have infinite accelerations at its edges, the timescale for collapse still decreases towards the edge in the outer part of the cylinder. For the particular set of parameters of the finite radius cylinder shown in Figure 2.5, the edge collapse timescale is roughly a factor of three less than the global collapse timescale, given by Equation 2.21, for a filament

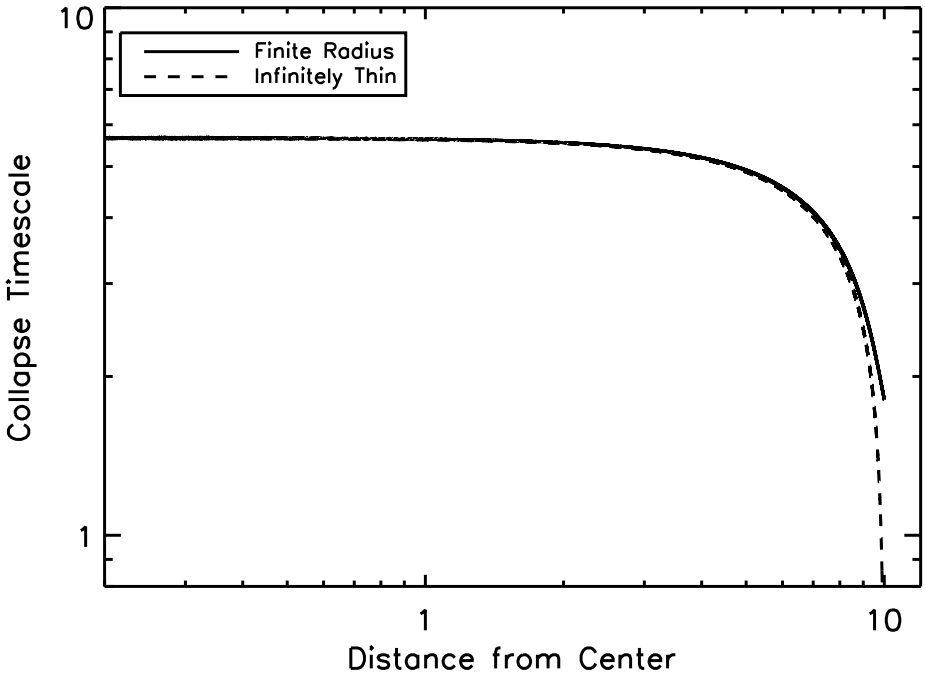

Figure 2.5: Collapse timescales of a cylinder with $L = 10$, $G = 1$, $\rho = 1$, and $R = 1$ are shown as the solid line and the collapse timescales of an infinitely thin cylinder with $L = 10$, $G = 1$, and $\lambda = \pi$ are shown as the dashed line. The collapse timescale of the infinitely thin cylinder becomes zero at a distance of 10.

with this line density. This reduction in collapse time at the edge is due to the density contrast at the edge.

A collapse timescale that decreases outwards leads to material at the edge running into material further inwards, which causes a build up of material. Such a density enhancement at the periphery of a cloud would then collapse on the local collapse timescale. We consider this edge collapse mode to be a third collapse mode that is a combination of a global and local collapse mode, since the initial accelerations are provided by the global gravitational potential while the final collapse only occurs within the local density enhancements along the edge of the cloud.

The majority of a filamentary cloud should still collapse roughly on the global collapse timescale, rather than the edge collapse timescale, as the material inward of the edge will slow the edge's collapse. This is further supported by the fact that for the cylinders in Figure 2.5, the collapse timescales for over 85% of the cylinders' lengths are within a factor of two of the global collapse timescale.

To test how important the sharp edges of our clouds are to the presence of an edge collapse mode, we examine a series of finite radius cylinders in which the density slowly decreases to zero, rather than abruptly dropping to zero, near the faces of each cylinder. We use a cylinder with R = 1, L = 10, ρ = 1, and G = 1 as our comparison, sharp edged cylinder. To create a tapered cylinder, we set the central density of the cylinder, ρ_0, to be equal to 1 and outside of a distance z_{edge} from the center of the cylinder, as measured along the central axis of the cylinder, we adopt a gaussian density profile:

$$\rho = \rho_0 \exp\left(\frac{-(z - z_{edge})^2}{2\sigma^2}\right). \tag{2.28}$$

We examine five tapered cylinders where the values of σ are 0.5, 1, 2, 4, and 6. Note that the case of $\sigma = 1$ corresponds to the taper having a size similar to the radius of the cylinder. We extend the tapered edge out to a length of 3σ, such that the density drops to less than 2% of the cylinder's central density. We choose the location where the tapered edge starts, z_{edge}, by requiring that the total mass of the tapered cylinder is the same as that of our comparison sharp edged cylinder. We then numerically calculate the instantaneous accelerations along these cylinders and convert these accelerations into collapse timescales, as done previously in this paper. The density profiles and collapse timescales for these cylinders are shown in Figure 2.6.

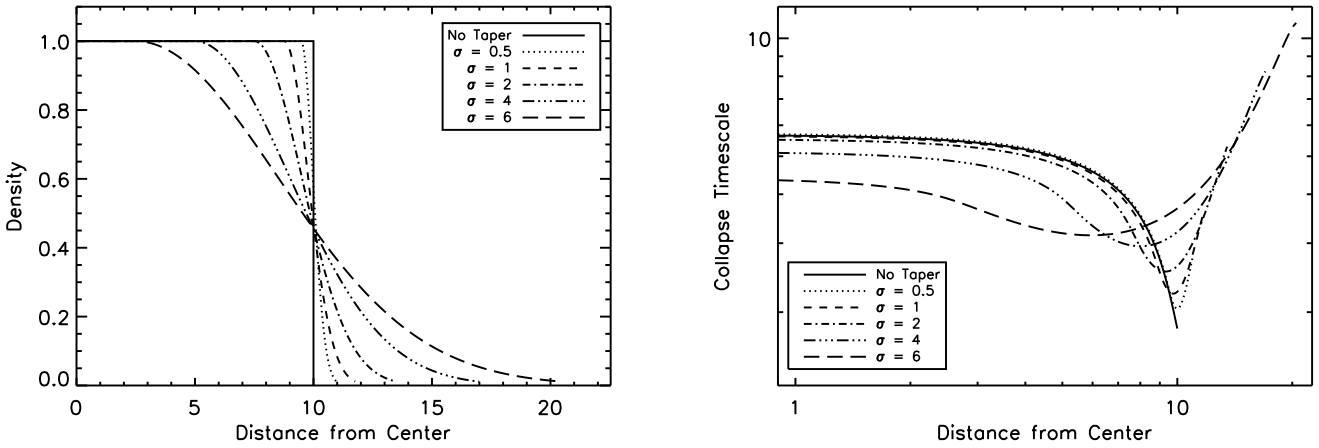

Figure 2.6: Density profiles (left) and collapse timescales (right) of tapered cylinders. For all cylinders, $G = 1$, $R = 1$, and the central density is $\rho = 1$. The solid line is for a cylinder with $L = 10$ and sharp edges. The dotted, dashed, dot-dash, dash-triple dot, and long dashed lines correspond to cylinders where σ is 0.5, 1, 2, 4, and 6, respectively, and where σ is the standard deviation of the gaussian profile used for the tapered edge. The location of the tapered edge has been chosen so that all of the cylinders have the same total mass. Note how the collapse timescale still decreases significantly towards the edge, even for the most strongly tapered cylinder.

As the length scale of the taper increases, the collapse timescale towards the edge increases and the collapse timescale of the interior decreases, thereby reducing the effectiveness of the edge collapse mode, as expected. A decrease in collapse timescale towards the edge, however, is still very prominent in all of the tapered cylinders. The ratio of the minimum collapse timescale (edge collapse) to the interior collapse timescale (global collapse) is 0.32 for the sharp edged cylinder and only increases to 0.40 for the $\sigma = 1$ cylinder. It is not until the $\sigma = 4$ cylinder, in which the central, uniform density section of the cylinder is just 60% of the length of the sharp edged cylinder, before the ratio of the minimum collapse timescale to the interior collapse timescale rises above 1/2. We therefore suggest that this edge collapse mode should still be significant in realistically tapered filaments. While we have not performed a similar calculation for a finite thickness, tapered disc, we expect that a very large taper would also be required before this edge effect becomes negligible in a disc.

2.4 DISCUSSION

2.4.1 Interpretation of Analytical Results

We have shown that weak density perturbations in spheres, discs, and filaments will collapse faster than the entire cloud, but that the significance of these local collapse modes depends strongly on the geometry of the cloud.

For spheres and discs, global collapse modes are significant. As shown in §2.3.2, the timescale for the collapse of perturbations in spheres is only dependent upon the strength of the perturbation and thus, very large perturbations are required for a spherical cloud to fragment. The collapse timescale for perturbations in discs, as shown in §2.3.3, is dependent upon the relative length scale of the perturbation, in comparison to the total size of the disc, but since thermal support sets a minimum size scale for collapse, roughly a Jeans length, we find that discs must be unrealistically large, having masses greater than 10^4 Jeans masses, for weak perturbations to collapse reasonably quicker than the entire disc. As such, discs also require large perturbations, possibly seeded by supersonic turbulence, in order for significant fragmentation to occur.

In §2.3.4, we find, however, that filamentary geometry provides a favorable situation for small perturbations to grow before global collapse overwhelms them. This situation occurs because the local collapse timescale in filaments has a stronger de-

pendance on the length scale of the perturbation than in discs or spheres. A filament needs to be only a few Jeans lengths long in order for local collapse to occur much more rapidly than global collapse, even with only weak perturbations. Thus, once filaments are formed, they are likely to fragment into multiple objects, independent of the nature of turbulence in the filaments, which suggests that star forming cores should readily occur in filamentary structures in molecular clouds. Recent observations have discovered a correlation between star forming cores and dense filaments, as discussed further in §2.4.2.2.

We have only examined the collapse timescales along the longest axis of our clouds and have assumed that our clouds are supported from collapsing along their short axis. This is not unreasonable as pressure support is most effective on small scales (i.e., scales smaller than the Jeans length). For an infinite, isothermal disc, regardless of the surface density, there is always an equilibrium configuration of material along the short axis in which the disc has a thickness of approximately a Jeans length (Spitzer, 1942, 1978) and for isothermal spheres, there is no shorter axis and thus, no extra collapse mode to account for. For an isothermal, infinite filament, there is a critical mass per unit length for the filament to be stable against radial collapse and at this critical mass per unit length, the filament has a radius of approximately a Jeans length (Stodólkiewicz, 1963; Ostriker, 1964). Below this critical value, a filament can be pressure confined (e.g., Inutsuka & Miyama 1997), but above this critical value, radial collapse cannot be prevented by thermal support alone.

Our long axis collapse modes increase the mass per unit length of a filament and could easily raise the mass per unit length of a subcritical filament above the critical value. If such a filament contains a weak perturbation, the perturbation will reach the critical mass per unit length before the rest of the filament and thus, radial collapse will occur first in the perturbation. This radial collapse will increase the speed at which the perturbation collapses and thus, will make fragmenting a filament even easier than what our analytic work suggests.

While the radial collapse mode may determine the late time density evolution of a perturbation, collapse along the long axis should still determine the final mass of the object as the majority of the mass accessible to a perturbation is along the long axis of the filament. Since our analytic results show that perturbations on the smallest length scales collapse the quickest and since thermal pressure sets a minimum collapse length scale at the Jeans length, filaments should fragment to form roughly Jeans mass objects separated by a few Jeans lengths.

This analytic work assumes that there are no effective large scale support mechanisms operating within a molecular cloud. If such a mechanism were present, molecular clouds could survive for multiple free fall times and even slow local collapse modes could occur. Possible support mechanisms discussed in the literature include driven turbulence (Bonazzola et al., 1992; Krumholz et al., 2006; Li & Nakamura, 2006) and magnetic fields (Mouschovias & Spitzer, 1976; Nakano, 1976; Shu, 1977; Shu et al., 1987).

Ballesteros-Paredes et al. (2009b) show that the galactic gravitational potential has a relatively negligible effect on a spherical molecular cloud, but for a filamentary cloud, the external potential can be larger than the self-gravity of the cloud. Ballesteros-Paredes et al. (2009a) examine the energy budget of the Taurus molecular cloud and find that over the entire cloud, the galactic tidal energy is larger than the gravitational energy and should act to disrupt the cloud. On the smaller scales of clumps, however, Ballesteros-Paredes et al. (2009a) find that the gravitational energy is much larger than the tidal energy and thus, in the Taurus molecular cloud, the galaxy's gravitational potential should prevent global collapse but should not significantly hinder small scale collapse.

2.4.2 Comparison with Simulations and Observations

In this section, we apply the results of our analysis to both simulations, in §2.4.2.1, and observations, in §2.4.2.2.

2.4.2.1 Simulations

Simulations of supersonic turbulence show that the fragmentation of three-dimensional clouds into sheets and filaments is a natural consequence of supersonic turbulence (e.g., Bate et al. 2002, 2003; Klessen et al. 2000; Ostriker et al. 2001; Clark & Bonnell 2004; Li et al. 2004; Vázquez-Semadeni et al. 2005). Magnetic fields are also only capable of providing support perpendicular to the field direction and thus, magnetically supported clouds will also tend to collapse to form sheets and filaments. As we have shown, once filamentary substructure forms, the filaments can readily fragment to form star forming cores. Thus, star formation may occur through a process of reduction of dimensions, wherein spherical and disc shaped clouds first fragment to form filaments and then star formation occurs within these filamentary structures (see also Larson 1985).

Sheet-like, or at least flattened, clouds would be expected if clouds assemble in large-scale flows from the ambient medium. Besides observational evidence (see e.g., Beaumont & Williams 2010), a whole series of numerical experiments has demonstrated that the formation of clouds due to sweep-up by shells or flow collisions can lead to flattened (yet turbulent) structures (Vázquez-Semadeni et al., 2007; Heitsch & Hartmann, 2008; Banerjee et al., 2009) that, in some cases, display ring-like structures, as seen in the more idealized experiments by Burkert & Hartmann (2004). Heitsch et al. (2008b) explicitly demonstrate that the ring-like filaments in their models are caused by global gravitational modes at the edge of the cloud. Yet from the current models it is difficult to see whether these ring structures will persist in a more general situation, where the colliding streams are not strongly spatially constrained. Unlike the idealized, truly two-dimensional models of Burkert & Hartmann (2004), the three-dimensional cloud-formation models do show local collapse modes induced by turbulence and/or strong cooling (see Heitsch et al. 2008a for a discussion of the timescales).

The preferential formation of density enhancements at the edges of filaments and discs, as would be caused by the edge collapse mode described in §2.3.5, does occur in various numerical simulations (e.g., Bastien 1983; Hartmann & Burkert 2007). In §2.3.5, we determined that while this edge collapse mode can be suppressed in filamentary structures by tapering the edges of the filament, the taper has to be quite large in order for the edge collapse mode not to be significant. Li (2001) examines the importance of sharp edges to the formation of a dense ring along the outer edge of a collapsing disc and finds that the formation of this ring is only suppressed when the edge of the disc is tapered and the length scale of the taper is at least comparable to the size of the uniform density portion of the disc. Similarly, for filaments, the simulations of Nelson & Papaloizou (1993) show that prolate spheroids, which are highly tapered cylinders, do not always form fragments at their ends.

Consideration of the short global free-fall time for finite molecular clouds suggests that it is hard to maintain a "quiescent" star formation mode whereby individual Jeans mass objects fall out of a "quasi-static" cloud. Rather, our results emphasize that the bulk of the cloud also partakes in the gravitational collapse. While observations of molecular clouds often refer to "quiescent" versus "clustered" star formation, the distinction in this work is between local and global collapse in a finite cloud. In our picture, global collapse inevitably occurs, but local collapse is more prone to happen at lower dimensions, namely in rings/edges for sheets, and at the ends of

filaments. Yet, note that this kind of local collapse occurring at the edges of clouds is still at least partially driven by global accelerations in all cases. Likewise, local, pre-seeded perturbations are more likely to grow and collapse in clouds of lower dimensionality; perturbations in sheets, if large enough, and filaments have more of a chance to collapse before global collapse ensues.

The similarity between the local and global collapse timescales in spheres and discs means that global collapse modes cannot be ignored in models or simulations of spherical or disc shaped molecular clouds. Thus, predictions of evolution timescales from models of cloud fragmentation in periodic boxes (Klessen et al., 2000; Ostriker et al., 2001; Heitsch et al., 2001; Li et al., 2004; Padoan & Nordlund, 2002; Vázquez-Semadeni et al., 2005), or quasi-static approaches (Myers, 2009), are strongly limited by their assumptions of boundary conditions and/or initial states. Furthermore, since periodic box models do not incorporate physical processes occurring on scales larger than the box length, such as global collapse, it is exceedingly difficult to accurately run them for longer than the background global collapse timescale. As such, while periodic box simulations accurately follow the evolution of strong density perturbations, they cannot follow the collapse of small perturbations to completion. In other words, they only give meaningful results on timescales that are shorter than the global collapse timescale in the absence of the periodic boundaries.

2.4.2.2 Observations

Filamentary structure in star forming clouds appears to be ubiquitous. Filaments are present in both high-mass and low-mass star forming regions and are detected from the largest scales of molecular clouds all the way down to the scale of individual star forming cores; although, individual cores tend to be less elongated as thermal pressure plays a larger role on smaller spatial scales (e.g., Schneider & Elmegreen 1979; Scalo 1985; Bally et al. 1987; Heyer et al. 1987; Kulkarni & Heiles 1988; Loren 1989; Nozawa et al. 1991; Tatematsu et al. 1993; Onishi et al. 1996; Lada et al. 1999; Jijina et al. 1999; Heithausen et al. 2002; Hartmann 2002; Johnstone et al. 2003; Lada et al. 2007; Myers 2009; Molinari et al. 2010; André et al. 2010). For instance, the Orion A molecular cloud is filamentary on large scales and contains filamentary substructure, including the integral shaped filament and the Orion Nebula Cluster (ONC) (e.g., Bally et al. 1987; Johnstone & Bally 1999). Such filamentary structure is seen in both gas tracers and in star counts (e.g., Bally et al. 1987; Hillenbrand &

Hartmann 1998). Radial velocity measurements of stars and gas around the ONC have revealed a large scale velocity gradient, which has been interpreted as global collapse along the long axis of the filamentary structure of the ONC (Fűrész et al., 2008; Tobin et al., 2009). The large scale structure of the Orion A molecular cloud has also been remarkably well reproduced by a simulation of a rotating disc with a density gradient (Hartmann & Burkert, 2007).

The presence of filamentary structures appears to be closely tied to the star formation process, as young protostars and bound prestellar objects are preferentially located within dense filaments (Hartmann, 2002; André et al., 2010). André et al. (2010) further note that Class 0 protostars and bound prestellar cores primarily exist in filaments that have mass per unit lengths larger than the critical mass per unit length at which an infinite, isothermal cylinder will be unstable to radial collapse (see §2.3.1), suggesting that the radial collapse mode of filaments plays a vital role in fragmenting a molecular cloud. This association of star forming cores with filaments is what we would expect given that our analytical results indicate that only filaments can readily fragment without strong perturbations.

2.5 CONCLUSIONS

We have analytically estimated the global collapse timescales of spherical, disk shaped, and filamentary molecular clouds, as well as the local collapse timescales for small perturbations in these same clouds. We have shown that local collapse modes with timescales less than the timescales for global collapse do exist for perturbed spheres, discs, and cylinders and that local collapse is more effective for lower dimensional objects. We find the square of the ratio of global to local collapse timescales is inversely dependent upon the square of the relative size of the perturbed region of a cylinder, is inversely dependent upon the relative size of the perturbed region of a disc and is independent of the relative size of the perturbed region of a sphere. Table 2.1 summarizes the most important derived equations relating to the collapse of perturbed spheres, discs, and cylinders.

We find that filamentary geometry is the most favorable situation for the smallest perturbations to grow before global collapse overwhelms them and that filaments containing only a few Jeans masses and weak density perturbations can readily fragment. Conversely, we find that weak perturbations in realistically sized discs and spherical clouds do not collapse significantly faster than the entire cloud. Global col-

lapse modes are significant in spheres and discs and cannot be ignored in simulations or models of such clouds. We also find that there exists an edge instability in discs and filaments that may lead to dense, locally collapsing structures along the periphery of these clouds. Our results suggest that star formation may occur through a process of reduction of dimensions, wherein spherical and disc shaped clouds first fragment to form filaments and then star formation occurs within these filamentary structures

2.6 ACKNOWLEDGMENTS

We would like to thank Lee Hartmann for originally bringing to our attention the tension between local and global collapse modes, as well as for many insightful discussions regarding the potential importance of global collapse modes. We would also like to thank Dr. Hartmann for a critical reading of an early version of this paper that has greatly improved the quality of this manuscript. We would also like to thank our anonymous referee for many useful changes to this paper. AP was partially supported by the Natural Sciences and Engineering Research Council of Canada graduate scholarship program. DJ acknowledges support from an NSERC Discovery Grant. FH gratefully acknowledges support by the NSF through grant AST 0807305, and by the NHSC through grant 1008. This research has made use of NASA's Astrophysics Data System.

Table 2.1. Summary of Key Analytic Equations

Quantity	3D Sphere	2D Disc	1D Cylinder
a_{exact}	$\frac{4\pi G\rho r}{3}\left(1+\frac{\epsilon R_1^3}{r^3}\right)$	$4G\Sigma\frac{R}{r}\left(\left[K\left(\frac{r}{R}\right)-E\left(\frac{r}{R}\right)\right]+\epsilon\frac{r}{R}\left[K\left(\frac{R_1}{r}\right)-E\left(\frac{R_1}{r}\right)\right]\right)$	$\frac{G\lambda}{L-d}-\frac{G\lambda}{L+d}+\frac{G\lambda\epsilon}{d-L_1}-\frac{G\lambda\epsilon}{L_1+d}$
$a_{approximate}$	$\frac{4\pi G\rho r}{3}\left(1+\frac{\epsilon R_1^3}{r^3}\right)$	$\frac{\pi G\Sigma r}{R}+\frac{\pi G\epsilon\Sigma R_1^2}{r^2}$	$\frac{G\lambda 2d}{L^2}\left(1+\frac{\epsilon L_1 L^2}{d^3}\right)$
t^2	$\frac{3}{2\pi G\rho}\left(1+\frac{\epsilon R_1^3}{r^3}\right)^{-1}$	$\frac{2R}{\pi G\Sigma}\left(1+\frac{\epsilon R R_1^2}{r^3}\right)^{-1}$	$\frac{L^2}{G\lambda}\left(1+\frac{\epsilon L_1 L^2}{d^3}\right)^{-1}$
$\frac{t_g^2}{t_l^2}$	$1+\epsilon$	$1+\frac{\epsilon R}{R_1}$	$1+\frac{\epsilon L^2}{L_1^2}$

Chapter 3

Aspect Ratio Dependence of Collapse Times

I have measured out my life with coffee spoons
T.S. Eliot

3.1 ABSTRACT

We investigate the collapse of non-spherical substructures, such as sheets and filaments, which are ubiquitous in molecular clouds. Such non-spherical substructures collapse homologously in their interiors but are influenced by an edge effect that causes their edges to be preferentially accelerated. We analytically compute the homologous collapse timescales of the interiors of uniform-density, self-gravitating filaments and find that the homologous collapse timescale scales linearly with the aspect ratio. The characteristic timescale for an edge-driven collapse mode in a filament, however, is shown to have a square-root dependence on the aspect ratio. For both filaments and circular sheets, we find that selective edge acceleration becomes more important with increasing aspect ratio. In general, we find that lower dimensional objects and objects with larger aspect ratios have longer collapse timescales. We show that estimates for star formation rates, based upon gas densities, can be overestimated by an order of magnitude if the geometry of a cloud is not taken into account.

3.2 INTRODUCTION

Molecular clouds are observed to have complex geometries and contain non-spherical substructures, including sheets and filaments (e.g., Schneider & Elmegreen 1979; Bally et al. 1987; Lada et al. 1999; Hartmann 2002; Johnstone et al. 2003; Lada et al. 2007; Myers 2009; Molinari et al. 2010; André et al. 2010). Recent *Herschel* observations, in particular, have revealed a plethora of filamentary structures within star-forming regions (e.g., André et al. 2010). Filamentary structures are seen on both molecular cloud scales as well as on the small scales of individual protostellar envelopes (e.g., André et al. 2010; Tobin et al. 2010; Hacar & Tafalla 2011). Such filamentary structures are also commonly predicted by star formation models and formed in molecular cloud simulations, although their formation mechanisms vary depending upon which model is used. Supersonic hydrodynamic and magnetohydrodynamic turbulence, gravo-turbulent models, gravitational amplification of anisotropies, flow collisions, and global gravitational accelerations have all been shown to be capable of forming filamentary structures (e.g., Lin et al. 1965; Klessen & Burkert 2001; Padoan et al. 2001; Burkert & Hartmann 2004; Hartmann & Burkert 2007; Padoan et al. 2007; Bate 2009; Vázquez-Semadeni et al. 2010, 2011).

The collapse modes of spherical and infinite, non-spherical structures have been thoroughly investigated in earlier works (e.g., Ledoux 1951; Stodólkiewicz 1963; Ostriker 1964; Larson 1969; Penston 1969; Shu 1977; Larson 1985; Inutsuka & Miyama 1992; Nakamura et al. 1993; Inutsuka & Miyama 1997; Fiege & Pudritz 2000; Curry 2000; Myers 2009), but the collapse properties of finite, non-spherical structures have only been considered recently and are much less understood, owing to their inherent global and local instabilities, as well as the critical importance of initial conditions (e.g., Bastien 1983; Bastien et al. 1991; Burkert & Hartmann 2004; Hsu et al. 2010; Pon et al. 2011; Toalá et al. 2012).

Simulations show that non-spherical structures collapse on longer timescales than equal-density spherical objects (e.g., Burkert & Hartmann 2004; Vázquez-Semadeni et al. 2007) and that non-spherical structures are prone to gravitational focusing, whereby strong density enhancements form at the edges of these objects (e.g., Bastien 1983; Burkert & Hartmann 2004; Hartmann & Burkert 2007; Heitsch et al. 2008b; Hsu et al. 2010). The longer collapse timescales of non-spherical objects, as well as the presence of selective edge acceleration, have also been analytically demonstrated (Burkert & Hartmann, 2004; Pon et al., 2011; Toalá et al., 2012).

While uniform-density spheres collapse homologously (e.g., Binney & Tremaine 1987), an edge effect in circular sheets and filaments produces a second mode through which these lower dimensional clouds can collapse, wherein the collapse is controlled by an infalling edge sweeping up material. It has not been clear, however, whether the edge of a lower dimensional structure will obtain sufficient momentum to be able to sweep up the interior, so that the collapse timescale is controlled by the selective edge acceleration, or whether the roughly homologously collapsing interior will slow down the collapsing edge enough such that the collapse timescale will approach the homologous collapse timescale of the interior.

Recently, Toalá et al. (2012) showed that the free-fall times of circular sheet-like ("2D" collapse) and filamentary clouds ("1D" collapse) depend strongly on the geometry of the cloud and, for both cases, are larger than that of a uniform sphere with the same volume density by a factor proportional to the square root of the initial aspect ratio, A. For circular sheets, the aspect ratio is given by $A = R(0)/H$, $R(0)$ being a sheet's initial radius and H its thickness, and for filaments, the aspect ratio is defined as $A = Z(0)/\mathcal{R}$, where $Z(0)$ is a filament's initial half-length and $\mathcal{R}$ is the radius. On the other hand, Pon et al. (2011) find that the collapse timescale of an infinitely thin filament varies linearly with the aspect ratio, rather than with the square root of the aspect ratio.

Toalá et al. (2012) obtain their analytic expressions for the free-fall times by integrating, over time, the accelerations at the edges of a circular sheet and cylinder under two different assumptions. In the first case, Toalá et al. (2012) assume that the mass of the cloud remains constant and that the density of the cloud remains spatially uniform over the entire collapse. This is equivalent to assuming that the collapse is homologous. In their second case, Toalá et al. (2012) assume that the density of the cloud remains spatially and temporally constant. For this second case, it is assumed that the collapse is dominated by the insweeping edge. These approximations are used to make the problem analytically tractable. Toalá et al. (2012) argue that these two approximations represent the extreme cases, where the collapse timescale is determined solely from either the homologously collapsing interior or from the selective edge acceleration, such that the actual collapse timescale should lie somewhere between the two derived timescales.

In Section 3.3.1, we calculate the collapse timescales of a uniform-density cylinder, under the assumption that the cylinder collapses homologously along its major axis. We use the first-order approximation to the acceleration that is valid in the interior

of the cylinder, rather than using the acceleration at the edge, as done by Toalá et al. (2012). In Section 3.3.2, we calculate the collapse timescale for a filament, under the approximation that the interior density remains spatially and temporally constant, by treating the gravitational force per unit mass on the edge as a rate of momentum transfer per unit mass, rather than as an acceleration, as done by Toalá et al. (2012). We thus take into account the effect of low velocity mass being accumulated by the edge. We compare our collapse timescales to previously obtained results in Section 3.3.3. In Section 3.4, we compare the relative importance of the homologous collapse mode and edge-driven collapse mode in filaments and circular sheets. We also discuss in Section 3.4 whether the collapse timescales of filaments and circular sheets have the same dependence upon the aspect ratio, as found by Toalá et al. (2012), as well as discussing the implications of our collapse timescales. Finally, we summarize our findings in Section 3.5.

3.3 COLLAPSE TIMESCALES OF UNIFORM DENSITY CYLINDERS

While circular sheets and cylinders are formally the same type of object, we differentiate between the two based upon which axis is longer and along which axis collapse is occurring. We refer to objects with radii larger than their heights, and collapsing radially, as finite, circular sheets and refer to objects with heights larger than their radii, and collapsing along their long, vertical axis, as cylinders. Thus, finite circular sheets represent "2D" sheets while cylinders represent "1D" filaments.

3.3.1 Homologous Collapse

The free-fall collapse timescale of a sphere is a well-studied problem (e.g., Binney & Tremaine 1987) and the homologous collapse timescale of the interior of a finite circular sheet is calculated by J. A. Toalá et al. (2012, in preparation [erratum]). For reference, we present derivations of the collapse timescales of these two objects in Appendices 3.7 and 3.8.

We examine a cylinder with a total mass M, a total length along the major axis of $2Z(t)$, and a volume density $\rho(t) = M/[2\pi\mathcal{R}^2 Z(t)]$, where $\mathcal{R}$ is the time-independent radius. We denote the distance of a mass element along the major axis from the center of the cylinder as z, the initial length of the cylinder as $2Z(0)$, and the initial

volume density as $\rho(0)$. The aspect ratio of the cylinder is defined as $A = Z(0)/\mathcal{R}$. The magnitude of the acceleration along the major axis of the cylinder, for points within the cylinder, is given by Burkert & Hartmann (2004) as

$$\begin{aligned} a(z,t) &= 2\pi G\rho(t)\big\{2z + \sqrt{\mathcal{R}^2 + (Z(t)-z)^2} \\ &\quad -\sqrt{\mathcal{R}^2 + (Z(t)+z)^2}\big\}. \end{aligned} \tag{3.1}$$

In a homologous collapse, the density remains spatially uniform, although not temporally constant, and all regions have the same collapse timescale. For a uniform-density object to collapse homologously, the acceleration across the object at any given time must be a linear function of the radial distance to the collapse center. Equation (3.1) is not a linear function of z and thus, the collapse of a filament is not homologous. Burkert & Hartmann (2004) find that the first-order approximation to the acceleration[1], under the condition that $|Z(t) - z| \gg \mathcal{R}$, is

$$a(z,t) \approx \pi G\mathcal{R}^2\rho(t)\left[\frac{2z}{Z(t)^2 - z^2}\right]. \tag{3.2}$$

While Equation (3.2) is also not a linear function of z, for the interior of a filament, where $z^2 \ll Z(t)^2$, the acceleration can be approximated by

$$a(z,t) \approx \pi G\mathcal{R}^2\rho(t)\left[\frac{2z}{Z(t)^2}\right]. \tag{3.3}$$

Since Equation (3.3) is a linear function of z, the assumption of homologous collapse is reasonable for the interior portion of a cylinder. As shown in Appendix 3.8, this is also the case for the interior of a circular sheet. While strictly Equation (3.3) should only be used to find accelerations of the interior of a cylinder, the collapse timescales in a homologous collapse are constant across the entire object and thus, evaluating this acceleration at the edge will yield the collapse timescale of the interior. In this paper, the ends of the major axis of a cylinder are referred to as the edges of the cylinder.

Equation (3.3) can be re-written in terms of the total mass of a cylinder. Evalu-

[1]Equation (11) of Burkert & Hartmann (2004) gives another form of this first-order approximation, but is missing a negative sign from the first term in the brackets. In our notation, Burkert & Hartmann's (2004) Equation (11) should read as $|a(z,t)| \approx \pi G\,\rho(t)R^2\left[-(Z(t)+z)^{-1} + (Z(t)-z)^{-1}\right]$.

ating this new expression at the edge, where $z = Z(t)$, yields

$$\frac{dv_0(t)}{dt} = \frac{GM}{Z(t)^2}, \tag{3.4}$$

where $v_0(t)$ is the velocity at the edge at time t. This differential equation has the same dependences on mass and length as in the spherical and circular sheet cases presented in Appendices 3.7 and 3.8. Equation (3.4) can be solved for the cylinder collapse timescale, τ_{1D},

$$\tau_{1D} = \sqrt{\frac{2}{3}}\, A\, \tau_{3D}, \tag{3.5}$$

where τ_{3D} is the classical free-fall timescale of a uniform-density sphere with the same volume density as the cylinder, as derived in Appendix 3.7. Thus, the homologous collapse timescale for a cylinder is linearly proportional to the aspect ratio.

3.3.2 Cylindrical Edge Collapse: A Constant Density Approximation

The exact solution for the accelerations of a cylinder, Equation (3.1), shows that nonlinear terms become significant toward edges, such that the edges are preferentially given more momentum than would be expected for homologous collapse. If edges are given sufficient momentum, the collapse of a cylinder may be dominated by the edges sweeping up interior material, such that the collapse occurs on a timescale faster than the homologous collapse timescale calculated in Section 3.3.1.

We now calculate the collapse timescale of a cylinder under the approximation that the material inside of the edge stays at a constant density and does not move inward until contacted by the insweeping edge. We assume that the only acceleration in the system is due to the gravitational force on the edge caused by the interior material and we assume that the edge sweeps up all material it contacts, such that the mass of the edge grows as it falls inward. We do not consider the gravitational force on one edge of the filament due to the other edge. For a cylinder with an aspect ratio of 10, the gravitational force due to the second edge only becomes equal to the force due to the uniform-density, interior material once the cylinder has shrunk to roughly one tenth of its original size. Thus, the collapse timescale is relatively unaffected by the presence of a mass concentration at the other edge. As argued by Toalá et al. (2012), the true collapse timescale should lie between the homologous

collapse approximation and this constant density approximation.

As given by Pon et al. (2011) and Toalá et al. (2012), the gravitational force per unit mass on the major axis and at the edge of a cylinder of length $2Z$, radius $\mathcal{R}$, and uniform-density ρ is

$$g = 2\pi\, G\, \rho \left[2Z(t) + \mathcal{R} - \sqrt{\mathcal{R}^2 + 4Z(t)^2} \right]. \tag{3.6}$$

Under the assumption that $Z(t) \gg \mathcal{R}$, the square root can be expanded and the force per unit mass, to lowest order, becomes

$$g \approx 2\pi\, G\, \rho\, \mathcal{R}. \tag{3.7}$$

Note that the force per unit mass is independent of the length of the cylinder. This approximation to the acceleration at the end of a cylinder is within 5% of the exact acceleration given by Equation (3.6) for aspect ratios above 5 and within 10% for an aspect ratio of 3.

By equating the gravitational force acting on the edge with the total rate of change of momentum of the edge, we find, in Appendix 3.9, that the length of the cylinder at a time t is given by

$$Z(t) \approx Z(0) - \frac{gt^2}{6}, \tag{3.8}$$

where $Z(0)$ is the initial length of the cylinder.

Equation (3.8) shows that the effect of the edge of a cylinder accreting low velocity mass is only to lower the effective acceleration by a factor of three below the acceleration that would be obtained by directly equating the gravitational force per unit mass to the acceleration of the edge. Substituting in the lowest order approximation to the force per unit mass at the edge yields a collapse timescale of

$$\tau_{\rm 1D} = \sqrt{\frac{6Z(0)}{2\pi\, G\, \rho\, \mathcal{R}}}, \tag{3.9}$$

$$\tau_{\rm 1D} = \sqrt{\frac{32A}{\pi^2}}\, \tau_{\rm 3D}, \tag{3.10}$$

where, as before, A is the original aspect ratio and $\tau_{\rm 3D}$ is the classical free-fall timescale of a uniform-density sphere with the same volume density as the cylinder.

3.3.3 Comparison to Previous Work

Pon et al. (2011) examine the accelerations of an infinitely thin, but finitely long, filament and find that the acceleration becomes infinite at the edge of such a filament. Because of this infinite acceleration, Pon et al. (2011) derive a first-order approximation to the accelerations of their infinitely thin filament that is identical to the first-order approximation to the accelerations of a finite radius cylinder derived in Section 3.3 as Equation (3.3).

We find that the homologous collapse timescale for a cylinder is $\sim 0.82A\,\tau_{\rm 3D}$. This differs significantly from the timescale found by Toalá et al. (2012) for the homologous collapse of a cylinder, $\sim 0.92\sqrt{A}\,\tau_{\rm 3D}$. We find that the collapse timescale for a homologously collapsing cylinder scales linearly with the aspect ratio, while Toalá et al. (2012) find a $\sqrt{A}$ relationship. The cause of the difference between these two results is that Toalá et al. (2012) use the acceleration at the edge, while we use a first-order approximation to the acceleration in the interior of a cylinder. Thus, we probe the collapse timescales of the interior of a cylinder while Toalá et al. (2012) are sensitive to the collapse dynamics at the edge of a cylinder.

We find that if the collapse of a cylinder is dominated by the preferential edge acceleration, such that the interior remains static and at a constant density until swept up by the edge, the collapse timescale is $\sqrt{32A/\pi^2}\,\tau_{\rm 3D}$. Toalá et al. (2012) find that the collapse timescale of a cylinder, under this constant density approximation, is $\sqrt{32A/(3\pi^2)}\,\tau_{\rm 3D}$. Since we show in Section 3.3.2 that the effect of accounting for the additional mass being accreted by the edge of the cylinder is to decrease the effective acceleration by a factor of three, it is unsurprising that the Toalá et al. (2012) collapse timescale is exactly a factor of $\sqrt{3}$ smaller than what we derive.

3.4 DISCUSSION

Figure 3.1 shows the exact accelerations, from Equation (3.1), of uniform-density cylinders with various aspect ratios. The aspect ratios shown range from 2.5 to 20 by factors of two. The units of acceleration in Figure 3.1 are $2\lambda G/Z$, where $\lambda = \pi\mathcal{R}^2\rho$, such that the linear approximations to the accelerations of all of the cylinders are given by the same solid line. The momentum deposited per unit length, per unit time of a cylinder can be found by multiplying the acceleration by a constant factor and thus, is not shown in Figure 3.1.

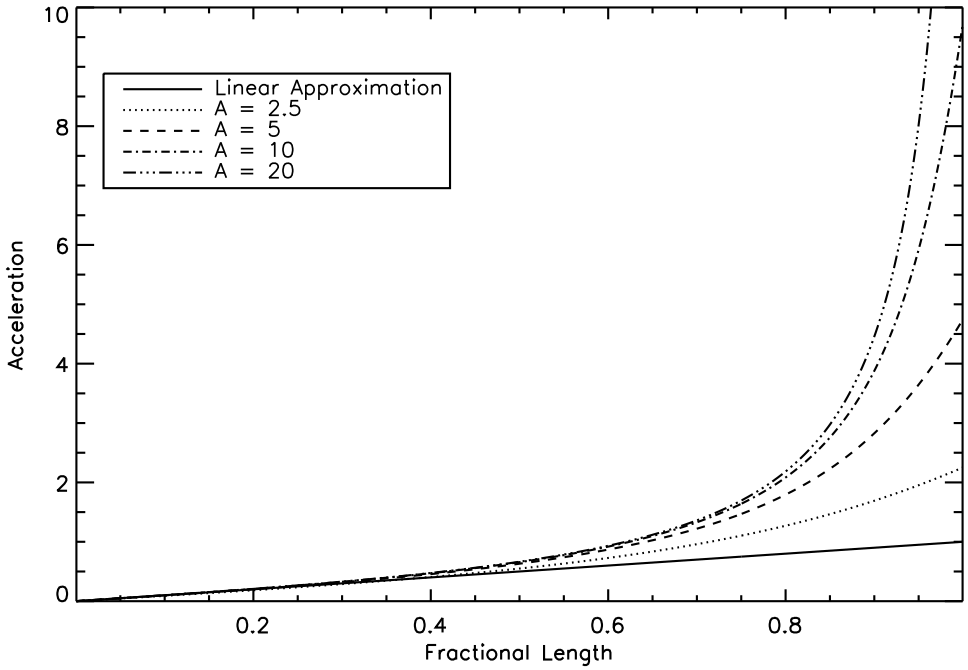

Figure 3.1: Radial accelerations, in units of $2\lambda G/Z$, for uniform-density cylinders with different aspect ratios. The dotted, dashed, dash-dotted, and dash-triple-dotted lines show the exact radial accelerations for cylinders with aspect ratios of 2.5, 5, 10, and 20, respectively. The solid line shows the first-order approximation to the accelerations for all four cylinders. Note how the assumption of homologous collapse becomes worse as the aspect ratio increases.

The exact accelerations of a radially collapsing, infinitely thin, unifor-density, circular sheet with mass M, radius $R(t)$, and surface density $\Sigma(t)$, are given by Equation (3.16) in Appendix 3.8, while the first-order approximations to these accelerations are given by Equation (3.17). Figure 3.2 shows these exact and first-order accelerations of a circular sheet in units of $4G\Sigma$. Figure 3.2 also shows the total momentum deposited per unit angle, per unit radial length, per unit time of a circular sheet, as a function of enclosed mass, for these two different acceleration equations, in units of $4G\Sigma R$. The momentum deposited per unit angle, per unit radial length, per unit time, is related to the acceleration via

$$p(r,t) = a(r,t)r. \tag{3.11}$$

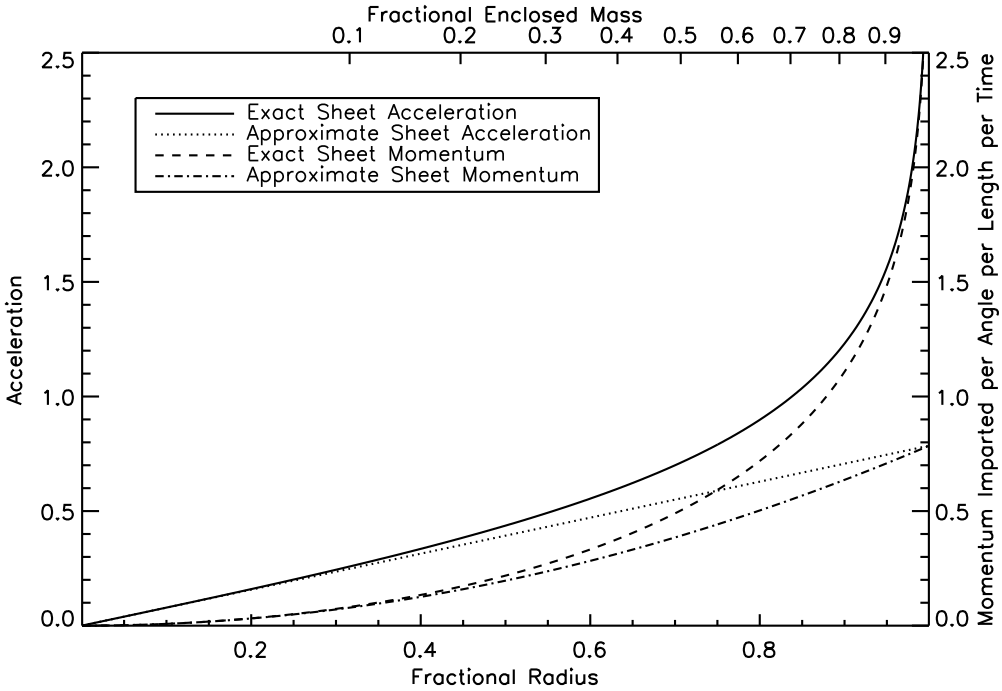

Figure 3.2: Exact radial accelerations, in units of $4G\Sigma$, for an infinitely thin, uniform-density, circular sheet are shown as the solid line. The first-order approximation to these accelerations is shown as the dashed line. The dotted and dash-dotted lines show the momentum imparted per unit angle, per unit radial length, per unit time, in units of $4G\,\Sigma^2 R$, based upon the exact and approximate accelerations, respectively. The lower x-axis shows the distance along the sheet as a fraction of the total radius and the upper x-axis gives the fraction of the total mass of the sheet within that radius.

Figures 3.1 and 3.2 show that, for the interiors of uniform-density cylinders and circular sheets, the accelerations can be well approximated by linear functions of distance. A comparison of Equations (3.1) and (3.16) to Equations (3.3) and (3.17) shows that this linear approximation is valid to within a factor of two for $z < 0.7Z$ in a uniform-density cylinder with an aspect ratio of 10 and for $r < 0.94R$ in a uniform-density circular sheet. Near the edges of cylinders and circular sheets, nonlinear terms become dominant and the accelerations become significantly larger than the first-order approximations. This suggests that the collapse of cylinders and circular sheets can be described as the combination of two separate collapse modes. The interiors of these objects collapse roughly homologously while the outer regions are dominated by an edge-driven collapse mode, wherein momentum is preferentially deposited toward the edges of the objects and collapse proceeds as the edges sweep up slower moving interior gas. This preferential edge acceleration has been previously identified in simulations and analytic work (e.g., Burkert & Hartmann 2004; Hartmann & Burkert 2007; Pon et al. 2011).

We associate the collapse timescales of Sections 3.3.1 and 3.3.2 with the two different collapse modes. We consider the homologous collapse timescale derived in Section 3.3.1 to be the characteristic collapse timescale of the interior of a cylinder and the constant density collapse timescale derived in Section 3.3.2 to be the characteristic collapse timescale for the edge-driven collapse mode in a cylinder.

The different dependences on aspect ratio, for a cylinder's collapse timescale, as derived in Sections 3.3.1 and 3.3.2, is thus explainable as being due to the different calculations probing different collapse modes. Our results suggest that the interior of a cylinder will collapse on a timescale proportional to A while the edge-driven collapse timescale will depend on $\sqrt{A}$. Furthermore, this suggests that the relative importance of the preferential edge acceleration will also depend upon the aspect ratio, with the edge collapse mode being more important in cylinders with larger aspect ratios. Such a trend is clearly seen in Figure 3.1.

3.4.1 Relative Importance of Preferential Edge Acceleration versus Homologous Collapse

While the actual collapse of a cylinder or a circular sheet will be a combination of the homologous collapse mode and the edge-driven collapse mode, it is possible that one of these modes will be dominant. If the edge-driven collapse mode is dominant, such

that the majority of the total momentum is injected at the edge, the collapse will proceed primarily by the edge falling in and sweeping up material. Alternatively, if the majority of the momentum imparted to an object is due to the linear term of the acceleration, the infalling edge will have insufficient momentum to significantly accelerate the material it sweeps up and the collapse will proceed roughly homologously, albeit with a slight density enhancement at the edge.

The total rate of momentum imparted to a circular sheet can be calculated by integrating the product of Equation (3.16) and the mass element over the entire sheet or by multiplying the total area under the dashed curve in Figure 3.2 by 2π. The total momentum imparted to a cylinder can be found by integrating Equation (3.1) over the entire cylinder and then multiplying by the total mass of the cylinder, or by multiplying the area under the appropriate curve in Figure 3.1 by the mass of the cylinder.

For an infinitely thin circular sheet, the total rate of momentum imparted to the sheet is finite, whereas for an infinitely thin filament, the total rate of momentum imparted is infinite. Thus, there is a maximum limit to the fractional contribution of the nonlinear components of the acceleration to the total momentum imparted to a circular sheet. For an infinitely thin circular sheet, almost twice as much momentum is imparted to the sheet due to the linear term in the acceleration than due to the nonlinear terms. Since the importance of preferential edge acceleration shrinks with decreasing aspect ratio, the linear acceleration term will dominate the momentum imparted for all circular sheets with finite height. Thus, it is expected that circular sheets should collapse roughly homologously.

Burkert & Hartmann (2004) simulate the collapse of uniform-density circular sheets and find that the collapse timescales of the sheets are only 20% shorter than the homologous collapse timescale that we calculate. This shortening of the timescale by 20% is almost exactly what would be expected given that nonlinear terms contribute an additional 50% to the momentum of infinitely thin circular sheets. Burkert & Hartmann (2004) also note that the interiors of their simulated circular sheets undergo significant collapse before encountering the edge, as would be expected only if the homologous collapse mode is significant in these circular sheets.

For uniform-density cylinders with aspect ratios larger than five, the nonlinear components of the acceleration impart more momentum to the cylinders than the linear component. The nonlinear components contribute relatively more momentum as the aspect ratio increases and by an aspect ratio of 10, the nonlinear components

contribute almost twice as much momentum as the linear component. Since realistic filaments have aspect ratios up to 60 (André et al., 2010), preferential edge acceleration may control the evolution of many observed filaments.

3.4.2 Interpretation

Equations (3.14), (3.19), and (3.4) are the differential equations describing the collapse of spheres, circular sheets, and cylinders, respectively, under the assumption of homologous collapse, and all three equations are of the form

$$\frac{dv_0}{dt} \sim \frac{GM}{\chi^2}, \tag{3.12}$$

where χ is the collapsing dimension. Because of the similarity in these differential equations, the collapse timescales of the three different objects are all of the form

$$\tau \sim \sqrt{\frac{\pi^2 \chi^3}{8GM}}. \tag{3.13}$$

When written in terms of the total mass of the cloud, the collapse timescales for all three objects are independent of the initial aspect ratio. This lack of dependence upon the aspect ratio is not trivial, as dimensional arguments place no constraints on the proportionality of the unitless aspect ratio.

The dependence of the homologous collapse timescales, of spheres, circular sheets, and cylinders, on the aspect ratio, when written in terms of the initial density, comes solely from the conversion between total mass and initial density. Thus, the proportionality of the aspect ratio naturally changes with the changing dimensionality of the initial cloud. Each reduction of dimension produces an additional $\sqrt{A}$ dependence in the collapse timescale. Since, by definition, $A > 1$, the "2D" and "1D" collapse timescales are larger than that of a sphere with the same volume density. Similarly, objects of the same dimensionality but with larger aspect ratios also take longer to collapse. The increasing importance of an edge collapse mode with increasing aspect ratio, in cylindrical structures, will partially reduce the difference in collapse times between cylinders with different aspect ratios, as well as the difference between circular sheets and cylinders. Such an edge-driven collapse, however, will still occur on timescales longer than the corresponding spherical collapse timescale due to the $\sqrt{A}$ dependence that the edge-driven collapse timescale has.

3.4.3 Implications

As discussed by Toalá et al. (2012), the spherical free-fall timescale, τ_{3D}, is often used to calculate collapse timescales, and thus star formation rates, from observed gas densities, regardless of geometry. Since recent observations reveal a multitude of non-spherical substructures within molecular clouds (e.g., Myers 2009; Molinari et al. 2010; André et al. 2010), using the spherical free-fall timescale underestimates collapse timescales and overestimates star formation rates. In particular, attempts to predict the total galactic star formation rate from the observed gas properties of the Milky Way, by dividing the total molecular mass of the galactic interstellar medium by the spherical free-fall time corresponding to the mean density and temperature of the molecular gas, produce values of at least 30 $M_{\odot}$ yr^{-1} (e.g., Zuckerman & Palmer 1974; Zuckerman & Evans 1974), while more direct, observational determinations of the galactic star formation rate, based upon emission from and number counts of young, massive stars, yield star formation rates closer to a few solar masses per year (e.g., Smith et al. 1978; Diehl et al. 2006; Misiriotis et al. 2006; Murray & Rahman 2010; Robitaille & Whitney 2010).

For a filamentary structure with an aspect ratio of 60, corresponding to the upper limit of observed filamentary aspect ratios (André et al., 2010), the homologous collapse timescale is a factor of almost 50 slower than the corresponding spherical free-fall time. The edge-driven collapse timescale, while faster than the homologous collapse timescale, is still almost 15 times slower than the spherical free-fall time. For a more typical aspect ratio of 10, both the homologous and edge-driven collapse timescales of such a filament would be roughly seven times slower than the spherical free-fall timescale. Thus, geometric considerations can account for a considerable portion of the discrepancy between observed and predicted galactic star formation rates, although they are unlikely to account for the entire discrepancy. For a further discussion on the implications of "1D" and "2D" collapsing objects having longer timescales, please see Pon et al. (2011) and Toalá et al. (2012).

The two collapse modes studied in this paper, the homologous and edge-driven collapse modes, are both global collapse modes. That is, these modes cause a cloud to collapse into one central object. Density perturbations within molecular clouds will introduce local collapse modes and these local collapse modes must operate on timescales less than the global collapse modes, as molecular clouds are observed to fragment into clusters of stars, rather than collapsing to form million solar mass stars.

Pon et al. (2011) examine the conditions under which local collapse modes are significantly faster than the homologous global collapse mode in spheres, circular sheets, and cylinders. They find that strong perturbations are required for local collapse modes to be significantly faster in circular sheets and spheres, but small ($\sim$10%) density perturbations in a cylinder can collapse significantly (three times) faster than the entire cylinder if the total length of the cylinder is greater than 10 times the length of the perturbation. Since thermal motions support perturbations smaller than the Jeans length and the radial length scale of a radially supported cylinder is also approximately the Jeans length (Stodólkiewicz, 1963; Ostriker, 1964), Pon et al. (2011) find that local collapse modes are most effective in high aspect ratio cylinders. Unfortunately, it is in these large aspect ratio cylinders that the preferential edge acceleration produces significantly faster collapse timescales than the homologous collapse timescale. Thus, cylinders, as well as circular sheets and spheres, may require strong density perturbations or large-scale support mechanisms for local collapse modes to be significantly faster than global collapse modes. Note, however, that preferential edge acceleration naturally produces strong density perturbations along the edges of circular sheets and filaments, as seen in simulations of both circular sheets (e.g., Burkert & Hartmann 2004) and filaments (e.g., Bastien 1983).

3.4.4 Caveats

Realistic cloud structures are not perfect uniform-density spheres, circular sheets, nor filaments, and deviations from such perfect, symmetrical shapes will influence the collapse properties of the clouds. For instance, Burkert & Hartmann (2004) show, via simulations, that deviations from axisymmetry produce gravitational focusing, whereby local density enhancements are readily formed.

For the timescales calculated in this paper, it is assumed that clouds have sharp density boundaries. More realistic clouds are likely to taper off slowly at the edges. The introduction of such density tapers at the edges of clouds is known to reduce the significance of the preferential edge acceleration, although such a taper has to be quite large in comparison to the size of the constant density interior before the preferential edge acceleration is significantly weakened (Nelson & Papaloizou, 1993; Li, 2001; Pon et al., 2011). As such, preferential edge acceleration may be slightly weaker in realistic clouds than assumed here, but edge-driven collapse modes should still be important for reasonably elongated filaments.

Star-forming regions are observed to be turbulent and this effect can provide support against gravitational collapse (e.g., Hennebelle & Chabrier 2011; Padoan & Nordlund 2011). Thermal pressure, rotation, and magnetic fields can also significantly alter the collapse of a cloud. Thermal pressure, however, is only effective at supporting objects on scales smaller than the Jeans length, whereas observed filaments are often much longer than the Jeans length (e.g., André et al. 2010). Burkert & Hartmann (2004) also point out that, if solid body rotation were supporting the interior of non-spherical clouds, the edge would still collapse due to the preferential edge acceleration, and if the exterior were rotationally supported, the central regions would be moving too rapidly and would expand. Finally, magnetic fields are only capable of providing support perpendicular to the field lines and thus, may not be capable of supporting filaments and circular sheets depending upon the orientation of the magnetic field. Models of filament formation predict that magnetic fields can be either parallel or perpendicular to the long axis of a filament (Nagai et al., 1998) and observational studies have found magnetic fields that are both perpendicular and parallel to the long axes of filamentary structures (Goodman et al., 1990; Houde et al., 2004; Vallée & Fiege, 2006, 2007; Schneider et al., 2010; Chapman et al., 2011; Sugitani et al., 2011).

The influence of collapse along the short axis of any cloud has not been considered because thermal support will generally be more effective at preventing collapse along shorter axes. In deriving the collapse timescales, the assumption that $A \gg 1$ has been utilized. While this assumption clearly breaks down at late times in the collapse, the collapse timescale should be primarily dependent upon the early stages of the collapse when infall velocities are still relatively small. Local collapse modes are also expected at later times in the collapse when, as a consequence of the density increase caused by the global collapse, the short dimension becomes larger than the Jeans length.

The cases considered in this paper, pure homologous collapse and pure edge-driven collapse, are idealized collapse modes and are likely to bracket the true mode of collapse.

3.5 SUMMARY AND CONCLUSIONS

We have calculated homologous collapse timescales for the interiors of uniform-density cylinders, based upon a first-order approximation to the accelerations along the major axis of the cylinders. We have also calculated the collapse timescale for a uniform-

density cylinder, under the approximation that the central density remains constant, by associating the gravitational force per unit mass on the edge with the rate of change of the momentum per unit mass of the edge. With these results, in conjunction with the homologous collapse timescales of uniform-density circular sheets calculated by J. A. Toalá et al. (2012, in preparation [erratum]) and reproduced in Appendix 3.8, we find that

- Two separate collapse modes are present within circular sheets and filaments. The interiors of these clouds collapse roughly homologously while the edges are preferentially given more momentum, such that the edges sweep up material and form density enhancements. The effect of preferential edge acceleration has been previously noted in simulations and analytic studies (e.g., Bastien 1983; Burkert & Hartmann 2004; Hartmann & Burkert 2007; Vázquez-Semadeni et al. 2007; Heitsch et al. 2008b; Hsu et al. 2010; Pon et al. 2011; Toalá et al. 2012).

- The homologous collapse mode is dominant in circular sheets while the edge-driven collapse mode dominates the momentum imparted to filaments with aspect ratios larger than 5.

- The homologous collapse timescales for the interiors of filamentary clouds scale linearly with $A = Z(0)/\mathcal{R}$, where $2Z(0)$ is the total initial length and $\mathcal{R}$ is the radius of the filamentary cloud. The edge-driven collapse mode (constant density collapse) of filamentary clouds produces collapse timescales that are proportional to $\sqrt{A}$. Thus, preferential edge acceleration is most important for clouds with large aspect ratios.

- Regardless of dimensionality, the acceleration, under the assumption of homologous collapse, can be expressed as

$$\frac{dv_0}{dt} \sim \frac{GM}{\chi^2},$$

  with χ as the collapsing dimension (e.g., radius R for spherical and sheet-like clouds, and the semimajor axis Z for a cylinder). Thus, each reduction of dimension produces an additional $\sqrt{A}$ dependence in the homologous collapse time.

- In general, lower dimensional objects ("1D" and "2D") and objects with higher

aspect ratios have larger collapse timescales than for a sphere with the same volume density.

- Estimates of star formation rates from gas densities can be overestimated by an order of magnitude, for realistic filamentary aspect ratios, if the geometry of a cloud is not taken into account.

3.6 ACKNOWLEDGEMENTS

A.P. was partially supported by the Natural Sciences and Engineering Research Council of Canada graduate scholarship program. J.A.T. thanks CONACyT, CONACyT-SNI (Mexico) and CSIC JAE-PREDOC (Spain) for a student grant. D.J. acknowledges support from an NSERC Discovery Grant. F.H. gratefully acknowledges support by the NSF through grant AST 0807305 and by the NHSC through grant 1008. E.V.S. acknowledges support from CONACYT Grant 102488. G.C.G. acknowledges support from UNAM-DGAPA grant PAPIIT IN106511. This research has made use of NASA's Astrophysics Data System and the astro-ph archive. We also thank our anonymous referee for many useful changes to this paper.

3.7 APPENDIX A: HOMOLOGOUS COLLAPSE TIMESCALE OF A SPHERE

The free-fall collapse timescale of a uniform-density sphere is a well-studied problem (e.g., Binney & Tremaine, 1987) and it is known that the collapse proceeds homologously. For a sphere with a volume density of ρ, the acceleration at a distance r from the center of the sphere, $a(r) = 4\pi G\rho r/3$, is linearly dependent upon the radial distance, as required for homologous collapse.

The governing differential equation for the collapse of a sphere is

$$\frac{dv_0(t)}{dt} = \frac{GM}{R(t)^2}, \tag{3.14}$$

where $v_0(t)$ is the velocity of the edge at time t, $R(t)$ is the total radius of the sphere at time t, and $M = 4\pi\rho(0)R(0)^3/3$ is the total mass of the sphere, with $\rho(0)$ being the volume density at $t = 0$. This differential equation is well known and can be solved

for the classical free-fall timescale of a sphere, τ_{3D},

$$\tau_{3D} = \sqrt{\frac{3\pi}{32G\rho(0)}}. \tag{3.15}$$

3.8 APPENDIX B: HOMOLOGOUS COLLAPSE TIMESCALE OF A CIRCULAR SHEET

The homologous collapse timescale of a circular sheet is derived in J. A. Toalá et al. (2012, in preparation [erratum]) and the general derivation is reproduced here. We consider a circular sheet with mass M, radius $R(t)$, and surface density $\Sigma(t)$, such that the initial radius and surface density are $R(0)$ and $\Sigma(0) = M/[\pi R(0)^2]$, respectively. Burkert & Hartmann (2004) show that for an infinitesimally thin circular sheet, the radial acceleration at a distance r from the center of the sheet is

$$a(r,t) = 4G\Sigma(t)\frac{R(t)}{r}\left[K\left(\frac{r}{R(t)}\right) - E\left(\frac{r}{R(t)}\right)\right], \tag{3.16}$$

where K is the first complete elliptic integral and E is the second complete elliptic integral. They note that the acceleration of such an infinitely thin sheet is infinite at the edge, where $r = R(t)$, but that in a sheet with finite thickness, the acceleration at the edge is finite.

Due to this infinite acceleration at the edge, it is common (e.g., Burkert & Hartmann 2004; Pon et al. 2011; Toalá et al. 2012) to use a first-order approximation to the acceleration,

$$a(r,t) \approx \pi G\Sigma(t)\frac{r}{R(t)}. \tag{3.17}$$

The terms excluded from the above equation are higher order terms of $r/R(t)$, such that the above equation is not valid at, or near, the edge of a circular sheet, but is reasonably accurate for most points within the interior of a circular sheet.

While we use Equation (3.17) in the following derivation, we assume that the sheet has a constant, finite height of H that is much smaller than the initial radius $R(0)$, such that we can define the aspect ratio as $A = R(0)/H$. We thus rewrite Equation (3.17) as

$$a(r,t) \approx \pi G\rho(t)H\frac{r}{R(t)}, \tag{3.18}$$

where $\rho(t) = \Sigma(t)/H$ is the volume density of the sheet at time t.

It is critical to note that the acceleration in Equation (3.18) is a linear function of the radius and, thus, this equation exactly describes a homologous collapse. That is, to first order, the accelerations of an infinitely thin, circular sheet will cause the sheet to collapse homologously. It is only the higher order terms of r/R that cause a deviation from homologous collapse.

Denoting the velocity at the edge as $v_0(t)$ and using the relation between the mass of a circular sheet and its volume density, $M = \pi R^3 \rho / A$, Equation (3.18) can be re-written as

$$\frac{dv_0}{dt} \approx \frac{GM}{R(t)^2}. \tag{3.19}$$

Equation (3.19) can be solved to show that the collapse timescale of a circular sheet, τ_{2D}, is

$$\tau_{2D} \approx \sqrt{\frac{4A}{3}}\,\tau_{3D}. \tag{3.20}$$

Thus, under the assumption of homologous collapse, the timescale for collapse of a circular sheet scales with $\sqrt{A}$.

3.9 APPENDIX C: UNIFORM-DENSITY COLLAPSING FILAMENT

Assuming that the only force on the edge of a cylinder is from the uniform-density interior material, this gravitational force from the interior must be equal to the rate of change of the momentum of the edge. From Newton's second law,

$$m(t)g = v(t)\frac{dm(t)}{dt} + m(t)\frac{dv(t)}{dt}, \tag{3.21}$$

where $v(t)$ is the velocity of the edge and $m(t)$ is the mass of the edge. We define the sign of the velocity such that $v(t)$ is positive for inward motions. See also Section 3.3.2 for other variable definitions. Since the mass at the edge increases as material is swept up

$$\frac{dm(t)}{dt} = \pi \mathcal{R}^2 \rho\, v(t). \tag{3.22}$$

Thus, the differential equation governing the motion of the edge is

$$m(t)g = \pi\mathcal{R}^2\rho\, v(t)^2 + m(t)\frac{dv(t)}{dt}. \tag{3.23}$$

For the remainder of this derivation, we drop the functional dependence on t from our notation. Rewriting the derivative of the velocity yields

$$\begin{aligned}
\frac{dv}{dt} &= \frac{dv}{dm}\frac{dm}{dt}, && (3.24)\\
\frac{dv}{dt} &= \frac{dv}{dm}\pi\mathcal{R}^2\rho\, v, && (3.25)\\
mg &= \pi\mathcal{R}^2\,\rho\, v^2 + m\frac{dv}{dm}\pi\mathcal{R}^2\,\rho\, v, && (3.26)\\
\frac{dv}{dm}v &= \frac{-v^2}{m} + \frac{g}{\pi\mathcal{R}^2\,\rho}. && (3.27)
\end{aligned}$$

This is an Abel differential equation of the second kind. It can be solved with the aid of the substitution

$$\begin{aligned}
v &= \frac{w}{m}, && (3.28)\\
\frac{dv}{dm} &= \frac{dw}{dm}\frac{1}{m} - \frac{w}{m^2}, && (3.29)\\
\frac{dw}{dm}\frac{w}{m^2} &= \frac{g}{\pi\mathcal{R}^2\,\rho}, && (3.30)\\
\frac{w^2 - w(t=0)^2}{2} &= \frac{(m^3 - m(t=0)^3)\; g}{3\pi\mathcal{R}^2\,\rho}. && (3.31)
\end{aligned}$$

At the beginning of the collapse, $m = 0$ and $v = 0$, such that $w(t = 0) = 0$. We have also used the fact that the gravitational force per unit mass, to lowest order, is constant over the collapse.

The edge velocity, as a function of the edge mass, is thus

$$v^2 = \frac{2m\, g}{3\pi\mathcal{R}^2\,\rho}. \tag{3.32}$$

Since the mass at the edge is equal to the mass swept up,

$$m = (Z(0) - Z)\pi\mathcal{R}^2\rho, \tag{3.33}$$

$$-\frac{dZ}{dt} = \sqrt{\frac{2(Z(0) - Z)\,g}{3}}, \tag{3.34}$$

$$t = \sqrt{\frac{6(Z(0) - Z)}{g}}, \tag{3.35}$$

$$Z = Z(0) - \frac{g\,t^2}{6}. \tag{3.36}$$

Chapter 4

Molecular Tracers of Turbulent Shocks in Giant Molecular Clouds

And I have known the eyes already, known them all –
The eyes that fix you in a formulated phrase,
And when I am formulated, sprawling on a pin,
When I am pinned and wriggling on the wall,
Then how should I begin
To spit out all the butt-ends of my days and ways?
And how should I presume?
T.S. Eliot

4.1 ABSTRACT

Giant molecular clouds contain supersonic turbulence and simulations of MHD turbulence show that these supersonic motions decay in roughly a crossing time, which is less than the estimated lifetimes of molecular clouds. Such a situation requires a significant release of energy. We run models of C-type shocks propagating into gas with densities around 10^3 cm^{-3} at velocities of a few km s^{-1}, appropriate for the ambient conditions inside of a molecular cloud, to determine which species and transitions dominate the cooling and radiative energy release associated with shock cooling of turbulent molecular clouds. We find that these shocks dissipate their energy primarily through CO rotational transitions and by compressing pre-existing magnetic fields. We present model spectra for these shocks and by combining these models

with estimates for the rate of turbulent energy dissipation, we show that shock emission should dominate over emission from unshocked gas for mid to high rotational transitions (J > 5) of CO. We also find that the turbulent energy dissipation rate is roughly equivalent to the cosmic ray heating rate and that the ambipolar diffusion heating rate may be significant, especially in shocked gas.

4.2 INTRODUCTION

Molecular line observations of giant molecular clouds (GMCs) yield line widths significantly larger than what would be expected from thermal motions alone (e.g., Larson 1981; Solomon et al. 1987). These large, nonthermal linewidths are generally interpreted as being due to supersonic turbulence, with Mach numbers on the order of 10 (e.g., Zuckerman & Evans 1974; McKee & Ostriker 2007). Zeeman splitting measurements of magnetic field strengths in molecular clouds show that these supersonic motions are on the order of the Alfvén speed, which suggests that magnetohydrodynamic (MHD) waves may play a significant role in molecular clouds (Crutcher, 1999; Crutcher et al., 2010).

Supersonic, hydrodynamic turbulence decays on the order of a free fall time (e.g., Goldreich & Kwan 1974; Field 1978; Elmegreen 1985) and thus, maintaining the turbulent support of GMCs for their entire lifetimes, estimated to be between 2 to 30 times longer than the free fall timescale (e.g., Mouschovias & Spitzer 1976; Shu 1977; Blitz & Shu 1980; Shu et al. 1987; Williams & McKee 1997; Elmegreen 2000; Hartmann et al. 2001; Mac Low & Klessen 2004), is a significant problem. Based on theoretical calculations (Arons & Max, 1975), it was believed that MHD turbulence would decay an order of magnitude slower than hydrodynamic turbulence, thereby preventing the dissipation of turbulent energy in GMCs; however, simulations of MHD turbulence show that MHD turbulence also decays on the order of a free fall time at the driving scale (Gammie & Ostriker, 1996; Mac Low et al., 1998; Stone et al., 1998; Mac Low, 1999; Padoan & Nordlund, 1999; Ostriker et al., 2001).

In MHD turbulence simulations, turbulent energy is dissipated via numerical viscosity and artificial viscosity in shock fronts. Under the assumption that the dissipated turbulent energy is lost as heat and rapidly radiated away, many MHD simulations are run with isothermal equations of state and thus, these simulations don't explicitly follow where the dissipated turbulent energy goes (e.g., Stone et al. 1998; Smith et al. 2000b). Basu & Murali (2001) made a first attempt to compare the CO

J = 1 → 0 luminosities of molecular clouds to what they predicted would be seen from molecular clouds based upon simple energetic arguments. Since then, however, little progress has been made in determining where this turbulent energy goes and whether there are any observational signatures of this dissipated energy.

Shocks increase the temperature and density of the shocked gas, which, in turn, can substantially alter the chemistry of the gas and the emission coming from the gas (e.g., Kaufman & Neufeld 1996b,a), thereby potentially providing a distinct signature and tracer of turbulent energy dissipation via shocks. For typical turbulent velocities and magnetic field strengths of molecular clouds, the magnetic field is capable of transmitting information about the presence of a shock to ions upstream of the shock front. This eliminates discontinuities in gas properties across the shock front and spreads out the thickness of the shock. In turn, this leads to lower temperatures in the shocked gas and prevents molecules from being dissociated. Such a shock is referred to as a continuous, or C-type, shock and is described in more detail in Mullan (1971), Draine (1980), and Draine & McKee (1993).

We run models of C-type, MHD shocks, based upon Kaufman & Neufeld (1996a), propagating into molecular gas with densities around 10^3 cm^{-3} at velocities of a few km s^{-1}, appropriate for the ambient conditions inside of a molecular cloud, to determine which species and transitions dominate the cooling and radiative energy release associated with shock cooling in turbulent molecular clouds. The shock velocities modeled are on the order of the typical turbulent velocity of molecular clouds, which are much lower than the velocities of protostellar outflows that have been the target of previous studies (e.g., Chernoff et al. 1982; Timmermann 1996; Kaufman & Neufeld 1996b,a). These shock models are combined with estimates for the rate of turbulent energy dissipation in molecular clouds to predict the integrated intensities of various shock excited lines coming from an entire molecular cloud and these integrated intensities are then compared to those from PDR models based upon Kaufman et al. (1999).

Typical scaling relations of GMCs are presented in Section 4.3.1 and the turbulent energy dissipation rate of molecular clouds is derived in Section 4.3.2. The shock and PDR models used in this paper are described in Sections 4.3.3-4.3.5 and the results of these models are presented in Section 4.4. In Section 4.5 the implications of these results are discussed and in Section 4.6, the rate of turbulent dissipation is compared to other known heating mechanisms in molecular clouds. Finally, our findings are summarized in Section 4.7.

4.3 SETUP

4.3.1 Scaling Relations of GMCs

Correlations between the size, density, and line of sight velocity dispersion of GMCs, as determined through CO observations, are well known and are collectively referred to as Larson's laws (e.g., Larson 1981; Solomon et al. 1987; Heyer & Brunt 2004). The best fitting scaling relations found by Solomon et al. (1987) are:

$$\sigma = 0.72\,(R/\mathrm{pc})^{0.5}\ \mathrm{km\ s^{-1}}, \tag{4.1}$$

$$\rho = 134\,(R/\mathrm{pc})^{-1}\,\mathrm{M_\odot\ pc^{-3}}, \tag{4.2}$$

where R is the effective radius (the radius of a spherical cloud with the same projected surface area as the observed cloud), σ is the one dimensional velocity dispersion (which we assume is equal to the observed line of sight velocity dispersion), and ρ is the average density. These relations suggest that a cloud with a mean density of 10^3 cm^{-3} has a radius of approximately 2 pc, a mass of 2000 M$_\odot$, a total molecular hydrogen column density of 1.2×10^{22} cm^{-2} (corresponding to a visual extinction of 12 through the entire cloud), and a one dimensional velocity dispersion of about 1 km s^{-1}.

The size-velocity relationship is fairly well established, although there is some evidence that the velocity dispersion of a molecular cloud may also depend upon the column density of that cloud (Heyer et al., 2009). The validity of the size-density relation, however, is much less certain, as the observed relationship may be only due to the limited dynamical range of current observations (Ballesteros-Paredes & Mac Low, 2002). For the shock models used in this paper, Larson's laws are only used to confirm that the simulated parameter range roughly corresponds to the properties of observed molecular clouds. Neither part of Larson's laws is used to calculate the integrated intensity of the shock emission.

Solomon et al. (1987) also found a correlation between the velocity dispersion and ^{12}CO J = 1 $\rightarrow$ 0 total luminosity, L$_{1\rightarrow0}$, of molecular clouds. In units of K km s^{-1} pc^{-2}, Solomon et al. (1987) found that the CO 1 $\rightarrow$ 0 luminosity is:

$$L_{1\rightarrow0} = 130\sigma^5. \tag{4.3}$$

The relationship between the magnetic field strength in a molecular cloud, B, and

the number density of hydrogen nuclei, n_H, is often expressed in the form

$$B = b\, n_H^k\, \mu\mathrm{G}, \tag{4.4}$$

where b and k are fitting parameters. A value of k = 0.5 corresponds to a constant magnetic energy density (McKee & Ostriker, 2007) and is expected from ambipolar diffusion collapse models (Fiedler & Mouschovias, 1993). A k = 0.5 relation is also expected if the turbulent velocity in a cloud is always roughly the Alfvén speed (e.g., Crutcher 1999). A value of k = 2/3, however, is predicted if magnetic fields are unimportant and a molecular cloud is able to maintain a roughly spherical shape during its collapse (Mestel, 1966; Crutcher, 1999; Crutcher et al., 2010).

Crutcher (1999) compiled Zeeman splitting observations and found b = 0.95 and k = 0.5 (McKee & Ostriker, 2007). The MHD simulations of Padoan & Nordlund (1999) exhibit a k = 0.4 relation and the relation b = 1, k = 0.5 is commonly adopted (e.g., Draine et al. 1983; Kaufman & Neufeld 1996b,a). Recently, Crutcher et al. (2010) examined all of the available Zeeman splitting observations, including those used by Crutcher (1999), and found that the best fit for the maximum observed line of sight magnetic field strength comes from the relation:

$$B_{max} = \begin{cases} 10\,\mu G & n_H < 300\ \mathrm{cm}^{-3} \\ 10\mu G\left(\frac{n_H}{300\,cm^{-3}}\right)^{0.65} & n_H \geq 300\ \mathrm{cm}^{-3}. \end{cases} \tag{4.5}$$

For densities greater than 300 cm^{-3}, the above relation corresponds to k = 2/3 and b = 0.25. Crutcher et al. (2010) also note that their data are consistent with having line of sight magnetic field strengths down to essentially zero.

The maximum magnetic field strengths that were fit by Crutcher et al. (2010) most likely correspond to cases where the magnetic field is highly aligned with the line of sight, such that the full magnetic field strength is measured. The average magnetic field strength along any random direction will thus be only half of the strength given by the above relation. For a cloud with an H_2 density of 10^3 cm^{-3}, the Crutcher et al. (2010) relation therefore predicts that the average magnetic field strength along any random direction is 17 μG. Intrinsic scatter in the magnetic fields strength between different clouds will also likely further reduce the average magnetic field strength.

4.3.2 Turbulent Energy Dissipation Rate

The turbulent energy density of a molecular cloud is approximately

$$E_{turb} = \frac{3}{2}\,\rho\sigma^2. \tag{4.6}$$

Following the discussion in Basu & Murali (2001), the mean turbulent energy dissipation rate per volume can be written as $\Gamma_{turb} = E_{turb}/t_d$, where t_d is the dissipation timescale. We define the flow crossing time of the cloud as $t_c = 2R/\sigma$ and introduce the ratio of the dissipation time to the flow crossing time as a new parameter: $\kappa = t_d/t_c$. The turbulent dissipation rate per volume is thus

$$\Gamma_{turb} = \frac{3\,\rho\,\sigma^3}{4\,\kappa\,R}. \tag{4.7}$$

As shown in Basu & Murali (2001), rather than writing the turbulent energy dissipation rate in terms of κ, the dissipation rate can be expressed in terms of the driving scale of the turbulence, λ:

$$\Gamma_{turb} = \eta\frac{\rho\,\sigma^3}{\lambda}, \tag{4.8}$$

where η is a dimensionless parameter that is a function of the density, velocity dispersion, and driving wavelength. Comparing equation 4.7 to equation 4.8 gives the relation

$$\kappa = \frac{3\,\lambda}{4\,\eta\,R}. \tag{4.9}$$

Periodic box simulations of MHD turbulence have found that for a variety of initial conditions, η has a value between 0.5 and 4 (Gammie & Ostriker, 1996; Stone et al., 1998; Mac Low, 1999; Ostriker et al., 2001). Unfortunately, there is no clear consensus on what scale turbulence is driven on. Protostellar outflows, which drive turbulence on small scales, appear to have enough energy to drive turbulence in active star forming regions (Quillen et al., 2005; Curtis et al., 2010; Arce et al., 2010). It is, however, unclear whether outflows are capable of driving turbulence across an entire molecular complex (Banerjee et al., 2007; Arce et al., 2010). Studies of density and velocity structure in molecular clouds find that the observed structures are only consistent with driving at size scales at, or above, the size of the cloud (e.g., Ossenkopf & Mac Low 2002; Brunt 2003; Heyer & Brunt 2004; Brunt et al. 2009; Padoan et al.

2009). Supersonic turbulence has also been observed in the Polaris Flare, which is devoid of any protostars (André et al., 2010).

For the remainder of this paper, a κ value of one will be adopted, for which the turbulent dissipation timescale is equal to the flow crossing time of the cloud. Via equation 4.9 and the numerical factors for η, this corresponds to a turbulent driving scale on the order of the size of a molecular cloud.

Equation 4.7 is a general result that can be applied to any cloud, given that the characteristic radius, density, and velocity dispersion are known. For this paper, the simplifying assumption that clouds are spherical will be made, such that the total turbulent energy dissipation rate is

$$L_{turb} = \frac{3\,\rho\,\sigma^3}{4\,\kappa R}\frac{4\pi\,R^3}{3}, \tag{4.10}$$

$$L_{turb} = \frac{\pi\,\rho\,\sigma^3\,R^2}{\kappa}. \tag{4.11}$$

If all of the dissipated turbulent energy is radiated away, the corresponding total integrated intensity, I_{turb}, is

$$I_{turb} = \frac{L_{turb}}{4\pi^2\,R^2}, \tag{4.12}$$

$$I_{turb} = \frac{\rho\,\sigma^3}{4\pi\,\kappa}. \tag{4.13}$$

This integrated intensity is independent of the size of the molecular cloud. For this paper, a mean mass per particle of 4.6×10^{-24} g, or about 2.77 amu, is adopted, and with this value, the above equation becomes

$$I_{turb} = 3.66 \times 10^{-7}\,\kappa^{-1}\left(\frac{n}{10^3\ \mathrm{cm^{-3}}}\right)\left(\frac{\sigma}{1\ \mathrm{km\ s^{-1}}}\right)^3\ \mathrm{ergs\ s^{-1}\ cm^{-2}\ steradian^{-1}}, \tag{4.14}$$

$$I_{turb} = 8.60 \times 10^{-18}\,\kappa^{-1}\left(\frac{n}{10^3\ \mathrm{cm^{-3}}}\right)\left(\frac{\sigma}{1\ \mathrm{km\ s^{-1}}}\right)^3\ \mathrm{ergs\ s^{-1}\ cm^{-2}\ arcseconds^{-2}}. \tag{4.15}$$

4.3.3 Shock Code

To determine which species and transitions dominate the cooling and radiative energy release associated with shock cooling of turbulent molecular clouds, we run models of C-type shocks based upon the models of Kaufman & Neufeld (1996a) with initial conditions corresponding to that expected for roughly one parsec sized molecular

clouds.

The code used first calculates the temperature, density, chemical abundance, and velocity profiles of a C-type shock. To do so, it calculates the cooling rates for rotational and vibrational transitions of H_2O, H_2, and CO (Neufeld & Kaufman, 1993); collisions between the neutral gas and cooler dust grains (Hollenbach & McKee, 1989); and H_2 dissociative cooling (Lepp & Shull, 1983; Hollenbach & McKee, 1989). The freezing out of molecules on dust grains is, however, not calculated by the code as the freezeout timescale is expected to be much longer than the shock cooling timescale.

Once the shock structure is determined, the code then calculates the integrated intensities of each molecular transition of interest by solving the partial differential equations for the line emission at each point and then integrating the emission over the entire shock profile. This extra step of determining individual line strengths, rather than just determining an overall cooling rate for a particular molecule, is only used for CO. In this later step, the code only includes rotational line emission for gas down to 10 K, unlike in Kaufman & Neufeld (1996a), where emission is only included from gas above 50K. No such temperature limitation is used when calculating the overall cooling rates for each molecule in the first half of the code. For a more detailed description of how this code works, please see Kaufman & Neufeld (1996a).

By equating the total kinetic energy dissipated by shocks to the turbulent energy dissipation rate of a molecular cloud, given by equation 4.11, we scale our shock models to predict the expected integrated intensities from each CO rotational line. That is, the integrated intensity of each line is set to the appropriate fraction of the integrated intensity given by equation 4.15. It is assumed that the shock emission is coming from a region larger than the size of the beam and each line is scaled equally under the assumption that all of the lines are optically thin. The effect of the lower lying lines being optically thick is discussed further in Section 4.5.6.

4.3.4 Shock Code Parameters

For each shock model, the same, roughly solar, chemical composition as used in Kaufman & Neufeld (1996b,a) is used. In particular, the initial CO number density is set to be 1.2×10^{-4} times that of the H nuclei number density and the initial H_2O abundance is set to 10^{-7}. As shown in Section 4.3.1, a one parsec sized molecular cloud is expected to have a density of approximately 10^3 cm^3. Thus, the initial H_2

density is set to be either $10^{2.5}$, 10^{3}, or $10^{3.5}$ cm^{-3} in these models.

If the velocity distribution of gas particles in a molecular cloud is gaussian in every direction, with a one dimensional velocity dispersion of σ, then the distribution of relative velocities between two gas particles in the cloud will also be gaussian in every direction with a one dimensional velocity dispersion of $\sqrt{2}\sigma$. Since the energy dissipation rate of a shock scales with the third power of the shock speed, the mean speed at which energy is dissipated at is the cube root of the mean cubed velocity difference between two gas particles, $< \Delta v^3 >^{1/3}$, which is roughly 2.4 σ. The shock velocity at which the peak energy dissipation rate occurs is slightly higher, approximately 3.2 σ. Thus, the characteristic shock velocity in a molecular cloud with a one dimensional velocity dispersion of 1 km s^{-1}, consistent with the size-velocity relation for a radius of 1 pc, is on the order of 2 to 3 km s^{-1}. For the remainder of this paper, we assume that the one dimensional velocity dispersion is a factor of 3.2 smaller than the shock velocity. The larger conversion factor of the two mentioned above is chosen so that the corresponding velocity dispersions, and thus the shock integrated intensities calculated in Section 4.4.1, are smaller.

Models with shock velocities of 2 and 3 km s^{-1} are computed. For a temperature of 10 K, these velocities correspond to Mach numbers of 12 and 17 respectively. While these velocities are appropriate for turbulent motions in a molecular cloud, they are much lower than the typical velocities of protostellar outflows and winds. Such higher velocity flows have been modeled extensively in the past and give rise to significantly higher post shock temperatures (e.g., Kaufman & Neufeld 1996b,a).

The strength of the magnetic field parallel to the shock front is initialized using the parameterizations k = 0.5 and b = 0.1 or 0.3, where b and k are defined in equation 4.4. The component of the magnetic field perpendicular to the shock front is always set to zero, as this component has no effect on the shock structure in our steady state, plane parallel models. Thus, the initial magnetic field strength ranges from 3 μG to 24 μG in the different models. For a weaker field parallel to the shock front, the shock thickness is smaller and the energy released in line radiation is relatively larger. This is why magnetic field strengths that are slightly lower than, although still generally consistent with, the average line of sight magnetic field strength given by the scaling relation of Crutcher et al. (2010) have been chosen.

The Alfvén speed is

$$v_A = \frac{B}{\sqrt{4\pi\,\rho}}. \tag{4.16}$$

Table 4.1. Shock Model Properties

Model	log(n) (cm^{-3})	v (km s^{-1})	b	B (μG)	Mach	M_A
(1)	(2)	(3)	(4)	(5)	(6)	(7)
n25v2b1	2.5	2	0.1	3	12	11
n25v3b1	2.5	3	0.1	3	17	16
n25v2b3	2.5	2	0.3	8	12	4
n25v3b3	2.5	3	0.3	8	17	5
n30v2b1	3	2	0.1	4	12	11
n30v3b1	3	3	0.1	4.	17	16
n30v2b3	3	2	0.3	13	12	4
n30v3b3	3	3	0.3	13	17	5
n35v2b1	3.5	2	0.1	8	12	11
n35v3b1	3.5	3	0.1	8	17	16
n35v2b3	3.5	2	0.3	24	12	4
n35v3b3	3.5	3	0.3	24	17	5

Note. — Col. (1) gives the model name, while cols. (2) and (3) give the logarithm of the initial density and shock velocity of each model respectively. Col. (4) gives the magnetic b parameter, as defined in equation 4.4, and col. (5) gives the resulting initial magnetic field strength. Cols. (6) and (7) give the Mach number and Alfvénic Mach number of the models respectively.

For our shock models, the Alfvénic Mach number, given by $M_A = v_{shock}/v_A$, ranges from 4 to 16.

Twelve shock models are run, one for each combination of initial density, shock velocity, and magnetic field b parameter. Table 4.1 gives the shock velocity, magnetic field strength, Mach number, and Alfvénic Mach number for each model. A naming convention of nWXvYbZ is adopted, where W.X is the logarithm of the initial H_2 number density in cm^{-3}, Y is the shock velocity in km s^{-1}, and Z is the magnetic b parameter.

4.3.5 PDR Model

The shocked gas in a molecular cloud is not the only source of molecular line emission. The cool, well-shielded gas and the warmer gas in the photodissociation region (PDR) at the cloud's surface, which is exposed to the interstellar radiation field (ISRF), will also contribute emission. To model this emission from unshocked gas, PDR models based on Kaufman et al. (1999) are used. As suggested by Kaufman et al. (1999), these plane parallel models are adjusted for spherical geometry by using the equation

$$L = \int 4\pi j(N) r^2 dr, \tag{4.17}$$

where r is the radial distance from the center of the cloud and j(N) is the emissivity at a column N from the surface of the cloud. Kaufman et al. (1999) estimate that this procedure produces results that are within a factor of 1.5 from intrinsically spherical PDR models. Furthermore, for any optically thin line, the resulting integrated intensity is doubled to account for photons originally emitted radially inwards.

The PDR models used have ISRFs of 3 Habing, where the average far ultraviolet ISRF in free space is 1.7 Habing or 1.6×10^{-3} erg cm^{-2} s^{-1} (Tielens, 2005), and microturbulent doppler line widths of 1.5 km s^{-1}, similar to the velocity dispersions of the shock models. It is assumed that the PDR emission fills the beam. These PDR models do not take into account the freezing out of CO onto dust grains.

A density of 10^3 H_{nuclei} per cm^3 is used for all of the comparison PDR models, which is comparable to the median initial density in the shock models. We believe that this is an appropriate comparison density for the $10^{3.5}$ cm^{-3} shock models because a density gradient should be present within realistic molecular clouds, with the density decreasing towards the periphery of the cloud, in order for the clouds to remain in pressure equilibrium. Thus, it is expected that the warm outer layers of molecular clouds, from which most of the PDR emission comes from, are at lower densities than the bulk of the cool, CO rich gas in the interior of the clouds from which most of the shock emission originates. In PDR models with densities below 10^3 H_{nuclei} per cm^3, CO only forms in the gas phase once the gas has cooled significantly, such that there is almost no emission in the mid to high J lines of CO. To be more conservative in our findings of when shock emission is stronger than PDR emission, we prefer using PDR models with densities of 10^3 H_{nuclei} per cm^3 for comparison with the 10^3 and $10^{2.5}$ cm^{-3} shock models, even though these PDR models may over predict the CO

emission from $10^{2.5}$ cm^{-3} gas. The results should be roughly consistent for the 10^3 cm^{-3} shock model

For the comparison PDR models, the size of the molecular cloud must also be known in order to know at what A_V to cut the model at. For each shock model, the Solomon et al. (1987) size-velocity relation is used to determine an appropriate, typical size for a cloud and then the CO column density of that cloud is determined under the assumptions that the cloud is spherical and has a typical CO abundance of 2×10^{-4} (Glover & Mac Low, 2011) throughout the entire cloud. This CO column density is then used to determine the appropriate depth of the comparison PDR model such that the PDR model has the same CO column density. The depths of the PDR models are chosen based upon a CO column density, rather than upon a hydrogen nuclei column density, because the initial chemical abundances used for the shock models are consistent with gas in which CO has already formed in the gas phase and because CO cooling dominates the energy budget of the shock models, as described later in Section 4.4.1.

Two shock models, n35v3b1 and n35v3b3, require CO column densities larger than the total CO column present at the maximum depth of the 10^3 cm^{-3} PDR model. The contribution from the most deeply embedded layers of this PDR model to the total emergent flux does, however, drop to negligible values for all of the CO lines. This is because the lower lines are optically thick and the gas temperature at high A_V is too low for any significant emission in the higher lines. Thus, we use the full extent of the 10^3 cm^{-3} PDR model as the comparison model for these two shock models and we do not believe that this failure to exactly match the CO column densities of these two models significantly affects our results.

4.3.6 Empirical CO 1 → 0 Luminosities

As described in Section 4.3.1, Solomon et al. (1987) found an empirical correlation between the velocity dispersion and ^{12}CO J = 1 → 0 total luminosity of molecular clouds. For the velocity dispersion corresponding to each of the shock models, the 1 → 0 integrated intensity expected from this Solomon et al. (1987) relation is calculated using a cloud radius from the Solomon et al. (1987) size-velocity relation and the assumption that molecular clouds are spherical. While we have used the size-velocity relationship in determining the comparison PDR spectra and in calculating the empirically expected 1 → 0 integrated intensity, we re-emphasize that this relationship

is not used at any time in the calculation of the expected shock spectra.

4.4 RESULTS

4.4.1 Shock Line Emission

In the upper panels of Figure 4.1, the neutral velocity, ion velocity, and density profiles of models n30v2b1 and n30v3b1 are shown. As typical in MHD, C-type shocks, the density and velocity profiles show no sharp discontinuities and the ion velocity decreases before the neutral velocity does. Due to mass conservation, the density and neutral velocity are inversely related to each other, and thus, the maximum density reached in model n30v3b1 is larger than that reached in model n30v2b1. The magnetic field strength and ion velocity are similarly inversely correlated.

The lower panels of Figure 4.1 show the temperature profiles of models n30v2b1 and n30v3b1 as well as the cooling profiles due to CO, H_2, and H_2O lines and gas-grain coupling. During the initial stages of a shock, where the gas temperature is still increasing, the rate of CO cooling increases in close tandem to the increase in temperature. After the gas has reached its peak temperature, the CO cooling rate remains higher than it was at the same temperature earlier in the shock. This is due to the higher gas densities in these later regions of the shock which allow for more efficient population of higher J CO states and thus, more effective CO cooling. The CO cooling rate is the least temperature sensitive of any of the plotted cooling terms, whereas the H_2 cooling rate shows a strong dependence with temperature. The H_2 cooling rate is strongly peaked around the temperature peak and shows the most significant change between the two shock models. While the gas-grain cooling rate is temperature dependent, it is also clearly larger at higher densities as the gas-grain cooling curves are skewed towards the higher density sides of the shocks. High frequency noise, which is likely numerical in nature, appears towards the end of both models in the CO cooling rate and thus, a boxcar smoothing algorithm has been applied to the CO cooling rates for distances larger than 0.06 pc in model n30v2b1 and for distances larger than 0.04 pc in model n30v3b1. This noise does not significantly affect our results as it only occurs over very limited spatial scales and occurs only when the cooling rates have decreased significantly, such that the noise does not significantly affect the total cooling rate. Furthermore, this noise only occurs when the temperature has dropped below 10 K, at which point the lack of

cosmic ray heating in our models becomes important (see Section 4.5.1). The other shock models are qualitatively similar to the ones shown in Figure 4.1 and thus, are not shown. The temperatures, densities, and timescales of the shocks are too low for any significant chemical changes to occur within the gas in any of the models and thus, the small changes in chemical abundance across the shock models are also not shown.

The dominant molecular coolant in all of these slow shock models is ^{12}CO, with 40 to 80% of the dissipated energy going into ^{12}CO rotational lines. A significant fraction, 15 to 60%, of the dissipated energy is not radiated away, but rather, goes towards compressing the magnetic field. In the models with the weakest shocks, those with b = 0.3 and a shock velocity of 2 km s^{-1}, the conversion of kinetic energy into magnetic energy is the most significant mechanism for dissipating kinetic energy. Molecular hydrogen rotational lines are the second most effective molecular coolant, but dissipate less than 1% of the shock energy in all but the models with b = 0.1 and a shock velocity of 3 km s^{-1}, which are the models with the strongest shocks. In these stronger shock models, H_2 lines account for between 7 and 21% of the energy dissipated, with H_2 cooling being more important at lower densities. All other cooling mechanisms are very minor in these shock models. A summary of where the energy goes in each model is given in Table 4.2. It should be noted that the sums of the cooling functions do not exactly equal the total kinetic energy dissipation rates. The total cooling rate, however, is never more than 5% discrepant from the kinetic energy dissipation rate. We believe that this discrepancy arises from difficulties with extending our shock cooling functions to low temperature but do not believe that this small discrepancy significantly affects our results.

The twelve modeled shocks are relatively weak shocks and produce density enhancements of at most a factor of $\sim$20, of order the Mach number. Such compressions are still smaller than the density contrast between the ambient material in molecular clouds and dense cores, which have densities of 10^5 cm^{-3} or above (e.g., Di Francesco et al. 2007). The maximum temperature in the shocked gas varies significantly, with the stronger shock models achieving maximum temperatures of approximately 150 K and the weaker shock models not even warming up to 20 K. The maximum density and temperature reached in each model is given in Table 4.3.

The cooling length of each shock is taken to be the full width at quarter maximum (FWQM) of the total cooling function profile. The cooling lengths range from 0.01 pc to 0.35 pc, with the high magnetic field strength and low density models having

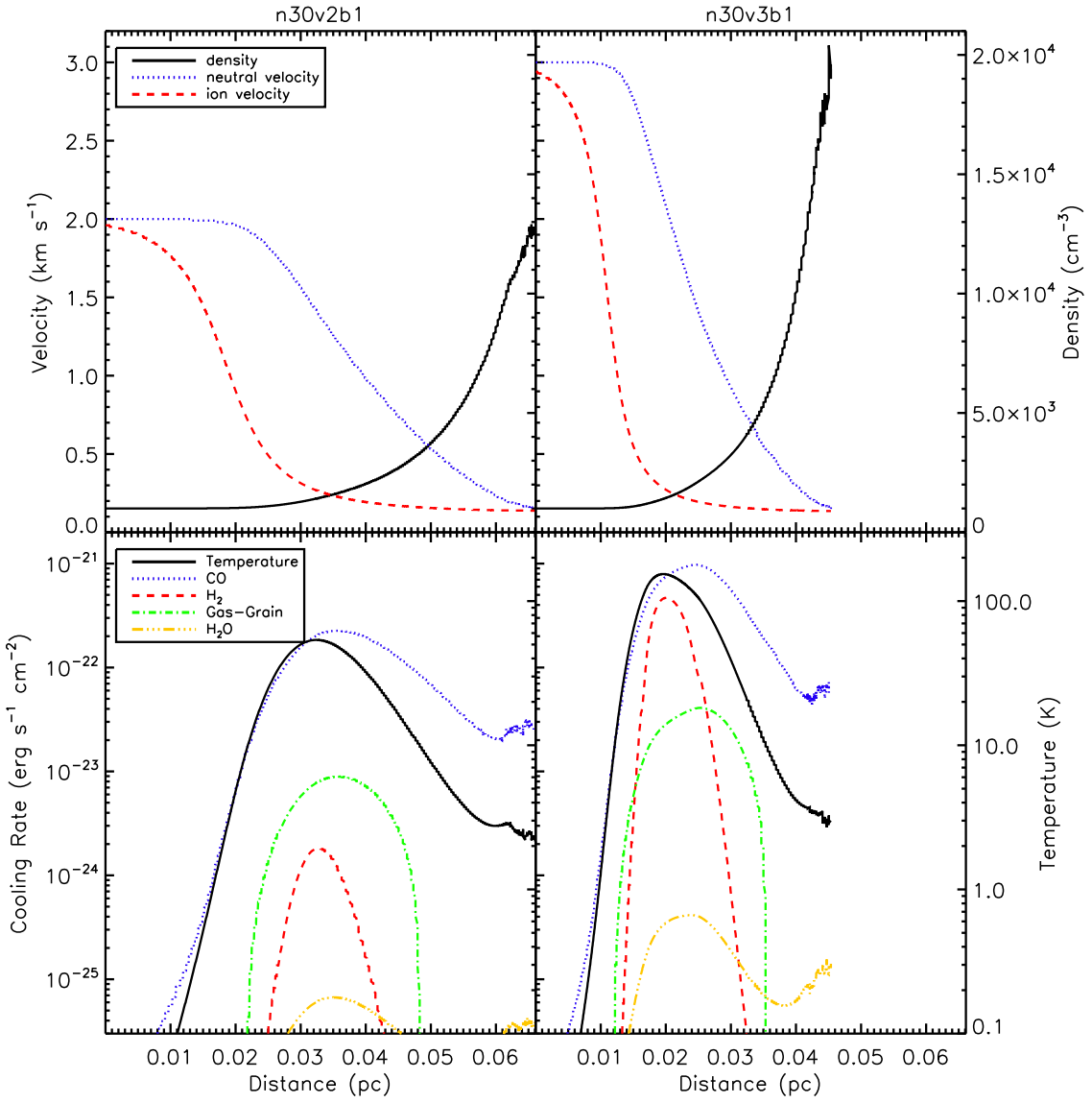

Figure 4.1: Various profiles for the models n30v2b1 and n30v3b1. The top row shows the density, neutral velocity, and ion velocity profiles as the solid (black), dotted (blue), and dashed (red) lines respectively. The velocity axis is given on the left hand border while the density axis is given on the right hand border. The bottom row shows the temperature profiles as the solid (black) lines and the cooling profiles due to CO, H_2, gas-grain interactions, and H_2O as the dotted (blue), dashed (red), dash-dotted (green), and dash-triple-dotted (yellow) lines respectively. The cooling rate axis is given on the left border and the temperature axis is given on the right border. The CO cooling profiles have been boxcar smoothed beyond a distance of 0.06 pc in model n30v2b1 and past 0.04 pc in model n30v3b1 due to the presence of high frequency noise. This noise is likely numerical in nature and should not significantly affect our results (see the text in Section 4.4.1). The left hand column shows profiles for the n30v2b1 model and the right hand column shows profiles from the n30v3b1 model. The x-axes of all four boxes are the same and the y-axes scaling is the same for both models.

Table 4.2. Sources of Energy Dissipation in the Shock Models

Model (1)	E_{CO} (2)	E_B (3)	E_{H_2} (4)	E_{dust} (5)	E_{H_2O} (6)
n25v2b1	76	23	0.8	2	0.02
n25v3b1	61	17	21	2	0.02
n25v2b3	42	56	<0.1	<0.1	0.01
n25v3b3	54	44	0.9	1	0.01
n30v2b1	76	26	0.2	2	0.02
n30v3b1	68	18	14	3	0.03
n30v2b3	43	54	<0.1	0.2	0.01
n30v3b3	55	41	0.3	2	0.02
n35v2b1	74	25	0.1	3	0.04
n35v3b1	72	19	7	4	0.04
n35v2b3	41	53	<0.1	1	0.03
n35v3b3	53	42	0.1	3	0.03

Note. — Col. (1) gives the model names. Cols. (2)-(6), respectively, list the percentage of the kinetic energy of the shock that is dissipated via CO rotational lines, increasing the magnetic field strength, H_2 lines, gas-grain collisions, and H_2O lines.

the largest cooling lengths. The corresponding cooling timescales range from 5×10^3 years to 3×10^5 years, with the longer cooling timescales corresponding to larger cooling lengths.

The volume filling factor of shocked gas in a molecular cloud, ff, can be calculated from

$$ff = \frac{\Gamma_{turb}\, d_{cool}}{\Delta E_k}, \tag{4.18}$$

where Γ_{turb} is the turbulent energy dissipation rate per volume (given by equation 4.7), d_{cool} is the cooling length of the shock, and ΔE_k is the kinetic energy dissipated per shock front area. Both d_{cool} and ΔE_k are calculated by the shock code but the cloud radius is required to calculate Γ_{turb}. For this filling factor calculation, we use the relatively well established size-velocity relation of Larson's laws, equation 4.1, to determine the appropriate cloud radius for each shock model. We reiterate, however, that the integrated intensities presented in Figures 4.2-4.4 and in Table 4.4 are derived independently of any part of Larson's laws. The volume filling factor of shocked gas is always between 0.02% and 0.5% of the cloud volume, except for the three weakest shock models, where the volume filling factor becomes as large as 2%. The cooling times, cooling lengths, and filling factors for all twelve models are given in Table 4.3.

Figure 4.2 shows the integrated intensities of CO rotational transitions as calculated from the shock models with densities of $10^{2.5}$ cm^{-3}. The CO spectra from the corresponding comparison PDR models, as well as the estimates for the J = 1 $\rightarrow$ 0 integrated intensities from the Solomon et al. (1987) scaling relation, are also shown in Figure 4.2. Figures 4.3 and 4.4 show the shock spectra from the models with densities of 10^3 cm^{-3} and $10^{3.5}$ cm^{-3} respectively, as well as the corresponding PDR spectra and Solomon et al. (1987) J = 1 $\rightarrow$ 0 integrated intensities. All integrated intensities are given in units of ergs s^{-1} cm^{-2} arcseconds^{-2}. The y-axis ranges in all Figures 4.3 to 4.4 are identical to facilitate comparisons between the different shock models. As explained in further detail in Section 4.5.1, CO spectra have not been calculated for any shock models with b = 0.3 and a shock velocity of 2 km s^{-1}.

In all of the cases considered, the PDR emission is significantly stronger, by approximately an order of magnitude, than the shock emission in the three lowest CO rotational transitions. The Solomon et al. (1987) ^{12}CO J = 1 $\rightarrow$ 0 integrated intensity is also larger than the predicted shock J = 1 $\rightarrow$ 0 integrated intensity in all of the models. On the other hand, in all of the models, the shock emission is stronger for all of the high J transitions. In the strongest, high density shock models, the shock

Table 4.3. Shock Model Properties

Model	$\log(n_{max})$ (cm^{-3})	T_{max} (K)	t_{cool} (10^4 years)	d_{cool} (pc)	ff (%)	R_B	R_{AD}
(1)	(2)	(3)	(4)	(5)	(6)	(7)	(8)
n25v2b1	3.7	56	6.4	0.06	0.38	14	54
n25v3b1	3.8	145	3.0	0.04	0.11	22	104
n25v2b3	3.1	11	28.5	0.35	2.15	4	10
n25v3b3	3.3	60	9.8	0.17	0.46	7	19
n30v2b1	4.1	54	2.6	0.03	0.16	14	57
n30v3b1	4.3	154	1.3	0.02	0.05	22	106
n30v2b3	3.6	13	11.8	0.14	0.87	4	9
n30v3b3	3.8	60	3.9	0.07	0.18	7	18
n35v2b1	4.6	53	1.1	0.01	0.07	14	55
n35v3b1	4.7	157	0.5	0.01	0.02	21	108
n35v2b3	4.1	17	4.9	0.06	0.36	4	9
n35v3b3	4.3	61	1.7	0.03	0.08	7	18

Note. — Col. (1) gives the model name while cols. (2) and (3) give the logarithm of the maximum density reached and the maximum temperature reached, respectively. Col. (4) gives the cooling time of the shocked gas and col. (5) gives the cooling length. The volume filling factor of shocked gas for a cloud compatible with the size-velocity relationship of molecular clouds is given in col. (6). Cols. (7) and (8) give the factors by which the magnetic field strength and ambipolar diffusion volume heating rate increase between the initial and shocked gas.

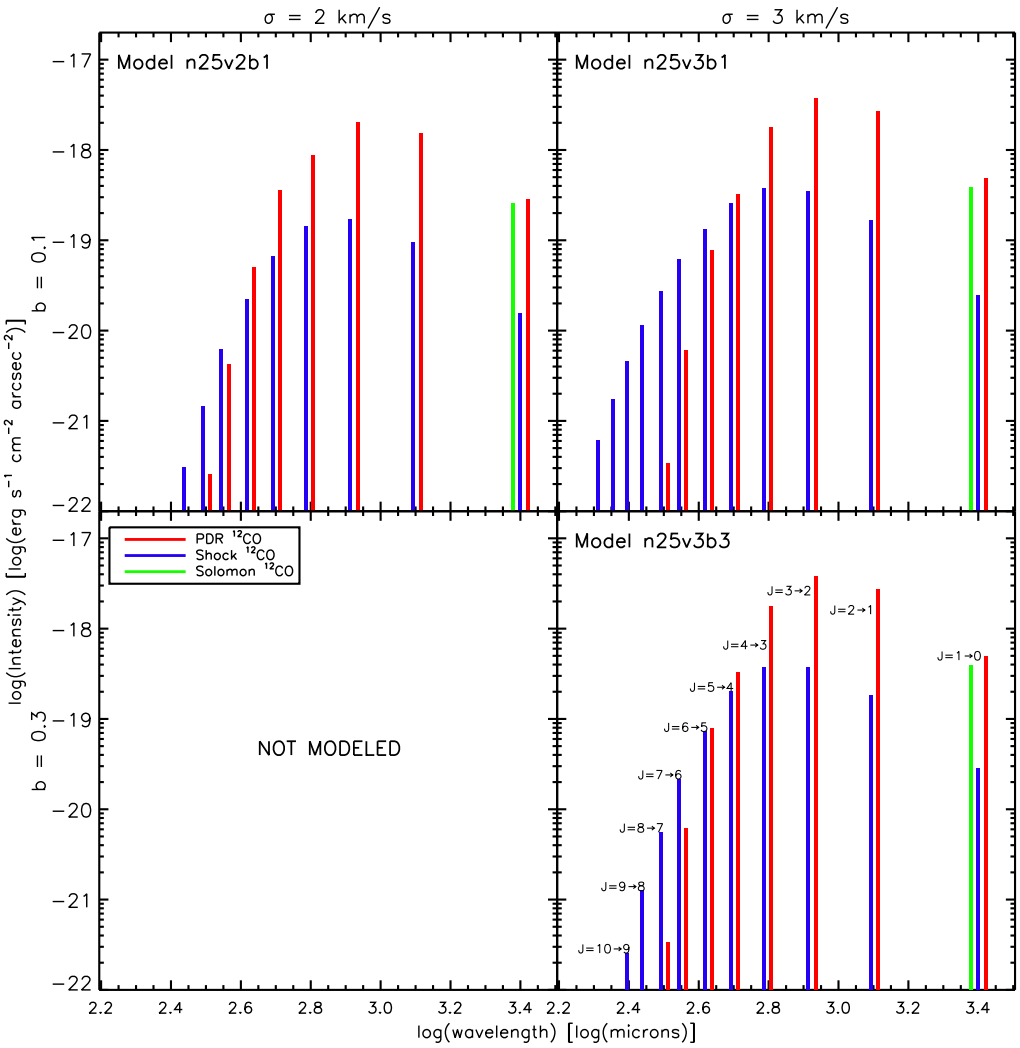

Figure 4.2: Integrated intensities of various ^{12}CO rotational transitions for shock models with densities of $10^{2.5}$ cm^{-3} in units of ergs s^{-1} cm^{-2} arcseconds^{-2}. The shock velocity and magnetic field b parameter used for each shock model are given on the top and left of the grid respectively, while the model name is given in the top left hand corner of each box. The green (lightest) lines show the Solomon et al. (1987) ^{12}CO J = 1 $\rightarrow$ 0 line strengths, the blue (darkest) lines show the CO shock spectra, and the red (medium) lines show the CO PDR spectra. The ten lowest rotational transitions of CO are labeled in the lower right grid panel. Note how the shock spectra dominate over the PDR spectra for high J transitions.

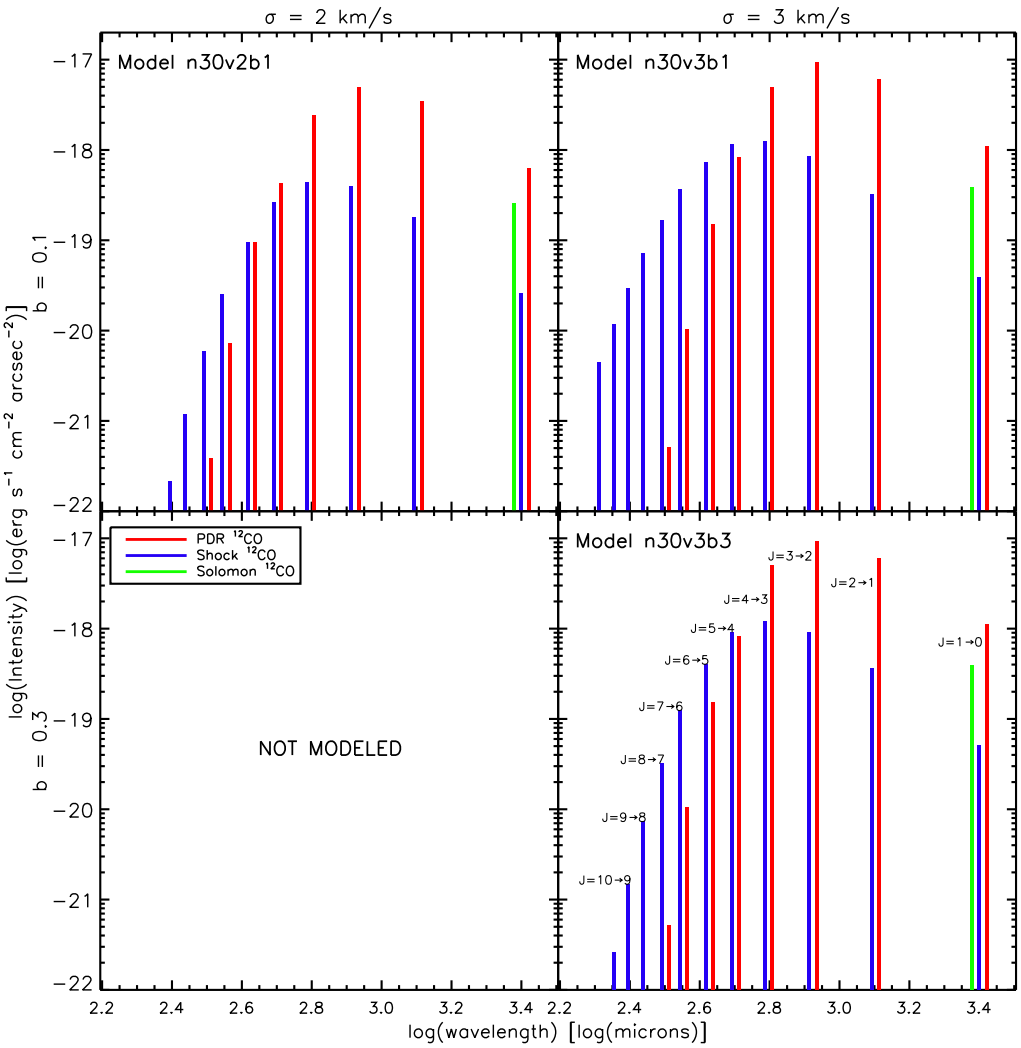

Figure 4.3: Integrated intensities of various ^{12}CO rotational transitions for shock models with densities of 10^3 cm^{-3} in units of ergs s^{-1} cm^{-2} arcseconds^{-2}. The shock velocity and magnetic field b parameter used for each shock model are given on the top and left of the grid respectively, while the model name is given in the top left hand corner of each box. The green (lightest) lines show the Solomon et al. (1987) ^{12}CO J = 1 $\rightarrow$ 0 line strengths, the blue (darkest) lines show the CO shock spectra, and the red (medium) lines show the CO PDR spectra. The ten lowest rotational transitions of CO are labeled in the lower right grid panel. Note how the shock spectra dominate over the PDR spectra for high J transitions.

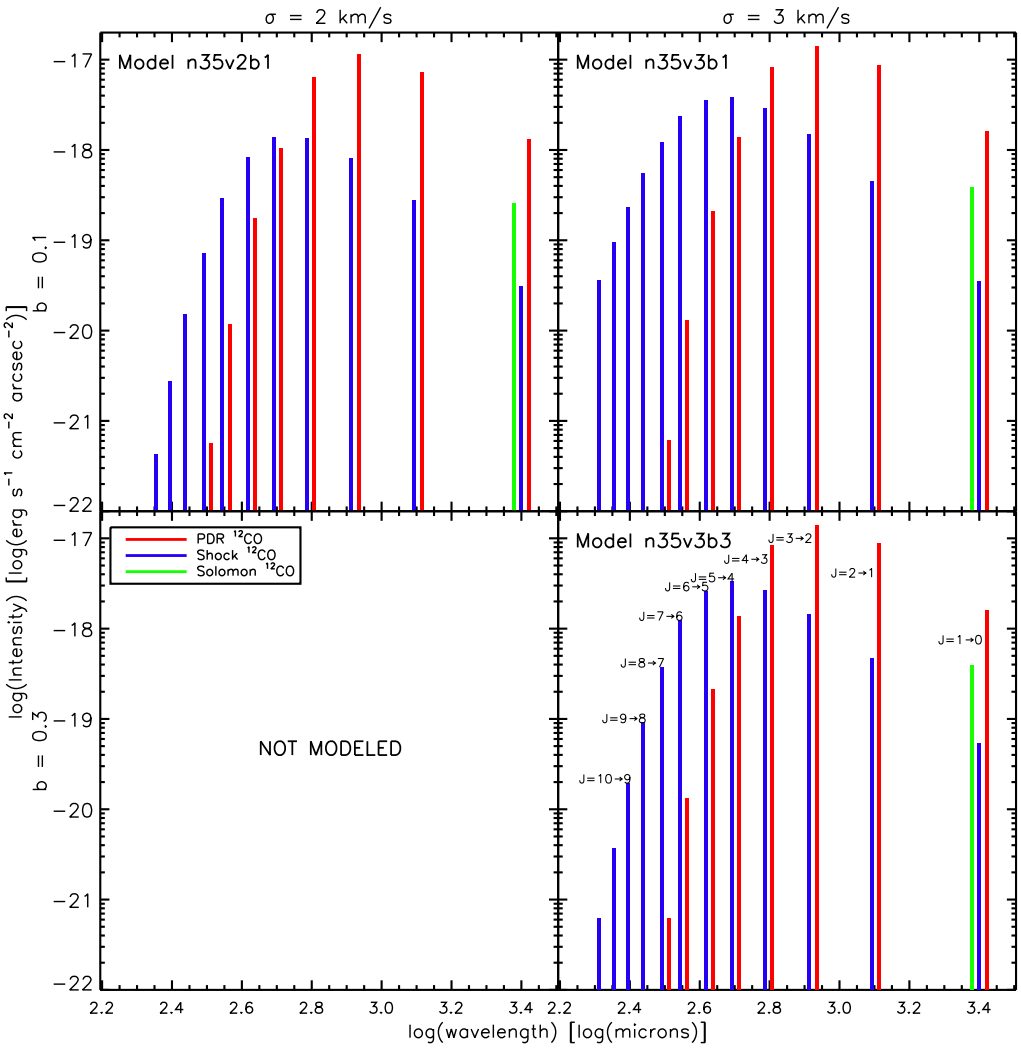

Figure 4.4: Integrated intensities of various ^{12}CO rotational transitions for shock models with densities of $10^{3.5}$ cm^{-3} in units of ergs s^{-1} cm^{-2} arcseconds^{-2}. The shock velocity and magnetic field b parameter used for each shock model are given on the top and left of the grid respectively, while the model name is given in the top left hand corner of each box. The green (lightest) lines show the Solomon et al. (1987) ^{12}CO J = 1 $\rightarrow$ 0 line strengths, the blue (darkest) lines show the CO shock spectra, and the red (medium) lines show the CO PDR spectra. The ten lowest rotational transitions of CO are labeled in the lower right grid panel. Note how the shock spectra dominate over the PDR spectra for high J transitions.

Table 4.4. Predicted H_2 Integrated Intensities

Model	S(0) (10^{-19} ergs s^{-1} cm^{-2} $arcseconds^{-2}$)	S(1) (10^{-19} ergs s^{-1} cm^{-2} $arcseconds^{-2}$)
(1)	(2)	(3)
n25v3b1	1.5	3.5
n30v3b1	3.0	6.9
n35v3b1	5.0	11

Note. — Col. (1) gives the model names while cols. (2) and (3) give the integrated intensities of the S(0) and S(1) lines, respectively, for the three shock models with significant H_2 cooling.

integrated intensity becomes larger than the PDR integrated intensity in the J = 5 $\rightarrow$ 4 line. The PDR emission in the higher J lines drops much more rapidly than the shock emission and the shock emission is an order of magnitude stronger in the J = 7 $\rightarrow$ 6 line in most models.

While the shock code does not calculate the individual strengths of the different H_2 rotational transitions, the lowest rotational levels should be in local thermodynamic equilibrium (LTE) at the modeled densities. Thus, it is assumed that all of the H_2 line ratios are given by their LTE values. At 50 K, the ratio of S(1) to S(0) is only 3.3×10^{-3}, but at 150 K, this ratio increases to 2.3. The S(2) and higher lines are negligible in comparison to the S(1) and S(0) lines at these temperatures. For the three models with significant H_2 emission, the expected integrated intensities of the S(1) and S(0) lines are given in Table 4.4.

While the PDR models used do not include the expected line strengths for H_2 rotational transitions, Kaufman et al. (2006) found that the S(1) and S(0) H_2 lines have integrated intensities of 7×10^{-20} ergs s^{-1} cm^{-2} $arcsecond^{-2}$ and 2×10^{-19} ergs s^{-1} cm^{-2} $arcsecond^{-2}$, respectively, in a PDR with a density of 10^3 cm^{-3} and an ISRF of 3 Habing. Therefore, the PDR H_2 integrated intensities are expected to be comparable to or slightly lower than the shock H_2 integrated intensities.

4.5 DISCUSSION

4.5.1 CO Lines

As mentioned in Section 4.4.1, no CO spectra are calculated for the models with b = 0.3 and a shock velocity of 2 km s^{-1}. This is because the maximum post shock temperatures in these three models, 11, 13, and 17 K, are on the order of the temperature expected from cosmic ray heating alone (e.g., Goldsmith 2001; Pan & Padoan 2009). The shock code used does not contain any additional heating sources, such as cosmic ray or photoelectric effect heating, and thus, underestimates the temperatures that would be achieved in these weak shocks. The combination of shock heating and cosmic ray heating must produce temperatures higher than that produced by cosmic ray heating alone. Note that in Figure 4.1, the gas temperature is initially less than 0.1 K and falls below 10 K by the end of the model due to the lack of these extra heating terms. As such, we do not consider the models with b = 0.3 and a shock velocity of 2 km s^{-1} to be valid. The lack of cosmic ray heating does not significantly affect the other models because the peak temperatures are much larger than 10 K in these models, indicating that shock heating is significantly stronger than what cosmic ray heating would be.

Figures 4.2-4.4 show that almost all of the emission from a molecular cloud in the lowest three rotational transitions of CO comes from unshocked gas. These figures also show, however, that most of the emission coming from the mid to high J CO lines (lines at or above $J = 7 \rightarrow 6$) comes from shocked gas. Not only should the integrated intensities of these lines be higher than predicted from PDR models, but the excitation temperatures derived from the line ratios of these lines should also be higher than a PDR model would predict. Thus, these mid to high J CO lines should serve as observational diagnostics of turbulent energy dissipating via shocks. Since CO accounts for the majority of the cooling via shocks, these mid to high J transitions of CO should be the best tracers of where the majority of the energy goes in turbulent shocks in molecular clouds.

Shock emission dominates at higher J transitions because the CO in the shocked gas is warmer than the majority of the CO in the rest of the cloud. While the outer layers of a molecular cloud can be quite warm, due to the incident ISRF, there is little CO in these warm outer regions. The majority of the CO flux in the PDR models comes from gas that is below 20 K. Since our low velocity shocks are C shocks, CO

survives the shock and radiates from gas at temperatures in excess of 50 K.

The Solomon et al. (1987) ^{12}CO J = 1 $\rightarrow$ 0 integrated intensity is larger than the predicted shock integrated intensity in all of the models, which confirms that shock emission is not the major source of emission in the 1 $\rightarrow$ 0 transition. While the comparison PDR models for the high density shock models over predict the 1 $\rightarrow$ 0 integrated intensity, compared to the Solomon et al. (1987) integrated intensity, the comparison PDR models for the $10^{2.5}$ cm^{-3} shock models have J = 1 $\rightarrow$ 0 integrated intensities in remarkably good agreement with the Solomon et al. (1987) integrated intensity. This slight discrepancy between some of the PDR models and the Solomon et al. (1987) relation is likely due to the characteristic line width, depth, and density of the clouds observed by Solomon et al. (1987) being slightly different than the values used in the PDR models.

4.5.2 Variation Across Parameter Space

The maximum temperature reached in the shocked gas increases with increasing Alfvénic Mach number and Mach number of the shock. All of the models with a shock velocity of 3 km s^{-1}, and thus a Mach number of 17, have higher maximum temperatures than all of the models with a shock velocity of 2 km s^{-1}, corresponding to a Mach number of 12. For models with the same Mach number, models with higher Alfvénic Mach numbers, those with lower magnetic b parameters, have higher maximum temperatures. A larger Alfvénic Mach number alone, however, does not necessarily imply a larger maximum temperature, as the models with b = 1 and a shock velocity of 2 km s^{-1} have roughly the same maximum temperature as the models with b = 3 and a shock velocity of 3 km s^{-1} despite having almost twice as large Alfvénic Mach numbers. The maximum temperature reached significantly affects the CO shock profile, as higher temperatures excite higher rotational states, which leads to considerably more emission in higher J transitions. As described further in Section 4.5.4, the effectiveness of H_2 cooling is also highly sensitive to the maximum temperature reached in the gas.

The fraction of energy going towards compressing the magnetic field is primarily dependent upon the Alfvénic Mach number of the shock, with more energy going into the magnetic field in the models with lower Alfvénic Mach numbers. Larger Alfvénic Mach numbers also produce smaller cooling lengths, cooling times, and filling factors.

The turbulent energy density of a molecular cloud is dependent upon both the

density and turbulent velocity dispersion of the cloud. Thus, the models with higher densities and higher shock velocities have larger integrated intensity scaling factors (see equation 4.15) and, consequently, higher integrated intensities for all CO transitions.

The critical densities for all the CO lines above the J = 3 → 2 line are greater than 10^5 cm^{-3} (Schöier et al., 2005). Therefore, larger initial densities make it easier for higher rotational states to be populated and, as such, more emission comes out in higher lying lines in the higher density models. This effect is clearly seen in the shock models with b = 0.1 and a shock velocity of 2 km s^{-1}, as the line with the largest integrated intensity shifts from the 3 → 2 line to the 4 → 3 and then finally to the 5 → 4 line as the density increases from $10^{2.5}$ cm^{-3} to 10^3 cm^{-3} and then to $10^{3.5}$ cm^{-3}. The peak of the PDR spectra remains at the 3 → 2 transition in all of the PDR comparison models because the same density is used for all of the PDR comparison models. This difference between the shock and PDR models causes the transition at which shock emission becomes larger than PDR emission to move to slightly lower transitions as the density of the shock model increases.

As described above, changes to the magnetic field strength, shock velocity, or initial gas temperature can significantly alter the shape and the scaling of the shock CO spectrum. None of these changes, however, alter the key result that shock emission dominates at mid to high J transitions, particularly from J = 7 → 6 and up.

The fraction of energy dissipated via CO cooling is not strongly correlated with any shock property. Only in the strongest shock models does the fraction of energy dissipated via CO weakly depend upon the initial density of the gas. For these strong shock models, the fraction of energy that is emitted via CO rotation lines increases by approximately 10% as the initial density increases from $10^{2.5}$ cm^{-3} to $10^{3.5}$ cm^{-3}.

An increase in the initial density of the gas weakly increases the effectiveness of gas-grain cooling, but this cooling term accounts for at most 4% of the shock cooling in any of the models. Much higher densities, densities closer to 10^5 cm^{-3}, are required before gas-grain coupling becomes reasonably efficient. Going from a density of $10^{2.5}$ cm^{-3} to $10^{3.5}$ cm^{-3} also decreases the cooling lengths, cooling times, and filling factors of all of the models by approximately a factor of 6.

4.5.3 Magnetic Field Compression

In our low velocity shock models, the energy that goes into compressing the magnetic field is of the same order of magnitude as the energy radiated away in CO rotational lines. It is, however, unclear where this injected magnetic energy would go. A local increase in magnetic field strength could further drive MHD waves, which would subsequently shock. In this case, more shocks would be required in order for all of the cloud's turbulent energy to be dissipated by CO cooling and our predicted line integrated intensities would have to be increased by a factor of two.

Alternatively, this magnetic energy may slowly leak out of the cloud via magnetic coupling with the external medium, as described by Elmegreen (1985) and seen in simulations by Eng (2002). This magnetic energy may also be dissipated on small scales via a process such as ambipolar diffusion.

4.5.4 H_2 Lines

Molecular hydrogen does not have a permanent dipole moment and thus, radiates through weak quadrapole transitions ($\Delta J = 2$). Furthermore, since hydrogen is so light, the rotational energy levels of molecular hydrogen are relatively widely spaced. These two effects make H_2 rotational emission highly temperature sensitive and temperatures in excess of 100 K are required for significant emission. This temperature sensitivity can be seen in the shock models, as H_2 emission is essentially negligible in all but the strongest shock models, which are the only models where the maximum temperature exceeds 100 K. In these models, the S(1) and S(0) H_2 lines have comparable integrated intensities to the CO $J = 7 \rightarrow 6$ line, although the H_2 lines are relatively stronger in the lower density models.

The lack of H_2 rotational emission from cool gas means that, aside from shocked gas, the only significant source of H_2 emission in a molecular cloud is the thin outer edge of the cloud's PDR where the temperature is high and H_2 is not rapidly photodissociated. Thus, H_2 rotational emission could be a very useful tracer of shocked gas in a molecular cloud. In particular, while the predicted S(0) shock integrated intensities are on the order of the S(0) PDR integrated intensity, the S(1) shock integrated intensities range from being five times to over 15 times larger than the S(1) PDR integrated intensity. The ratio of S(1)/S(0) at the 150 K maximum temperature of the strongest shocks, approximately 2.3, is also significantly different from the ratio of these lines in the Kaufman et al. (2006) comparison PDR models, roughly 0.3.

H_2 cooling may be even more significant in gas that is lacking in gas phase CO, as this shocked gas is likely to reach higher temperatures with the effectiveness of CO cooling reduced. This increase in H_2 shock emission in CO sparse gas, such as the "dark gas" in the periphery of a molecular cloud (e.g. Wolfire et al. 2010), may naturally produce a limb brightening effect for H_2 rotational emission in molecular clouds, as observed in Taurus by Goldsmith et al. (2010).

In all of our shock models, cooling from vibrational transitions of H_2 is negligible because temperatures on the order of a few thousand Kelvin are required to excite higher energy vibrational states (Kaufman & Neufeld, 1996a).

4.5.5 Other Shock Tracers

Water is known to be an effective coolant in high velocity shocks (Kaufman & Neufeld, 1996a) but water cooling is negligible in all of our shock models. This is because water is only formed in gas with a temperature of a few hundred Kelvin (Elitzur & de Jong, 1978; Elitzur & Watson, 1978) and is only effeciently liberated from dust grains, due to sputtering, in 15 km s^{-1} or faster shocks (Draine et al., 1983). Low velocity shocks are also very ineffective at heating dust grains, meaning that thermal sublimation of water off of dust grains is completely negligible in our low velocity shocks (Draine et al., 1983).

At the low densities of our shock models, the interaction timescale of gas with dust grains is long compared to the cooling time such that only a few percent of the energy is ever liberated via gas-grain interactions in the models. Densities closer to 10^5 cm^{-3} are needed before gas-grain coupling becomes effective.

While CO line radiation and the compression of magnetic fields are the dominant coolants in our low velocity shocks, other molecular lines, which have not been included in our shock models, may still be valuable tracers of shocked gas. In particular, molecular lines that are sensitive to increased temperature could provide shock tracers in different wavelength regimes. Molecular transitions that are sensitive to density may also be useful shock tracers, but are less likely to be as useful as temperature sensitive lines since the maximum densities reached in the shocked gas are less than the gas density of prestellar cores.

4.5.6 Additional Caveats

In scaling the shock models to predict the total strength of the shock emission from an entire molecular cloud, it was assumed that all of the turbulent energy of the cloud is dissipated at one particular shock strength. In reality, energy will be dissipated through a variety of different strength shocks, either due to different shock velocities or different strengths of the magnetic field parallel to the shock front. Furthermore, Smith et al. (2000a) show that high velocity shocks dominate energy dissipation in driven turbulence while Smith et al. (2000b) show that if the turbulence is decaying, low velocity shocks dissipate most of the energy. If energy is dissipated through lower velocity shocks, then our calculated line integrated intensities will overestimate the actual emission from molecular clouds in lines with higher excitation temperatures. If turbulence is driven at scales much smaller than the size of the cloud, however, then our line strengths should be increased by a factor of κ^{-1} (see Section 4.3.2 for a discussion on how κ relates to the driving scale of turbulence).

Another factor of two uncertainty in the shock integrated intensities comes from the assumption that the energy in magnetic field fluctuations in the cloud is negligible. While some MHD simulations have shown that the turbulent kinetic energy dominates over the energy in magnetic field fluctuations, particularly for smaller initial magnetic fields (Padoan & Nordlund, 1999; Padoan et al., 2000; Heitsch et al., 2001), other simulations find that these magnetic field fluctuations have energy on the order of the kinetic energy of the turbulence (Stone et al., 1998; Ostriker et al., 2001). If the energy in magnetic field fluctuations is on par with the kinetic energy of turbulence, the line integrated intensities would have to be scaled up by a factor of two to account for the dissipation of this additional energy.

In scaling up the shock models to estimate the total integrated intensities from an entire cloud, the integrated intensity of every line in a particular model has been multiplied by the same factor and no optical depth effects have been taken into account. These optical depth effects, however, should not be significant for the higher rotational transitions of CO, where the CO transitions are effective at tracing shock emission, as the PDR models indicate that the CO lines are only optically thick up to, and including, the J = 5 $\rightarrow$ 4 transition. As for shock emission in the lower rotational transitions of CO, this emission is likely to be absorbed by the ambient gas and thereby will serve as a heating source for the ambient gas. Note, however, that the expected CO integrated intensity at these low transitions is much less than

the PDR integrated intensity, which indicates that this extra shock heating will have only a very minor effect on the temperature, and thus the spectrum, of the ambient gas.

In deriving the total turbulent energy dissipation rate of a molecular cloud, it was assumed that turbulence decays in a crossing time. Recently, Basu et al. (2009) and Basu & Dapp (2010), discovered a long lived magnetic tension driven mode in their thin disc simulations of flattened molecular clouds, arising from interactions between the disc and an external magnetic field, which was able to preserve a significant fraction of the turbulent energy of the cloud for much longer than the crossing time. The existence of such a long lived MHD mode would significantly reduce the required energy dissipation rate of a molecular cloud and, therefore, our predicted line integrated intensities as well. This long lived mode, however, has not been noticed in any further simulations, including the 3D simulations of collapsing cores done by Kudoh & Basu (2011), who did look for this particular MHD mode. Kudoh & Basu (2011) suggest that the absence of this mode in their simulations may be due to the very small density contrast between the discs and surrounding gas in their simulations.

The line ratios from these shock models are independent of the scaling of the lines and thus, are not affected by the above uncertainties. The line ratios of the shock models are also independent of the assumption of spherical geometry.

The turbulent energy of molecular clouds may also not be dissipated completely through shocks. Smith et al. (2000b) and Stone et al. (1998) find, in their simulations of turbulence, that only 50% of the turbulent energy is dissipated through artificial viscosity, due to the presence of shock fronts, while the other 50% is dissipated through numerical viscosity, representative of small scale dissipation distributed relatively uniformly across the cloud. It is possible that some of this uniformly dissipated energy should have been dissipated in weak shocks or vortices that were not resolved in these simulations and thus, we consider that 50% is only a lower limit for the fraction of energy dissipated in intermittent structures (i.e. shocks).

An alternative model for turbulent dissipation, where energy is dissipated through magnetized vortices, has also been put forward (Godard et al., 2009). In the Godard et al. (2009) turbulent dissipation region (TDR) model, small vortices on the order of a few tens of AU heat gas to temperatures of nearly 1000 K via ion-neutral friction. The spectral signature of such a TDR model should be significantly different from our low velocity shock models because the TDR model produces temperatures much higher than what can be obtained from slow shocks.

All of the shock models have been run with standard, roughly solar, metal abundances. In lower metallicity clouds, the abundance of CO will be reduced. The gas phase CO abundance will also be lower at higher densities, due to freeze out of CO onto dust grains (e.g., Goldsmith 2001), and in the outer layers of molecular clouds, where CO is readily photodissociated (e.g., Wolfire et al. 2010). The reduction of gas phase CO may lead to higher post shock temperatures, which would change the resulting CO spectrum and could affect which cooling mechanism is dominant. H_2 line cooling and the deposition of energy into magnetic fields may also be more important for dissipating kinetic energy in CO poor gas. Further low metallicity shock models, however, are needed to confirm this.

The CO spectrum predicted from the PDR model is dependent upon the chemistry put into the models. In particular, any chemical effects which would increase the temperature in the outer CO layers, such as an increase in PAH heating, would shift the PDR spectrum towards higher rotational transitions. The PDR models used also have a relatively low interstellar radiation field of 3 G_0. In active, high-mass star forming regions, the ambient ISRF is likely to be much higher, due to the presence of previously formed, massive, young stars and thus, the PDR emission from these regions is likely to be much stronger and peaked towards much higher J transitions. As such, our model comparisons should only be used for relatively quiescent, low-mass star forming regions in which the ambient ISRF is relatively low, rather than in strong UV environments such as the Orion Bar.

4.5.7 Observational Potential

The total energy dissipated by shocks cannot be directly observed because some of the turbulent energy is not radiated away, but rather goes into increasing magnetic field strengths. Furthermore, many of the low lying CO lines are not readily observable, because these transitions are dominated by emission from unshocked gas. This ambient gas emission, however, does drop rapidly at higher J numbers and the CO J $= 6 \rightarrow 5$ (691.47308 GHz) and $7 \rightarrow 6$ (806.651806 GHz) transitions are dominated by shock emission in most of our models. Thus, these higher rotational CO transitions act as shock tracers and by fitting shock models to the observed strengths of multiple high J CO transitions, the total shock luminosity of a cloud can be estimated.

The Herschel Space Observatory's Heterodyne Instrument for the Far Infrared (HIFI) and Spectral and Photometric Imaging Receiver (SPIRE) both have the nec-

essary wavelength coverage and sensitivity to be able to detect the CO J = 5 → 4, 6 → 5, and 7 → 6 lines, if they are as bright as we predict in our shock models. These two Herschel instruments also cover the J = 8 → 7 wavelength but our predicted line strengths for this transition are at the limits of what could be detected within a few hours of observing time. From the ground, the James Clerk Maxwell Telescope's (JCMT) receiver W is capable of observing at the wavelength of the CO J = 6 → 5 transition while the Atacama Pathfinder Experiment (APEX) and the Caltech Submillimeter Observatory (CSO) have instruments that operate in the appropriate wavelength regimes to detect both the 6 → 5 and 7 → 6 lines. The CO J = 6 → 5 and 7 → 6 lines also lie within bands 9 and 10, respectively, of the Atacama Large Millimeter Array (ALMA). ALMA, with its superb resolution, may resolve individual shock fronts and thus, provide information regarding the properties of individual shocks.

Some care must be taken when choosing a location in a molecular cloud to observe, as there are other sources of high J CO line emission that have not included in the comparison PDR models. High velocity protostellar outflows will generate large shocks that can easily produce temperatures of hundreds of Kelvin. Such strongly shocked gas will radiate significantly in high J lines (e.g., Kaufman & Neufeld 1996b,a). Embedded high-mass stars will also significantly heat nearby gas and lead to high J line emission. Thus, while turbulent dissipation should occur in active, high-mass star forming regions, the spectral signatures of low velocity, turbulence induced shocks may only be readily detectable in quiescent regions of low-mass star forming molecular complexes. Water emission can be used as a discriminant between low velocity, turbulent shocks and the stronger shocks produced by outflows, as little water emission is predicted from our models while stronger shocks are expected to cool significantly via water lines (e.g., Kaufman & Neufeld 1996a).

The temperature sensitivity of the S(0) and S(1) lines of H_2, at 28.2 μm and 17.0 μm respectively, makes these lines potential shock tracers. The atmospheric transmission at 28.2 μm is, however, very poor, and thus, it is extremely difficult to observe the S(0) line with ground based facilities. The expected weakness of these two lines makes observations of H_2 emission even more problematic.

4.6 GLOBAL HEATING

4.6.1 Cosmic Rays

In the cold, well shielded, central regions of molecular clouds, cosmic ray heating is believed to be the dominant heating term (e.g., Goldsmith 2001), but the general cosmic ray ionization rate in the galaxy is not particularly well known. Estimates for the cosmic ray ionization rate in dense gas vary from 10^{-16} s^{-1} (Caselli et al., 1998; Liszt, 2003; Doty et al., 2004) to 10^{-18} s^{-1} (Caselli et al., 1998, 2002; Flower et al., 2007; Hezareh et al., 2008) but commonly lie between 1×10^{-17} s^{-1} and 5×10^{-17} s^{-1} (Williams et al., 1998; van der Tak & van Dishoeck, 2000; Doty et al., 2002; Wakelam et al., 2005; Bergin et al., 2006; Maret & Bergin, 2007; Goicoechea et al., 2009). While the spread in cosmic ray ionization rates may simply be due to spatially varying rates (e.g., van der Tak et al. 2006), some of the scatter is likely due to uncertainties in the chemical models used to determine the ionization rates, as changes in known reaction rates (e.g., Dalgarno 2006) and the inclusion of non-equilibrium chemistry (Lintott & Rawlings, 2006) have changed the results of ionization rate calculations.

For this paper, a cosmic ray ionization rate range of 1×10^{-17} s^{-1} to 5×10^{-17} s^{-1} is adopted and, since each cosmic ray ionization deposits approximately 20 eV into the gas (Goldsmith, 2001), the volume heating rate by cosmic rays is taken to be

$$\Gamma_{cr} = 0.3 \text{ to } 1.6 \times 10^{-27} \left(\frac{n}{\text{cm}^{-3}}\right) \text{ergs s}^{-1} \text{ cm}^{-3}. \tag{4.19}$$

This cosmic ray heating rate is shown in Figure 4.5.

4.6.2 Turbulent Heating

If the turbulent energy of a cloud is not dissipated through localized shocks, but rather is dissipated relatively uniformly across the cloud, then this turbulent energy dissipation will act more as a general heating mechanism for the cloud and will yield the heating rate given by equation 4.7. For the sole purpose of comparing the turbulent energy dissipation rate to the cosmic ray heating rate, both the size-velocity and density-size relationships from Solomon et al. (1987) are used to rewrite the turbulent energy dissipation rate in terms of only κ and the gas density. Using these two scaling

relations, the turbulent energy heating rate can be written as

$$\Gamma_{turb} = 5.86 \times 10^{-25}\, \kappa^{-1}\, \epsilon \left(\frac{n}{10^3\,\mathrm{cm}^{-3}}\right)^{0.5} \text{ ergs cm}^{-3}, \tag{4.20}$$

where ϵ is the fraction of the dissipated turbulent energy that acts as a global heating mechanism. The simulations of Smith et al. (2000b) and Stone et al. (1998) both suggest that roughly half of the turbulent energy of a cloud may be dissipated uniformly across a cloud instead of in localized shocks and thus, suggest that $\epsilon = 0.5$ (see Section 4.5.6 for further discussion on ϵ). Furthermore, the magnetic energy injected by shocks may also decay and lead to a global heating of the cloud. Figure 4.5 shows the turbulent heating rates, as a function of density, for $\epsilon = 1$ and $\epsilon = 0.5$. As before, a fixed κ value of 1 is used.

4.6.3 Ambipolar Diffusion

One potentially important energy dissipation mechanism that is usually not included in simulations (e.g., Stone et al. 1998; Mac Low 1999) is ambipolar diffusion. From their numerical simulations, Padoan et al. (2000) find that the ambipolar heating rate in well shielded molecular gas is given by

$$\Gamma_{ambi} = \left(\frac{<|B|>}{10\,\mu G}\right)^4 \left(\frac{M_A}{5}\right)^2 \left(\frac{<n>}{320\,\mathrm{cm}^{-3}}\right)^{-\frac{3}{2}} 10^{-24} \text{ ergs cm}^{-3}\ \mathrm{s}^{-1}, \tag{4.21}$$

where $< |B| >$ is the volume averaged magnetic field strength, M_A is the Alfvénic Mach number of the turbulence, and $< n >$ is the volume averaged number density. Applying Larson's laws and a density-magnetic field strength scaling relation with k = 0.5 converts this equation to the form:

$$\Gamma_{ambi} = 2.6 \times 10^{-24}\, b^2 \left(\frac{n}{10^3\,\mathrm{cm}^{-3}}\right)^{-0.5} \text{ ergs cm}^{-3}\ \mathrm{s}^{-1}. \tag{4.22}$$

Figure 4.5 shows this ambipolar diffusion heating rate, as a function of density, evaluated for the two b parameters previously used for our shock models, b = 0.1 and 0.3.

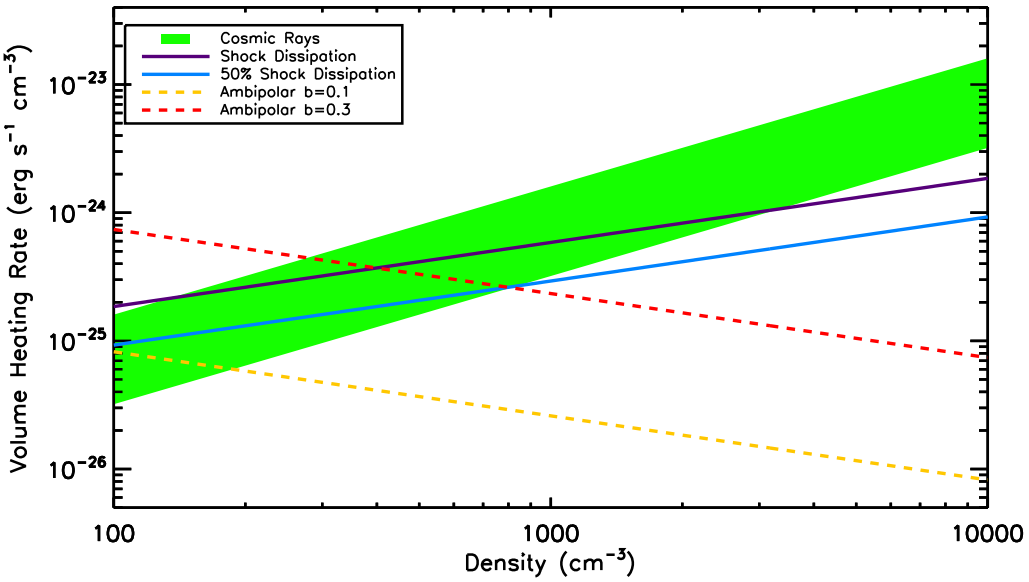

Figure 4.5: Various heating rates for well shielded molecular gas. The shaded (green) region shows the range of cosmic ray heating rates, the dark (purple) solid line shows the total shock turbulent energy dissipation rate, the light (blue) solid line shows 50% of the shock turbulent dissipation rate, and the dark (red) and light (yellow) dotted lines show the ambipolar diffusion heating rates for b values of 0.3 and 0.1 respectively.

4.6.4 Discussion

For gas with a density larger than 10^3 cm^{-3}, the cosmic ray heating rate is the dominant heating term. The turbulent energy dissipation rate is comparable to the cosmic ray heating rate around a density of 10^3 cm^{-3} and becomes larger than the cosmic ray heating rate at lower densities.

Goldsmith (2001) examine the thermal balance of molecular clouds and find that the ambient temperature of well shielded gas, at a density of 10^3 cm^{-3}, is 10 K. We took the Goldsmith (2001) prescriptions for cooling and heating and increased the cosmic ray heating by a factor of two to reproduce the effect of having a turbulent energy dissipation heating rate equivalent to the cosmic ray heating rate. With this increased heating rate, we find a slightly higher equilibrium temperature of 13 K. Pan & Padoan (2009) present a more detailed thermal balance model that also includes a turbulent heating term and, for a 1 pc sized cloud, find similar gas temperatures of 13 to 17 K, depending upon the cosmic ray heating rate used.

This small change in temperature is well within the intrinsic scatter of observed gas temperatures in molecular clouds (e.g., Bergin & Tafalla 2007). Since the cosmic ray heating rate is also uncertain by at least a factor of two, the finding of previous thermal balance studies that the ambient temperatures of molecular clouds are roughly consistent with heating by cosmic ray ionization alone (e.g., Bergin et al. 2006) is not in conflict with the presence of heating from turbulent dissipation at the rate calculated above. The above agreement between observations and models does, however, constrain the turbulent heating rate to not be significantly greater than estimated above. This implies that κ cannot be much less than one, similar to the findings of Basu & Murali (2001). Padoan et al. (2000) also note that if turbulent heating is significant in a molecular cloud, then a positive temperature-velocity dispersion relation is expected, as observed by Jijina et al. (1999).

The significance of ambipolar diffusion to the thermal balance of a cloud is highly dependent upon the strength of the magnetic field. For a strong field, b = 0.3, ambipolar diffusion should be the dominant heating process in well shielded gas with an average density of 100 cm^{-3}, and should be comparable to other heating processes at a density of 10^3 cm^{-3}. Gas at densities of 100 cm^{-3}, however, may not necessarily be well shielded and may instead be dominated by the ISRF. If magnetic field strengths are slightly lower, corresponding to b = 0.1, the ambipolar diffusion rate is negligible for all densities greater than or equal to 100 cm^{-3}. It should also be noted that

the ambipolar diffusion heating rate becomes larger at lower densities, unlike the turbulent and cosmic ray heating rates, because the typical collision speed between ions and neutrals increases with decreasing density.

Shocks will cause both the density and magnetic field strength to increase. The change in the density will be proportional to the change in the magnetic field strength, given the flux freezing approximation made in the shock models. The Alfvén speed in the gas will thus also increase by a factor proportional to the square root of the change in the magnetic field strength. If the magnetic field strength is locally increased by a factor of q by a shock and the velocity dispersion of a cloud remains relatively unchanged, then the ambipolar diffusion heating rate in the shocked gas will be

$$\Gamma_{ambi,shocked} \;=\; q^{1.5}\,\Gamma_{ambi,0}, \tag{4.23}$$

where $\Gamma_{ambi,0}$ is the ambipolar diffusion dissipation rate in the unshocked gas. Thus, the postshock gas will have its ambipolar diffusion heating rate increased.

Table 4.3 gives the factors by which the magnetic field strength and the ambipolar diffusion heating rate increase in each of the shock models. The magnetic field increases in strength by a factor of 4 to 22 and the ambipolar diffusion heating rate increases by one to two orders of magnitude. Even for the weakest magnetic field models, the ambipolar diffusion heating rate in the shocked gas is greater than the rate at which energy is injected into the magnetic field through the shock and thus, this enhanced ambipolar diffusion rate may provide an efficient mechanism for dissipating the injected magnetic energy. Furthermore, this enhanced ambipolar diffusion rate should add an extra heating source to the shocked gas, thereby increasing the CO flux that will emerge at higher J transitions.

The above discussion regarding heating rates is only relevant for the well shielded centers of molecular clouds, as photoelectric heating due to the ISRF will dominate the heating in the outer PDR zones of molecular clouds (e.g., Kaufman et al. 1999). The heating rates shown in Figure 4.5 were also derived using Larson's laws, which, as discussed in Section 4.3.1, have recently been called into question.

4.7 CONCLUSIONS

We have run models of MHD, C-type shocks, based on Kaufman & Neufeld (1996b), for shock velocities of 2 and 3 km s^{-1} and initial densities between $10^{2.5}$ and $10^{3.5}$

cm^{-3}. CO is found to be the dominant molecular coolant with 40% to 80% of the shock energy being emitted in CO rotational lines. All other line cooling processes are negligible, except for H_2 line cooling in the models with the very strongest shocks, in which H_2 cooling accounts for 5% to 20% of the total shock cooling. Between 20% and 60% of the shock energy also goes into compressing the magnetic field.

The expected CO spectrum from each of the shock models has been calculated and PDR models, based on Kaufman et al. (1999), were used to determine the expected contribution of CO emission from not only the cold, well shielded interior of a molecular cloud, but also from the warm outer layers of the cloud. The PDR emission dominates for low J transitions of CO but the shock emission is larger at mid to high J transitions. In all models the shock emission is larger than the PDR emission in the $J = 7 \rightarrow 6$ transition and the shock emission can dominate as low as the $J = 5 \rightarrow 4$ transition, depending upon the shock model. The $J = 6 \rightarrow 5$ and $7 \rightarrow 6$ should serve as shock tracers and should be detectable with current observational facilities.

The turbulent energy dissipation rate is larger than the cosmic ray heating rate for densities less than 10^3 cm^{-3}. The presence of such an additional heating term is, however, still consistent with previous thermal balance studies, given the uncertainty in the cosmic ray heating rate and the range of observed molecular cloud temperatures. The ambipolar diffusion heating rate is negligible at high densities and low magnetic field strengths but can be dominant at lower densities and higher magnetic field strengths. Ambipolar diffusion is also enhanced in the shocked gas and may provide a mechanism for the dissipation of energy injected into the magnetic field by a shock.

4.8 ACKNOWLEDGEMENTS

We would like to thank Shantanu Basu for helpful suggestions on the role of magnetic fields in molecular clouds as well as our anonymous referee for many useful changes to this paper. AP is partially supported by the Natural Sciences and Engineering Research Council of Canada (NSERC) graduate scholarship program and DJ is supported by a NSERC Discovery Grant. This research has made use of NASA's Astrophysics Data System.

Chapter 5

Orion-Eridanus Superbubble

There will be time, there will be time
To prepare a face to meet the faces that you meet;
There will be time to murder and create,
And time for all the works and days of hands
That lift and drop a question on your plate;
Time for you and time for me,
And time yet for a hundred indecisions,
And for a hundred visions and revisions,
Before the taking of a toast and tea.
T.S. Eliot

5.1 ABSTRACT

Winds and supernovae from high-mass star forming regions create large scale cavities in the interstellar medium filled with hot, ionized gas, which are referred to as superbubbles. The Orion molecular clouds are the nearest high-mass star forming regions currently forming stars and have blown a 20° x 45° superbubble that stretches into Eridanus. This Orion-Eridanus superbubble is peculiar in numerous ways. It is significantly more elongated than would be expected for a bubble its size, the major axis of the bubble is not perpendicular to the Galactic plane, and there are unusually bright filaments in the Eridanus half of the bubble, the half of the bubble most distant from the Orion molecular clouds. We fit Kompaneets models, models of bubbles being blown into exponential atmospheres by continuous driving sources, to the

Orion-Eridanus superbubble. We find that the bubble's elongation and orientation cannot be explained by expansion into the Galaxy's exponential disk atmosphere and that some secondary process not included in the Kompaneets model must control the evolution of the shape of the bubble. The Eridanus filaments are too wide and emit too strongly in Hα emission to be equilibrium structures illuminated solely by the Orion star forming region. They may, instead, have formed when the superbubble encountered and compressed a pre-existing, ionized gas cloud within the last Myr, such that the filaments are now out of equilibrium and slowly recombining. The filaments have ionized column densities on the order of 10^{20} cm^{-2}.

5.2 INTRODUCTION

High-mass stars account for only a small fraction of the total mass of stars in the Galaxy, but dominate the energetics of the molecular clouds in which they form and significantly alter the conditions of the interstellar medium (ISM) in their vicinity (e.g. Zinnecker & Yorke 2007). High-mass stars also produce large fluxes of ionizing radiation that form large HII regions (e.g. Shields 1990). The strong winds of massive stars, coupled with the supernova blast waves created when these stars die, also create large, low density cavities in the ISM that are filled with very hot gas (e.g. Heiles 1976; McCray & Kafatos 1987; Staveley-Smith et al. 1997; Heyer et al. 1998; Churchwell et al. 2006, 2007; Bagetakos et al. 2011). Extremely large, ionized bubbles that are formed from the collective energies of an OB association are referred to as superbubbles.

The closest high mass star forming region to the Sun that is currently forming massive stars is the Orion star forming region (see Appendix 5.10.1 or Bally 2008 for more details), containing the Orion molecular clouds, which is located at a distance of 400 pc from the Sun (Hirota et al., 2007; Sandstrom et al., 2007; Menten et al., 2007). The Orion star forming region is surrounded by a highly elongated superbubble, with dimensions of $20^\circ \times 45^\circ$ (Bally, 2008), that is referred to as the Orion-Eridanus superbubble. Prominent Hα features that have been associated with the Orion-Eridanus superbubble include Barnard's Loop in the constellation of Orion (e.g., Pickering 1890; Barnard 1894; Sivan 1974; Reynolds & Ogden 1979) and filamentary features in the constellation of Eridanus that we will hereafter refer to as the Eridanus filaments (e.g., Reynolds & Ogden 1979). Johnson (1978) broke the Eridanus filaments into three separate arcs, with Arc A being the eastern most arc,

Arc B the western most, and Arc C being the southern extension of the filaments below the intersection of Arcs A and B. The superbubble is also associated with an H I cavity (Menon, 1957; Heiles & Habing, 1974; Heiles, 1976; Green, 1991; Burrows et al., 1993; Brown et al., 1995; Kalberla et al., 2005) and enhanced soft, 0.25 and 0.75 keV, x-ray emission (Davidsen et al., 1972; Williamson et al., 1974; Naranan et al., 1976; Long et al., 1977; Fried et al., 1980; Nousek et al., 1982; Singh et al., 1982; McCammon et al., 1983; Marshall & Clark, 1984; Garmire et al., 1992; Burrows et al., 1993; Guo et al., 1995; Snowden et al., 1995a, 1997). Please see Appendix 5.10 for a more detailed review of prior observations of the superbubble. In this chapter, all references to north or south refer to increasing or decreasing declination and references to east or west refer to increasing or decreasing right ascension, unless otherwise specified.

There are a number of peculiar features of the Orion-Eridanus superbubble. It is unusually elongated for its size, as models of bubbles typically produce much more spherical bubbles (e.g., Koo & McKee 1990; Brown et al. 1995). Models of the Orion-Eridanus superbubble also typically have the bubble elongated parallel to the Galactic plane (e.g., Reynolds & Ogden 1979; Burrows et al. 1993; Burrows & Zhiyu 1996; Lee & Chen 2009), rather than being elongated perpendicular to the plane as would be expected for a bubble expanding into the exponential atmosphere of the Galactic disk (e.g., Basu et al. 1999). The nature and formation mechanism of the Eridanus filaments are also enigmatic.

Kompaneets (1960) derived the structure of a bubble blown into an exponential atmosphere by a supernova explosion and Basu et al. (1999) extended this work to model bubbles, in exponential atmospheres, driven by constant energy sources such as stellar winds or series of supernova explosions. We will hereafter refer to such a continuous energy injection model as a Kompaneets model. Kompaneets models have been used to fit both observed (Basu et al., 1999) and simulated superbubbles (Stil et al., 2009), and have been shown to reasonably reproduce the shape of superbubbles as determined through more involved modeling (Mac Low et al., 1989).

Basu et al. (1999) fit the W4 superbubble with a Kompaneets model and found that while such a model could reasonably fit the morphology of the W4 superbubble, the Kompaneets model required a scale height for the Galactic disk of only 25 pc, which is much smaller than the typical value derived for the Galactic disk of 100 to 150 pc (Kalberla & Kerp, 2009). Basu et al. (1999) were also able to fit the location of the ionization front in the W4 superbubble with their Kompaneets model.

Following the methodology of Basu et al. (1999), we attempt to fit the Orion-Eridanus superbubble with a Kompaneets model. In Section 5.3.1 we describe Kompaneets models in more detail and in Section 5.3.2, we describe the observational constraints we use in fitting the superbubble. We present the two best fitting models of the superbubble, where the Eridanus end is pointed towards and away from the Sun, in Sections 5.4.1 and 5.4.2, respectively. Physical properties of the superbubble, based upon the best fitting models, are presented in Section 5.5. We discuss the quality of these fits and possible alternate explanations for the shape and size of the superbubble in Section 5.6. In Section 5.7 we discuss the general properties of the Eridanus filaments and we briefly describe two possible formation scenarios for the filaments. Finally, in Section 5.8, we summarize our findings. We also include, in Appendix 5.10, a thorough review of previous observations of the Orion-Eridanus superbubble and a discussion of previous interpretations of the bubble morphology.

5.3 MODEL SETUP

5.3.1 Model Description

Kompaneets (1960) derived a semi-analytic solution for the propagation of a supernova shock wave into a purely exponential atmosphere. This model was modified by Basu et al. (1999) to allow for a continuous injection of energy, as would be produced from stellar winds or a succession of supernovae. The three key assumptions of the Kompaneets model are: (1) the pressure within the bubble is spatially uniform, (2) the bubble expands in the direction of the surface normal at all locations, and (3) the expansion speed of the bubble is given by Hugoniot jump conditions for a strong shock, where the exterior pressure is negligible compared to the interior pressure.

In a Kompaneets model, the shape of a bubble is fully described by one parameter, $\tilde{y}$, using the notation of Basu et al. (1999). The $\tilde{y}$ parameter can take any value from zero to two, with the bubble becoming more elongated at higher values of $\tilde{y}$ and with the top end of the bubble reaching an infinite distance from the driving source when $\tilde{y} = 2$.

To convert model size scales to physical units, one length scale must be specified. This length scale can be the scale-height of the exponential atmosphere or the length of one feature of the bubble, specified by giving the distance to and angular size of the feature. The pressure within the bubble, expansion velocity, time since the

creation of the bubble, surface density of the bubble wall, interior temperature, driving luminosity, and initial density of the exponential atmosphere at the location of the driving source can all be given in physical units if two of these parameters are specified. Furthermore, the location of the ionization front can also be determined if, in addition to two of the above mentioned parameters, the ionizing luminosity of the source and the temperature of the bubble wall are also given. This technique of fitting both the bubble wall and ionization front was used by Basu et al. (1999) and we follow a similar methodology in our model fits. See also Table 1 of Basu et al. (1999) for the dimensional relationships between model parameters and Appendix A of Basu et al. (1999) for a more detailed description of Kompaneets models.

More sophisticated semi-analytic models, where the shell velocity is calculated by following momentum in a thin shell approximation, are available in the literature (e.g., Mac Low & McCray 1988; Bisnovatyi-Kogan et al. 1989). Simulations of expanding bubbles that fully integrate the relevant hydrodynamic equations (Tomisaka & Ikeuchi, 1986; Mac Low et al., 1989; Tenorio-Tagle et al., 1990) or magnetohydrodynamic equations (Tomisaka, 1992, 1998; Stil et al., 2009) have also been run. The Kompaneets approximations, however, have been shown to provide an excellent first order solution for the shape of a bubble expanding in an exponential atmosphere (e.g., Mac Low et al. 1989).

5.3.2 Observational Constraints

The primary image used in this paper for determining the shape of the Orion-Eridanus superbubble is a wide field Hα mosaic taken by astrophotographers (Di Cicco & Walker, 2009), which initially contained no specific astrometric information and was not calibrated to a known intensity scale. We identify 18 bright stars in the image and use their locations, as given in the Hipparcos database (van Leeuwen, 2007) to astrometrically calibrate the image. This image is shown in Figure 5.1 and the most prominent Hα features are labeled in this figure.

For this paper, we make the assumption that the Hα emission best traces the walls of the superbubble and we fit to this Hα emission preferentially over H I emission. We choose Hα over H I because superbubble walls do not necessarily have to trap all of the ionizing photons coming from a source, such that neutral hydrogen may only be present at significant distances from the bubble walls. The Kompaneets model predicts that the superbubble walls should appear strongly in Hα (Basu et al., 1999).

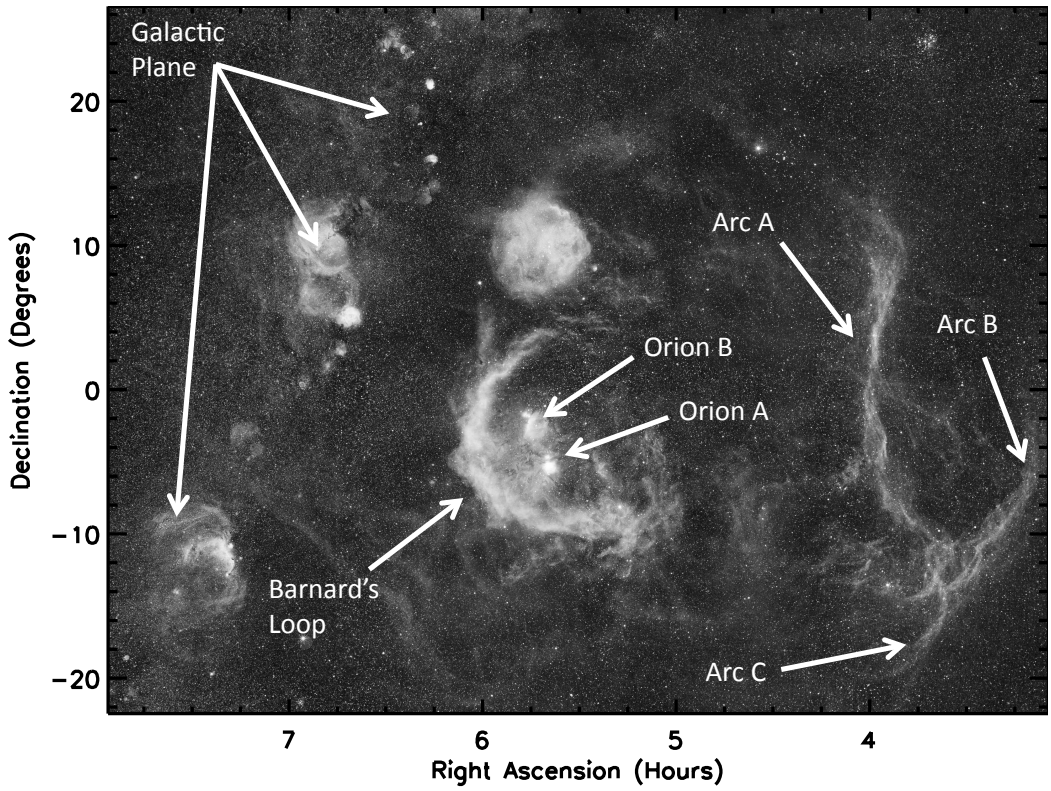

Figure 5.1: Orion-Eridanus superbubble as seen in Hα. Labels for the various major components of the bubble have been added to the image from Di Cicco & Walker (2009). Arcs A, B, and C are collectively referred to as the Eridanus filaments.

While there is some debate in the literature regarding whether Arcs A and B are part of the Orion-Eridanus superbubble (e.g., Boumis et al. 2001), we consider the Arcs to be part of the superbubble and fit to these Arcs accordingly. We do not believe that Barnard's Loop is half of a small spherical bubble with a radius of approximately 50 pc. One of the primary reasons we believe that the Orion-Eridanus superbubble stretches from Barnard's Loop to the Eridanus filaments is that diffuse x-ray emission, potentially coming from the hot plasma within the superbubble, is detected from the Orion star forming region out to Arc B (e.g., Snowden et al. 1995a). For a more in-depth discussion of why these Arcs may be part of the superbubble, please see Appendix 5.10.11.

We do not, however, consider Arc C to be part of the bubble wall. The reasons for this are threefold. First, the bottom edge of Barnard's loop points roughly towards the intersection of Arcs A and B, and for Arc C and Barnard's loop to be part of the bubble wall, the bubble wall would have to have a discontinuity that is not predicted by a Kompaneets model. Second, diffuse 0.75 keV x-ray emission from the interior of the superbubble does not extend significantly below the intersection of Arcs A and B (e.g. Snowden et al. 1997), indicating that the gas below this intersection is cooler, as would be expected if the lower edge of the bubble wall goes through this intersection of Arcs A and B (see also Appendix 5.10.4). Third, and finally, it is difficult to find a bubble that is as smooth as predicted in a Kompaneets model in which Arcs A, B, and C all are wall segments, given that all three arcs intersect at the same point with different centers of curvature. If Arc C were part of the bubble wall, the bubble's apparent axis ratio would drop to approximately 1.5, rather than being greater than 2.

While the Hα image is used to constrain the extent of the superbubble in right ascension and declination, there are also limited observational constraints on the distance to the near and far side of the superbubble. Studies of interstellar absorption features in stellar spectra towards the Eridanus half of the bubble reveal a wall of gas moving towards the Sun at a distance of approximately 180 pc, which could be the near wall of the superbubble (Guo et al., 1995; Burrows & Zhiyu, 1996; Welsh et al., 2005). A lack of a detection of the far wall of the superbubble in such absorption studies (Guo et al., 1995; Burrows & Zhiyu, 1996; Welsh et al., 2005), as well as a proper motion study of Arc A (Boumis et al., 2001), suggest that the far wall of the superbubble is greater than 500 pc away. Such a large depth of the superbubble, approximately 300 pc, is much larger than the north-south extent of the superbubble

on the sky, approximately 150 pc. For the eastern, Orion end of the superbubble, we adopt a distance of 400 pc, corresponding to the distance of the Orion star forming region (Menten et al., 2007). See Appendix 5.10.5 for a more detailed review of past absorption line studies towards the superbubble. These absorption studies use lines coming from neutral, rather than ionized, gas. Thus, these studies do not necessarily trace the ionized wall of the bubble and may give a near distance that is too small and a far distance that is too large.

A typically used value for the average rate of mechanical energy deposited into the ISM by an OB association is 10^{38} ergs s^{-1} (e.g., Heiles 1987; Mac Low & McCray 1988; Shull & Saken 1995; Bally 2001), although the Orion star forming region is believed to have an average mechanical energy input rate of only 2×10^{37} ergs s^{-1} (Reynolds & Ogden, 1979; Brown et al., 1994). The pressure, P / k, of the bubble, from x-ray measurements, is estimated to be between 1 and 5×10^4 cm^{-3} K (Burrows et al., 1993; Guo et al., 1995; Burrows & Zhiyu, 1996). At the height of the Orion star forming region, approximately 130 pc below the Galactic plane (Bally, 2008), models of the Galactic disk predict that the density of the ambient gas into which the bubble is being blown is roughly 0.5 cm^{-3} (Kalberla & Kerp, 2009). Observations, however, suggest that the ambient density near the Orion star forming region may have been closer to 1 cm^{-3} before the superbubble was formed (Heiles, 1976; Ferriere et al., 1991; Brown et al., 1995). The luminosity of ionizing photons from the Orion star forming region is roughly 3.8×10^{49} s^{-1} (Reynolds & Ogden, 1979) and the superbubble wall is likely at a temperature of 8000 K (Basu et al., 1999). See also Appendix 5.10.9 for a review of previously derived physical properties of the superbubble.

5.4 MODEL FITTING

5.4.1 Model T: Towards the Sun

Interpreting the absorption features detected at a distance of approximately 180 pc as the near wall of the bubble (Frisch et al., 1990; Guo et al., 1995; Burrows & Zhiyu, 1996; Welsh et al., 2005), we first attempt to fit a model in which the superbubble is oriented with the Eridanus end pointed towards the Sun and where the near side of the bubble is only approximately 180 pc distant. The free parameters for this fit are the position of the eastern most point of the bubble, the orientation of the major axis of the bubble in the plane of the sky, the elongation of the bubble (as controlled by

the $\tilde{y}$ parameter), the inclination of the bubble with respect to the plane of the sky, and the maximum width of the bubble. For all fits, the Orion end of the superbubble is assumed to be 400 pc away, corresponding to the estimated distance of the Orion star forming region (Menten et al., 2007). The location of the driving source is not used as an input parameter, but rather, is derived from the model. The scale-height of the ISM exterior to the bubble and parallel to the major axis of the bubble is also obtained from the model fit. Due to the complex structure of the region, all fitting is done by eye, and the best fit model is chosen as the one that appears to match the Hα morphology the closest while still obeying the above stated distance constraints. No data sets besides the Hα are used in determining which model is the best fitting model. We estimate the relative error of this fitting below.

The best fitting model for this bubble orientation is shown in the top panel of Figure 5.2 and will hereafter be referred to as model T. On the top panel of Figure 5.2, the position of the driving source, as predicted by the Kompaneets model, is denoted with an asterisk and is roughly coincident with the position of the Orion B molecular cloud. A schematic diagram of this model is shown in the top panel of Figure 5.3 and the basic parameters of this model are given in Table 5.1.

In this model, the intensity of Barnard's Loop, which is expected to be relatively high due to the proximity of the loop to the driving source, is enhanced due to limb brightening. Some faint emission noticeable along the north and south edges of the bubble also appears to be enhanced by limb brightening. The closest point on the near side of the bubble is located at a distance of 171 pc from the Sun. In this model, both Arcs A and B lie along the same plane perpendicular to the major axis of the superbubble. That is, the filaments trace the bubble wall at a particular, constant distance from the driving source. Given the orientation of the bubble towards the Sun, Arc A traces the near side of the bubble while Arc B traces the far side of the bubble. The sense of curvature of Arc A comes out naturally from this model fit. Reasonably good fits can also be obtained, although not shown, where Arc B corresponds to the end cap of the bubble and Arc A is a feature on the near side of the bubble. The major axis of the superbubble makes an angle of 85° with respect to the normal of the Galactic plane. Because the fits are tightly constrained by the size of Barnard's Loop and the requirement that the near side be approximately 180 pc distant, no adequate fits are found with a value of $\tilde{y}$ below 1.999 or with a scale-height differing by more than 1% from that of model T.

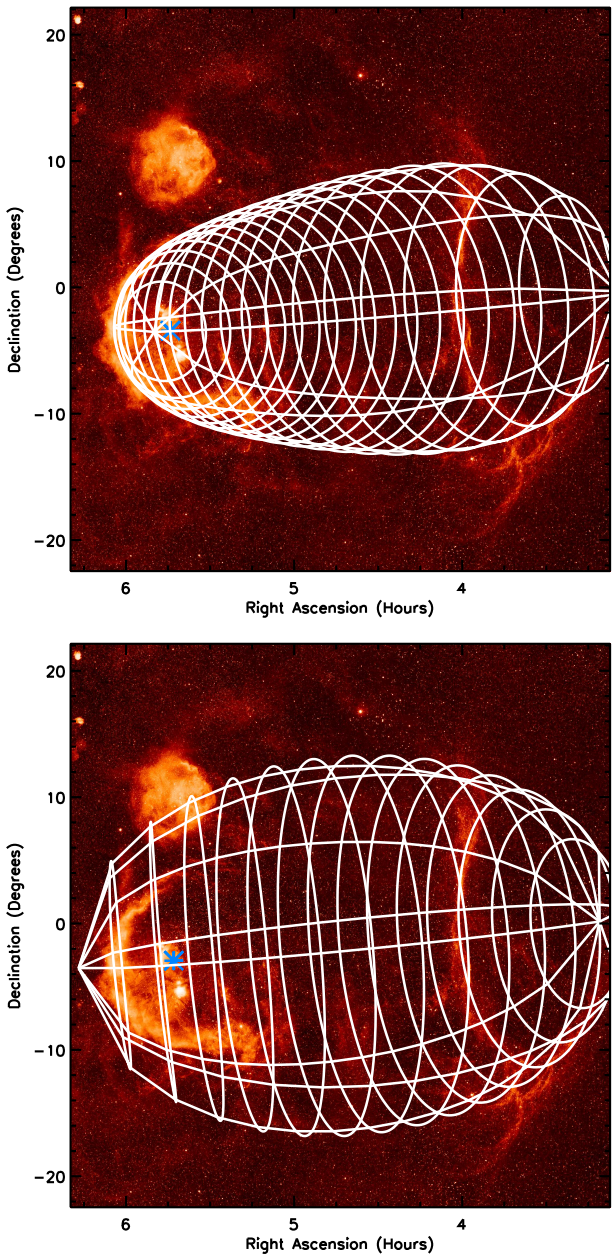

Figure 5.2: Best fit Kompaneets models of the Orion-Eridanus superbubble, white lines, overplotted on the Hα image of Di Cicco & Walker (2009). The top panel shows the best fit for a bubble oriented towards the Sun, model T, while the bottom panel shows the best fit for a bubble oriented away from the Sun, model A. The asterisks denote the locations of the driving sources in the Kompaneets models and bubble parameters are given in Table 5.1.

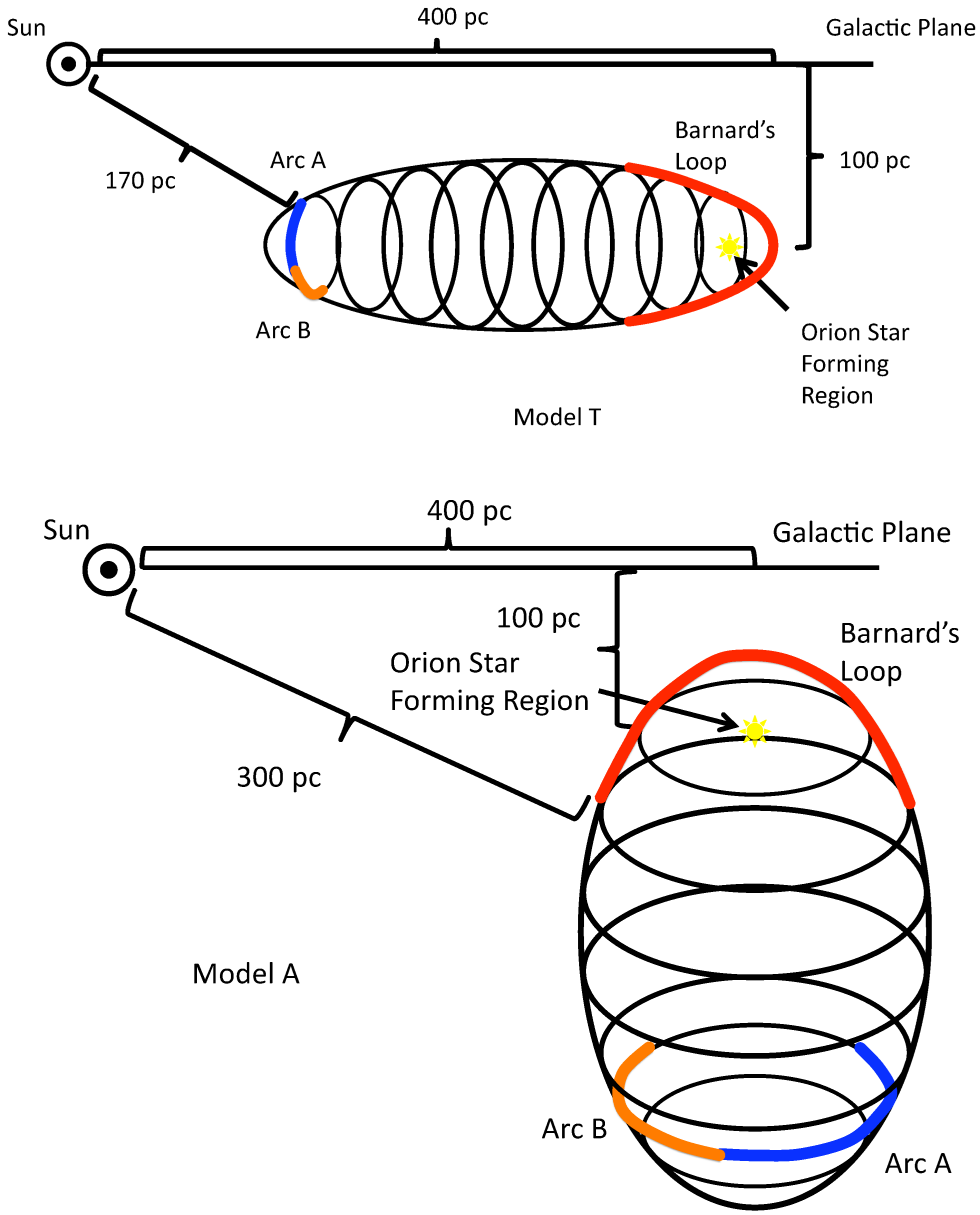

Figure 5.3: Schematic diagram of models T and A. Model T is shown on the top panel and model A is shown on the bottom panel. In each of these schematic diagrams, the superbubble major axis is inclined roughly 30° into the page, in order to match the offset between the superbubble axis and the normal to the Galactic plane apparent in Figure 5.1.

Table 5.1. Kompaneets Model Properties

Model (1)	$\tilde{y}$ (2)	H (pc) (3)	d_{min} (pc) (4)	d_{max} (pc) (5)	θ (°) (6)
T	1.9995	15	170	400	85
A	1.945	40	305	540	35

Note. — Col. (1) gives the model name, while cols. (2) and (3) give the value of the $\tilde{y}$ parameter and the scale-height of the exponential atmosphere, respectively. Cols. (4) and (5), respectively, give the distance to the closest and farthest point on the superbubble wall. The maximum distance in model T occurs at the Orion end while the far side of the bubble near the location of Arc A is only 275 pc distant. Col. (6) gives the angle that the major axis of the superbubble makes with the normal to the Galactic plane.

5.4.2 Model Fit A: Away from the Sun

There is some evidence that Arc A is located at a distance greater than 500 pc (see Appendix 5.10.11). Thus, we attempt to find a second model fit where the bubble is oriented away from the Sun, such that Arc A resides on the far side of the bubble. For this model orientation, we find that Barnard's Loop cannot be accurately fit and thus, the position of the driving source is used as a fitting parameter, rather than the location of the eastern most part of the bubble, as was done for model T. As before, the other fitting parameters used are the orientation of the major axis of the bubble in the plane of the sky, the elongation of the bubble, the inclination of the bubble with respect to the plane of the sky, and the maximum width of the bubble. The source location is constrained to lie near the Orion B molecular cloud and the far eastern edge of the bubble is assumed to be at a distance of 400 pc. Once again, all fitting is done by eye.

The best fitting model for this orientation is shown in the bottom panel of Figure 5.2 and will hereafter be referred to as model A. A schematic diagram of this model is given in the top panel of Figure 5.3 and the basic parameters of this model are given in Table 5.1.

In model A, Arc A is located at a distance of 500 pc and the closest point on the near side of the bubble is just over 300 pc distant from Earth. The maximum minor axis diameter of the bubble is 220 pc in model A, as compared to 100 pc in model T. Model A does not fit Barnard's Loop, nor any of the weak emission to the north of the bubble but, however, does fit some weak features seen to the south of the bubble and does a reasonable job fitting the Eridanus filaments. As in model T, Arc B and Arc A both lie in the same plane perpendicular to the major axis of the bubble at a fixed distance from the driving source. Model A has the major axis of the superbubble making an angle of 35° with respect to the normal to the Galactic plane. A slight reduction in the $\tilde{y}$ parameter also produces a reasonable fit where Arc B is the end cap of the bubble. Because there is no tight distance constraint on the Eridanus end and no constraints on the shape of the Orion end, a much wider array of models produce reasonable fits for a bubble oriented away from the Sun. All reasonable bubble fits, however, have $\tilde{y} > 1.7$ and scale-heights less than 60 pc.

5.5 PHYSICAL PROPERTIES OF THE BUBBLE

For the two best fitting models, the interior pressure, expansion velocity, age, wall density, and interior temperature of the superbubble can be determined by specifying the driving luminosity and the initial density of the exponential atmosphere at the height of the source. We choose to adopt a driving luminosity of 2×10^{37} ergs s^{-1} (Reynolds & Ogden, 1979; Brown et al., 1994) and an initial density range of 0.5 to 1 cm^{-3} (Heiles, 1976; Ferriere et al., 1991; Brown et al., 1995; Kalberla & Kerp, 2009). The initial density range chosen is the same as will be used for the ionization front fitting in Section 5.5.7.

5.5.1 Pressure

One of the known problems with a Kompaneets model is that it predicts that the top of an expanding superbubble will reach an infinite distance from the driving source in a finite time. Realistic bubbles will not obtain the high, late time velocities predicted by a Kompaneets model. At later times in a bubble's evolution, when the expansion velocity given by the Hugoniot jump conditions becomes supersonic, a pressure gradient is likely to form with the pressure being greatest towards the base of the atmosphere. At this time, the Kompaneets model assumption of constant pressure becomes invalid. Deviations away from exponential atmosphere profiles at large heights may also limit the expansion velocities of real superbubbles.

Because a Kompaneets model will overpredict the late stage expansion velocity of a superbubble, such a model is also expected to slightly underpredict the pressure at late times of a bubble's expansion. For the range of densities adopted above, the thermal pressure, P / k, within the bubble is between 0.7 and 0.9×10^4 K cm^{-3} in model T and between 0.9 and 1.1×10^4 K cm^{-3} in model A. These values are close to, but slightly lower than, the observationally determined thermal pressure of 10^4 to 5×10^4 K cm^{-3} (Burrows et al., 1993; Guo et al., 1995; Burrows & Zhiyu, 1996), consistent with the underprediction.

Basu et al. (1999) suggest that for a bubble fit with a Kompaneets model, the best estimate for the pressure within the bubble at later times in the bubble's evolution is given by the interior pressure of the Kompaneets model when the expansion speed of the top of the bubble reaches the sound speed within the bubble. They argue that when the expansion speed becomes supersonic, a pressure gradient will form within the bubble and the interior pressure of the lower section of the bubble will

remain roughly constant throughout the remainder of the bubble's evolution. Using this approach, we find that models T and A are consistent with thermal pressures, P / k, of approximately 9×10^4 K cm^{-3} and 1.5×10^4 K cm^{-3}, respectively, for the Orion-Eridanus superbubble. This range of values is therefore generally consistent with observationally derived pressures for the superbubble, given the uncertainties involved with determining an accurate pressure from a Kompaneets model. The top cap of the superbubble becomes supersonic when $\tilde{y}$ is 1.768 and 1.886 in models T and A, respectively. The typical ISM pressure, P / k, is only on the order of 3×10^3 K cm^{-3} (e.g., Kalberla & Kerp 2009), and thus, the superbubble is clearly over-pressured and should be expanding, as observed (e.g., Reynolds & Ogden 1979).

5.5.2 Age

Because Kompaneets models tend to overpredict the expansion velocities of superbubbles, they are known to also slightly underpredict the ages of superbubbles (Komljenovic et al., 1999; Stil et al., 2009). Thus, the ages derived below for models T and A should be considered lower limits. Stil et al. (2009) fit Kompaneets models to simulations of superbubbles expanding into stratified, magnetic media and show that while their Kompaneets model ages are too small, they are still accurate to within a factor of four. Stil et al. (2009), however, do not simulate bubbles as highly elongated as the Orion-Eridanus superbubble.

Model T predicts an age of approximately 0.5 Myr for the Orion-Eridanus superbubble while model A predicts an age of approximately 2.5 Myr. These ages are consistent with previously calculated dynamical ages of the superbubble, which are on the order of a few megayears (e.g., Brown et al. 1994). These ages are also in agreement, given that they may be underestimated by a factor of four, with the ages of Orion OB1b, c, and d, 2 to 8 Myr, 2 to 6 Myr, and <2 Myr, respectively (Brown et al., 1994; Bally, 2008), but do not provide any significant constraints on which group initially formed the superbubble. Orion OB1a, with an age of 8 to 12 Myr (Brown et al., 1994), may be marginally too old to be the driving source of the superbubble.

5.5.3 Density

The density of the bubble wall can be calculated from the ideal gas equation of state if the pressure in the wall and temperature in the wall are known. The temperature

of an ionized bubble shell is expected to be approximately 8000 K (Basu et al., 1999) and thus, we adopt this temperature for the bubble wall. This value is in rough agreement with the temperature of 5.5×10^3 K calculated by Heiles et al. (2000) for the Orion-Eridanus superbubble wall. We also assume that the pressure within the bubble wall is equal to the interior pressure of the bubble and we choose to adopt the observed range of interior pressures for the bubble, 1 to 5×10^4 K cm^{-3} (Burrows et al., 1993; Guo et al., 1995; Burrows & Zhiyu, 1996), rather than using the model derived pressures, because of the Kompaneets model's known problem of underestimating the pressure at late times. Since we assume that the bubble interior has a constant pressure and that the bubble wall has a constant temperature, the density of the wall must also be spatially constant, for the wall to be in pressure equilibrium with the interior.

For this range of pressure and temperature, the density within the bubble wall is between 1 and 6 cm^{-3}. Alternatively, if the expansion velocity is taken to be 15 km s^{-1} and the ram pressure on the shell wall is assumed to be equal to the interior thermal pressure, the shell wall would have a density on the order of 1 cm^{-3}. These densities are consistent with the wall densities derived by Reynolds & Ogden (1979) and Heiles (1989). If the lower wall temperature measurement by Heiles et al. (2000) is used or the bubble wall pressure is twice the interior pressure, as predicted by Bisnovatyi-Kogan & Silich (1995), the above calculated wall densities would increase by approximately a factor of two. Alternatively, if the bubble pressures derived from the final Kompaneets model shapes are used, the wall densities would be as much as a factor of 1.5 smaller.

5.5.4 Interior Bubble Temperature

Following the methodology of Basu et al. (1999), we assume that the interior temperature of the superbubble follows the equation from Weaver et al. (1977) for the temperature at the center of a spherical bubble:

$$T = 63.6 \left(\frac{L_0}{R_s} \right) K, \tag{5.1}$$

where T is the bubble temperature, L_0 is the mechanical energy luminosity of the bubble, and R_s is the equivalent spherical radius given by

$$R_s = \left(\frac{125}{154\pi}\right)^{1/5} L_0^{1/5} \rho_0^{-1/5} t^{3/5}, \tag{5.2}$$

where ρ_0 is the initial density at the height of the driving source and t is the time since the formation of the superbubble. From this equation, model T should have an interior temperature of 5×10^6 K and model A, a temperature of 4×10^6 K. The photoevaporation of any small gas clumps remaining within the superbubble wall will cool the bubble interior and this quenching may cause the estimated temperature of the interior to be slightly overestimated (McKee et al., 1984). From x-ray observations, the interior temperature of the superbubble has been observationally determined to be 1 to 4 $\times 10^6$ K (Williamson et al., 1974; Naranan et al., 1976; Long et al., 1977; Burrows et al., 1993; Guo et al., 1995), which is consistent with our model temperatures.

5.5.5 Expansion Speed

In models T and A, the expansion velocities of the bubble at the location of Arc A are roughly 7500 km s^{-1} and 120 km s^{-1}, respectively. These values, especially that for model T, are unreasonably high. As discussed previously, it is a known problem of the Kompaneets model that the expansion velocities are overestimated at late times, particularly after the expansion speed of the top of the superbubble becomes supersonic. This transition to supersonic velocities occurs approximately 0.15 Myr and 0.25 Myr before the bubble reaches its current configuration in models T and A, respectively. At this time, the material which will end up near the position of Arc A is moving at a speed of 230 km s^{-1} in model T and 120 km s^{-1} in model A.

By assuming that the material in the bubble wall that will end up at the location of Arc A enters a momentum-conserving phase once the top cap becomes supersonic, we can estimate a more reasonable current expansion speed for the material near Arc A. We model this gas as a planar sheet with a surface density equal to the surface density on the bubble at the location of the streamline that will end up on Arc A at the time at which the top cap becomes supersonic. We assume that the sheet moves directly from its location at the time the top cap becomes supersonic to the current position of Arc A. We find that the expansion velocity of the material in Arc A would

have only decreased to approximately 160 km s^{-1} in model T and 95 km s^{-1} in model A. Given the angles between the expansion velocities of Arc A and the line of sights to Arc A in models T and A, 27° and 7°, respectively, the expected observed line of sight velocities from these two models are 140 and 94 km s^{-1}. These velocities are much higher than the observationally determined line of sight expansion velocity of 15 km s^{-1} (e.g., Reynolds & Ogden 1979).

The expansion velocity of the bubble must have been larger than the currently observed 15 km s^{-1} in the past, however, as an average speed of 35 km s^{-1} is required for the bubble to expand to its 300 pc total length, assuming an upper limit of 8 Myr for the age of the bubble, based upon the time since the formation of Orion OB1b (Brown et al., 1994). This average speed of 35 km s^{-1} is still small compared to the model predictions. If the bubble is only 2 Myrs old, the required average expansion speed would be even larger. It should be noted that while Kompaneets models overpredict expansion velocities, they still produce superbubble shapes comparable to those produced by more accurate numerical methods (Basu et al., 1999; Komljenovic et al., 1999).

5.5.6 Atmospheric Scale-Height

Kompaneets model parameters can be used to calculate the scale-height of the exponential atmosphere into which a bubble is blowing. For model T, the scale-height is only 15 pc, while for model A, the scale height is 40 pc. Both of these values are significantly smaller than the typical 150 pc scale-height derived for the Galaxy (e.g. Dickey & Lockman 1990; Heyer et al. 1998; Kalberla & Kerp 2009), but are similar to the value of 25 pc derived for the scale height of the galaxy by Basu et al. (1999) during their fitting of a Kompaneets model to the W4 superbubble. For a further discussion of these scale heights, see Section 5.6.1.

5.5.7 Ionization Front Fitting

As shown by Basu et al. (1999), it is possible to calculate whether, and where, an ionization front will break-out of a particular superbubble wall, given the initial density of the ambient gas at the location of the source, the ionizing photon flux of the source, the temperature of the material in the bubble wall, and the gas pressure of the bubble wall. We choose to set the gas pressure in the bubble wall to be equal to the gas pressure within the bubble. We adopt a temperature of 8000 K for the

Table 5.2. Ionization Front Parameters

	T (K) (1)	P/k (K cm^{-3}) (2)	L (s^{-1}) (3)	n_0 (cm^{-3}) (4)
high	8000	5×10^4	4×10^{49}	1
low	8000	1×10^4	4×10^{49}	0.5

Note. — Col. (1) gives the adopted temperature of the bubble wall. Cols. (2), (3), and (4), respectively, give the adopted ranges for the bubble wall's pressure, ionizing luminosity, and the initial density of the exponential atmosphere at the height of the driving source. The first row gives the highest value used and the second row gives the lowest value used.

bubble wall (Basu et al., 1999) and a bubble pressure, P / k, of either 1×10^4 or 5×10^4 K cm^{-3} (Burrows et al., 1993; Guo et al., 1995; Burrows & Zhiyu, 1996). We also investigate initial densities of 0.5 and 1 cm^{-3} (Heiles, 1976; Ferriere et al., 1991; Brown et al., 1995; Kalberla & Kerp, 2009) and an ionizing luminosity of 4×10^{49} s^{-1} (Reynolds & Ogden, 1979). A summary of the parameter range investigated is given in Table 5.2. An ionization front will remain within a bubble wall if the depth required to absorb all of the ionizing photons is larger than the line-of-sight depth of the bubble wall, such that

$$\left(\frac{\Phi_* \, cos(\phi) \, kT}{2\pi \, N_s \, P_s \, \alpha_b \, s^2} \right) > 1, \tag{5.3}$$

where Φ_* is the ionizing luminosity of the source, ϕ is the angle between the surface normal of the wall and the line-of-sight from the source to the wall, k is the Boltzmann constant, T is the temperature in the wall, N_s is the surface density of the wall, P_s is the pressure in the wall, α_b is the recombination coefficient of Hydrogen, and s is the distance from the shell wall to the ionizing source. Note that N_s is dependent upon the initial gas density at the height of the source.

For the above adopted parameter ranges, we find that ionizing photons are capable

of fully penetrating the superbubble wall everywhere if the bubble has the shape of model T. For a bubble with the shape of model A, ionizing photons also breakout everywhere for all combinations of the above ionization parameters except for the case where the pressure, P / k, is 5×10^4 K cm^{-3} and the initial density is 1.0 cm^{-3}. In this one case, the ionizing photons are trapped in the lower half of the bubble. For both models T and A, there is no combination of ionization parameters in the adopted parameter range for which the ionizing photons are still trapped within the bubble wall at the distance of the Eridanus filaments.

Star formation preferentially occurs within regions of the Galaxy that are over dense and over pressured with respect to the ambient ISM (Bergin & Tafalla, 2007). If Barnard's Loop was partially formed from the overdensity associated with the Orion star forming region, then the density and pressure of Barnard's Loop should be slightly higher than otherwise expected. If the initial density of the exponential atmosphere is increased to 5 cm^{-3}, thereby increasing the total mass swept up by the bubble, and the pressure within the bubble wall is increased to P/k = 10^5 K cm^{-3}, thereby increasing the density within the wall, then the ionizing photons become fully trapped within Barnard's Loop for model T. As such, Barnard's Loop may still be fully trapping the ionizing photons from the Orion star forming region, due to the enhanced mass associated with the star formation event, for both models T and A. Since molecular clouds are typically on the order of a few to tens of parsecs in size (Bergin & Tafalla, 2007), it is unlikely that this increased pressure and density would extend significantly towards the Eridanus end of the superbubble.

Basu et al. (1999) are able to fit a Kompaneets model to the W4 superbubble in which the ionization front breaks out of the bubble approximately half way up the bubble, but also require a larger than expected initial density of 10 cm^{-3} in order for there to be enough material in the lower bubble wall to fully trap the ionizing photons.

5.6 DISCUSSION

5.6.1 Quality of Fits

In Sections 5.4.1 and 5.4.2, two different model fits of the Orion-Eridanus superbubble were presented. Neither model is completely satisfactory and the following discussion evaluates the advantages and disadvantages of each model.

On first glance, model T would seem to provide the better fit of the superbubble, as it is capable of reproducing the morphology of the bubble on both the Orion and Eridanus ends, while model A clearly fails to match the size and shape of Barnard's Loop. Model T also has the advantage that the location of the driving source is not a fitting parameter, as is the case in model A. The alignment of the driving source with the Orion B molecular cloud in model T serves as an independent verification that the model may be accurately describing the structure of the superbubble.

The failure of model A to reproduce the size of Barnard's Loop is not, however, completely unexpected. The Kompaneets model used assumes that the atmosphere into which the bubble is expanding is a pure exponential atmosphere and does not take into account the presence of any density enhancements, such as that provided by a giant molecular cloud. The greater density and pressure of a molecular cloud would hinder the expansion of a superbubble in the direction of that cloud. Thus, if the bulk of the molecular cloud complex that gave rise to the Orion star forming region were originally located to the east of the driving source of the superbubble, it would be expected that the observed size of the superbubble in this direction would be smaller than predicted by a Kompaneets model. The failure of model A to match the size of Barnard's Loop might simply be due to the expansion of the superbubble being slowed by the excess material present in and around the Orion star forming region.

One of the advantages of model T is that it readily explains the presence of the 180 pc distant wall of material moving towards the Sun detected via absorption line studies (e.g., Welsh et al. 2005), as this material would just be the near wall of the superbubble. Model A, unfortunately, cannot account for this gas, as the nearest point on model A is over 300 pc distant. If model A were correct, this 180 pc distant gas would have to be unassociated with the Orion-Eridanus superbubble, although not necessarily unassociated with the Orion star forming region. On the other hand, model T is not compatible with the lack of detection of the far side of the superbubble at any distance within 500 pc by absorption line studies (e.g., Welsh et al. 2005), as the far side of model T, towards Arc A, is located at a distance of approximately 275 pc from the Sun. It is, however, possible that the far side of the bubble is receding at a velocity similar to that of the local bubble wall, such that the far side cannot be easily disentangled from spectral features due to the local bubble (see also Appendix 5.10.11.2). Model A is compatible with this observational non-detection of the far wall, as the far side of model A is slightly greater than 500 pc distant from the Sun.

No good bubble fits are found with a near side distance of 180 pc and a far side distance greater than 500 pc. Since the absorption measurement distances are based upon absorption lines from neutral gas, the near side distance to the bubble wall may be underestimated and the far side distance overestimated if ionizing photons from Orion can penetrate the bubble wall and ionize material outside of the superbubble. A tri-axial bubble model, unlike the cylindrically symmetric Kompaneets model, may be required to fit the Orion-Eridanus bubble if its line of sight depth is indeed greater than 300 pc and its north-south extent is only 150 pc. See Appendix 5.10.5 for a more detailed review of previous absorption line studies towards the superbubble.

Model A is compatible with the proper motion study of Boumis et al. (2001), which places Arc A at a distance greater than 500 pc, while model T is not. Boumis et al. (2001), however, use the estimated radial expansion speed of the superbubble, 15 km s^{-1}, as the tangential velocity of Arc A. It is not entirely clear that the tangential velocity of Arc A should be equivalent to the radial expansion velocity, as this assumption essentially prescribes the angle between the space velocity of Arc A and the line of sight. In model T, the angle between the line of sight and the expansion velocity of Arc A is only 27°, thereby predicting that if the line of sight velocity is 15 km s^{-1}, the tangential velocity should only be 7 km s^{-1}. Such a lower tangential velocity is consistent with the limits Boumis et al. (2001) place on the proper motion of Arc A, even if Arc A were only 200 pc distant. For reference, in model A, the expansion velocity of Arc A is only 7° inclined to the line of sight. In models T and A, the angle between the expansion velocity of Arc B and the line of sight is 48° and 52°, respectively, such that Arc B may be the better candidate for detecting a proper motion. No such proper motion study has yet to be conducted for Arc B.

Since Arc A has a higher characteristic radial velocity than Arc B (Reynolds & Ogden, 1979), Arc A should be on the back side of the bubble and Arc B should be on the front side, as in model A, if the two Arcs are on different sides of the bubble. Towards the Eridanus half of the superbubble, two velocity components are detected in both Hα and H I (Menon, 1957; Reynolds & Ogden, 1979) and the measured velocity of Arc B is more consistent with the higher of the two velocity components detected towards the superbubble, indicating that Arc B should be on the far wall of the bubble, as in model T. See Appendix 5.10 for a more detailed description of past radial velocity measurements. Interpretation of these velocities, however, is confused by the presence of a strong velocity gradient across Arc B, as well as foreground material along the line of sight towards the northern half of Arc A

(e.g., Magnani et al. 1985). Figure 5.4 shows the integrated intensities of Hα emission coming from the Eridanus filaments, as observed by the Wisconsin H-Alpha Mapper (WHAM) (Haffner et al., 2003), plotted as contours over the centroid velocities of this Hα emission. The velocity gradient across Arc B is particularly prominent in Figure 5.4. Differences in expansion velocity across the bubble and varying angles between the line of sight and the expansion velocity of the bubble wall across the bubble will further complicate the velocity fields seen towards the bubble.

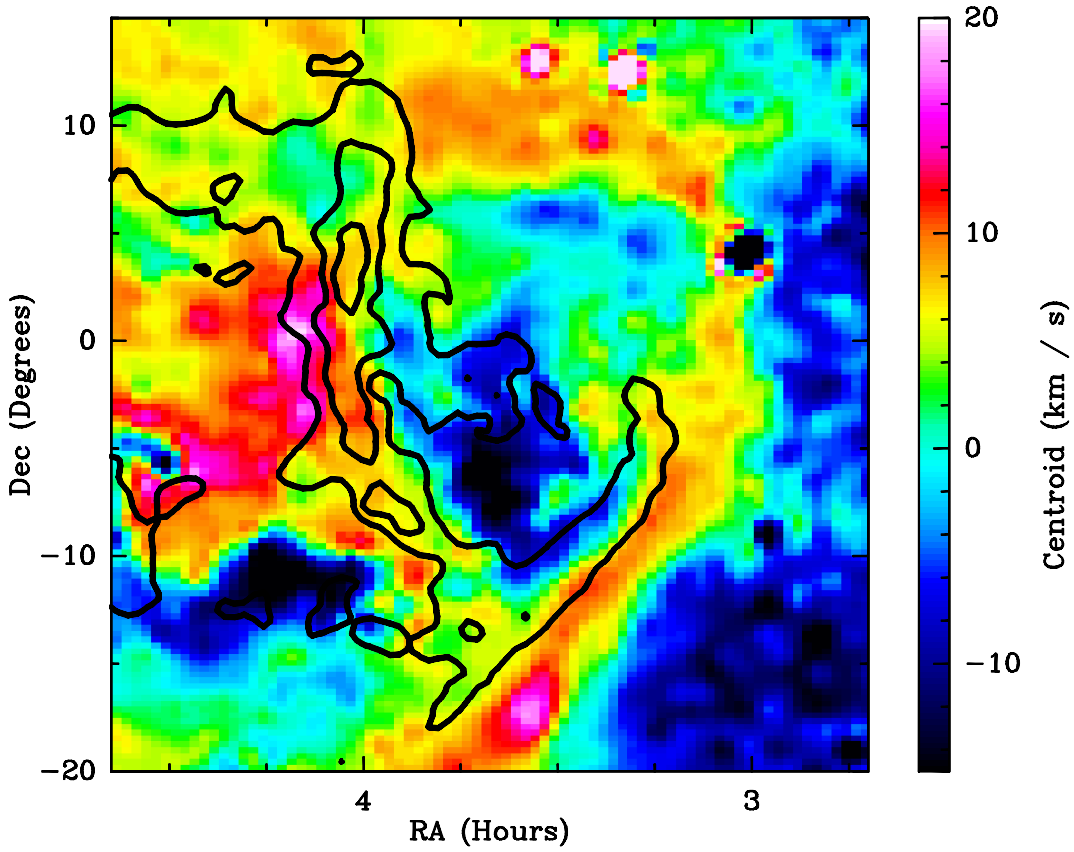

Figure 5.4: Centroid velocities, with respect to the local standard of rest, of Hα, from the WHAM survey, are shown in the color scale, while the contours show the integrated intensity of the Hα line. The contours are logarithmically spaced with each contour representing a factor of two increase in integrated intensity. The lowest contour corresponds to an integrated intensity of 10 Rayleighs. Only the Eridanus side of the bubble is shown and Arcs A and B appear as the two prominent filaments on the left and right sides of the figure, respectively.

The soft x-ray emission coming from the direction of the superbubble drops sig-

nificantly towards the location of Arc A (e.g., Snowden et al. 1995a). This decrease in x-ray intensity is usually ascribed to extinction from Arc A (e.g., Guo et al. 1995; Snowden et al. 1995a, 1997), which would require Arc A to be on the near side of the superbubble, as in model T, if the x-ray emission is coming from the interior of the bubble. Alternatively, it is possible that this extinction may be due to gas between the front of the superbubble and the Sun, such as the small molecular cloud MBM 18 (e.g., Magnani et al. 1985). As shown in Figure 5.5, both models T and A do a reasonable job of bounding the 0.75 keV soft x-ray enhancement associated with the Orion-Eridanus superbubble. Please see Appendices 5.10.4 and 5.10.6 for a review of past x-ray and CO measurements towards the superbubble.

Both models T and A require Galactic atmospheres with exponential scale heights much smaller than what is typically believed to exist in the Galaxy. These small scale-heights are motivated by the observed elongation of the Orion-Eridanus superbubble, because, in a Kompaneets model, a bubble remains roughly spherical until the bubble has expanded to a radial size of a few scale-heights (Basu et al., 1999). This elongation of the bubble is seen in both the Hα data and the x-ray data. Since the Eridanus filaments are approximately 200 pc distant from the Orion star forming region, any model of the Orion-Eridanus superbubble that has a scale-height of 150 pc produces a large, spherical bubble that does not reasonably fit the superbubble.

The small scale-heights of models T and A, if they are to be believed, require significant vertical compression of the gas in the vicinity of the Orion star forming region to have occurred. Some compression is expected for over-densities in the disk due to the extra gravitational force of the over-densities. The Parker instability (Parker, 1966) can also further decrease the scale-height of the interstellar medium. Alternatively, such a discrepancy in scale heights may suggest that neither model adequately describes the processes controlling the elongation of the superbubble. The W4 superbubble is another highly elongated superbubble and Basu et al. (1999) require a Kompaneets model with a scale-height of 25 pc to fit the elongation of the W4 superbubble. West et al. (2007), however, examine the HI gas in the vicinity of the superbubble and find that the scale-height of the gas is 140 $\pm$ 40 pc, indicating that for the W4 superbubble, some process not included in the Kompaneets model must control the elongation of the bubble.

The vertical Galactic scale-height is much smaller than the scale-height along the plane of the disk (e.g., Kalberla & Kerp 2009) and thus, superbubbles should preferentially blow out perpendicular to the Galactic plane. Figure 5.1 shows that

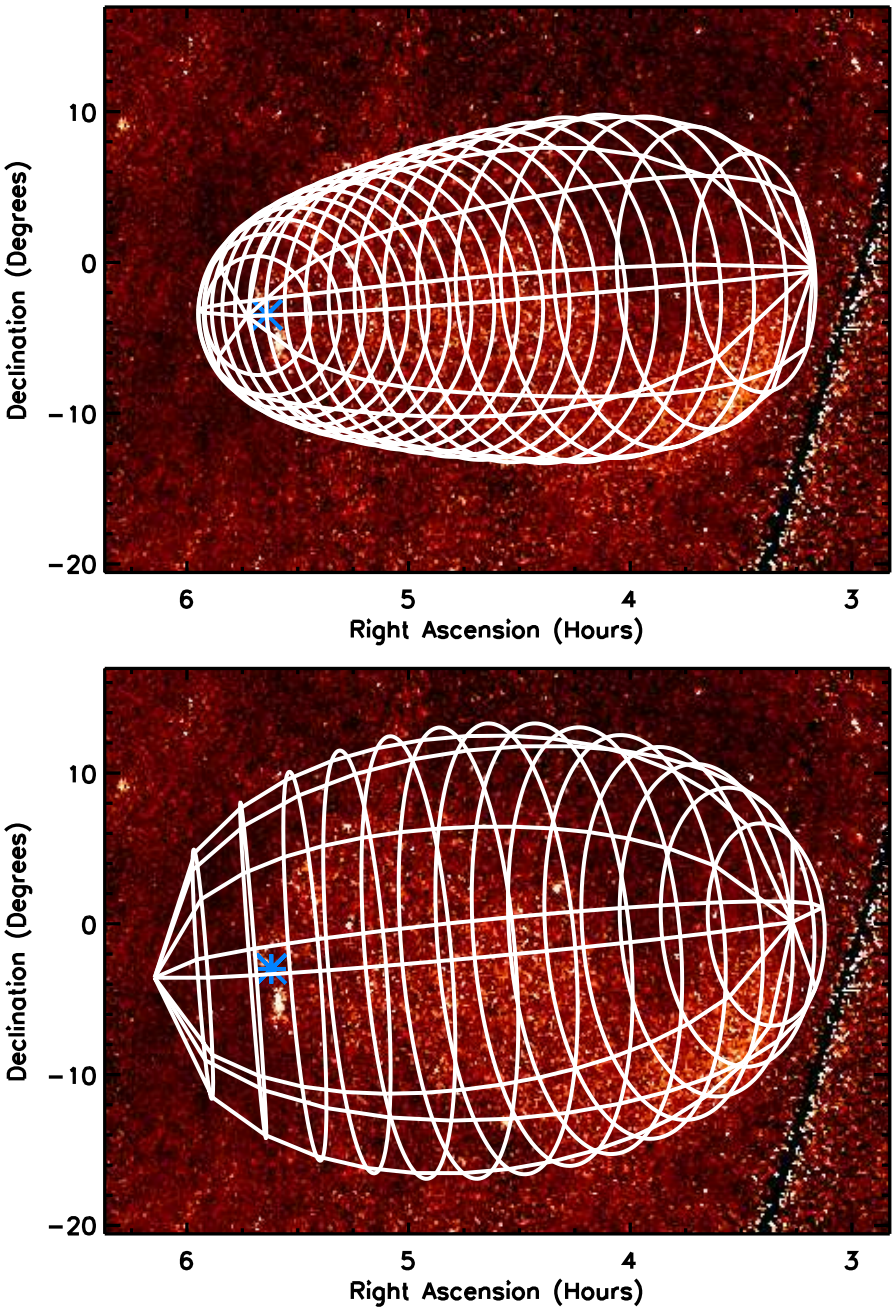

Figure 5.5: Diffuse, 0.75 keV, R45 band, x-ray emission observed by the ROSAT satellite (Snowden et al., 1997). The top panel overplots model T, the best fitting model oriented towards the Sun, while the bottom panel overplots model A, the best fitting model oriented away from the Sun. Both models do a reasonable job of bounding the soft x-ray emission.

the Orion-Eridanus superbubble is not expanding perpendicular to the Galactic plane, with the bubble major axis inclined by approximately 30° from the Galactic plane normal on the plane of the sky. Depending upon the inclination of the bubble out of the plane of the sky, the bubble's major axis can be significantly farther from alignment with the Galactic normal.

Model T has the superbubble inclined at an angle of 85° with respect to the normal of the Galactic plane and thus, the superbubble in this model is nearly parallel to the Galactic plane. Such an extreme inclination makes model T incompatible with the notion that the elongation of the superbubble is due solely to the natural gradient of the Galactic disk's density. Such an orientation parallel to the Galactic plane, however, is not completely unreasonable for a superbubble. Heiles (1979) identify 63 H I shells and supershells within the Galaxy and note that these shells are preferentially elongated parallel to the Galactic plane.

Model A has the superbubble aligned almost as close to perpendicular to the Galactic plane as possible, with an angle of only 35° between the superbubble's major axis and the Galactic normal. While model A is still not particularly well aligned with the Galactic normal, it is plausible that a 35° difference in orientation could be due to a secondary process occurring in conjunction with the exponential atmosphere of the Galactic disk leading to the elongation of the bubble.

Both models A and T are able to explain portions of the bubble's morphology but neither model satisfactorily explains all of the properties of the Orion-Eridanus superbubble. While we slightly prefer model A over model T, we do not believe either model adequately describes the Orion-Eridanus superbubble. This indicates that some physics not included in the Kompaneets model likely plays an important role in determining the morphology of the superbubble.

5.6.2 Ionization Front

If the elongation of the Orion-Eridanus superbubble is not due to an unusually small scale-height for the ambient Galactic gas and is, rather, due to some other physical affect not included in the Kompaneets model, then the Kompaneets model fits presented in Sections 5.4.1 and 5.4.2 would underestimate the scale-height of the ISM into which the bubble is expanding and therefore underpredict the column density of gas in the bubble wall on the Eridanus side. The ionization front fits of Section 5.5.7 would thus overestimate the ability of ionizing photons to penetrate the bubble wall.

Furthermore, any overdensities not accounted for by the exponential atmosphere, such as additional material in the giant molecular cloud out of which the Orion star forming region formed, would also increase the ability of gas along the edge of the bubble to trap the ionizing photons above that predicted in Section 5.5.7.

The Hα emission coming from the superbubble wall is from reprocessed ionizing photons absorbed by the wall and thus, the Hα emission is dependent upon the total rate at which ionizing photons deposit energy into the wall. Where the ionizing photons are completely contained within the bubble wall, the wall Hα brightness should decrease roughly with the square of the distance from the source. The brightness of the wall will decrease considerably more sharply at the point where the ionizing photons breakout of the bubble. For the Orion-Eridanus superbubble, if the ionization front breaks out at the edge of Barnard's Loop, as in the enhanced density and pressure ionization front model described in Section 5.5.7 for model T, this would provide an explanation for why the Hα intensity drops so sharply at the western edge of Barnard's Loop.

LDN 1551 lies to the north of the Orion-Eridanus superbubble, given the bubble boundary in both models T and A. Moriarty-Schieven et al. (2006) examine this small molecular cloud and find evidence that it has been partially photoevaporated by the Orion star forming region. Lee & Chen (2009) thus suggest that LDN 1551, as well as LDN 1558 and LDN 1563 for similar reasons, must be on the edge of the Orion-Eridanus superbubble for these clouds to be influenced by the ionizing radiation from the Orion star forming region. We instead suggest that these clouds lie outside the superbubble, based upon the confinement of the 0.75 keV x-ray emission, but are still irradiated by ionizing radiation from the Orion star forming region that is penetrating the bubble wall past the edge of Barnard's Loop. This breakout of the ionizing photons would also partially explain the extension of the H I cavity to higher declinations near a right ascension of 4^h 40^m, as seen in the Leiden/Argentine/Bonn (LAB) Galactic H I Survey (Hartmann & Burton, 1997; Arnal et al., 2000; Bajaja et al., 2005; Kalberla et al., 2005) (see also Appendix 5.10.3).

We also propose that the southern H I void extension seen between right ascensions of 3^h 30^m and 5^h, which is associated with EXE2 (see also Appendices 5.10.3 and 5.10.4), a 0.25 keV x-ray enhancement (Burrows et al., 1993; Snowden et al., 1995a; Hartmann & Burton, 1997; Arnal et al., 2000; Bajaja et al., 2005; Kalberla et al., 2005), may also be formed from ionizing photons penetrating the wall of the superbubble. The prominent H I filament seen at a declination of -13° and at nega-

tive velocities in the LAB data could be the near side half of the lower edge of the superbubble if the ionizing photons are only breaking out along the far side half of the lower edge of the bubble. Ionizing photons penetrating the superbubble wall would also explain the diffuse Hα emission coming from outside of the Hα features we have identified as being the bubble wall. More detailed modeling should, however, be done to test these speculations.

Barnard's Loop may also be slightly porous to ionizing photons as NGC 2149, GN 05.51.4, VDB64, and the Crossbones all show evidence of being affected by the superbubble, despite Barnard's Loop being between these small molecular clouds and the Orion star forming region (Lee & Chen, 2009). We note that soft, non-ionizing UV photons that penetrate the superbubble wall can also help shape clouds outside of the superbubble.

5.6.3 Alternatives

Both the elongation and orientation of the Orion-Eridanus superbubble are at odds with what would naively be expected for a bubble expanding in the exponential atmosphere of the Galactic disk. In this section, we address physical processes not included in the Kompaneets model that may strongly influence the evolution of the shape of a superbubble.

5.6.3.1 Magnetic Field

One potentially significant element missing from the Kompaneets model is magnetic fields. The local Galactic magnetic field is oriented towards a Galactic longitude of 85°, parallel to the Galactic plane (Rand & Lyne, 1994; Heiles, 1996). Assuming that the initial magnetic field direction in the vicinity of the Orion star forming region is similarly directed, given the close proximity of the Orion star forming region to the Sun, the magnetic field direction near the Orion-Eridanus superbubble is expected to have an inclination with respect to the plane of the sky of approximately 50°. Polarization and Zeeman splitting measurements near, but outside of the bubble, confirm that the magnetic field is parallel to the Galactic plane and inclined roughly 50° to the plane of the sky (Appenzeller, 1974; Heiles, 1997).

Inside of the bubble, the polarization directions of starlight are not compatible with magnetic fields oriented parallel to the Galactic plane (e.g., Appenzeller 1974). Appenzeller (1974) find a reasonably good fit to their polarization data from a mag-

netic pocket model, where the magnetic field lines towards the Orion half of the bubble are pulled into an orientation more perpendicular to the Galactic plane by a Parker instability (Parker, 1966). Heiles (1997) also find a reasonable fit with a paraboloid model, which treats the bubble as a worm/chimney structure and attributes the current magnetic field orientation to expansion motions from the bubble, rather than to a pre-existing magnetic pocket.

Models of bubbles expanding into atmospheres containing magnetic fields show that magnetic fields partially suppress expansion perpendicular to the magnetic fields (e.g., Tomisaka 1992, 1998; Stil et al. 2009). Stil et al. (2009) ran simulations of superbubbles expanding into stratified media with magnetic fields oriented parallel to the Galactic disk and show, however, that such bubbles still become elongated perpendicular to the Galactic plane due to the density stratification of the atmospheres. Thus, it is unlikely that the Galactic magnetic field would produce a bubble oriented parallel to the Galactic plane, as in model T. The major axis of the superbubble in model T also makes an angle of 45° with the local magnetic field, making it even more unlikely that the Galactic magnetic field would create the structure seen in model T.

The projection of the major axis of the superbubble in model A onto the Galactic plane, however, is reasonably well aligned with the magnetic field direction, with the projection being within 10° of the magnetic field direction. If a vertical component were added to the expected magnetic field configuration, the magnetic field would naturally channel the superbubble into an orientation similar to what is observed. Without this vertical component, the superbubble would only become elongated along the magnetic field line direction and would not tilt towards the Galactic plane, as observed.

Stil et al. (2009) also show that if the magnetic field in the Galactic plane is oriented towards the observer, Kompaneets models fit to a superbubble's shape underpredict the scale-height of the gas by factors of two to three because the magnetic fields create more elongated bubbles than would otherwise be expected. This could partially explain the low scale-heights derived from models T and A. While Stil et al. (2009) are unable to reproduce the factor of 4 to 10 reduction in scale-height required by the best fitting models of the W4 and Orion-Eridanus superbubbles, a magnetic field oriented perpendicular to the Galactic disk would further contribute to the elongation of a superbubble (Komljenovic et al. 1999; West et al. 2007; Bailey personal communication 2008). Such an orientation of the magnetic field could be created by a Parker instability (Parker, 1966; Appenzeller, 1974; Basu et al., 1997) or by prior

supernova (Heiles, 1997; West et al., 2007). The preferential expansion of the bubble along the line of sight would also help explain the large ratio between the apparent depth of the bubble, 300 pc if the near side is at 180 pc and the far side is more than 500 pc distant, and the north-south width of the bubble, roughly 150 pc.

Since the magnetic field direction is 50° inclined to the plane of the sky towards the superbubble, however, the effective shortening of the width of the superbubble will be significantly reduced compared to the best case models of Stil et al. (2009), in which the magnetic field is perfectly aligned with the line of sight. Thus, magnetic fields alone may not be capable of explaining the significant elongation of the Orion-Eridanus superbubble.

5.6.3.2 Turbulence and Shear

Shear from Galactic differential rotation can elongate a bubble over time and will eventually decrease the minor axis of a bubble ellipsoid at a given height (Tenorio-Tagle & Palous, 1987; Palous et al., 1990). The timescale over which Galactic shear is expected to be effective, however, is on the order of a hundred megayears (Heiles, 1979; Tomisaka, 1998), whereas the age of the oldest star forming group in the Orion star forming region is only 10 megayears (Brown et al., 1994). As such, Galactic shear is unlikely to play a significant role in determining the shape of the Orion-Eridanus superbubble. Similarly, the timescale for the Coriolis force to become effective, 50 Myr (Tomisaka, 1998), is too large for the Coriolis effect to be important. The Orion-Eridanus superbubble is also unlikely to be affected by a warp in the Galactic disk as the warp in the Milky Way only becomes prominent beyond a galactocentric radius of 9 kpc (Kalberla & Kerp, 2009).

Large scale simulations of the ISM show that turbulent flows and density inhomogeneities can generate reasonably elongated superbubbles (Korpi et al., 1999; de Avillez & Breitschwerdt, 2005), including bubbles that are elongated parallel to the Galactic plane (de Avillez & Breitschwerdt, 2005). Turbulent motions in the ISM will not only directly influence the shape of a growing superbubble by acting on the superbubble walls, but they will also indirectly influence the growth of a superbubble by altering the density profile of the gas into which the superbubble expands. We do not expect the Galactic disk to have a perfect exponential atmosphere and significant deviations from such an exponential atmosphere could channel an expanding superbubble towards a particular direction.

The Orion star forming region is on the edge of a spiral arm (Menon, 1957) and the density gradient associated with the arm-interarm transition could also enhance any elongation parallel to the plane.

5.6.3.3 Secondary Driving Source

There are at least four separate subgroups of stars in Orion that have formed over the last 10 Myrs (Brown et al., 1994). The winds and supernovae from the oldest subgroups will have altered the conditions in the interstellar medium into which the Orion-Eridanus superbubble has been blown. Previous generations of star formation may have created low density channels in the interstellar medium that could have led to the elongation of the Orion-Eridanus superbubble, although it is unclear whether such previous star formation activity could induce the level of elongation observed, especially considering that all of the subgroups are on the Orion side of the bubble.

The ISM into which the superbubble is expanding may also have been affected by a foreground OB subgroup. One potential source of such a subgroup is the IC 2118 cloud. IC 2118 is located 2° to the north west of Rigel and is roughly 200 pc from the Sun, placing the cloud approximately 200 pc in front of the Orion star forming region (Kun et al., 2001). IC 2118 contains on the order of 100 solar masses of molecular gas and is known to harbor tens of young stellar objects with masses up to a solar mass, which have ages on the order of a few megayears (Kun et al., 2001, 2004). Higher mass stars, and their subsequent supernova, may have been present in IC 2118 in the past.

There are three massive stars of note that are located between the Sun and the Orion-Eridanus superbubble. Betelgeuse is a 17 solar mass supergiant and its unusual proper motion has led to speculation that it is either a runaway star from IC 2118 or that it is a runaway from Orion OB1a and has undergone two velocity kicks, from either supernovae or multibody interactions (Harper et al., 2008; Bally, 2008). Rigel is a massive supergiant star that is 245 pc from the Sun and externally illuminating the IC 2118 cloud (Bally, 2008). Rigel has no significant radial velocity (Kharchenko et al., 2007) or proper motion (Høg et al., 2000) with respect to IC 2118, suggesting that it may have formed near its present location. Similarly, Saiph (κ Ori), another massive star, is located 220 pc from the Sun (Bally, 2008). As suggested by Bally (2008), the presence of three massive stars between the Sun and Orion further suggest that an OB subgoup, approximately 5 to 10 Myr, exists between the Sun and Orion.

The presence of massive stars between Orion and the Sun would have created an additional cavity in the ISM that, upon merging merging with the bubble created by the Orion star forming region, would have created a cavity elongated towards the Sun. Since IC 2118, Betelgeuse, Rigel, and Saiph are still on the Orion side of the superbubble, it is not clear, however, whether such a merger of bubbles could explain the elongation of the superbubble into the constellation of Eridanus or whether the limited star formation in IC 2118 could significantly impact the ISM on the scales necessary to significantly alter the morphology of the Orion-Eridanus superbubble.

5.6.3.4 Edge Identification

The apparent elongation of the superbubble could also be due to a misidentification of the location of the bubble wall. The Hα features fit in Section 5.3 may not trace the true exterior of the bubble. The H I and dust features lying outside of the Hα features may trace the true walls of the bubble. Such a larger bubble would have a lower elongation, and thus not require as small of a scale-height for the exponential atmosphere. These H I and dust features also appear to trace out a bubble that is closer to being perpendicular to the Galactic plane, at least on the plane of the sky, especially given the southern extension of H I filaments associated with EXE2. It is possible that some of the Hα emission could be coming from clouds within the bubble that were not fully swept into the wall of the bubble or could be coming from material injected into the bubble from the Orion star forming region. Such interior material would prevent the full ionizing flux from the Orion star forming region from reaching the true walls of the superbubble. Since the soft x-ray enhancement is relatively well confined by the Hα filaments, however, we consider it unlikely that the bubble walls extend significantly past the apparent Hα boundary of the superbubble.

5.7 Eridanus Filaments

5.7.1 General Properties

The existence of strong intensity enhancements in filamentary structures, the Eridanus filaments, merits a closer examination of the nature of Arc A and B, as Kompaneets models do not predict the formation of any filamentary features. As mentioned in Section 5.6.2, the Hα brightness of a shell of material, which fully traps the ionizing photons coming from an ionizing source and is in ionization equilibrium, should vary

with the square of the distance from the ionizing source, because the Hα emission is solely due to the reprocessing of the ionizing photons from the source. For the Eridanus filaments to be brighter in Hα then the parts of the shell closer to the Orion star forming region, the filaments must either trap a greater fraction of the ionizing photons or must be powered by a separate ionization source, assuming that the filaments are in ionization equilibrium. Given the lack of an obvious secondary energy source for the filaments, we focus on the former suggestion for now. It is, however, unclear where the extra mass required to trap significantly more ionizing photons would have come from, as both models A and T predict that there is relatively little mass towards the top of the superbubble out of which the filaments could be formed. For the Eridanus filaments to trap a greater fraction of the ionizing photons than nearby wall segments, the ionizing photons must fully break out of the bubble wall eastward of the Eridanus filaments, which is consistent with all of the ionization front models examined in Section 5.5.7.

The Eridanus filaments are part of the bubble wall and thus, should have the same temperature and pressure of the bubble wall as derived in Section 5.5. That is, they should have a temperature of 8000 K, as typical for an ionization front, and a density of 1 to 6 cm^{-3}, based upon the assumption that the bubble wall is in pressure equilibrium with the interior of the bubble. At a temperature of 8000 K, a Hα intensity of 1 Rayleigh corresponds to an emission measure of 2.25 pc cm^{-6} (Haffner et al., 2003), and the emission measure, EM, is related to the depth, R, and density, ρ, of the ionized material via

$$EM = \int \rho^2 dR. \tag{5.4}$$

Since the typical observed intensity of the filaments is 15 to 25 Rayleighs in the WHAM data (Haffner et al., 2003), the depth of the ionized material in these filaments must be on the order of 1 to 50 pc, given a filament density of 1 to 6 cm^{-3}. The filaments thus have typical column densities of ionized material on the order of 0.2 to 1.7×10^{20} cm^{-2}, which corresponds to visual extinctions between 0.01 and 0.1. These column densities are consistent with the column density of a few times 10^{20} derived towards the southern half of Arc A (Heiles, 1989; Burrows et al., 1993; Guo et al., 1995; Snowden et al., 1995a).

Both Arcs A and B have widths of approximately 1.5°. If the Arcs are 180 pc distant, they would have physical widths of 5 pc, while if they are 500 pc distant,

their widths would be closer to 13 pc. These widths lie within the estimated range of the depths of the Arcs, such that the observations are consistent with the Arcs being filamentary structures. Due to the large range of acceptable depths, however, the Arcs could be edge on sheets with aspect ratios as large as 10. We believe that it is much more likely that the Arcs are filamentary structures, rather than nearly perfectly edge on sheets. By requiring that the Arcs have depths similar to their observed widths, we thus select a preferred density range of 1.5 to 3 cm^{-3} for the Arcs, based upon the observed emission measures.

Since Arc A is roughly 25° long and Arc B is 15° long, the total mass of ionized gas in the filaments would be approximately 3×10^2 solar masses, if the filaments are 180 pc distant, or 3×10^3 solar masses, if the filaments are 500 pc distant.

The peak intensity of Arc A, 70 Rayleighs, requires an unrealistically large depth of 160 pc for a density of 1 cm^{-3}, but only requires a depth of 4 pc for a density of 6 cm^{-3}. At this higher density, the peak intensity would correspond to a column density of 4.9×10^{20} cm^{-2}, which is still smaller than the column density of 1.9×10^{21} cm^{-2} derived towards the northern half of Arc A (Heiles et al., 2000). The higher column density estimated by Heiles et al. (2000) could be due to neutral hydrogen also being present in Arc A, as would be expected if the ionizing photons from the Orion star forming region are fully trapped within Arc A. The much larger peak intensity of Barnard's Loop, 250 Rayleighs, is also likely due to a further increase in the density of the Loop, rather than being due to a very large line of sight depth.

Towards the center of the bubble, the Hα intensity is approximately 5 Rayleighs, which, for a density of 3 cm^{-3}, corresponds to a depth of approximately 1 pc and for a density of 1.5 cm^{-3}, corresponds to a depth of 4 pc. Such a depth would yield a column density on the order of 10^{19} cm^{-2} for the superbubble wall. In model T, the wall thickness near the location of Arc A is less than 0.001 pc and in model A, the bubble wall thickness can only be at most 0.7 pc, depending upon the adopted value of the initial density at the location of the driving source. It is somewhat unsurprising that the observationally derived wall thicknesses are larger than those predicted by the Kompaneets model fits, since, as mentioned in Section 5.6.2, the Kompaneets models may have underpredicted the scale-height of the gas, and thus, underpredicted the surface density and thickness of the bubble wall.

5.7.2 Ionization Depth

The depth to which ionizing photons can ionize material, d, is given by

$$d = \left(\frac{\Phi_*}{4\pi\, n^2\, \alpha_b\, s^2} \right), \tag{5.5}$$

where Φ_* is the total ionizing luminosity of the source, n is the density of the gas, α_b is the recombination coefficient for hydrogen, and s is the distance to the ionizing source. Note that equation 5.3 can be derived from 5.5 by taking into account the incidence angle of the photons on the bubble wall, ϕ, and by using the ideal gas equation of state. In both models T and A, Arcs A and B are approximately 220 pc distant from the ionizing source. For an ionizing luminosity of 4×10^{49} s^{-1} and a density of 1.5 cm^{-3}, corresponding to a filament diameter of 13 pc, the ionizing photons can be absorbed within 3 pc at the distance of the Arcs. For a density of 3 cm^{-3}, corresponding to a filament diameter of 5 pc, the ionizing photons are absorbed within 1 pc at the distance of the Arcs. For both of these cases, the depth to which the Orion star forming region can ionize the Eridanus filaments is less than the observed width of the ionized material in the filaments. Note that since we find that the filaments are roughly cylindrical, the line of sight depth of the filaments from the Orion star forming region must be comparable to the width of the filament derived from the size of the filament on the plane of the sky.

The depth to which ionizing photons penetrate can be increased by decreasing the density of the filaments, but such a change will also increase the required depth of the filaments to yield the observed Hα intensity. Such a fix would require the filaments to be relatively edge on sheets, which we consider to be rather unlikely. Similarly, if the filaments don't have smooth surfaces, but are instead porous, then the apparent width of the filaments could overestimate the true depth to which ionizing photons are penetrating, as the filaments would be a composite of overlapping gas segments. Such a scenario, however, would reduce the volume filling factor of the filaments, such that the depth of the filaments would again have to be increased significantly.

Alternatively, the flux of ionizing photons reaching the Eridanus filaments may be higher than expected, either due to the Orion star forming region having a larger ionizing luminosity than previously estimated or because of a secondary ionization source, such as shocks, a recent UV flash, or the hot plasma filling the bubble (Boumis et al., 2001). An ionizing luminosity of approximately 2×10^{50} s^{-1} is required for the Orion

star forming region to ionize 5 to 13 pc of material in the Eridanus filaments. This is five times larger in comparison to the ionizing luminosity of 4×10^{49} s^{-1} estimated by Reynolds & Ogden (1979). O'Dell et al. (2011) also independently determined the ionizing luminosity of the Orion star forming region to be 1.9×10^{49} s^{-1}, based upon the O-star models of Heap et al. (2006) and the spectral classifications of stars in the Orion star forming region by Goudis (1982), and 2.5×10^{49} s^{-1} based upon the Hβ brightness of Barnard's Loop. It seems unlikely that the ionizing luminosity of Orion has been consistently underestimated by an order of magnitude.

Strong shocks are also capable of ionizing hydrogen, but Reynolds & Ogden (1979) show that a 20 to 30 km s^{-1} shock, on the order of the observed radial expansion speed of the bubble, would not produce enough Hα emission to explain the brightness of the Eridanus filaments.

The discrepancy between the observed thickness of the Eridanus filaments and the depth to which ionizing photons from Orion can ionize material can be resolved if the Eridanus filaments are not equilibrium objects. Since the recombination rate of hydrogen is dependent upon the square of the density of the gas, a greater column of gas can be ionized by the same ionizing flux if the gas is at a lower density. If the Eridanus filaments were formed via the compression of a pre-existing gas cloud, the column of ionized gas within the final compressed filament would be larger than the column that could be currently ionized. Since strong shocks can produce up to a factor of four of an increase in density, they can decrease the depth to which ionizing photons can penetrate by a factor of 16 and thus, the compression of a pre-existing, ionized gas cloud by a strong shock could produce a structure with the observed thickness and brightness of the Eridanus filaments.

For a hydrogen recombination coefficient of 2.6×10^{-13} cm^3 s^{-1}, the recombination time is approximately 1.2 Myr $(n/cm^{-3})^{-1}$, such that for a density on the order of a few cm^{-3}, the recombination time is just slightly less than 10^6 years. While this timescale is shorter than the age of the superbubble, it is not unrealistically small for the Eridanus filaments to still be in a non-equilibrium phase. In models T and A, the Arcs are roughly 50 and 90 pc distant from the end cap of the superbubble, respectively, and if the end cap of the bubble were travelling at the internal sound speed of the bubble, the end cap would have traversed this distance in 2 to 4×10^5 years. This is on the order of the recombination timescale, such that the Arcs may have formed when the bubble cap swept through the current location of the Arcs. The time since the bubble end cap was at the location of Arc B would be even smaller

if the two Arcs were not equidistant from the driving source and Arc B was located closer to the end cap.

The derived wall thickness, one to four pc, is very similar to the depth to which ionizing photons can penetrate the wall, three to five pc, and thus, the wall brightness can be explained by a model in which the walls are in ionization equilibrium. Alternatively, if the bubble wall only has a column density of 3×10^{18} cm^{-2}, as suggested by Burrows et al. (1993), much of this Hα emission may be coming from gas outside of the bubble that has been ionized by the photons passing through the bubble wall, rather than coming from the bubble wall itself. O'Dell et al. (2011) also show that Barnard's Loop is consistent with being ionized by the bright stars of the Orion star forming region.

It should be noted that the presence of additional material within the superbubble, such as material photo-ablated from the Orion GMCs, would absorb additional UV photons and cause the UV radiation field to decrease faster than predicted from geometric effects alone. In particular, dust photo-ablated from the Orion GMCs would be particularly effective at absorbing UV photons. Such material within the bubble would not emit significant Hα flux, as the amount of Hα intensity emitted per unit column density is much lower at 10^6 Kelvin, as in the interior of the bubble, then it is at 10^4 Kelvin, as in the bubble wall. Material within the bubble would reduce the UV flux reaching the Eridanus filaments, making it even more difficult to explain the Eridanus filaments as being in ionization equilibrium with the Orion star forming region.

5.7.3 Origin

The origin of the significant column density enhancement in the Eridanus filaments is an open question. The Eridanus filaments may have formed when the superbubble impacted a pre-existing gas cloud and swept up the gas into a dense ring around the outside of the bubble, as suggested above. The original gas cloud that was compressed could have been related to previous star formation events that occurred in one of the older Orion subgroups and the formation mechanism of the Eridanus filaments may bear some similarities to the formation of bipolar rings in planetary nebula and supernova remnants, as such rings are believed to form when a fast outflow impacts a previously ejected shell of material (Soker, 2002).

An alternative possibility is that the breaking out of the ionization front at an

earlier time may have resulted in a pressure discontinuity that funneled material into a ring at the height of the filaments, although it is unlikely that such a mechanism could operate on the appropriate timescale and it is unclear if there would be enough material in the upper part of the bubble to even account for the significant column density increase in the Arcs.

5.8 CONCLUSIONS

The Orion star forming region is the closest high-mass star forming region and is blowing a large, 20° by 45°, superbubble into the ISM. We fit Kompaneets models, models of bubbles driven by continuous energy sources expanding into exponential atmospheres, to the Orion-Eridanus superbubble. We find marginal fits for the cases where the superbubble is directed towards and away from the Sun and we derive the location of the ionization front for reasonable parameter ranges.

The advantages(+) and disadvantages(-) of the best fitting model oriented towards the Sun (model T) are that:

+ The model accurately traces both Barnard's Loop and the Eridanus filaments and the driving source in the model is consistent with the location of the Orion B molecular cloud.

+ The near side of the model is approximately 180 pc away, consistent with the detection of a wall of gas with negative velocities at this distance (e.g., Welsh et al. 2005).

+ Arc A is on the near side of the bubble and thus, could produce the absorption features seen in diffuse x-ray emission (e.g., Snowden et al. 1995a), while Arc B is on the far side of the bubble, which is expected since the typical velocity associated with Arc B is similar to that of the larger of two velocity components detected towards the Eridanus half of the bubble (Reynolds & Ogden, 1979).

- The scale-height required to fit the elongation of the bubble, 15 pc, is much smaller than the generally accepted scale-height for the Galactic disk, 100 to 150 pc (Kalberla & Kerp, 2009).

- The bubble is elongated almost parallel to the Galactic plane, which is perpendicular to the expected density gradient in the disk.

- The model places Arc A on the near side of the bubble and Arc B on the backside, such that Arc A should have a more negative velocity than Arc B, whereas observations reveal that Arc A has a more positive velocity (Haffner et al., 2003).

- The far side of the bubble in the model is less than 300 pc distant, whereas absorption studies have not detected the far side within 500 pc (e.g., Welsh et al. 2005).

- Arc A is 200 pc distant, which is inconsistent with the upper limits for the proper motion of Arc A derived by Boumis et al. (2001).

- The bubble orientation is not well aligned with the local magnetic field.

The advantages and disadvantages of the best fitting model oriented away from the Sun (model A) are that:

+ The model accurately traces the Eridanus filaments.

+ The far side of the model, as well as Arc A, are over 500 pc distant, consistent with non-detections in absorption and proper motion studies (e.g., Boumis et al. 2001; Welsh et al. 2005).

+ Arc B is located closer to the Sun than Arc A, as suggested from radial velocities (Haffner et al., 2003).

+ The major axis of the bubble is more closely aligned with the normal to the Galactic plane, with the major axis being 35° offset from the normal.

+ The projection of the bubble onto the Galactic plane is in the direction of the local magnetic field.

- The scale-height of the model, 40 pc, is smaller than expected.

- The model does not reproduce the shape of Barnard's Loop.

- The near side of the bubble is over 300 pc distant and thus, this model cannot explain the absorption features detected at a distance of 180 pc (e.g., Welsh et al. 2005).

- Arc B is on the near side of the bubble, opposite of what is suggested from radial velocities (Haffner et al., 2003), and Arc A is on the far side of the bubble, such that it cannot be the cause of absorption features seen in diffuse x-ray surveys (e.g., Snowden et al. 1995a).

In general, we find that to fit the elongation Orion-Eridanus superbubble, a Kompaneets model requires a small scale-height of 15 to 40 pc, which is lower than the typical 100 to 150 pc scale-height derived for the Galactic disk (Kalberla & Kerp, 2009). This low value, however, is consistent with the scale-height of 25 pc found by Basu et al. (1999), via similar Kompaneets fitting of the W4 superbubble.

While we slightly prefer model A over model T, we find that neither model does an adequate job in fitting the Orion-Eridanus superbubble. As such, we find that the morphology of the Orion-Eridanus superbubble cannot be solely due to the typical density gradient in the Galactic disk and a second physical process not included in the Kompaneets model must play an important role in shaping the morphology of the superbubble. Models of superbubbles expanding in magnetized media show that magnetic fields can suppress the expansion of a superbubble perpendicular to the field direction and can lead to an underestimation of the scale-height of the ambient gas (Stil et al., 2009). Turbulent flows in the interstellar medium (e.g., de Avillez & Breitschwerdt 2005) and secondary driving sources may also be capable of explaining the unusual elongation and orientation of the Orion-Eridanus superbubble. The Hα emission from the superbubble may also not be accurately tracing the superbubble walls.

We propose that the ionizing photons from the Orion-Eridanus superbubble are fully trapped within Barnard's Loop but breakout of the superbubble at the western edges of the loop. Such a breakout would explain the sudden drop off of Hα emission at the edge of the loop. We show that this location of the ionization front breaking out is possible given plausible values for the interior pressure of the bubble, the initial density of the ambient medium, and the ionizing luminosity of the Orion star forming region. We also note that such a breakout of ionizing photons would explain the apparent partial photoevaporation of LDN 1551, LDN 1558, and LDN 1563 to the north of the superbubble (Moriarty-Schieven et al., 2006; Lee & Chen, 2009), without requiring the edge of the superbubble to extend up to these clouds. We also suggest that the penetration of ionizing photons through the bubble wall to the west of Barnard's Loop may also be partially responsible for the creation of an H I void to the south of the bubble, located between right ascensions of 3^h 30^m and 5^h (Hartmann

& Burton, 1997; Arnal et al., 2000; Bajaja et al., 2005; Kalberla et al., 2005), which is also coincident with an enhancement in 0.25 keV x-rays (e.g., Burrows et al. 1993).

We find that the observed Hα widths and intensities of Arcs A and B are too large for the Arcs to be equilibrium structures ionized by the Orion star forming region. We find that the arcs have ionized columns of approximately 10^{20} cm^{-2}. An ionizing luminosity of approximately 2×10^{50} s^{-1} would be required to keep the full widths of the Arcs ionized, whereas the Orion star forming region only has an ionizing luminosity of 4×10^{49} s^{-1} (Reynolds & Ogden, 1979). We suggest that the Arcs may have formed in the last 10^5 years from the compression of a pre-existing gas cloud such that they are not in ionization equilibrium.

5.9 ACKNOWLEDGEMENTS

We would like to heartily thank Dr. Basu for providing some of his code to calculate the surface densities of Kompaneets bubbles, as well as for general advice on dealing with superbubbles. AP was partially supported by the Natural Sciences and Engineering Research Council of Canada graduate scholarship program. DJ acknowledges support from an NSERC Discovery Grant. This research has made use of NASA's Astrophysics Data System. The Wisconsin H-Alpha Mapper is funded by the National Science Foundation. This research has made use of the SIMBAD database, operated at CDS, Strasbourg, France

5.10 Appendix A: OBSERVATIONAL OVERVIEW

5.10.1 Orion Star Forming Region

The Orion star forming region is the nearest OB star forming region to the Sun currently forming massive stars and is located 400 pc away in the constellation of Orion (Hirota et al., 2007; Sandstrom et al., 2007; Menten et al., 2007). The Orion star forming region is approximately 130 pc below the Galactic plane and is centered around a Galactic longitude and latitude of 210° and −20°, respectively (Bally, 2008). There are at least four subgroups of young stars located in Orion, with the oldest, Orion OB1a, being approximately 10 Myr old and the youngest, Orion OB1d, still in the process of forming stars (Brown et al., 1994). Current star formation in Orion is primarily localized within two molecular clouds, the Orion A molecular cloud in the

south and the Orion B molecular cloud in the north (Bally, 2008). There is a velocity gradient along these molecular clouds with the centroid velocity, with respect to the local standard of rest, going from 11 km s^{-1} at the north end of Orion B to 2 km s $^{-1}$ at the south end of Orion A (Bally, 2008). Figure 5.1, from Di Cicco & Walker (2009), shows the structure of the Orion-Eridanus superbubble in Hα and Orion A and B are labeled on this figure.

There are 7 stellar systems within Orion that contain O type stars, with all but λ Ori being located within Barnard's Loop, and none of these systems are surrounded by sharply bounded HII regions, suggesting that most of this flux escapes to relatively large distances (Humphreys, 1978; Reynolds & Ogden, 1979). The luminosity of ionizing photons from the Orion star forming region is roughly 2 to 4×10^{49} s^{-1} (Reynolds & Ogden, 1979; O'Dell et al., 2011). A typically used value for the average rate of mechanical energy deposited into the ISM by an OB association is 10^{38} ergs s^{-1} (e.g., Heiles 1987; Mac Low & McCray 1988; Shull & Saken 1995; Bally 2001), although the Orion star forming region is believed to have an average mechanical energy input rate of only approximately 2×10^{37} ergs s^{-1} (Reynolds & Ogden, 1979; Brown et al., 1994). The total energy output over the lifetime of the Orion star forming region so far, including supernovae and winds, is approximately 10^{52} ergs (Brown et al., 1994). Weaver et al. (1977) estimate that roughly 20% of an OB association's energy will go into the kinetic energy of a driven bubble, thereby suggesting that the Orion-Eridanus superbubble should have a total kinetic energy on the order of 2×10^{51} ergs. For a more complete review of the Orion star forming region, see Bally (2008).

5.10.2 Hα

The east side of the superbubble is dominated by a bright crescent of Hα emission that was first discovered in optical photographs by Pickering (1890) and Barnard (1894), which is now referred to as Barnard's Loop. Barnard's Loop, see Figure 5.1, is centered around the Orion star forming region, spans roughly 10° east to west, and spans 15° north to south. The width of Barnard's Loop is roughly 2°.

The west side of the superbubble is composed of a hook shaped Hα feature, in the constellation of Eridanus, that was first discovered on Hα images and Palomar Observatory Sky Survey (POSS) plates by Meaburn (1965, 1967). Johnson (1978) broke this hook into three separate arcs, all of which are labeled on Figure 5.1. Arc A is the eastern half of the hook and arcs from a right ascension (RA) and declination

of (4^h 00^m, 10°) to (3^h 45^m, -10°). The western half of the hook is denoted as Arc B and spans from roughly (3^h 15^m, 0°) to (3^h 45^m, -10°). Arc C is the southern extension of the hook, extending from the intersection of Arcs A and B to (4^h 00^m, -20°). The three Arcs all have widths of approximately 1.5°. The region between Barnard's Loop and the Eridanus filaments also displays a significantly enhanced Hα flux (e.g., Reynolds et al. 1974). For the remainder of this paper, when we refer to Arcs A, B, and C, we will be specifically referring to the Hα emitting regions.

The superbubble's major axis makes an angle of approximately 30° with the Galactic plane. The Galactic plane is clearly visible as a line of increased nebulosity and is labeled on Figure 5.1. The dimensions of the superbubble are approximately 20° by 45°.

There have been numerous Hα surveys of the superbubble (e.g., Pickering 1890; Barnard 1894; Elliott & Meaburn 1970; Elliott 1973; Isobe 1973; Sivan 1974; Reynolds et al. 1974; Johnson 1978; Reynolds & Ogden 1979; Boumis et al. 2001) and one of the more recent large scale maps of the region was made by the Wisconsin H-Alpha Mapper (WHAM) team (Haffner et al., 2003). All further Hα data, unless otherwise stated, will be taken from the WHAM dataset.

Within Barnard's Loop, the Hα intensity reaches a peak value of almost 250 Rayleighs and is typically on the order of 100 Rayleighs. The Hα intensity drops fairly rapidly to the west of Barnard's Loop to 20 Rayleighs and then continues to drop until the intensity becomes approximately 5 Rayleighs in the center of the superbubble, around a right ascension and declination of (4^h 40^m, -2°). Arc A is the brightest of the Eridanus filaments, with a peak intensity of 70 Rayleighs and a typical intensity closer to 25 Rayleighs. Arcs B and C have slightly lower typical intensities of 15 and 10 Rayleighs, respectively. Heiles et al. (2000) estimate the reddening towards one location in Arc A, based upon the relative observed intensities of Hα, [N II], and 2325 MHz radio continuum emission, and suggest that the unabsorbed Hα intensity towards the Arcs may be as much as a factor of 3.7 higher than observed. To the west of Arc B, the Hα intensity drops to 1 Rayleigh.

Reynolds & Ogden (1979) present Hα and [N II] spectra at targeted locations across the superbubble and find that many of the locations within the bubble show line splitting. In the Reynolds & Ogden (1979) data, the two line components have velocities, relative to the local standard of rest, of 3 and -25 km s^{-1}, suggesting an expansion velocity on the order of 15 to 20 km s^{-1} (Reynolds & Ogden, 1979).

Figure 5.4 shows the velocity centroids across the Eridanus filaments using the

WHAM Hα data. The velocity centroids towards Arc A are at slightly more positive velocities than Arc B, although there is a fairly prominent velocity gradient across the two Arcs, with the gas along the outside edge of the Arcs having centroid velocities more than 10 km s^{-1} larger than the inner edge of the Arcs. Arc B is more clearly defined in Figure 5.4, possibly due to the presence of foreground material in the direction of Arc A (see Appendix 5.10.11). Reynolds & Ogden (1979) suggest a characteristic velocity of 11 km s^{-1} for Arc A and 3 km s^{-1} for Arc B. The centroid velocity of gas in Barnard's Loop varies from -5 km s^{-1} to 7 km s^{-1}.

5.10.3 H I

Large scale maps of 21 cm emission from neutral hydrogen reveal a large H I cavity in the vicinity of the superbubble (Menon, 1957; Heiles & Habing, 1974; Heiles, 1976; Green, 1991; Burrows et al., 1993; Brown et al., 1995; Kalberla et al., 2005). The cavity extends between declinations of -15° and 10° and from a right ascension of 3^h to 5^h 30^m. The cavity extends weakly to a declination of almost 20° near a right ascension of 4^h 40^m and to a declination of -25° between right ascensions of 3^h 30^m and 5^h. These additional extensions make the H I cavity appear to be elongated perpendicular to the Hα cavity. Gas associated with the bubble wall can be seen from -30 to +30 km s^{-1}. Figure 5.6 shows the integrated intensity of 21 cm emission, for -10 km s^{-1} $\leq v_{lsr} \leq$ 20 km s^{-1}, from the Leiden/Argentine/Bonn (LAB) Galactic H I Survey (Hartmann & Burton, 1997; Arnal et al., 2000; Bajaja et al., 2005; Kalberla et al., 2005), with the WHAM Hα integrated intensities overplotted as contours.

The H I lines in the region of the superbubble show complex line structure and are often double peaked. Menon (1957) identify one component at a v_{LSR} of 12 km s^{-1} and another at -5 km s^{-1}. Heiles (1976) detect an elliptical ring towards the superbubble, between velocities of 21 km s^{-1} and -10 km s^{-1}, which is largest at 5 km s^{-1} and decreases in size towards larger and smaller velocities. They interpret this ring as being evidence of an H I void with a 30 km s^{-1} extent. This velocity extent is consistent with an expansion velocity of the superbubble of 15 km s^{-1} (see Appendix 5.10.2). Due to the confusion of the region, it is not, however, clear whether all of these rings are part of one coherent object or if the various arcs are clouds at different distances along the line of sight.

As shown in Figure 5.6, there are numerous H I features which correlate well with integrated Hα emission features. In the LAB data, filamentary H I emission near Arc

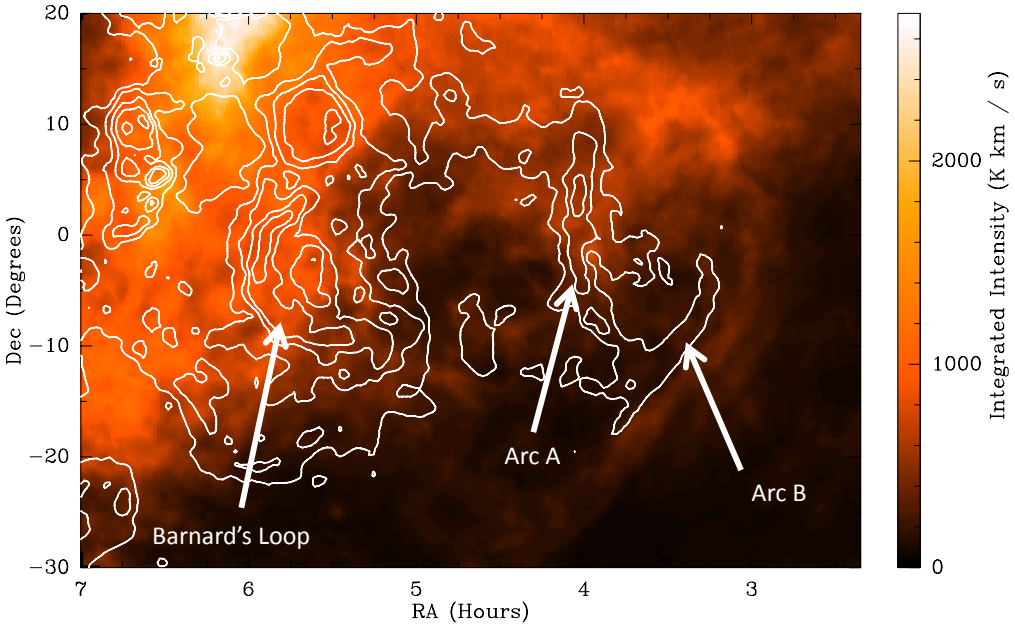

Figure 5.6: H I integrated intensities between -10 km s^{-1} $\leq v_{lsr} \leq$ 20 km s^{-1} from the LAB Galactic H I Survey are shown in the color scale. The contours are integrated intensities of Hα from the WHAM survey and are logarithmically spaced with each contour corresponding to a factor of two increase in intensity, as in Figure 5.4. The lowest contour corresponds to an integrated intensity of 10 Rayleighs. The locations of Arc A, Arc B, and Barnard's Loop are labeled.

A can be seen at velocities from 20 km s^{-1} down to approximately -2 km s^{-1}. At velocities between 0 and 10 km s^{-1}, the H I is slightly offset to the west of Arc A, while between 10 and 20 km s^{-1}, the H I is essentially coincident with Arc A. This is in contrast to Reynolds & Ogden (1979) who, using the 18 km $s^{-1} < v_{lsr} <$ 21 km s^{-1} data of Heiles (1976), place the H I filament slightly to the east of Arc A.

There is a long H I filament just to the west of Arc B that traces the entire length of the Arc. This H I filament does not stop at the bottom of Arc B, but rather, continues to run along the western edge of Arc C down to a declination of -30°. This filament is centered around 9 km s^{-1} (Verschuur, 1973). This filament traces the southern extension of the main H I cavity that extends down to a declination of almost -30° between right ascensions of 3^h45^m and 5^h0^m. Faraday rotation measurements indicate that a partially ionized region, with a line of sight magnetic field of order 10 μGauss, lies between the H I filament and Arcs B and C. This spatial morphology is consistent with the Hα coming from the ionized interior edge of a shell and the H I coming from the neutral exterior of the shell that is shielded from the ionizing photons of the Orion star forming region by the inner regions of the shell. There also exists a second, fainter H I filament further to the west, which is centered closer to 5 km s^{-1} (Verschuur, 1973).

While two velocity components are detected in both Hα and H I surveys towards the superbubble (e.g., Reynolds & Ogden 1979; Kalberla et al. 2005), ostensibly tracing the near and far sides of the superbubble, the velocities derived for these two sides are not in agreement between the different tracers. The H I velocities for the two components are both higher, by 9 and 20 km s^{-1}, than the Hα velocities. Similarly, the H I gas detected closest to Arcs A and B have velocities that are 9 and 6 km s^{-1}, respectively, higher than the Hα velocities of Arcs A and B. H I gas with similar velocities to the Arcs is only detected westward of both Arcs. It is unclear why there is such a difference between the velocities of the gas being traced by H I and Hα towards the superbubble.

In both H I and Hα studies, the gas near Arc B has a velocity similar to the larger of the two velocity components detected and thus, this suggests that Arc B should be associated with the far wall of the superbubble. Figure 5.4, however, reveals a fairly strong velocity gradient across Arc B, such that it is not entirely clear which velocity should be associated with Arc B.

There is a prominent H I filament running along a declination of approximately -13°, between right ascensions of 4^h and 5^h, at a velocity near -10 km s^{-1}. This filament

is shown in Figure 5.7, which shows the integrated LAB H I intensity between -12 and -6 km s^{-1}. This H I filament lies just to the south of a faint Hα enhancement that traces the southern extent of the Hα shell.

While Arcs A and B are not connected at their northern ends, the H I filaments tracing these two Arcs appear to connect at their northern ends. This region is, however, relatively confused, because there is significant emission extending down from the Galactic plane to a Galactic latitude of approximately -40° along the north edge of the superbubble. In the northwest corner of the loop formed by Arcs A and B, where there is little Hα emission, there also lies the end of an 80° long H I filament that has a characteristic velocity relative to the local standard of rest of -8 km s^{-1}, the western half of which was dubbed the Pisces Ridge (Fejes & Wesselius, 1973). The end of this ridge can be seen in Figure 5.7.

Considerable H I emission is also detected near the Orion star forming region and Barnard's Loop.

5.10.4 X-Ray

Rocket and satellite based x-ray surveys show that there is a diffuse enhancement of soft, 0.25 and 0.75 keV, x-rays towards the Orion-Eridanus superbubble (Davidsen et al., 1972; Williamson et al., 1974; Naranan et al., 1976; Long et al., 1977; Fried et al., 1980; Nousek et al., 1982; Singh et al., 1982; McCammon et al., 1983; Marshall & Clark, 1984; Garmire et al., 1992; Burrows et al., 1993; Guo et al., 1995; Snowden et al., 1995a, 1997). Figure 5.8 shows the 0.25 keV and 0.75 keV bands of the Rosat mission, which are the R12 and R45 bands, respectively, of Snowden et al. (1997). The enhanced 0.75 keV x-ray emission extends from the Orion star forming region to Arc B and does not significantly extend above or below the Hα declination limits of the superbubble. This 0.75 keV x-ray emission drops sharply across Arc B and is reasonably well anticorrelated with Hα and H I emission (Brown et al., 1995; Snowden et al., 1995a). There is also a significant decrease in 0.75 keV x-ray emission towards Arc A and to the right of the top of Arc A, where the end of the Pisces Ridge is seen in H I. The 0.25 keV emission also decreases towards the location of Arc A and drops sharply across the location of Arc B.

The most prominent difference between the 0.25 keV and 0.75 keV maps is that there is 0.25 keV emission extending below the Hα southern boundary, while the 0.75 keV emission is fairly well contained within the Hα boundaries. The 0.25 keV

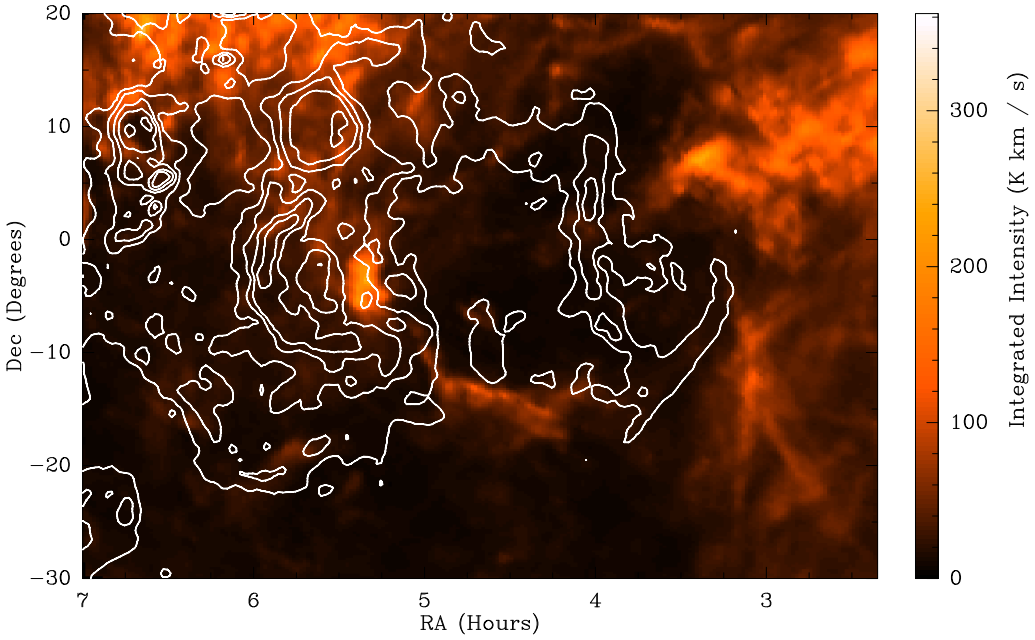

Figure 5.7: H I integrated intensities between -12 km $s^{-1} \leq v_{lsr} \leq -6$ km s^{-1} from the LAB Galactic H I Survey are shown in the color scale. The contours are integrated intensities of Hα from the WHAM survey and are logarithmically spaced with each contour corresponding to a factor of two increase in intensity. The lowest contour corresponds to an integrated intensity of 10 Rayleighs. Note the prominent filament at a declination of -13°. The region displayed and contours are the same as in labeled Figure 5.6.

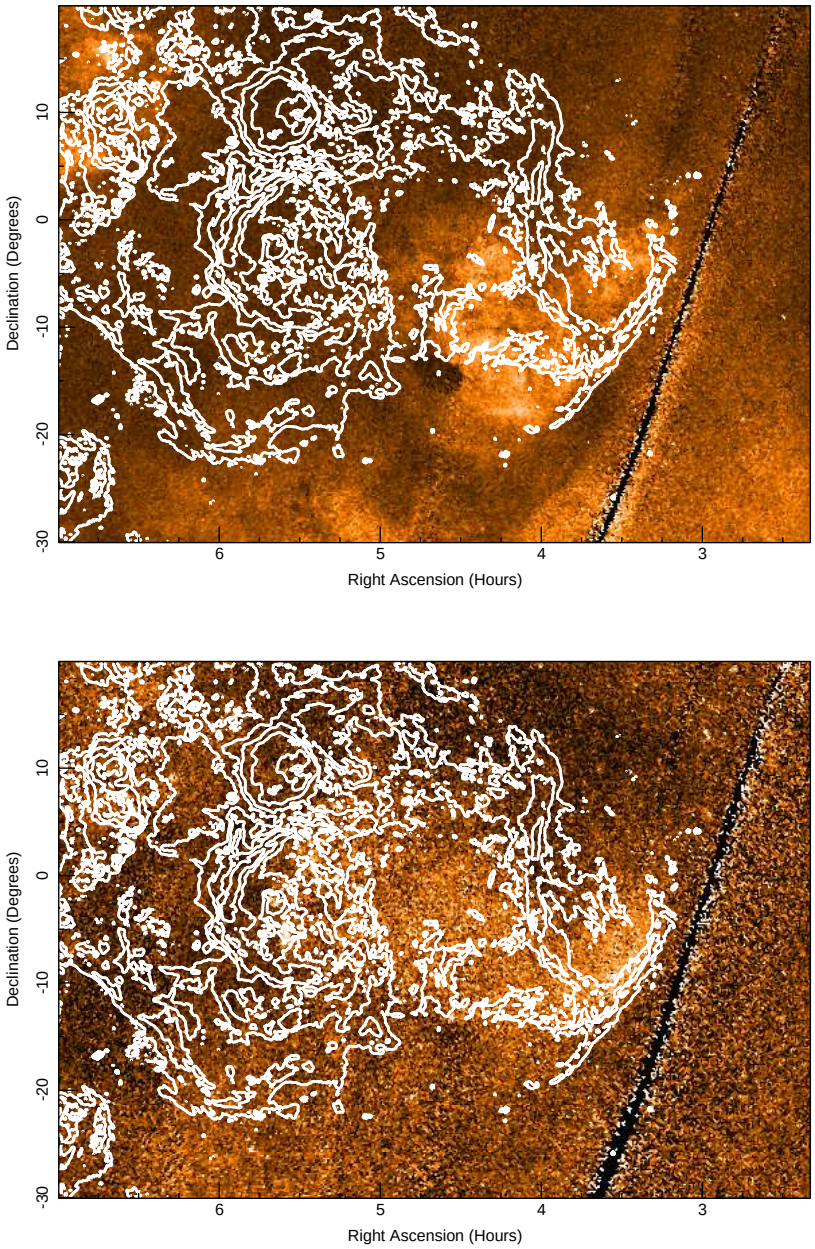

Figure 5.8: Diffuse x-ray emission observed by the ROSAT satellite (Snowden et al., 1997). The top panel shows the 0.25 keV, R12 band and the bottom panel shows the 0.75 keV, R45 band. The contours are Hα integrated intensity contours that start at 10 Rayleighs and increase by factors of two. The Hα data are a composite of the Virginia Tech Spectral Line Survey (VTSS), Southern H-Alpha Sky Survey Atlas (SHASSA), and the WHAM survey (Finkbeiner, 2003). The region shown is the same as in labeled Figure 5.6.

emission partially fills the H I void extending down to a declination of -20°, between right ascensions of 4^h and $4^h\ 30^m$, with the x-ray emission preferentially filling the northwest side of the H I extension. The 0.25 keV emission also does not extend as close to the Orion star forming region as the 0.75 keV emission.

Spectral fits to the x-ray data suggest that the intervening column of absorbing H I gas is at most 1×10^{20} cm^{-2} towards the Eridanus half of the bubble (Burrows et al., 1993; Guo et al., 1995). The one exception is that towards the southern regions of Arc A, absorption columns on the order of 4×10^{20} are derived (Burrows et al., 1993; Guo et al., 1995). Towards the Orion half of the bubble, the absorbing column is estimated to be between 4×10^{20} cm^{-2} and 7×10^{20} cm^{-2} (Guo et al., 1995; Snowden et al., 1995a). The greater absorbing column towards Orion would explain the more eastward extent of the 0.75 keV emission, as 0.25 keV x-ray photons are more easily absorbed than 0.75 keV photons (Guo et al., 1995; Snowden et al., 1995a).

While there seems to be some consensus that the x-ray emission coming from within the Hα limits of the superbubble, dubbed the Eridanus X-ray Enhancement 1 (EXE1) by Burrows et al. (1993), is generated by hot plasma within the bubble, there is some controversy over the nature of the 0.25 keV southern extension, which was named the Eridanus X-ray Enhancement 2 (EXE2) by Burrows et al. (1993). Burrows et al. (1993) consider EXE1 and EXE2 to be physically separate and suggest that EXE2 could be a bubble blown by a single star, although they don't rule out the possibility that EXE2 is a small-scale blowout of the superbubble. Brown et al. (1995), on the other hand, suggest that EXE1 and EXE2 are both related to the superbubble and are not physically separate. Snowden et al. (1995a) note that the superbubble is on the edge of a larger scale 0.25 keV enhancement, see also Snowden et al. (1995b), and they interpret the EXE2 emission to be coming from a diffuse hot halo background. Heiles et al. (1999) suggest that the extended 0.25 keV emission is due to hot gas that has leaked out of the superbubble and subsequently cooled slightly. Heiles et al. (1999) further point out that no receding portion of the superbubble is detected in either Hα or H I for locations between Arc A and B and suggest that this is due to there being a hole in the back of the superbubble through which this hot gas can escape. Burrows et al. (1993) find that EXE1 is slightly warmer than EXE2, with EXE1 having a temperature of 2.2×10^6 K and EXE2 having a temperature of 1.5×10^6 K.

5.10.5 Absorption Lines

Multiple groups have observed interstellar absorption lines in the spectra of stars in the direction of the superbubble. Since Orion is near the Galactic anti-center, Galactic rotation is mainly in the plane of the sky towards Orion and thus, radial velocities alone do not strongly constrain distances to absorption features seen towards the superbubble. The superbubble is, however, relatively nearby and, therefore, the distances to many stars showing absorption are well known and provide upper limits for the distances to various absorbing clouds.

Ionized calcium and sodium absorption lines are detected towards Barnard's Loop at velocities, with respect to the LSR, between -20 and 20 km s^{-1}, suggesting an expansion velocity of 20 km s^{-1} for the superbubble (e.g., Hobbs 1969; Marschall & Hobbs 1972; Cowie et al. 1979), consistent with the expansion velocity of 15 km s^{-1} suggested by Reynolds & Ogden (1979) from Hα emission (see Appendix 5.10.2).

Towards Orion, absorption features are detected around a v_{LSR} of 7 km s^{-1} in the spectra of stars at distances greater than 140 pc and these absorption features are believed to be due to the expanding shell of the local bubble (e.g., Frisch et al. 1990; Burrows & Zhiyu 1996; Lallement et al. 2003; Welsh et al. 2005). This emission is unlikely to be associated with the superbubble, as the gas is moving towards the Orion star forming region, rather than away from it. Conversely, it is unlikely that the Hα emission detected at positive velocities is associated with the local bubble wall, as the local bubble does not contain an obvious ionizing radiation source.

The local bubble wall has a temperature of a few hundred Kelvin, a density on the order of a few cm^{-3}, and a column density near 10^{20} cm, although the local bubble wall is likely to be considerably non-homogeneous (Frisch et al., 1990). Note that the column density of the local bubble is consistent with the x-ray absorption columns derived towards the Eridanus side of the bubble.

At a distance of approximately 200 pc, the first negative velocity component appears towards the Orion half of the superbubble at a LSR velocity of approximately -25 km s^{-1} (Frisch et al., 1990). Towards the Eridanus filaments, emission features are seen between -8 km s^{-1} and -20 km s^{-1} in stars more distant than 180 pc, which are usually interpreted as being due to the near, approaching side of the superbubble (Guo et al., 1995; Burrows & Zhiyu, 1996; Welsh et al., 2005). These absorption features occur at velocities intermediate between the lowest velocity component detected in Hα and in H I. This relatively close distance to the near side of the superbubble is

primarily constrained by two stars from Guo et al. (1995) and three stars from Welsh et al. (2005). Guo et al. (1995) detect sodium absorption lines towards HD 22558, which they estimate to be at a distance of 167 pc based upon spectroscopic parallax, and HD 23393, which has a distance of 229 pc based upon the Hipparcos catalog (van Leeuwen, 2007). Welsh et al. (2005) detect sodium or calcium absorption lines towards HD 27563, HD 29227, and HD 20404, which have distances of 232 pc, 268 pc, and 218 pc, respectively, based upon Hipparcos data. A fourth star in the Welsh et al. (2005) sample, HD 30211, also had a very weak detection of an absorption line at -15 km s^{-1} and a relatively small Hipparcos based distance of 163 pc.

While the near side of the superbubble and the wall of the local bubble are readily detected, there are no unambiguous detections of positive velocity gas associated with the back of the superbubble in the spectra of stars within 500 pc (Guo et al., 1995; Burrows & Zhiyu, 1996; Welsh et al., 2005). Since the positive velocity component of Hα emission associated with the bubble occurs at a velocity similar to that of the local bubble wall, the lack of a clear detection of a back side of the bubble may only be due to confusion between the absorption created by the local bubble and the superbubble wall (e.g., Burrows et al. 1993). Alternatively, if the back wall were fully ionized, NaI lines may not be readily detectable, because neutral sodium traces gas with temperatures less than 1000K (Lallement et al., 2003). Based upon Lyman α to 21 cm ratios, the back side of the bubble, however, has been estimated to be within 540 pc towards (l, b) = (215°, -26°) and within 465 pc towards (l, b) = (209°, -37°) (Savage & Jenkins, 1972; Heiles, 1976; Long et al., 1977).

5.10.6 Molecular Emission

The Orion star forming region contains two well studied giant molecular clouds, Orion A and B, that are actively forming stars and contain roughly 10^5 $M_\odot$ of material (e.g., Bally 2008). Towards the Eridanus side of the bubble, there are three molecular clouds detected with masses of approximately 100 $M_\odot$, but these clouds may be unassociated with the superbubble (Magnani et al., 1996). These clouds were first detected by Magnani et al. (1985) and are denoted as MBM 16, 18, and 20. The locations of these three clouds are indicated on Figure 5.9, which shows the CO detections made by Magnani et al. (2000) in their southern galactic hemisphere CO survey.

MBM 16 is located towards (l, b) = (172°, -38°), which places it approximately 5 degrees to the west of the top of Arc A, and has an area greater than 5 square degrees

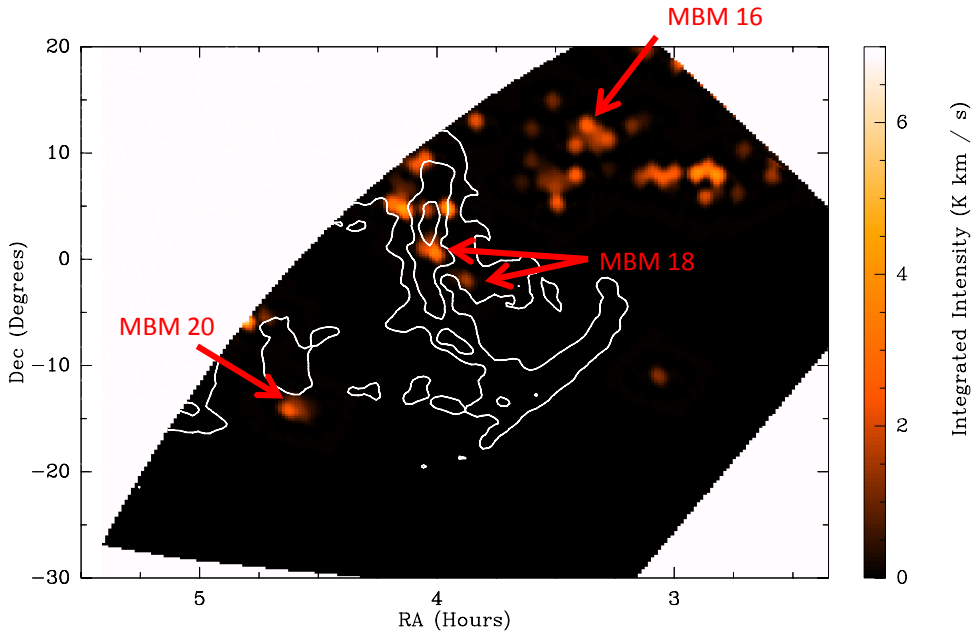

Figure 5.9: CO J = 1 → 0 integrated intensities from the southern galactic hemisphere CO survey of Magnani et al. (2000). The contours are integrated intensities of Hα from the WHAM survey and are logarithmically spaced with each contour corresponding to a factor of two increase in intensity. The lowest contour corresponds to an integrated intensity of 10 Rayleighs. The region displayed and contours are the same as in labeled Figure 5.6.

(Magnani et al., 1985). The central LSR velocity of the cloud's CO emission is 7.4 km s^{-1}, although velocity components are also seen at 5.5 and 3.0 km s^{-1} (Magnani et al., 1985). Gir et al. (1994) associate the CO emission with H I emission centered at 9.9 km s^{-1}. MBM16 is located within 120 pc of the Sun (Magnani & de Vries, 1986; Hobbs et al., 1988; Lallement et al., 2003), which would place MBM 16 between Earth and the near side of the superbubble wall. Based upon this distance, MBM 16 should be relatively close to the local bubble wall.

MBM 18, which is also known as L1569, is a 2.6 square degree cloud centered near (l, b) = (189°, -36°) and has a CO, centroid, LSR velocity between 8 and 10 km s^{-1} (Magnani et al., 1985; Penprase, 1993; Gir et al., 1994; Magnani et al., 2000). H I gas at velocities near 10 km s^{-1} has also been associated with the cloud (Burrows et al., 1993; Gir et al., 1994). This CO central velocity is very similar to the 11 km s^{-1} velocity of Hα emission coming from Arc A. MBM 18 is coincident with the middle of Arc A, where a linear Hα feature lying along a Galactic longitude of 190° crosses the Arc. MBM 18 is elongated in the direction of this crossing Hα feature and contains two distinct peaks of CO emission (Magnani et al., 1985). The peak column density found for MBM 18 is approximately 2×10^{21} cm^{-3} (Penprase et al., 1990; Penprase, 1992, 1993) and the density of MBM 18 is estimated to range from 100 cm^{-3} to 3000 cm^{-3} (Penprase, 1993).

The distance to MBM 18 is not particularly well known, with estimates based upon star counts, stellar reddening, and absorption line studies ranging from 65 to 220 pc (Magnani & de Vries, 1986; Franco, 1988; Penprase et al., 1990; Penprase, 1992, 1993; Lallement et al., 2003). MBM 18 may lie on the near side of the superbubble and may have been formed due to compression from the superbubble (e.g., Burrows et al. 1993), or, alternatively, may be part of the Taurus-Auriga star forming complex (e.g., Li et al. 2000), which is located approximately 140 pc from the Sun (Kenyon et al., 2008).

While there are some weaker CO detections along the northern half of Arc A, at velocities between 7 and 12 km s^{-1}, there are no CO detections along the bottom half of Arc A or along Arc B (Magnani et al., 2000; Aoyama et al., 2002).

MBM 20, which is also known as L1642, is a 1.3 square degree cloud centered near (l, b) = (211°, -36.5°) (Magnani et al., 1985, 1996). It has a characteristic velocity, with respect to the LSR, of 1 km s^{-1} and is located near the southern edge of the superbubble, within the southern extension of the H I void (Gir et al., 1994; Magnani et al., 2000). While Burrows et al. (1993) suggest that MBM20 may have formed

from compression due to the superbubble, Snowden et al. (1995a) find that MBM 20 is within the local bubble, based upon x-ray absorption. This closer distance is supported by absorption line studies, which find a distance less than 161 pc (Penprase, 1993; Hearty et al., 2000).

5.10.7 100 Micron Emission

The Infrared Astronomical Satellite (IRAS) observed the vast majority of the sky at 100 microns (Neugebauer et al., 1984). Figure 5.10 shows the IRAS 100 micron map of the superbubble with overlaid Hα contours. This dust continuum emission is strongly anti-correlated with the x-ray emission (e.g., Burrows et al. 1993; Snowden et al. 1995a) and correlated with far ultraviolet emission (Jo et al., 2011). A 100 micron filament lies parallel to Arc B, but is offset roughly 30 minutes to the west of Arc B, such that the 100 micron filament lies near the observed H I filament in this region. An increase in 100 micron emission can also be seen along Arc A, although the dust emission along the top half of Arc A is not perfectly aligned with the Hα emission of Arc A. The superbubble can be seen as a shell in the IRAS data, with stronger emission appearing along the higher declination edge of the bubble. The lower cavity wall also traces Arc C and extends towards the EXE2 region. MBM 16, 18, and 20 can all be seen in the 100 micron map, as well as the Orion star forming region.

5.10.8 Magnetic Field Structure

For a summary of the magnetic field morphology towards the Orion half of the superbubble, please see Section 5.6.3.1. The number of magnetic field measurements towards the Eridanus half is considerably lower than towards the Orion side, but there is evidence that the magnetic field is parallel to Arc B (Mathewson & Ford, 1970; Verschuur, 1973). Zeeman splitting measurements towards the Eridanus side of the bubble suggest that the line of sight magnetic field is on the order of 5 to 10 μG (Troland & Heiles, 1982; Heiles, 1989). Such a magnetic field strength would produce a magnetic pressure, P / k, of approximately 3×10^4 K cm^{-3}, which is on the order of the thermal pressure within the bubble, 10^4 to 5×10^4 K cm^{-3} (Burrows et al., 1993; Guo et al., 1995; Burrows & Zhiyu, 1996).

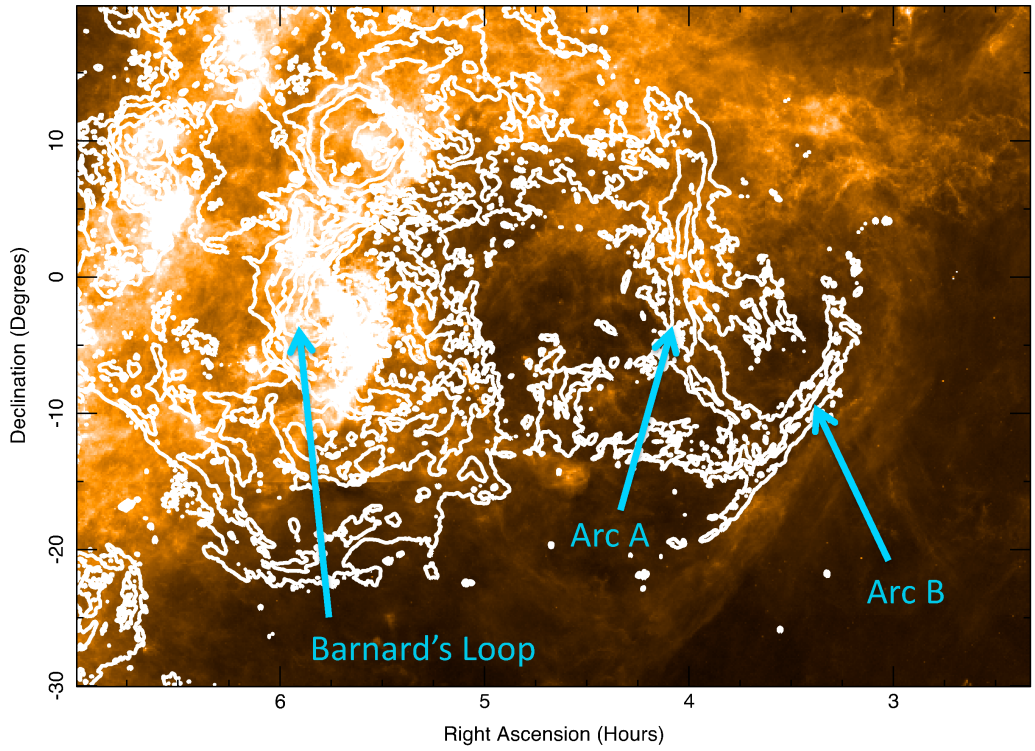

Figure 5.10: 100 micron intensities from the IRAS mission and reprocessed by the IRIS group (Miville-Deschênes & Lagache, 2005) are shown in the linear color scale. The contours are integrated intensities of Hα from a combination of the Virginia Tech Spectral Line Survey (VTSS), Southern H-Alpha Sky Survey Atlas (SHASSA), and the WHAM survey (Finkbeiner, 2003). The lowest contour represents 10 Rayleighs and each contour corresponds to an increase of a factor of two in intensity. Arc A, Arc B, and Barnard's Loop are labeled. The region displayed and contours are the same as in Figure 5.8.

5.10.9 Bubble Properties

Estimates of the kinetic energy of the expanding superbubble are typically on the order of a few times 10^{51} ergs, but range from 1.7×10^{50} ergs to 3.7×10^{51} ergs (Heiles, 1976; Reynolds & Ogden, 1979; Brown et al., 1995; Burrows & Zhiyu, 1996).

From the ratios of different x-ray bands, the temperature of the superbubble has been determined to be on the order of 1 to 4 $\times 10^6$ K (Williamson et al., 1974; Naranan et al., 1976; Long et al., 1977; Burrows et al., 1993; Guo et al., 1995). Guo et al. (1995) also detect a temperature gradient inside the bubble. They derive a temperature of roughly 1.2×10^6 K near Arcs A and B and a temperature of 1.7×10^6 K for the eastern half of the bubble. Highly ionized species, such as O VI and C IV, are detected in emission and absorption towards the interior of the superbubble, indicating that the interior contains gas at temperatures above 2×10^5 K (e.g, York 1974; Kregenow et al. 2006), although Kregenow et al. (2006) show that these lines may be tracing regions of shock heating, as the emission correlates well with Hα intensity towards Arc B.

X-ray data have been used to determine that the interior pressure, P / k, of the superbubble is 1×10^4 to 5×10^4 cm^{-3} K (Burrows et al., 1993; Guo et al., 1995; Burrows & Zhiyu, 1996). Burrows & Zhiyu (1996), however, suggest that the pressure, P / k, at the Eridanus end of the bubble might be as low as 1200 cm^{-3} K. The interior density of the superbubble has also been estimated to be between 0.004 and 0.015 cm^{-3}, roughly consistent with the estimated temperature and pressure of the interior (Burrows et al., 1993; Guo et al., 1995; Burrows & Zhiyu, 1996).

In the shell wall of the superbubble, Heiles et al. (2000) estimate that the electron temperature is 5.5×10^3 K, which is similar to the 8000 K temperature expected in an ionization front (Reynolds & Ogden, 1979; Basu et al., 1999). O'Dell et al. (2011) derive an electron temperature of 5960 K for Barnard's Loop and Madsen et al. (2006) derive a temperature of 6000 to 6500 K for the bubble wall.

Reynolds & Ogden (1979) derive an electron density of 1.1(D/400 pc)$^{0.5}$ cm^{-3} for the Arcs while Heiles (1989) derive a density of 6 cm^{-3} for the H I filament tracing Arcs B and C. From their H I data, Heiles (1976) and Brown et al. (1995) estimate that the initial density of the bubble was 1.5 (D/400 pc)$^{-1}$ cm^{-3} and 0.9 cm^{-3}, respectively.

The column density of HI in the direction of the Eridanus side of the bubble is approximately 1×10^{20} cm^{-2} (Burrows et al., 1993; Guo et al., 1995). Much of this

column may be due to the local bubble wall and Burrows et al. (1993) estimate that the column density of the superbubble is closer to 3×10^{18} cm^{-2} (Burrows et al., 1993; Guo et al., 1995). Towards the Orion half of the bubble, the absorbing column is larger, with column densities between 4×10^{20} cm^{-2} and 7×10^{20} cm^{-2} (Guo et al., 1995; Snowden et al., 1995a). The H I filament tracing Arc B and Arc C, the H I filament at a declination of -13°, and the southern half of Arc A all have column densities on the order of a few times 10^{20} cm^{-2} (Heiles, 1989; Burrows et al., 1993; Guo et al., 1995; Snowden et al., 1995a). Towards the northern half of Arc A, Heiles et al. (2000) derive a column density of 1.9×10^{21} cm^{-2}.

5.10.10 Nature of the Bubble

While Barnard's Loop and the Eridanus filaments were originally treated as separate phenomena, a fairly sizeable body of evidence has been compiled indicating that there is a superbubble in the direction of Orion/Eridanus. The presence of weak Hα filaments that trace out the outline of a large bubble and connect Barnard's Loop and the Eridanus filaments, as well as the apparent lack of any ionizing source of the Eridanus filaments other than the Orion star forming region, strongly suggests the presence of a superbubble (e.g., Reynolds & Ogden 1979). A large void is also seen in H I data and H I filaments are detected just outside of the Hα filaments (e.g., Kalberla et al. 2005). These H I filaments would correspond to neutral material shielded by the Hα filaments. This void structure is also clearly seen in 100 micron data (Neugebauer et al., 1984). Perhaps the most definitive evidence for the existence of a superbubble comes from the detection of diffuse, 0.75 keV x-ray emission that is bounded by the Hα filaments and stretches all the way from the Orion star forming region to Arc B (e.g., Snowden et al. 1997). The hot, tenuous plasma within the superbubble would emit this x-ray emission. Absorption studies have also detected a wall of material moving towards the Sun, 180 pc distant, that is well explained as being the near wall of the superbubble (e.g., Welsh et al. 2005). There are a few small, molecular clouds that may have formed when the bubble wall compressed a pre-existing gas cloud (Burrows et al., 1993), but these molecular clouds may just be coincidentally located along the line of sight.

Originally, it was suggested that the superbubble was generated by supernovae in Orion, with Reynolds & Ogden (1979) suggesting progenitor supernova 2×10^6 years ago and Cowie et al. (1979) advocating for an additional supernova 3×10^5 years

ago, as the dynamical age of the bubble is on the order of a few megayears (Brown et al., 1994). O'dell et al. (1967) also suggested that the bubble could be formed from radiation pressure, but it is now believed that the superbubble was generated partially by winds from the high-mass stars in Orion (e.g., Burrows et al. 1993). Such a wind driven bubble would require a wind on the order of 0.3 to 1×10^{36} ergs s^{-1} (Burrows et al., 1993), which the Orion star forming region could supply (Reynolds & Ogden, 1979; Brown et al., 1994). Brown et al. (1995) determine that a supernova from a runaway star could produce a bubble of the appropriate size and velocity but could not sweep up enough mass to match the observed column densities. Such a supernova, however, could create a low density void for a wind driven bubble to expand into (Brown et al., 1995).

The various estimates for the kinetic energy of the superbubble, 1.7×10^{50} ergs to 3.7×10^{51} ergs (Heiles, 1976; Reynolds & Ogden, 1979; Brown et al., 1995; Burrows & Zhiyu, 1996) are generally consistent with the total kinetic energy that the Orion star forming region could have deposited into a bubble, approximately 2×10^{51} ergs (Brown et al., 1994).

5.10.11 Nature of Arc A

Reynolds & Ogden (1979) were the first to suggest that Arc A might be part of a large superbubble created by the Orion star forming region. This interpretation of Arc A being a filament associated with the superbubble, however, has recently come under question, and the precise nature of Arc A is not yet agreed upon (e.g., Boumis et al. 2001).

Part of the difficulty in deciphering the properties of Arc A is that there are gas clouds unrelated to the superbubble that also lie along the line of sight towards Arc A. The local bubble wall is generally present along any sight line and portions of the north half of Arc A are spatially coincident with MBM 18. There is also a large, diffuse, 100 micron bright swath of emission extending down from the Galactic plane to the north edge of Arc A and there is a separate Hα filament that crosses Arc A just to the south of MBM 18. Focusing observational efforts on the lower half of Arc A, where there is little additional CO or 100 micron emission, may provide the best opportunity to constrain the properties of Arc A without foreground or background contamination.

5.10.11.1 Arguments Against the Association of Arc A with the Superbubble

Boumis et al. (2001) derive an upper limit to the proper motion of Arc A of 0.13″ yr^{-1} by tracking the location of a sharp edge of Arc A, near (l, b) = (188.7°, -36.1°), over a 45 year time span. If Arc A is 200 pc distant, this proper motion would constrain the tangential motion of the Arc to be less than 6 km s^{-1}. At distances of 400 and 600 pc, the Arc would require tangential velocities less than 11 and 17 km s^{-1}, respectively. Boumis et al. (2001) assume that the tangential velocity of the bubble is roughly equal to the line of sight expansion velocity derived by Reynolds & Ogden (1979), 15 km s^{-1}, and derive a minimum distance to Arc A of 530 pc. Based upon this large distance, they suggest that Arc A might be unassociated with Arc B and the superbubble. Such a conclusion, however, is dependent upon the assumption that the radial velocity of Arc A is the same as the velocity of Arc A in the plane of the sky, as discussed in Section 5.6.1. No such proper motion study has yet been conducted for Arc B.

The H I gas closest to Arc A has a centroid velocity of approximately 20 km s^{-1} (Heiles, 1976) and Welsh et al. (2005) note that no absorption line study has detected gas with velocities at or above 20 km s^{-1}. Since these studies have examined stars out to approximately 500 pc, Welsh et al. (2005) argue that Arc A must be more than 500 pc distant. Furthermore, while in both H I and Hα studies the gas near Arc B has a velocity similar to the larger of the two velocity components detected, thereby suggesting that Arc B is associated with the far wall of the superbubble, the H I and Hα emitting gas regions near Arc A have velocities larger than either of the two components detected in H I and Hα towards the Eridanus side of the bubble. It is unclear what is the cause of this velocity difference, be it due to some residual momentum left over from the formation of the Arc, to foreground or background material along the line of sight confusing the line centroid from Arc A, to Arc A being separate from the bubble altogether, or some other physical process.

The H I gas closest to Arc A has a centroid velocity of approximately 20 km s^{-1} (Welsh et al., 2005), while the Hα emission from Arc A has a centroid velocity closer to 10 km s^{-1} (Reynolds & Ogden, 1979). For a constant Galactic rotation speed of 220 km s^{-1}, a radial velocity of 20 km s^{-1}, in the direction of Orion, would correspond to a distance of 2.2 kpc and a velocity of 10 km s^{-1} would correspond to a distance of 1.1 kpc. As noted by Green & Padman (1993), because Orion is near l = 180°,

the motion due to Galactic rotation of any gas cloud towards Orion will be mainly in the plane of the sky and thus, radial velocities do not provide a good measure of distance.

From a combination of dust continuum, HI, and Hα data, Heiles et al. (1999) estimate that the electron density in Arc A is approximately 1 cm^{-3} and find that Arc A must have a depth between 32 and 120 pc. Since the width of Arc A would be 14 pc at a distance of 400 pc, Heiles et al. (1999) conclude that Arc A is not a filament, but rather, an edge on sheet. Such a large sheet depth in the plane of the sky would be difficult to reconcile with a model where Arc A is part of the bubble wall. Heiles et al. (2000), however, apply this same technique to Barnard's Loop and find that Barnard's Loop must also have a depth of 160 pc. Heiles et al. (2000) note that by modifying their assumed grain size distribution, they can reduce their depth by a factor of four and increase their electron density by a factor of two. As such, the observed fluxes from Arc A should still be consistent with a filamentary model.

There is an abrupt drop in Hα intensity to the west of Arc B, along with a corresponding drop in H_2 emission. Ryu et al. (2006) interpret this intensity change as being due to Arc B absorbing most of the UV photons from the Orion star forming region, although this may also be partly due to a significant decrease in the column density of gas along the line of sight to the west of Arc B. In contrast, the Hα and H_2 intensities immediately to the west of Arc A are not significantly less than the intensities to the east of Arc A. From this, Ryu et al. (2006) conclude that Arc A does not lie along the line of sight between the Orion star forming region and Arc B, as Arc A does not appear to be absorbing all of the UV photons traveling westward from the Orion star forming region. They note that this is consistent with Arc A being unassociated with the superbubble. This requirement that Arc A and B lie along different sight lines from Orion can, however, also be satisfied for models where Arc A is associated with the superbubble.

5.10.11.2 Arguments for Association of Arc A with the Superbubble

Arcs A and B appear to join smoothly in the plane of the sky and in velocity space. There is no obvious discontinuity suggesting that the two Arcs are located at significantly different distances.

If the superbubble is split into four quadrants, centered on the Orion star forming region, then the Hα flux is the same in each quadrant, as would be expected if

the emission is entirely due to reprocessed ionizing radiation from the Orion star forming region (Reynolds & Ogden, 1979). Not including Arc A's flux would make the Eridanus side of the superbubble under luminous, although flux equality between all of the quadrants would only be expected if the ionizing photons from the Orion star forming region never break out of the superbubble wall.

If Arc A is not associated with the superbubble, it is very uncertain what would be ionizing Arc A. Based on Cox (1972) and Raymond (1976), Reynolds & Ogden (1979) note that a 20-30 km s^{-1} shock would not produce enough Hα emission to explain the brightness of the Eridanus filaments. A higher [O III] to Hα ratio than seen by Reynolds & Ogden (1979) would also be expected for ionization due to hard UV, soft x-rays, or cosmic rays (Bergeron & Souffrin, 1971). Furthermore, there are no stars on the Eridanus side of the bubble that would have had enough energy to have formed a separate bubble which Arc A might be part of (Heiles, 1976). For a hydrogen recombination coefficient of 2.6×10^{-13} cm^3 s^{-1} and a density on the order of a few cm^{-3}, the recombination time is just slightly less than 10^5 years. This short recombination time makes it somewhat unlikely, although not unreasonable, that Arc A was ionized by a short duration event in the recent past. The H I filament associated with Arc A is offset to the west of Arc A, as would be expected if the Orion star forming region is responsible for ionizing Arc A.

Arc A is clearly associated with a decrease in soft x-ray emission, even along the southern region of the Arc, which would be expected only if Arc A were between the Sun and the interior of the superbubble, such that the Arc could absorb the x-rays coming from the hot interior of the bubble (e.g., Guo et al. 1995; Snowden et al. 1995a, 1997). A model in which Arc A is on the near side of the bubble, at a distance of approximately 180 pc, would be fully consistent with this x-ray absorption. As mentioned previously, however, the centroid velocities of Hα and H I emission from Arc A are not compatible with the velocities of the near side of the bubble. Arc A also has a larger characteristic velocity than Arc B, suggesting that Arc A should be farther towards the back side of the superbubble than Arc B, which has velocities consistent with the back side of the bubble.

The near side of the superbubble is detected at velocities between -8 and -20 km s^{-1} in absorption studies (e.g., Welsh et al. 2005). This velocity range is more positive than the lower of the two Hα velocity components, -25 km s^{-1}, but more negative than the lower H I velocity component, -5 km s^{-1}. If the higher of the two detected velocity components, in both H I and Hα, corresponds to the far side of the

bubble and if the far bubble wall were to appear in absorption studies at a velocity intermediate to that in H I and Hα studies, as the near side does, then it would be expected that the far bubble wall would appear at velocities between 3 and 12 km s^{-1}. Since the local bubble wall has a velocity of 7 km s^{-1}, it is likely that any absorption features due to the far bubble wall of the superbubble could be readily confused with absorption due to the local bubble. Therefore, the lack of a detection of the far bubble wall in absorption studies can be simply explained by confusion between the local bubble wall and the far bubble wall. Furthermore, the Hα centroid of Arc A, 11 km s^{-1}, is much lower than the 20 km s^{-1} value adopted by Welsh et al. (2005) in their absorption line survey and absorption lines at 11 km s^{-1} could be more readily confused with absorption due to the local bubble, or even MBM 18, which has a velocity of 8 to 10 km s^{-1}. Heiles (1979) also note that in their catalogue of H I shells and supershells, many have only one side detected.

Chapter 6

Conclusion

No! I am not Prince Hamlet, nor was meant to be;
Am an attendant lord, one that will do
To swell a progress, start a scene or two,
Advise the prince; no doubt, an easy tool,
Deferential, glad to be of use,
Politic, cautious, and meticulous;
Full of high sentence, but a bit obtuse;
At times, indeed, almost ridiculous –
Almost, at times, the Fool.
T.S. Eliot

6.1 SUMMARY

Stars form in giant molecular clouds. GMCs are large, dynamic entities and the nature of the motions within these GMCs plays a significant role in the process of star formation. In turn, once star formation has commenced within a molecular cloud, feedback processes from protostars and newly formed stars can significantly alter the dynamics of a GMC.

For this dissertation, I have studied the large scale motions within GMCs in order to better understand the dynamical state of GMCs and how this relates to star formation. In Chapters 2 and 3, I studied how molecular clouds collapse due to their self gravity, by calculating the dependence of gravitational collapse timescales on the dimensions and aspect ratios of molecular clouds. Giant molecular clouds, however,

are more complex than relatively uniform gas clouds simply collapsing under their own self gravity. GMCs are known to contain supersonic turbulence and in Chapter 4, I studied the nature of turbulence in molecular clouds by predicting where the turbulent energy will go after being dissipated in shock fronts. Finally, in Chapter 5, I examined in detail one example of star formation feedback affecting the structure of the surrounding interstellar medium by fitting Kompaneets models to the Orion-Eridanus superbubble. The primary results of this research are presented below.

For realistically sized, uniform density spheres and circular sheets, local collapse modes are only significantly faster than global collapse modes if there are very strong density perturbations in the objects. Thus, global collapse modes cannot be ignored in quasistatic collapse models of spheres and circular sheets. For filaments with lengths on the order of ten Jeans lengths or more, local collapse modes can proceed significantly faster than the global collapse mode for relatively small density perturbations. In the absence of large scale support mechanisms, this suggests that star formation should occur through a process of reduction of dimensions, wherein spherical and disc shaped clouds first collapse to form filaments and then these filaments fragment to form prestellar cores.

While the interiors of uniform density circular sheets and filaments collapse homologugsly, more momentum is preferentially injected towards the edges of these objects during gravitational collapse than would be expected for a purely homologous collapse. This extra momentum gives rise to an edge-driven collapse mode. This edge-driven collapse mode becomes more important for lower dimensional objects and for objects with larger aspect ratios. For circular sheets, the momentum imparted to the edge due to this edge-driven collapse mode is never greater than the momentum required for the disk to collapse homologously, such that circular sheets should collapse on their interior homologous collapse timescales. For filaments with realistic aspect ratios, however, the momentum injected at the edges is much greater than would be injected for purely homologous collapse. As such, filaments should be dominated by the edge-driven collapse mode.

The homologous collapse mode of a circular sheet scales with the square root of the aspect ratio while the homologous collapse mode of a filament scales linearly with the aspect ratio. The edge-drvien collapse mode of a filament, however, scales with the square root of the aspect ratio. For the same gas density, collapse timescales increase with increasing aspect ratio and are larger for lower dimensional shapes. Star formation rates, calculated from collapse timescales derived from observed gas

densities, can be overestimated by an order of magnitude if the geometry of clouds are not taken into account.

Regardless of whether turbulence is driven by large scale, global collapse or from feedback on small scales after local collapse modes have proceeded to form protostars, supersonic turbulence is prevalent throughout molecular clouds and can have significant effects on the dynamical state of molecular clouds. This turbulence, however is predicted to decay rapidly (e.g., Stone et al. 1998). Turbulent energy dissipation rates in giant molecular clouds are on the order of the cosmic ray heating rate in well shielded gas. For molecular gas, with densities near 1000 cm^{-3}, shocks with velocities of a few kilometers per second dissipate the majority of their energy in CO rotational transitions, although a significant fraction of this energy also goes into compressing magnetic fields. Molecular hydrogen lines can account for up to 20% of the shock cooling, but H_2 lines are only prominent in the strongest shocks, in which the peak gas temperature exceeds 100 K. At the increased densities of the post-shock gas, the ambipolar diffusion energy dissipation rate is comparable to the turbulent energy dissipation rate. Therefore, the energy deposited into the magnetic field by a shock may be quickly dissipated by ambipolar diffusion.

The CO emission from shocked gas in low J rotational transitions is much weaker than the the CO emission from unshocked gas in molecular clouds. At mid-J transitions, near CO $J = 5 \rightarrow 4$, the shocked gas emission starts to become larger than the unshocked gas emission, such that mid-J CO transitions, such as the CO $J = 7 \rightarrow 6$ and $8 \rightarrow 7$ transitions, should serve as observable tracers of turbulent energy dissipating in shock fronts within giant molecular clouds.

While turbulence may support a cloud against gravitational collapse, local collapse modes must eventually lead to the creation of stars. These stars, once formed, will interact with the molecular clouds out of which they form and, especially in high-mass star forming regions, can significantly alter the state of the surrounding interstellar medium. In particular, high-mass stars can create large superbubbles in the ISM, such as the nearby Orion-Eridanus superbubble. While Kompaneets models can be fit to the morphology of the Orion-Eridanus superbubble, regardless of whether the superbubble is oriented towards or away from the Sun, the best fitting models require an unrealistically small scale height for the Galactic disk in order to explain the elongation of the superbubble. The best fitting models are also farther from being perpendicular to the plane of the Galaxy than would be expected for a bubble expanding in a pure exponential atmosphere. Some additional process not included

in the Kompaneets model, such as turbulent motions, must control the evolution of the morphology of the Orion-Eridanus superbubble.

The Eridanus filaments are too large and have too high of an Hα emission measure to be equilibrium structures ionized by the Orion star forming region. They may have formed from the compression of previously ionized gas, when the superbubble expanded into an existing gas cloud, and are now out of ionization equilibrium and slowly recombining.

6.2 AVENUES FOR FUTURE RESEARCH

6.2.1 Collapse Timescales

In Chapters 2 and 3, collapse timescales of various idealized molecular clouds were calculated under the approximation that accelerations remain constant throughout a cloud's collapse. To better follow the changing acceleration profile throughout a cloud during its collapse, hydrodynamical simulations of collapsing clouds could be run. I have begun to run such simulations of collapsing filaments but this effort has been hampered by the difficulty of preventing collapse along the shorter axes of a filament from dominating the dynamics of the simulation. Such simulations, however, may be able to probe the interplay between collapse modes along different axes.

The collapse timescale work presented in Chapters 2 and 3 has shown that star formation rates can be significantly overestimated if the geometry of clouds are not taken into consideration. Typical estimates for the star formation rate of the Galaxy, which are based upon gas densities, are usually higher than the observed star formation rate (e.g., Zuckerman & Palmer 1974; Zuckerman & Evans 1974; Robitaille & Whitney 2010). An attempt should be made to see if this discrepancy can be explained by a reasonable distribution of filamentary gas clouds or if unrealistically large filament aspect ratios would be required.

The Herschel Space Observatory has already started to reveal filamentary structure within molecular clouds and has hinted at a characteristic filament width (André et al., 2010; Arzoumanian et al., 2011). Continued observations will yield better constraints on the actual distribution of cloud shapes, which can then be examined analytically as done in this dissertation. All of the calculations in this dissertation were done under the assumption that the bulk of a molecular cloud has a uniform density. Further observational constraints on the density profile of filaments would

be useful for determining the initial conditions of future analytic or computational calculations of the collapse timescales of non-uniform density objects. Observations of star formation activity at the ends of filamentary structures would also help confirm the presence and significance of the edge-driven collapse mode.

6.2.2 Shocks

6.2.2.1 Extension of Shock Models

While the shock models presented in Chapter 4 are a good first start at determining where the turbulent energy in molecular clouds goes, there are many areas where these shock models could be improved. The models presented in this dissertation only include a fairly small range of chemical species and this chemical complexity could be significantly improved. While the shock code likely currently has all of the most energetically important species, there could be additional species that are sensitive to the increased temperature and density of shock fronts that would provide useful further tracers of shocked gas. These additional tracers would be particularly useful at wavelengths other than the wavelengths of the mid-J CO lines, in order to allow additional telescopes and instruments to observe shock tracing lines.

The addition of further molecular species to the shock code could reveal line ratios that could be used to distinguish between heating from low velocity turbulent shocks and protostellar feedback (e.g., high velocity shocks from outflows). Lines that are found to be sensitive to protostellar heating, and not turbulent heating, could be used to estimate and remove the contribution of protostellar heating to other shock tracing lines. This would allow for observations of shock tracing lines from extragalactic GMCs, which will inevitably contain emission from gas heated by protostellar feedback due to the larger spatial scales lying within the beam in these extragalactic sources, to probe the nature of turbulent dissipation in a large variety of extragalactic environments. This is analogous to how PDR models were used in this dissertation to determine which CO lines are emitted primarily by shocked gas, rather than the unshocked gas heated by the interstellar radiation field. The shock models can also be extended to slightly higher velocities to probe molecular cloud collisions in merging galaxies and could be adjusted so that the relative line ratios of H_2 are consistently calculated.

In the outer regions of molecular clouds, most of the gas phase carbon is present as either atomic or ionized carbon and there is very little CO present (e.g., Wolfire et al.

2010). Since the models of Chapter 4 show that CO is the primary coolant of shocks in the CO-rich interiors of molecular clouds, CO poor dark molecular gas must cool through different mechanisms. Possible species of interest for cooling dark molecular gas include H_2, C^+ and atomic carbon (e.g., Kaufman et al. 1999; Goldsmith et al. 2010; Lesaffre et al. 2013). The shock models could be run with much lower initial abundances of CO to investigate how dark molecular gas cools.

High-mass star formation tends to occur in higher density gas than low-mass star formation. Some infrared dark clouds are believed to be sites of high-mass star formation and these IRDCs have typical densities closer to 10^5 cm^{-3}, rather than 10^3 cm^{-3} as in low-mass star forming regions (Rathborne et al., 2006). All of the models presented in this dissertation were run for the lower densities of low-mass star forming regions. I have already begun to run shock models for higher densities, corresponding to the typical conditions of IRDCs, and a larger suite of simulations would be useful in predicting the emission coming from shocks in IRDCs.

To predict the total emission coming from shocks in a GMC, the shock models in Chapter 4 were scaled to the total turbulent energy dissipation rate of the cloud under the assumption that all of the energy is dissipated in shocks of the same strength as in the model. Clearly, in realistic clouds there will be a range of shock strengths. High resolution molecular cloud simulations could be used to predict a reasonable range of initial shock conditions, including magnetic field orientation, magnetic field strength, shock velocity, initial gas density and the chemical composition of the gas, such that an appropriate range of shock models could be combined to predict the shocked gas emission from a molecular cloud. The post processing of molecular cloud simulations with the results of shock models would also create predictions for the shock spectra and spatial distribution of shock emission from different cloud formation models (e.g., Kumar & Fisher 2013). Comparing these simulations to observations of shock tracing lines would help determine which models are most similar to actual star forming molecular clouds.

6.2.2.2 Observations

Observations of lines identified as being potentially shock dominated lines would determine whether these lines can be detected at levels above those predicted by PDR models, and thus, confirm whether the intensities of these lines are increased via shocks. The exact intensities of these lines would also constrain the global turbulent

energy dissipation rate of molecular clouds, since the shock models presented in Chapter 4 yield scaling relationships between individual line intensities and the turbulent energy dissipation rate of a cloud. Similarly, these observations would constrain the dissipation timescale of turbulence as well as the driving scale of the turbulence, assuming that numerical models are correct in that turbulence decays on the crossing time at the driving scale (e.g., Stone et al. 1998).

Single dish telescopes, which have relatively large beams (i.e., low resolutions), are well suited for measuring the average emission from a cloud because many shock fronts can be simultaneously detected by such a telescope. Thus, single dish telescopes can be used to determine the total energy dissipation rate of molecular clouds or other average properties of the turbulence. To obtain measurements of individual shock fronts, interferometers, consisting of multiple dishes working together as a large array, must be used, because interferometers have much higher resolutions than single dish telescopes. The higher resolution of an interferometer also has the benefit of increasing the effective brightness of any shock tracing line, since the beam dilution of the shock fronts would be significantly reduced.

Interferometric observations can confirm that excess line emission has small-scale structure, rather than being more uniformly distributed, thereby demonstrating that this extra emission is coming from localized shock fronts. By isolating individual shocks, these observations would allow for the determination of the distribution of shock strengths within a molecular cloud, based upon the ratios of the observed lines. This could differentiate between different proposed theories for the state of turbulence in molecular clouds, such as whether the turbulence is super-Alfvénic or sub-Alfvénic and whether it is driven or decaying.

The spatial distribution of shocks within a molecular cloud would also yield information on the mechanism through which substructures in clouds are formed. If the locations of shocks correlate well with prominent density substructures, then it is likely that turbulent motions play a significant role in forming this substructure. If magnetic fields dominate the formation of substructure, a much weaker correlation would be expected between the shock locations and the locations of dense substructures. Observations of shock tracers in the dark molecular gas in the periphery of clouds may also reveal signs of cloud collisions and shed light on the formation mechanisms of entire giant molecular clouds.

6.2.2.3 Observational Facilities

There are numerous current and upcoming facilities that are capable of observing shock tracing lines. The Herschel Space Observatory, launched by the European Space Agency, is a 3.5 meter submillimeter telescope located at the Earth-Sun L2 Lagrange point that was launched in 2009 (Pilbratt et al., 2010). Herschel is expected to run out of cryogens early in 2013, at which point observations with Herschel will cease (Pilbratt et al., 2010). The Heterodyne Instrument for the Far-Infrared (HIFI), located on Herschel, is a high resolution spectrograph capable of operating between 490 GHz and 1250 GHz, and between 1410 GHz and 1910 GHz (de Graauw et al., 2010). This spectral range includes every CO rotational transition from the J = 5 → 4 transition up to the 16 → 15 transition, with the exception of the J = 12 → 11 and 11 → 10 transitions. Being above the Earth's atmosphere, Herschel is capable of observing higher rotational transitions of CO than can be obtained from the ground.

Using HIFI, I have already conducted 1.4 hours of observations of the CO J = 6 → 5 and 5 → 4 lines towards Perseus B1-East (B1-E). B1-E is in the Perseus molecular cloud, a nearby low-mass star forming region, and is devoid of any protostars (Sadavoy et al., 2012). Using eight hours of HIFI time, I have also mapped four IRDCs in CO J = 10 → 9, 9 → 8 and 8 → 7. I am currently in the processes of reducing these data, but an early analysis of the B1-E data suggests that I have detected shock emission.

The Stratospheric Observatory for Infrared Astronomy (SOFIA) is run in partnership by the National Aeronautics and Space Administration (NASA) and the German Aerospace Center. SOFIA is a 2.5 meter telescope mounted on a Boeing 747 and operates at an altitude of 45000 feet (Young et al., 2012). First light on SOFIA was obtained in 2010 (Young et al., 2012). SOFIA has the German Receiver for Astronomy at Terahertz Frequencies (GREAT) instrument, which is capable of observing the C^+ cooling line at 158 microns (Heyminck et al., 2008), which may be an effective tracer of shocks in dark molecular gas (Lesaffre et al., 2013). The Field Imaging Far-Infrared Line Spectrometer (FIFI LS), which will also be capable of mapping the 158 micron C^+ line (Klein et al., 2010), and the Echelon Cross Echelle Spectrograph (EXES), which can operate at wavelengths between 5 and 28.5 microns (Richter et al., 2010), are currently being commissioned for SOFIA. Molecular hydrogen lines may be effective coolants of shocks in dark molecular gas and the four lowest H_2 transitions occur at wavelengths of 28.2 μm, 17.0 μm, 12.3 μm and 9.7 μm, all of which lie within atmospheric transmission windows (Goldsmith et al., 2010). Thus, EXES will

be capable of observing multiple H_2 lines.

The Atacama Pathfinder Experiment (APEX) is a single dish, submillimeter telescope run by the Max Planck Institute for Radio Astronomy, Onsala Space Observatory and European Southern Observatory. Apex was inaugurated in 2005 (Güsten et al., 2006). APEX consists of a single 12 meter diameter prototype dish from the Atacama Large Millimeter Array (ALMA) located on the Chajnantor plateau in Chile (Güsten et al., 2006). The CO J = 9 → 8, 8 → 7, 7 → 6 and 6 → 5 lines all lie within atmospheric transmission windows and can be observed from a high, dry site such as the Chajnantor plateau. ZEUS-2 is a submillimeter spectrometer being built by Cornell University that, upon completion, will be capable of observing all four of these mid-J lines and will be operated on APEX (Ferkinhoff et al., 2010). The Carbon Heterodyne Array of the MPIfR (CHAMP+) instrument is a 14 pixel Heterodyne array that is currently available for use with APEX and can observe the CO J = 8 → 7, 7 → 6 and 6 → 5 lines (Kasemann et al., 2006).

ALMA, once completed in 2013, will be comprised of 50 12 meter antennas, forming the main array, and an additional 12 seven meter antennas and four 12 meter antennas, comprising a compact array (Schieven, 2012). The maximum baseline for the full ALMA array will be 16 km and ALMA will provide resolutions on the order of 0.01″ (Schieven, 2012). ALMA will have at least seven separate receiving bands operating at frequencies from 84 GHz to 950 GHz (Schieven, 2012). Band nine will include the CO J = 6 → 5 line, while band 10 will include the CO J = 7 → 6 and 8 → 7 lines (Schieven, 2012). While the array is currently under construction on the Chajnantor Plateau in Chile, the partially completed array has been used for scientific observations since 2011 (Herrera et al., 2012).

The Cerro Chajnantor Atacama Telescope (CCAT) is a 25 meter telescope that is planned to be constructed on the Chajnantor Plateau in Chile by an international team of universities, including Cornell University and Caltech (Sebring, 2010). The telescope is expected to be completed in 2017 and will provide exceptional single dish, submillimeter observations of mid-J CO transitions (Sebring, 2010).

The James Webb Space Telescope (JWST) is an infrared telescope run by NASA that will, hopefully, be launched in 2018. The JWST will have a 6.5 meter telescope and will be positioned at the Sun-Earth L2 Lagrange point (Gardner et al., 2006). The Mid-Infrared Instrument (MIRI) on the JWST will be capable of operating at wavelengths between 5 and 28.5 microns (Wright et al., 2008), and thus will be capable of observing rotational transitions of H_2.

6.2.3 Superbubbles

There are now two highly elongated bubbles, the W4 superbubble and the Orion-Eridanus superbubble, with Kompaneets fits requiring scale heights much smaller than expected for the Galactic disk. A natural extension of the work presented in Chapter 5 would be to identify additional elongated superbubbles and apply the same Kompaneets modeling to those bubbles. A statistical survey of the fraction of bubbles that are elongated and cannot be fit with Kompaneets models with reasonable scale heights would indicate the relative importance of whatever secondary process is shaping the Orion-Eridanus superbubble.

Additional simulations of expanding superbubbles, with additional physics, may reveal possible processes that could elongate a superbubble. Simulations of bubbles expanding into pre-existing gas clouds may also reveal whether such an interaction could create features similar to the Eridanus filaments.

As identified in Chapter 5, Arc B is a prime candidate for a proper motion survey to determine the three dimensional expansion velocity of the Eridanus filaments. Given the confused nature of the top half of Arc A, it may also be illuminating to determine the proper motion of the bottom half of Arc A, in contrast to the Boumis et al. (2001) survey that focused on the top half of the Arc. Parallax measurements of the arcs would also greatly constrain the geometry of the Eridanus half of the superbubble.

Go make some new disaster,
That's what I'm counting on,
You're someone else's problem,
Now I only want you gone,
GLaDOS

Look at me still talking
when there's Science to do...
I've experiments to run.
There is research to be done...
I'm doing Science and I'm still alive.
GLaDOS

Bibliography

André, P., Basu, S., & Inutsuka, S. 2009, in Structure Formation in Astrophysics, ed. Chabrier, G. (Cambridge University Press), 254–287

Andre, P., Ward-Thompson, D., & Barsony, M. 1993, Astrophysical Journal, 406, 122

Andre, P., Ward-Thompson, D., & Barsony, M. 2000, in Protostars and Planets IV, ed. V. Mannings, A. P. Boss, & S. S. Russell (Tucson, AZ: Univ. Arizona), 59–96

André, P., Men'shchikov, A., Bontemps, S., et al. 2010, Astronomy and Astrophysics, 518, L102

Aoyama, H., Mizuno, N., Onishi, T., Mizuno, A., & Fukui, Y. 2002, in 8th Asian-Pacific Regional Meeting, Volume II, ed. S. Ikeuchi, J. Hearnshaw, & T. Hanawa (Tokyo: Astron. Soc. Japan), 125

Appenzeller, I. 1974, Astronomy and Astrophysics, 36, 99

Arce, H. G., Borkin, M. A., Goodman, A. A., Pineda, J. E., & Halle, M. W. 2010, Astrophysical Journal, 715, 1170

Arce, H. G., Shepherd, D., Gueth, F., et al. 2007, in Protostars and Planets V, ed. B. Reipurth, D. Jewitt, & K. Keil (Tucson, AZ: Univ. Arizona Press), 245–260

Arnal, E. M., Bajaja, E., Larrarte, J. J., Morras, R., & Pöppel, W. G. L. 2000, Astronomy and Astrophysics, Supplement Series, 142, 35

Arons, J., & Max, C. E. 1975, Astrophysical Journal, Letters to the Editor, 196, L77

Arzoumanian, D., André, P., Didelon, P., et al. 2011, Astronomy and Astrophysics, 529, L6

Audit, E., & Hennebelle, P. 2005, Astronomy and Astrophysics, 433, 1

Bagetakos, I., Brinks, E., Walter, F., et al. 2011, Astronomical Journal, 141, 23

Bajaja, E., Arnal, E. M., Larrarte, J. J., et al. 2005, Astronomy and Astrophysics, 440, 767

Ballesteros-Paredes, J., Gómez, G. C., Loinard, L., Torres, R. M., & Pichardo, B. 2009a, Monthly Notices of the RAS, 395, L81

Ballesteros-Paredes, J., Gómez, G. C., Pichardo, B., & Vázquez-Semadeni, E. 2009b, Monthly Notices of the RAS, 393, 1563

Ballesteros-Paredes, J., Hartmann, L., & Vázquez-Semadeni, E. 1999, Astrophysical Journal, 527, 285

Ballesteros-Paredes, J., Klessen, R. S., Mac Low, M., & Vazquez-Semadeni, E. 2007, in Protostars and Planets V, ed. B. Reipurth, D. Jewitt, & K. Keil (Tucson, AZ: Univ. Arizona Press), 63

Ballesteros-Paredes, J., & Mac Low, M.-M. 2002, Astrophysical Journal, 570, 734

Bally, J. 2001, in Astronomical Society of the Pacific Conference Series, Vol. 231, Tetons 4: Galactic Structure, Stars and the Interstellar Medium, ed. C. E. Woodward, M. D. Bicay, & J. M. Shull (San Francisco, CA: ASP), 204

Bally, J. 2008, in Handbook of Star Forming Regions, Volume I, ed. Reipurth, B. (San Francisco, CA: ASP Monograph Publications), 459

Bally, J., Lanber, W. D., Stark, A. A., & Wilson, R. W. 1987, Astrophysical Journal, Letters to the Editor, 312, L45

Banerjee, R., Klessen, R. S., & Fendt, C. 2007, Astrophysical Journal, 668, 1028

Banerjee, R., Vázquez-Semadeni, E., Hennebelle, P., & Klessen, R. S. 2009, Monthly Notices of the RAS, 398, 1082

Barnard, E. E. 1894, Popular Astronomy, 2, 151

Bastien, P. 1983, Astronomy and Astrophysics, 119, 109

Bastien, P., Arcoragi, J., Benz, W., Bonnell, I., & Martel, H. 1991, Astrophysical Journal, 378, 255

Basu, S., Ciolek, G. E., Dapp, W. B., & Wurster, J. 2009, New Astronomy, 14, 483

Basu, S., & Dapp, W. B. 2010, Astrophysical Journal, 716, 427

Basu, S., Johnstone, D., & Martin, P. G. 1999, Astrophysical Journal, 516, 843

Basu, S., Mouschovias, T. C., & Paleologou, E. V. 1997, Astrophysical Journal, Letters to the Editor, 480, L55

Basu, S., & Murali, C. 2001, Astrophysical Journal, 551, 743

Bate, M. R. 2009, Monthly Notices of the RAS, 397, 232

Bate, M. R., Bonnell, I. A., & Bromm, V. 2002, Monthly Notices of the RAS, 336, 705

—. 2003, Monthly Notices of the RAS, 339, 577

Beaumont, C. N., & Williams, J. P. 2010, Astrophysical Journal, 709, 791

Bergeron, J., & Souffrin, S. 1971, Astronomy and Astrophysics, 14, 167

Bergin, E. A., Maret, S., van der Tak, F. F. S., et al. 2006, Astrophysical Journal, 645, 369

Bergin, E. A., & Tafalla, M. 2007, Annual Review of Astronomy and Astrophysics, 45, 339

Bergin, E. A., Phillips, T. G., Comito, C., et al. 2010, Astronomy and Astrophysics, 521, L20

Binney, J., & Tremaine, S. 1987, Galactic Dynamics (Princeton, NJ: Princeton Univ. Press)

Bisnovatyi-Kogan, G. S., Blinnikov, S. I., & Silich, S. A. 1989, Astrophysics and Space Science, 154, 229

Bisnovatyi-Kogan, G. S., & Silich, S. A. 1995, Reviews of Modern Physics, 67, 661

Blitz, L., & Shu, F. H. 1980, Astrophysical Journal, 238, 148

Bonazzola, S., Perault, M., Puget, J. L., et al. 1992, Journal of Fluid Mechanics, 245, 1

Bonnell, I. A., & Bate, M. R. 2002, Monthly Notices of the RAS, 336, 659

Bonnell, I. A., Bate, M. R., & Zinnecker, H. 1998, Monthly Notices of the RAS, 298, 93

Bonnell, I. A., Larson, R. B., & Zinnecker, H. 2007, in Protostars and Planets V, ed. B. Reipurth, D. Jewitt, & K. Keil (Tucson, AZ: Univ. Arizona Press), 149

Bonnell, I. A., Vine, S. G., & Bate, M. R. 2004, Monthly Notices of the RAS, 349, 735

Boumis, P., Dickinson, C., Meaburn, J., et al. 2001, Monthly Notices of the RAS, 320, 61

Brown, A. G. A., de Geus, E. J., & de Zeeuw, P. T. 1994, Astronomy and Astrophysics, 289, 101

Brown, A. G. A., Hartmann, D., & Burton, W. B. 1995, Astronomy and Astrophysics, 300, 903

Brunt, C. M. 2003, Astrophysical Journal, 583, 280

Brunt, C. M., Heyer, M. H., & Mac Low, M. 2009, Astronomy and Astrophysics, 504, 883

Burkert, A., & Hartmann, L. 2004, Astrophysical Journal, 616, 288

Burrows, D. N., Singh, K. P., Nousek, J. A., Garmire, G. P., & Good, J. 1993, Astrophysical Journal, 406, 97

Burrows, D. N., & Zhiyu, G. 1996, in Roentgenstrahlung from the Universe, ed. H. U. Zimmermann, J. Trümper, & H. Yorke (MPE Rep. 263; Garching: MPE), 221

Cami, J., Bernard-Salas, J., Peeters, E., & Malek, S. E. 2010, Science, 329, 1180

Carroll, B. W., & Ostlie, D. A. 2007, An Introduction to Modern Astrophysics (2nd ed.; New York: Addison-Wesley)

Carroll, J. J., Frank, A., Blackman, E. G., Cunningham, A. J., & Quillen, A. C. 2009, Astrophysical Journal, 695, 1376

Caselli, P., Walmsley, C. M., Terzieva, R., & Herbst, E. 1998, Astrophysical Journal, 499, 234

Caselli, P., Walmsley, C. M., Zucconi, A., et al. 2002, Astrophysical Journal, 565, 344

Chabrier, G. 2005, in Astrophysics and Space Science Library, Vol. 327, The Initial Mass Function 50 Years Later, ed. E. Corbelli, F. Palla, & H. Zinnecker (Dordrecht: Springer), 41–52

Chapman, N. L., Goldsmith, P. F., Pineda, J. L., et al. 2011, Astrophysical Journal, 741, 21

Chen, H., Myers, P. C., Ladd, E. F., & Wood, D. O. S. 1995, Astrophysical Journal, 445, 377

Chen, X., Arce, H. G., Zhang, Q., et al. 2010, Astrophysical Journal, 715, 1344

Chernoff, D. F., McKee, C. F., & Hollenbach, D. J. 1982, Astrophysical Journal, Letters to the Editor, 259, L97

Churchwell, E., Povich, M. S., Allen, D., et al. 2006, Astrophysical Journal, 649, 759

Churchwell, E., Watson, D. F., Povich, M. S., et al. 2007, Astrophysical Journal, 670, 428

Clark, P. C., & Bonnell, I. A. 2004, Monthly Notices of the RAS, 347, L36

Cowie, L. L., Songaila, A., & York, D. G. 1979, Astrophysical Journal, 230, 469

Cox, D. P. 1972, Astrophysical Journal, 178, 143

Crapsi, A., van Dishoeck, E. F., Hogerheijde, M. R., Pontoppidan, K. M., & Dullemond, C. P. 2008, Astronomy and Astrophysics, 486, 245

Crutcher, R. M. 1999, Astrophysical Journal, 520, 706

Crutcher, R. M., Hakobian, N., & Troland, T. H. 2009, Astrophysical Journal, 692, 844

Crutcher, R. M., Wandelt, B., Heiles, C., Falgarone, E., & Troland, T. H. 2010, Astrophysical Journal, 725, 466

Curry, C. L. 2000, Astrophysical Journal, 541, 831

Curtis, E. I., Richer, J. S., Swift, J. J., & Williams, J. P. 2010, Monthly Notices of the RAS, 408, 1516

Dalgarno, A. 2006, Proceedings of the National Academy of Science, 103, 12269

Dauphas, N., & Chaussidon, M. 2011, Annual Review of Earth and Planetary Sciences, 39, 351

Davidsen, A., Shulman, S., Fritz, G., et al. 1972, Astrophysical Journal, 177, 629

de Avillez, M. A., & Breitschwerdt, D. 2005, Astronomy and Astrophysics, 436, 585

de Graauw, T., Helmich, F. P., Phillips, T. G., et al. 2010, Astronomy and Astrophysics, 518, L6

Di Cicco, D., & Walker, S. 2009, S&T, 117, 66

Di Francesco, J., Evans, II, N. J., Caselli, P., et al. 2007, in Protostars and Planets V, ed. B. Reipurth, D. Jewitt, & K. Keil (Tucson, AZ: Univ. Arizona Press), 17

Di Francesco, J., Johnstone, D., Kirk, H., MacKenzie, T., & Ledwosinska, E. 2008, Astrophysical Journal, Supplement Series, 175, 277

Dickey, J. M., & Lockman, F. J. 1990, Annual Review of Astronomy and Astrophysics, 28, 215

Diehl, R., Halloin, H., Kretschmer, K., et al. 2006, Nature, 439, 45

Dole, H., Lagache, G., Puget, J.-L., et al. 2006, Astronomy and Astrophysics, 451, 417

Doty, S. D., Schöier, F. L., & van Dishoeck, E. F. 2004, Astronomy and Astrophysics, 418, 1021

Doty, S. D., van Dishoeck, E. F., van der Tak, F. F. S., & Boonman, A. M. S. 2002, Astronomy and Astrophysics, 389, 446

Draine, B. T. 1980, Astrophysical Journal, 241, 1021

Draine, B. T., & McKee, C. F. 1993, Annual Review of Astronomy and Astrophysics, 31, 373

Draine, B. T., Roberge, W. G., & Dalgarno, A. 1983, Astrophysical Journal, 264, 485

Dunham, M. M., Chen, X., Arce, H. G., et al. 2011, Astrophysical Journal, 742, 1

Elitzur, M., & de Jong, T. 1978, Astronomy and Astrophysics, 67, 323

Elitzur, M., & Watson, W. D. 1978, Astronomy and Astrophysics, 70, 443

Elliott, K. H. 1973, Astronomy and Astrophysics, 26, 279

Elliott, K. H., & Meaburn, J. 1970, Astrophysics and Space Science, 7, 252

Elmegreen, B. G. 1985, Astrophysical Journal, 299, 196

—. 2000, Astrophysical Journal, 530, 277

Elmegreen, B. G., & Lada, C. J. 1977, Astrophysical Journal, 214, 725

Elmegreen, B. G., & Scalo, J. 2004, Annual Review of Astronomy and Astrophysics, 42, 211

Eng, C. 2002, PhD thesis, University of Illinois at Urbana-Champaign

Enoch, M. L., Evans, II, N. J., Sargent, A. I., et al. 2008, Astrophysical Journal, 684, 1240

Enoch, M. L., Lee, J.-E., Harvey, P., Dunham, M. M., & Schnee, S. 2010, Astrophysical Journal, Letters to the Editor, 722, L33

Evans, N., Calvet, N., Cieza, L., et al. 2009, ArXiv e-prints

Falgarone, E., Pety, J., & Hily-Blant, P. 2009, Astronomy and Astrophysics, 507, 355

Falgarone, E., & Puget, J. L. 1986, Astronomy and Astrophysics, 162, 235

Fejes, I., & Wesselius, P. R. 1973, Astronomy and Astrophysics, 24, 1

Ferkinhoff, C., Nikola, T., Parshley, S. C., et al. 2010, in Society of Photo-Optical Instrumentation Engineers (SPIE) Conference Series, Vol. 7741, Society of Photo-Optical Instrumentation Engineers (SPIE) Conference Series

Ferriere, K. M., Mac Low, M.-M., & Zweibel, E. G. 1991, Astrophysical Journal, 375, 239

Ferrini, F., Marchesoni, F., & Vulpiani, A. 1983, Astrophysics and Space Science, 96, 83

Fűrész, G., Hartmann, L. W., Megeath, S. T., Szentgyorgyi, A. H., & Hamden, E. T. 2008, Astrophysical Journal, 676, 1109

Fiedler, R. A., & Mouschovias, T. C. 1993, Astrophysical Journal, 415, 680

Fiege, J. D., & Pudritz, R. E. 2000, Monthly Notices of the RAS, 311, 105

Field, G. B. 1978, in IAU Colloq. 52: Protostars and Planets, ed. T. Gehrels (Tucson, AZ: Univ. Arizona Press), 243

Field, G. B., Blackman, E. G., & Keto, E. R. 2008, Monthly Notices of the RAS, 385, 181

Finkbeiner, D. P. 2003, Astrophysical Journal, Supplement Series, 146, 407

Flower, D. R., Pineau Des Forêts, G., & Walmsley, C. M. 2007, Astronomy and Astrophysics, 474, 923

Franco, G. A. P. 1988, Astronomy and Astrophysics, 202, 173

Fried, P. M., Nousek, J. A., Sanders, W. T., & Kraushaar, W. L. 1980, Astrophysical Journal, 242, 987

Frisch, P. C., Sembach, K., & York, D. G. 1990, Astrophysical Journal, 364, 540

Gammie, C. F., & Ostriker, E. C. 1996, Astrophysical Journal, 466, 814

Gardner, J. P., Mather, J. C., Clampin, M., et al. 2006, Space Sci. Rev., 123, 485

Garmire, G. P., Nousek, J. A., Apparao, K. M. V., et al. 1992, Astrophysical Journal, 399, 694

Gazol, A., Vázquez-Semadeni, E., & Kim, J. 2005, Astrophysical Journal, 630, 911

Gir, B.-Y., Blitz, L., & Magnani, L. 1994, Astrophysical Journal, 434, 162

Glover, S. C. O., & Mac Low, M.-M. 2011, Monthly Notices of the RAS, 412, 337

Godard, B., Falgarone, E., & Pineau Des Forêts, G. 2009, Astronomy and Astrophysics, 495, 847

Goicoechea, J. R., Pety, J., Gerin, M., Hily-Blant, P., & Le Bourlot, J. 2009, Astronomy and Astrophysics, 498, 771

Goldreich, P., & Kwan, J. 1974, Astrophysical Journal, 189, 441

Goldsmith, P. F. 2001, Astrophysical Journal, 557, 736

Goldsmith, P. F., Heyer, M., Narayanan, G., et al. 2008, Astrophysical Journal, 680, 428

Goldsmith, P. F., Velusamy, T., Li, D., & Langer, W. D. 2010, Astrophysical Journal, 715, 1370

Goodman, A. A., Bastien, P., Menard, F., & Myers, P. C. 1990, Astrophysical Journal, 359, 363

Goudis, C. 1982, The Orion Complex: A Case Study of Interstellar Matter (Dordrecht: Reidel)

Green, D. A. 1991, Monthly Notices of the RAS, 253, 350

Green, D. A., & Padman, R. 1993, Monthly Notices of the RAS, 263, 535

Guo, Z., Burrows, D. N., Sanders, W. T., Snowden, S. L., & Penprase, B. E. 1995, Astrophysical Journal, 453, 256

Güsten, R., Nyman, L. Å., Schilke, P., et al. 2006, Astronomy and Astrophysics, 454, L13

Hacar, A., & Tafalla, M. 2011, Astronomy and Astrophysics, 533, A34

Haffner, L. M., Reynolds, R. J., Tufte, S. L., et al. 2003, Astrophysical Journal, Supplement Series, 149, 405

Harper, G. M., Brown, A., & Guinan, E. F. 2008, Astronomical Journal, 135, 1430

Hartmann, D., & Burton, W. B. 1997, Atlas of Galactic Neutral Hydrogen (Cambridge: Cambridge Univ. Press)

Hartmann, L. 2002, Astrophysical Journal, 578, 914

Hartmann, L., Ballesteros-Paredes, J., & Bergin, E. A. 2001, Astrophysical Journal, 562, 852

Hartmann, L., & Burkert, A. 2007, Astrophysical Journal, 654, 988

Heap, S. R., Lanz, T., & Hubeny, I. 2006, Astrophysical Journal, 638, 409

Hearty, T., Fernández, M., Alcalá, J. M., Covino, E., & Neuhäuser, R. 2000, Astronomy and Astrophysics, 357, 681

Heiles, C. 1976, Astrophysical Journal, Letters to the Editor, 208, L137

—. 1979, Astrophysical Journal, 229, 533

—. 1987, Astrophysical Journal, 315, 555

—. 1989, Astrophysical Journal, 336, 808

—. 1996, Astrophysical Journal, 462, 316

—. 1997, Astrophysical Journal, Supplement Series, 111, 245

Heiles, C., & Habing, H. J. 1974, Astronomy and Astrophysics, Supplement Series, 14, 1

Heiles, C., Haffner, L. M., & Reynolds, R. J. 1999, in Astronomical Society of the Pacific Conference Series, Vol. 168, New Perspectives on the Interstellar Medium, ed. A. R. Taylor, T. L. Landecker, & G. Joncas (San Francisco, CA: ASP), 211

Heiles, C., Haffner, L. M., Reynolds, R. J., & Tufte, S. L. 2000, Astrophysical Journal, 536, 335

Heithausen, A., Bertoldi, F., & Bensch, F. 2002, Astronomy and Astrophysics, 383, 591

Heitsch, F., Burkert, A., Hartmann, L. W., Slyz, A. D., & Devriendt, J. E. G. 2005, Astrophysical Journal, Letters to the Editor, 633, L113

Heitsch, F., & Hartmann, L. 2008, Astrophysical Journal, 689, 290

Heitsch, F., Hartmann, L. W., & Burkert, A. 2008a, Astrophysical Journal, 683, 786

Heitsch, F., Hartmann, L. W., Slyz, A. D., Devriendt, J. E. G., & Burkert, A. 2008b, Astrophysical Journal, 674, 316

Heitsch, F., Mac Low, M., & Klessen, R. S. 2001, Astrophysical Journal, 547, 280

Hennebelle, P., & Audit, E. 2007, Astronomy and Astrophysics, 465, 431

Hennebelle, P., Banerjee, R., Vázquez-Semadeni, E., Klessen, R. S., & Audit, E. 2008, Astronomy and Astrophysics, 486, L43

Hennebelle, P., & Chabrier, G. 2011, Astrophysical Journal, Letters to the Editor, 743, L29

Hennebelle, P., Mac Low, M.-M., & Vazquez-Semadeni, E. 2009, in Structure Formation in Astrophysics, ed. G. Chabrier (Cambridge University Press), 205

Hennebelle, P., & Pérault, M. 1999, Astronomy and Astrophysics, 351, 309

Herrera, C. N., Boulanger, F., Nesvadba, N. P. H., & Falgarone, E. 2012, Astronomy and Astrophysics, 538, L9

Heyer, M., Krawczyk, C., Duval, J., & Jackson, J. M. 2009, Astrophysical Journal, 699, 1092

Heyer, M. H., Brunt, C., Snell, R. L., et al. 1998, Astrophysical Journal, Supplement Series, 115, 241

Heyer, M. H., & Brunt, C. M. 2004, Astrophysical Journal, Letters to the Editor, 615, L45

Heyer, M. H., Vrba, F. J., Snell, R. L., et al. 1987, Astrophysical Journal, 321, 855

Heyminck, S., Güsten, R., Hartogh, P., et al. 2008, in Society of Photo-Optical Instrumentation Engineers (SPIE) Conference Series, Vol. 7014, Society of Photo-Optical Instrumentation Engineers (SPIE) Conference Series

Hezareh, T., Houde, M., McCoey, C., Vastel, C., & Peng, R. 2008, Astrophysical Journal, 684, 1221

Hillenbrand, L. A., & Hartmann, L. W. 1998, Astrophysical Journal, 492, 540

Hirota, T., Bushimata, T., Choi, Y. K., et al. 2007, Publications of the ASJ, 59, 897

Hoare, M. G., Kurtz, S. E., Lizano, S., Keto, E., & Hofner, P. 2007, in Protostars and Planets V, ed. B. Reipurth, D. Jewitt, & K. Keil (Tucson, AZ: Univ. Arizona Press), 181–196

Hobbs, L. M. 1969, Astrophysical Journal, 157, 135

Hobbs, L. M., Penprase, B. E., Welty, D. E., Blitz, L., & Magnani, L. 1988, Astrophysical Journal, 327, 356

Høg, E., Fabricius, C., Makarov, V. V., et al. 2000, Astronomy and Astrophysics, 355, L27

Hollenbach, D., & McKee, C. F. 1989, Astrophysical Journal, 342, 306

Houde, M., Dowell, C. D., Hildebrand, R. H., et al. 2004, Astrophysical Journal, 604, 717

Hsu, W., Hartmann, L., Heitsch, F., & Gómez, G. C. 2010, Astrophysical Journal, 721, 1531

Humphreys, R. M. 1978, Astrophysical Journal, Supplement Series, 38, 309

Inutsuka, S., & Miyama, S. M. 1992, Astrophysical Journal, 388, 392

—. 1997, Astrophysical Journal, 480, 681

Isobe, S. 1973, in IAU Symposium, Vol. 52, Interstellar Dust and Related Topics, ed. J. M. Greenberg & H. C. van de Hulst (Dordrecht: Reidel), 433

Jijina, J., Myers, P. C., & Adams, F. C. 1999, Astrophysical Journal, Supplement Series, 125, 161

Jo, Y.-S., Min, K.-W., Seon, K.-I., Edelstein, J., & Han, W. 2011, Astrophysical Journal, 738, 91

Johnson, P. G. 1978, Monthly Notices of the RAS, 184, 727

Johnstone, D., & Bally, J. 1999, Astrophysical Journal, Letters to the Editor, 510, L49

Johnstone, D., Fiege, J. D., Redman, R. O., Feldman, P. A., & Carey, S. J. 2003, Astrophysical Journal, Letters to the Editor, 588, L37

Johnstone, D., Wilson, C. D., Moriarty-Schieven, G., et al. 2000, Astrophysical Journal, 545, 327

Kalberla, P. M. W., Burton, W. B., Hartmann, D., et al. 2005, Astronomy and Astrophysics, 440, 775

Kalberla, P. M. W., & Kerp, J. 2009, Annual Review of Astronomy and Astrophysics, 47, 27

Kasemann, C., Güsten, R., Heyminck, S., et al. 2006, in Society of Photo-Optical Instrumentation Engineers (SPIE) Conference Series, Vol. 6275, Society of Photo-Optical Instrumentation Engineers (SPIE) Conference Series

Kaufman, M. J., & Neufeld, D. A. 1996a, Astrophysical Journal, 456, 611

—. 1996b, Astrophysical Journal, 456, 250

Kaufman, M. J., Wolfire, M. G., & Hollenbach, D. J. 2006, Astrophysical Journal, 644, 283

Kaufman, M. J., Wolfire, M. G., Hollenbach, D. J., & Luhman, M. L. 1999, Astrophysical Journal, 527, 795

Kenyon, S. J., Gómez, M., & Whitney, B. A. 2008, in Handbook of Star Forming Regions, Volume I, ed. Reipurth, B. (San Francisco, CA: ASP Monograph Publications), 405

Kharchenko, N. V., Scholz, R.-D., Piskunov, A. E., Röser, S., & Schilbach, E. 2007, Astronomische Nachrichten, 328, 889

Kirk, H., Johnstone, D., & Di Francesco, J. 2006, Astrophysical Journal, 646, 1009

Klein, R., Poglitsch, A., Raab, W., et al. 2010, in Society of Photo-Optical Instrumentation Engineers (SPIE) Conference Series, Vol. 7735, Society of Photo-Optical Instrumentation Engineers (SPIE) Conference Series

Klessen, R. S., & Burkert, A. 2001, Astrophysical Journal, 549, 386

Klessen, R. S., Heitsch, F., & Mac Low, M. 2000, Astrophysical Journal, 535, 887

Komljenovic, P. T., Basu, S., & Johnstone, D. 1999, in Astronomical Society of the Pacific Conference Series, Vol. 168, New Perspectives on the Interstellar Medium, ed. A. R. Taylor, T. L. Landecker, & G. Joncas (San Francisco, CA: ASP), 299

Kompaneets, A. S. 1960, Soviet Physics Doklady, 5, 46

Koo, B.-C., & McKee, C. F. 1990, Astrophysical Journal, 354, 513

Korpi, M. J., Brandenburg, A., Shukurov, A., & Tuominen, I. 1999, Astronomy and Astrophysics, 350, 230

Koyama, H., & Inutsuka, S. 2000, Astrophysical Journal, 532, 980

—. 2002, Astrophysical Journal, Letters to the Editor, 564, L97

Kramer, C., Stutzki, J., Rohrig, R., & Corneliussen, U. 1998, Astronomy and Astrophysics, 329, 249

Kregenow, J., Edelstein, J., Korpela, E. J., et al. 2006, Astrophysical Journal, Letters to the Editor, 644, L167

Kroupa, P. 2001, Monthly Notices of the RAS, 322, 231

Krumholz, M. R., Matzner, C. D., & McKee, C. F. 2006, Astrophysical Journal, 653, 361

Krumholz, M. R., & McKee, C. F. 2008, Nature, 451, 1082

Kudoh, T., & Basu, S. 2011, Astrophysical Journal, 728, 123

Kulkarni, S. R., & Heiles, C. 1988, in Galactic and Extragalactic Radio Astronomy, ed. Kellermann, K. I. & Verschuur, G. L. (Berlin:Springer), 95

Kumar, A., & Fisher, R. T. 2013, Monthly Notices of the RAS, 431, 455

Kun, M., Aoyama, H., Yoshikawa, N., et al. 2001, Publications of the ASJ, 53, 1063

Kun, M., Prusti, T., Nikolić, S., Johansson, L. E. B., & Walton, N. A. 2004, Astronomy and Astrophysics, 418, 89

Lada, C. J. 1987, in IAU Symposium, Vol. 115, Star Forming Regions, ed. M. Peimbert & J. Jugaku, 1–17

Lada, C. J., Alves, J., & Lada, E. A. 1999, Astrophysical Journal, 512, 250

Lada, C. J., Alves, J. F., & Lombardi, M. 2007, in Protostars and Planets V, ed. B. Reipurth, D. Jewitt, & K. Keil (Tucson, AZ: Univ. Arizona Press), 3

Lada, C. J., & Lada, E. A. 2003, Annual Review of Astronomy and Astrophysics, 41, 57

Lallement, R., Welsh, B. Y., Vergely, J. L., Crifo, F., & Sfeir, D. 2003, Astronomy and Astrophysics, 411, 447

Larson, R. B. 1969, Monthly Notices of the RAS, 145, 271

—. 1981, Monthly Notices of the RAS, 194, 809

—. 1985, Monthly Notices of the RAS, 214, 379

Lazarian, A. 2005, in American Institute of Physics Conference Series, Vol. 784, Magnetic Fields in the Universe: From Laboratory and Stars to Primordial Structures., ed. E. M. de Gouveia dal Pino, G. Lugones, & A. Lazarian, 42–53

Ledoux, P. 1951, Ann. Astrophy., 14, 438

Lee, H.-T., & Chen, W. P. 2009, Astrophysical Journal, 694, 1423

Lepp, S., & Shull, J. M. 1983, Astrophysical Journal, 270, 578

Lesaffre, P., Pineau des Forêts, G., Godard, B., et al. 2013, Astronomy and Astrophysics, 550, A106

Li, J. Z., Hu, J. Y., & Chen, W. P. 2000, Astronomy and Astrophysics, 356, 157

Li, P. S., Norman, M. L., Mac Low, M., & Heitsch, F. 2004, Astrophysical Journal, 605, 800

Li, Z. 2001, Astrophysical Journal, 556, 813

Li, Z., & Nakamura, F. 2006, Astrophysical Journal, Letters to the Editor, 640, L187

Lin, C. C., Mestel, L., & Shu, F. H. 1965, Astrophysical Journal, 142, 1431

Lintott, C. J., & Rawlings, J. M. C. 2006, Astronomy and Astrophysics, 448, 425

Liszt, H. 2003, Astronomy and Astrophysics, 398, 621

Lombardi, M., Alves, J., & Lada, C. J. 2010, Astronomy and Astrophysics, 519, L7

Long, K. S., Patterson, J. R., Moore, W. E., & Garmire, G. P. 1977, Astrophysical Journal, 212, 427

Loren, R. B. 1989, Astrophysical Journal, 338, 902

Mac Low, M. 1999, Astrophysical Journal, 524, 169

Mac Low, M., & Klessen, R. S. 2004, Reviews of Modern Physics, 76, 125

Mac Low, M., Klessen, R. S., Burkert, A., & Smith, M. D. 1998, Physical Review Letters, 80, 2754

Mac Low, M.-M., & McCray, R. 1988, Astrophysical Journal, 324, 776

Mac Low, M.-M., McCray, R., & Norman, M. L. 1989, Astrophysical Journal, 337, 141

Madsen, G. J., Reynolds, R. J., & Haffner, L. M. 2006, Astrophysical Journal, 652, 401

Magnani, L., Blitz, L., & Mundy, L. 1985, Astrophysical Journal, 295, 402

Magnani, L., & de Vries, C. P. 1986, Astronomy and Astrophysics, 168, 271

Magnani, L., Hartmann, D., Holcomb, S. L., Smith, L. E., & Thaddeus, P. 2000, Astrophysical Journal, 535, 167

Magnani, L., Hartmann, D., & Speck, B. G. 1996, Astrophysical Journal, Supplement Series, 106, 447

Maret, S., & Bergin, E. A. 2007, Astrophysical Journal, 664, 956

Marschall, L. A., & Hobbs, L. M. 1972, Astrophysical Journal, 173, 43

Marshall, F. J., & Clark, G. W. 1984, Astrophysical Journal, 287, 633

Mathewson, D. S., & Ford, V. L. 1970, MmRAS, 74, 139

Matzner, C. D. 2002, Astrophysical Journal, 566, 302

—. 2007, Astrophysical Journal, 659, 1394

McCammon, D., Burrows, D. N., Sanders, W. T., & Kraushaar, W. L. 1983, Astrophysical Journal, 269, 107

McCray, R., & Kafatos, M. 1987, Astrophysical Journal, 317, 190

McKee, C. F., & Ostriker, E. C. 2007, Annual Review of Astronomy and Astrophysics, 45, 565

McKee, C. F., & Tan, J. C. 2003, Astrophysical Journal, 585, 850

McKee, C. F., van Buren, D., & Lazareff, B. 1984, Astrophysical Journal, Letters to the Editor, 278, L115

Meaburn, J. 1965, Nature, 208, 575

—. 1967, ZAp, 65, 93

Menon, T. K. 1957, in IAU Symposium, Vol. 4, Radio astronomy, ed. H. C. van de Hulst (Cambridge: Cambridge University Press), 56

Men'shchikov, A., André, P., Didelon, P., et al. 2010, Astronomy and Astrophysics, 518, L103

Menten, K. M., Reid, M. J., Forbrich, J., & Brunthaler, A. 2007, Astronomy and Astrophysics, 474, 515

Mestel, L. 1966, Monthly Notices of the RAS, 133, 265

Misiriotis, A., Xilouris, E. M., Papamastorakis, J., Boumis, P., & Goudis, C. D. 2006, Astronomy and Astrophysics, 459, 113

Miville-Deschênes, M.-A., & Lagache, G. 2005, Astrophysical Journal, Supplement Series, 157, 302

Mohr, P. J., Taylor, B. N., & Newell, D. B. 2012, Reviews of Modern Physics, 84, 1527

Molinari, S., Swinyard, B., Bally, J., et al. 2010, Astronomy and Astrophysics, 518, L100

Moriarty-Schieven, G. H., Johnstone, D., Bally, J., & Jenness, T. 2006, Astrophysical Journal, 645, 357

Motte, F., Andre, P., & Neri, R. 1998, Astronomy and Astrophysics, 336, 150

Mouschovias, T. C., & Spitzer, Jr., L. 1976, Astrophysical Journal, 210, 326

Mouschovias, T. C., & Tassis, K. 2009, Monthly Notices of the RAS, 400, L15

Mullan, D. J. 1971, Monthly Notices of the RAS, 153, 145

Murray, N., & Rahman, M. 2010, Astrophysical Journal, 709, 424

Myers, P. C. 2009, Astrophysical Journal, 700, 1609

Myers, P. C., Dame, T. M., Thaddeus, P., et al. 1986, Astrophysical Journal, 301, 398

Myers, P. C., Ladd, E. F., & Fuller, G. A. 1991, Astrophysical Journal, Letters to the Editor, 372, L95

Nagai, T., Inutsuka, S.-I., & Miyama, S. M. 1998, Astrophysical Journal, 506, 306

Nakamura, F., Hanawa, T., & Nakano, T. 1993, Publications of the ASJ, 45, 551

Nakano, T. 1976, Publications of the ASJ, 28, 355

Naranan, S., Shulman, S., Friedman, H., & Fritz, G. 1976, Astrophysical Journal, 208, 718

Nelson, R. P., & Papaloizou, J. C. B. 1993, Monthly Notices of the RAS, 265, 905

Neufeld, D. A., & Kaufman, M. J. 1993, Astrophysical Journal, 418, 263

Neugebauer, G., Habing, H. J., van Duinen, R., et al. 1984, Astrophysical Journal, Letters to the Editor, 278, L1

Nousek, J. A., Fried, P. M., Sanders, W. T., & Kraushaar, W. L. 1982, Astrophysical Journal, 258, 83

Nozawa, S., Mizuno, A., Teshima, Y., Ogawa, H., & Fukui, Y. 1991, Astrophysical Journal, Supplement Series, 77, 647

Nutter, D., & Ward-Thompson, D. 2007, Monthly Notices of the RAS, 374, 1413

O'Dell, C. R., Ferland, G. J., Porter, R. L., & van Hoof, P. A. M. 2011, Astrophysical Journal, 733, 9

O'dell, C. R., York, D. G., & Henize, K. G. 1967, Astrophysical Journal, 150, 835

Omukai, K. 2007, Publications of the ASJ, 59, 589

Onishi, T., Mizuno, A., Kawamura, A., Ogawa, H., & Fukui, Y. 1996, Astrophysical Journal, 465, 815

Oort, J. H. 1932, Bull. Astron. Inst. Netherlands, 6, 249

Ossenkopf, V., & Mac Low, M. 2002, Astronomy and Astrophysics, 390, 307

Ostriker, E. C., Stone, J. M., & Gammie, C. F. 2001, Astrophysical Journal, 546, 980

Ostriker, J. 1964, Astrophysical Journal, 140, 1056

Padoan, P., Juvela, M., Goodman, A. A., & Nordlund, Å. 2001, Astrophysical Journal, 553, 227

Padoan, P., Juvela, M., Kritsuk, A., & Norman, M. L. 2009, Astrophysical Journal, Letters to the Editor, 707, L153

Padoan, P., & Nordlund, Å. 1999, Astrophysical Journal, 526, 279

—. 2002, Astrophysical Journal, 576, 870

—. 2011, Astrophysical Journal, 730, 40

Padoan, P., Nordlund, Å., Kritsuk, A. G., Norman, M. L., & Li, P. S. 2007, Astrophysical Journal, 661, 972

Padoan, P., Zweibel, E., & Nordlund, Å. 2000, Astrophysical Journal, 540, 332

Palous, J., Franco, J., & Tenorio-Tagle, G. 1990, Astronomy and Astrophysics, 227, 175

Pan, L., & Padoan, P. 2009, Astrophysical Journal, 692, 594

Parker, E. N. 1966, Astrophysical Journal, 145, 811

Penprase, B. E. 1992, Astrophysical Journal, Supplement Series, 83, 273

—. 1993, Astrophysical Journal, Supplement Series, 88, 433

Penprase, B. E., Blades, J. C., Danks, A. C., & Crane, P. 1990, Astrophysical Journal, 365, 241

Penston, M. V. 1969, Monthly Notices of the RAS, 145, 457

Pickering, W. H. 1890, The Sidereal Messenger, 9, 2

Pilbratt, G. L., Riedinger, J. R., Passvogel, T., et al. 2010, Astronomy and Astrophysics, 518, L1

Pineda, J. E., Goodman, A. A., Arce, H. G., et al. 2010, Astrophysical Journal, Letters to the Editor, 712, L116

Pineda, J. E., Arce, H. G., Schnee, S., et al. 2011, Astrophysical Journal, 743, 201

Planck Collaboration, Ade, P. A. R., Aghanim, N., et al. 2013, ArXiv e-prints

Pon, A., Johnstone, D., & Heitsch, F. 2011, Astrophysical Journal, 740, 88

Pon, A., Johnstone, D., & Kaufman, M. J. 2012a, Astrophysical Journal, 748, 25

Pon, A., Plume, R., Friesen, R. K., et al. 2009, Astrophysical Journal, 698, 1914

Pon, A., Toalá, J. A., Johnstone, D., et al. 2012b, Astrophysical Journal, 756, 145

Quillen, A. C., Thorndike, S. L., Cunningham, A., et al. 2005, Astrophysical Journal, 632, 941

Rand, R. J., & Lyne, A. G. 1994, Monthly Notices of the RAS, 268, 497

Rathborne, J. M., Jackson, J. M., & Simon, R. 2006, Astrophysical Journal, 641, 389

Raymond, J. C. 1976, PhD thesis, Univ. Wisconsin, Madison

Remijan, A. J., Markwick-Kemper, A., & ALMA Working Group on Spectral Line Frequencies. 2007, in Bulletin of the American Astronomical Society, Vol. 39, American Astronomical Society Meeting Abstracts, 963

Reynolds, R. J., & Ogden, P. M. 1979, Astrophysical Journal, 229, 942

Reynolds, R. J., Roesler, F. L., & Scherb, F. 1974, Astrophysical Journal, Letters to the Editor, 192, L53

Richter, M. J., Ennico, K. A., McKelvey, M. E., & Seifahrt, A. 2010, in Society of Photo-Optical Instrumentation Engineers (SPIE) Conference Series, Vol. 7735, Society of Photo-Optical Instrumentation Engineers (SPIE) Conference Series

Riess, A. G., Filippenko, A. V., Challis, P., et al. 1998, Astronomical Journal, 116, 1009

Robitaille, T. P., & Whitney, B. A. 2010, Astrophysical Journal, Letters to the Editor, 710, L11

Ryden, B. 2003, Introduction to cosmology (Addison Wesley)

Ryu, K., Min, K.-W., Park, J.-W., et al. 2006, Astrophysical Journal, Letters to the Editor, 644, L185

Sadavoy, S. I., Di Francesco, J., Bontemps, S., et al. 2010, Astrophysical Journal, 710, 1247

Sadavoy, S. I., di Francesco, J., André, P., et al. 2012, Astronomy and Astrophysics, 540, A10

Sakai, N., Shiino, T., Hirota, T., Sakai, T., & Yamamoto, S. 2010, Astrophysical Journal, Letters to the Editor, 718, L49

Salpeter, E. E. 1955, Astrophysical Journal, 121, 161

Sandstrom, K. M., Peek, J. E. G., Bower, G. C., Bolatto, A. D., & Plambeck, R. L. 2007, Astrophysical Journal, 667, 1161

Savage, B. D., & Jenkins, E. B. 1972, Astrophysical Journal, 172, 491

Scalo, J. M. 1985, in Protostars and Planets II, ed. D. C. Black & M. S. Matthews (Tucson, AZ: Univ. Arizona Press), 201

Schieven, G., ed. 2012, Observing with ALMA: A Primer for Early Science, ALMA Doc. 1.1, ver. 1.1

Schmid-Burgk, J. 1967, Astrophysical Journal, 149, 727

Schnee, S., Di Francesco, J., Enoch, M., et al. 2012, Astrophysical Journal, 745, 18

Schneider, N., Csengeri, T., Bontemps, S., et al. 2010, Astronomy and Astrophysics, 520, A49

Schneider, S., & Elmegreen, B. G. 1979, Astrophysical Journal, Supplement Series, 41, 87

Schöier, F. L., van der Tak, F. F. S., van Dishoeck, E. F., & Black, J. H. 2005, Astronomy and Astrophysics, 432, 369

Sebring, T. 2010, in Society of Photo-Optical Instrumentation Engineers (SPIE) Conference Series, Vol. 7733, Society of Photo-Optical Instrumentation Engineers (SPIE) Conference Series

Sellgren, K., Werner, M. W., Ingalls, J. G., et al. 2010, Astrophysical Journal, Letters to the Editor, 722, L54

Shields, G. A. 1990, Annual Review of Astronomy and Astrophysics, 28, 525

Shu, F. H. 1977, Astrophysical Journal, 214, 488

—. 1992, The Physics of Astrophysics. Volume II: Gas Dynamics. (Mill Valley, CA: University Science Books)

Shu, F. H., Adams, F. C., & Lizano, S. 1987, Annual Review of Astronomy and Astrophysics, 25, 23

Shull, J. M., & Saken, J. M. 1995, Astrophysical Journal, 444, 663

Singh, K. P., Manchanda, R. K., Narana, S., & Sreekantan, B. V. 1982, Astrophys. Lett., 23, 47

Sivan, J. P. 1974, Astronomy and Astrophysics, Supplement Series, 16, 163

Smith, L. F., Biermann, P., & Mezger, P. G. 1978, Astronomy and Astrophysics, 66, 65

Smith, M. D., Mac Low, M., & Heitsch, F. 2000a, Astronomy and Astrophysics, 362, 333

Smith, M. D., Mac Low, M., & Zuev, J. M. 2000b, Astronomy and Astrophysics, 356, 287

Snowden, S. L., Burrows, D. N., Sanders, W. T., Aschenbach, B., & Pfeffermann, E. 1995a, Astrophysical Journal, 439, 399

Snowden, S. L., Freyberg, M. J., Plucinsky, P. P., et al. 1995b, Astrophysical Journal, 454, 643

Snowden, S. L., Egger, R., Freyberg, M. J., et al. 1997, Astrophysical Journal, 485, 125

Soker, N. 2002, Astrophysical Journal, 577, 839

Solomon, P. M., Rivolo, A. R., Barrett, J., & Yahil, A. 1987, Astrophysical Journal, 319, 730

Spitzer, L. 1978, Physical processes in the interstellar medium (Wiley, New York)

Spitzer, Jr., L. 1942, Astrophysical Journal, 95, 329

Stahler, S. W., & Palla, F. 2005, The Formation of Stars (John Wiley + Sons, Inc)

Staveley-Smith, L., Sault, R. J., Hatzidimitriou, D., Kesteven, M. J., & McConnell, D. 1997, Monthly Notices of the RAS, 289, 225

Stil, J., Wityk, N., Ouyed, R., & Taylor, A. R. 2009, Astrophysical Journal, 701, 330

Stodólkiewicz, J. S. 1963, Acta Astron., 13, 30

Stone, J. M., Ostriker, E. C., & Gammie, C. F. 1998, Astrophysical Journal, Letters to the Editor, 508, L99

Sugitani, K., Nakamura, F., Watanabe, M., et al. 2011, Astrophysical Journal, 734, 63

Swift, J. J., & Welch, W. J. 2008, Astrophysical Journal, Supplement Series, 174, 202

Tatematsu, K., Umemoto, T., Kameya, O., et al. 1993, Astrophysical Journal, 404, 643

Tenorio-Tagle, G., & Palous, J. 1987, Astronomy and Astrophysics, 186, 287

Tenorio-Tagle, G., Rozyczka, M., & Bodenheimer, P. 1990, Astronomy and Astrophysics, 237, 207

Tielens, A. G. G. M. 2005, The Physics and Chemistry of the Interstellar Medium (Cambridge, UK: Cambridge University Press)

Timmermann, R. 1996, Astrophysical Journal, 456, 631

Toalá, J. A., Vázquez-Semadeni, E., & Gómez, G. C. 2012, Astrophysical Journal, 744, 190

Tobin, J. J., Hartmann, L., Furesz, G., Mateo, M., & Megeath, S. T. 2009, Astrophysical Journal, 697, 1103

Tobin, J. J., Hartmann, L., Looney, L. W., & Chiang, H.-F. 2010, Astrophysical Journal, 712, 1010

Tohline, J. E. 1980, Astrophysical Journal, 239, 417

Tomisaka, K. 1992, Publications of the ASJ, 44, 177

—. 1998, Monthly Notices of the RAS, 298, 797

Tomisaka, K., & Ikeuchi, S. 1986, Publications of the ASJ, 38, 697

Troland, T. H., & Heiles, C. 1982, Astrophysical Journal, 252, 179

Vallée, J. P., & Fiege, J. D. 2006, Astrophysical Journal, 636, 332

—. 2007, Astronomical Journal, 133, 1012

van der Tak, F. F. S., Belloche, A., Schilke, P., et al. 2006, Astronomy and Astrophysics, 454, L99

van der Tak, F. F. S., & van Dishoeck, E. F. 2000, Astronomy and Astrophysics, 358, L79

van Leeuwen, F. 2007, Astronomy and Astrophysics, 474, 653

Vázquez-Semadeni, E., Banerjee, R., Gómez, G. C., et al. 2011, Monthly Notices of the RAS, 414, 2511

Vázquez-Semadeni, E., Colín, P., Gómez, G. C., Ballesteros-Paredes, J., & Watson, A. W. 2010, Astrophysical Journal, 715, 1302

Vázquez-Semadeni, E., Gómez, G. C., Jappsen, A. K., et al. 2007, Astrophysical Journal, 657, 870

Vázquez-Semadeni, E., Kim, J., Shadmehri, M., & Ballesteros-Paredes, J. 2005, Astrophysical Journal, 618, 344

Vázquez-Semadeni, E., Ryu, D., Passot, T., González, R. F., & Gazol, A. 2006, Astrophysical Journal, 643, 245

Verschuur, G. L. 1973, Astronomical Journal, 78, 573

Wakelam, V., Selsis, F., Herbst, E., & Caselli, P. 2005, Astronomy and Astrophysics, 444, 883

Ward-Thompson, D., André, P., Crutcher, R., et al. 2007, in Protostars and Planets V, ed. B. Reipurth, D. Jewitt, & K. Keil (Tucson, AZ: Univ. Arizona Press), 33–46

Weaver, R., McCray, R., Castor, J., Shapiro, P., & Moore, R. 1977, Astrophysical Journal, 218, 377

Welsh, B. Y., Sallmen, S., & Jelinsky, S. 2005, Astronomy and Astrophysics, 440, 547

West, J. L., English, J., Normandeau, M., & Landecker, T. L. 2007, Astrophysical Journal, 656, 914

Wilkins, G. W. 1989, The IAU Style Manual, International Astronomical Union

Williams, J. P., Bergin, E. A., Caselli, P., Myers, P. C., & Plume, R. 1998, Astrophysical Journal, 503, 689

Williams, J. P., & McKee, C. F. 1997, Astrophysical Journal, 476, 166

Williamson, F. O., Sanders, W. T., Kraushaar, W. L., et al. 1974, Astrophysical Journal, Letters to the Editor, 193, L133

Wolfire, M. G., Hollenbach, D., & McKee, C. F. 2010, Astrophysical Journal, 716, 1191

Wright, G. S., Reike, G., Barella, P., et al. 2008, in Society of Photo-Optical Instrumentation Engineers (SPIE) Conference Series, Vol. 7010, Society of Photo-Optical Instrumentation Engineers (SPIE) Conference Series

Wyse, A. B., & Mayall, N. U. 1942, Astrophysical Journal, 95, 24

York, D. G. 1974, Astrophysical Journal, Letters to the Editor, 193, L127

Young, E. T., Becklin, E. E., Marcum, P. M., et al. 2012, Astrophysical Journal, Letters to the Editor, 749, L17

Zinnecker, H., & Yorke, H. W. 2007, Annual Review of Astronomy and Astrophysics, 45, 481

Zuckerman, B., & Evans, II, N. J. 1974, Astrophysical Journal, Letters to the Editor, 192, L149

Zuckerman, B., & Palmer, P. 1974, Annual Review of Astronomy and Astrophysics, 12, 279

Zwicky, F. 1933, Helvetica Physica Acta, 6, 110